International Hydrology Programme

Water and Carbon Cycles in Terrestrial Ecosystems

-The Textbook for Fifteenth IHP Training Course in 2005-

Edited by Tetsuya Hiyama

Hydrospheric Atmospheric Research Center, Nagoya University

United Nations Educational Scientific and Cultural Organization

Prepared for the Fifteenth IHP Training Course on Water and Carbon Cycles in Terrestrial Ecosystems, 26 February - 11 March, 2006, Nagoya and Chiba, Japan

Working Group for IHP Training Course,
Sub-Committee for IHP,

Japan National Commission for UNESCO
Chairperson: Prof. H. Uyeda, Nagoya University

Secretariat:
Mr. K. Akiyama, Ministry of Education, Culture, Sports, Science and Technology
Mr. T. Minami, Ministry of Education, Culture, Sports, Science and Technology
Ms. T. Miwa, Ministry of Education, Culture, Sports, Science and Technology
Mr. A. Yamamoto, Nagoya University

Members:
Prof. K. Takeuchi, Yamanashi University
Prof. Y. Fukushima, Research Institute for Humanity and Nature
Mr. M. Kunitomo, Ministry of Land Infrastructure and Transport
Dr. M. Sugi, Japan Meteorological Agency
Dr. K. Nakane, National Research Institute for Earth Science and Disaster Prevention
Dr. H. Ohno, National Institute for Agro-Environmental Sciences
Prof. K. Nakamura, Nagoya University
Prof. Y. Yamaguchi, Nagoya University
Prof. Y. Ishizaka, Nagoya University
Prof. T. Hiyama, Nagoya University
Prof. A. Morimoto, Nagoya University

Published in 2006 by the Hydrospheric Atmospheric Research Center (HyARC), Nagoya University, and United Nations Educational Scientific and Cultural Organization (UNESCO)

Printed by Nagoya University COOP
ISBN: 4-9980619-6-8
Cover: *Hydrangea*

Preface

The general aim of the 15th IHP Training Course was to help participants develop their basic knowledge of water and carbon cycles in terrestrial ecosystems in finding the solution for current global environmental problems, which are of great importance for many countries. The course is part of the UNESCO International Hydrological Programme (IHP) and is held every Japanese fiscal year which starts in April. The participants, mainly from Asia-Pacific regions, are given a series of lectures and practical training for about two weeks. Until 1996, the course mainly focused on general hydrology, but since that time has concentrated on specific themes, such as snow hydrology (1998), remote sensing (1999), limnology (1999), hydrology related to head water management (2000), hydrogen and oxygen isotopes in hydrology (2002), precipitation and water resources (2003), and the effect of air pollutants on the atmospheric environment and climate change (2004).

This year, the 15th IHP Training Course with a theme of "Water and Carbon Cycles in Terrestrial Ecosystems" was held from February 26 to March 11, 2006 at Nagoya and Chiba, Japan, which included many lectures and practicals. This IHP short course focused on understanding the responses of terrestrial ecosystems to global change. Micrometeorological and biogeochemical knowledge and techniques, including the use of stable isotopes of H_2O and CO_2 and numerical modeling, are the basis for understanding the responses. The problems of terrestrial ecosystems and ways of solving them depend very much on the features of nature and human activity in the region. In this sense, participants can gain an essential and comprehensive idea of ways of planning, managing, and monitoring problems in terrestrial ecosystems in their own countries.

The 15th course included contributions from professionals/experts in universities and research institutes, led by Prof. Tetsuya Hiyama, Prof. Takeshi Ohta, Prof. Yasushi Yamaguchi, Prof. Tetsuzo Yasunari, and Dr. Eiichi Konohira of Nagoya University, Prof. Atsushi Higuchi of Chiba University, Prof. Kouki Hikosaka of Tohoku University, Prof. Hideaki Shibata of Hokkaido University, Prof. Tsutomu Yamanaka of University of Tsukuba, and Dr. Akihiko Itou of Japan Agency for Marine-Earth Science and Technology.

The course would not have been possible without management support. Dr. Giuseppe Arduino and his staff in the UNESCO Jakarta office took care of the arrangements for the participants. The IHP Training Course is continuously supported by the Ministry of Education, Culture, Sports, Science, and Technology.

November 22, 2006

Hiroshi Uyeda

Chairperson of Working Group for IHP Training Course
Director, Hydrospheric Atmospheric Research Center,
Nagoya University

Acknowlegements

I would like to express my sincere thanks to all the authors for their immense contribution to this textbook. It would not have been published without their considerable efforts. Thanks are extended to Prof. Hiroshi Uyeda, the chairperson of the working group of the IHP Training Course and Director of the Hydrospheric Atmospheric Research Center (HyARC), Nagoya University, Japan.

The support from the Japan National Commission for UNESCO, sub-committee of IHP led by Prof. Kuniyoshi Takeuchi from Yamanashi University, and the working group of IHP Training Course is highly acknowledged. Thanks are also extended to Mr. Kazuo Akiyama and Mr. Tetsuhito Minami from the Ministry of Education, Culture, Sports, Science and Technology of Japan, Mr. Akihiro Yamamoto from Nagoya University, Japan for sharing the role of secretariat, and the staff (Dr. Tae Toba, Ms. Tsuyako Mizuno, Ms. Saori Haga, and Ms. Mariko Kayaba) of HyARC, Nagoya University, Japan for their local arrangements and technical editing of this textbook.

Part of this IHP training course was co-organized by the 21st Century COE Program at Nagoya University: "Dynamics of the Sun-Earth-Life Interactive System (SELIS)." Thus in total, six candidates have been supported financially, in part, by funds from the 21st Century COE Program at Nagoya University. Finally, we thank the staff of SELIS (Ms. Kaori Iwata and others).

November 22, 2006

Tetsuya Hiyama
Hydrospheric Atmospheric Research Center,
Nagoya University

Editor

List of the contributors

Lectures

Chapter 1 Canopy-Scale Fluxes of Heat, Water Vapor, and Carbon Dioxide in Various Terrestrial Ecosystems
T. Hiyama

Chapter 2 The Water Cycle in Forested Areas
T. Ohta

Chapter 3 Biogeochemical Processes of Carbon in Forested Ecosystem
H. Shibata

Chapter 4 Biogeochemical Processes of Nitrogen in Forested Ecosystem
E. Konohira

Chapter 5 Assessment of Plant-Water Relations using Stable Isotope Tracers
T. Yamanaka

Chapter 6 Integrated use of vegetation indices and surface temperature space obtained from Earth observation satellites dataset
A. Higuchi

Chapter 7 Observation of Global Vegetation Variations by Satellite Remote Sensing
Y. Yamaguchi

Chapter 8 Role of Vegetation in the Earth Climate System
T. Yasunari

Chapter 9 Plant responses to elevated CO_2 concentration at different scales: leaf, whole plant, canopy, and population
K. Hikosaka

Chapter 10 Dynamic Global Vegetation Model - Linkage between Water and Carbon Cycles -
A. Ito

Practice Sessions

P1 Measurement and Estimation of Canopy-Scale Fluxes
T. Hiyama

P2 Satellite Measurements of Vegetation Condition and NPP
Y. Yamaguchi

P3 Satellite Measurements of Vegetation and Hydrologic Condition
A. Higuchi

Technical Tours

T1 Flux Research Site of a Secondary Forest at Seto
T. Ohta

T2 Terrestrial Environment Research Center (TERC), University of Tsukuba
T. Yamanaka

T3 Center for Environmental Remote Sensing (CEReS), Chiba University
A. Higuchi

T4 The Earth Simulator Center, JAMSTEC
A. Ito

Current address of the contributors (alphabetical order)

A. Higuchi.....Center for Environmental Remote Sensing (CEReS), Chiba University
e-mail: higu@faculty.chiba-u.jp

K. Hikosaka.....Graduate School of Life Sciences, Tohoku University
e-mail: hikosaka@mail.tains.tohoku.ac.jp

T. Hiyama.....Hydrospheric Atmospheric Research Center (HyARC),
Nagoya University
e-mail: hiyama@hyarc.nagoya-u.ac.jp

A. Itou.....Center for Global Environmental Research,
National Institute for Environmental Studies
e-mail: itoh@nies.go.jp

E. Konohira..... Nonprofit Organization Morinoza
e-mail: konohira@inacatv.ne.jp

T. Ohta.....Graduate School of Bioagricultural Sciences, Nagoya University
e-mail: takeshi@agr.nagoya-u.ac.jp

H. Shibata.....Field Science Center for Northern Biosphere, Hokkaido University
e-mail: shiba@fsc.hokudai.ac.jp

Y. Yamaguchi.....Graduate School of Environmental Studies, Nagoya University
e-mail: yasushi@nagoya-u.jp

T. Yamanaka.....Terrestrial Environment Research Center (TERC),
University of Tsukuba
e-mail: tyam@suiri.tsukuba.ac.jp

T. Yasunari.....Hydrospheric Atmospheric Research Center (HyARC),
Nagoya University
e-mail: yasunari@hyarc.nagoya-u.ac.jp

Contents

Part I

Textbook

Chapter 1

Canopy-Scale Fluxes of Heat, Water Vapor, and Carbon Dioxide in Various Terrestrial Ecosystems

Tetsuya HIYAMA
Hydrospheric Atmospheric Research Center (HyARC),
Nagoya University, Nagoya 464-8601, Japan
Tel: +81-52-789-3478
Fax: +81-52-789-3436
e-mail: hiyama@hyarc.nagoya-u.ac.jp

1.1 Introduction

This chapter briefly describes the basics of canopy-scale fluxes of heat, water vapor, and carbon dioxide in terrestrial ecosystems. The chapter first introduces temporal and spatial scales related to terrestrial ecosystems, and then describes basic equations for radiation, heat, water and carbon balances. Because canopy-scale fluxes are closely related to turbulence within the atmospheric boundary layer (ABL), the basics of the atmospheric turbulence and the key variables are presented. After explaining important flux correction methodologies, an example of flux determination over a terrestrial ecosystem is offered. Finally, land surface models (LSMs) to contribute to climate modeling are described.

Figure 1.1 shows spatial and temporal scales of physical and ecological phenomena (Wu, 1999). The important phenomena that contribute to spatial scales related to terrestrial vegetation are, from smaller to larger, 1) atmospheric turbulence, 2) atmospheric convection, 3) seasonal vegetation cycles (phenology), 4) soil moisture variations, and 5) carbon dioxide variations. 1) & 2) are directly related to canopy-scale fluxes of heat, water vapor, and carbon dioxide, and they are important phenomena for diurnal vegetation activities. 3) & 4) are determinant factors for the seasonal changes of terrestrial ecosystems themselves. Then global carbon balance and variations 5) are affected in conjunction with climate variations. Response of terrestrial ecosystems to climate variability will be introduced later in Chapter 10.

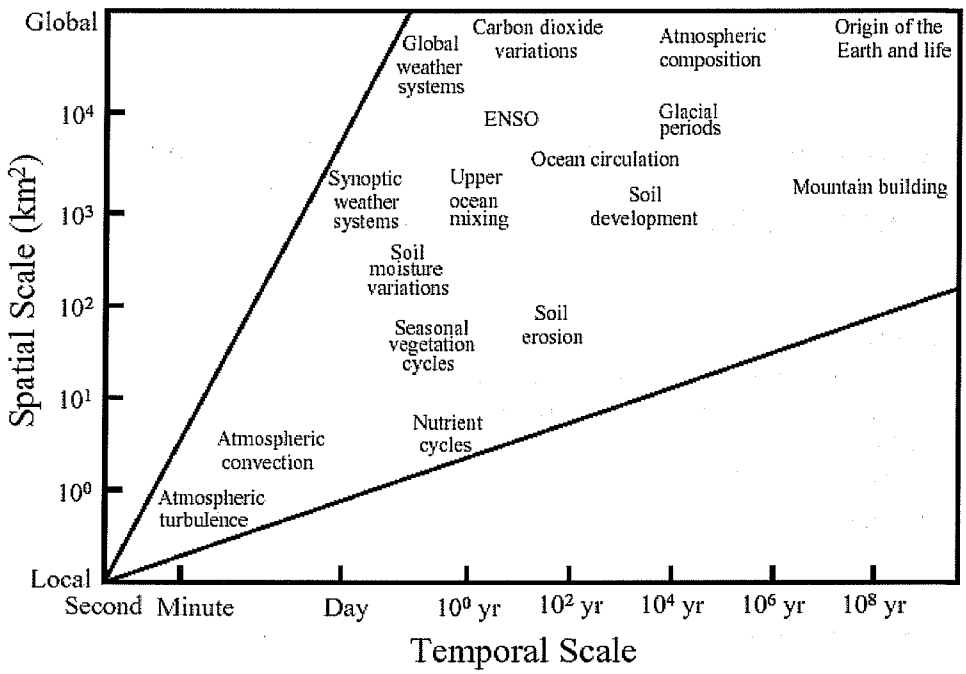

Figure 1.1 Spatial and temporal scales of physical and ecological phenomena (modified from Wu, 1999).

1.2 Basic equations

The fundamental equations representing key processes on the surface are those for radiation balance, heat balance, water balance and carbon balance. Momentum exchange is also an important factor for the heat and water balances by means of turbulent heat transport.

Short-wave radiation emitted by the sun is reflected, absorbed and transmitted by the atmosphere. For every 100 units of energy reaching earth, 46 are absorbed by the surface (Figure 1.2). Long-wave (infrared) radiation effects depend on the temperature and emissivity of the land and the atmosphere. Global mean net long-wave radiation on the surface is 15% and is upward (emitted) from the surface to the atmosphere. Thus, net radiation absorbed by the surface is 31% of the energy reaching earth.

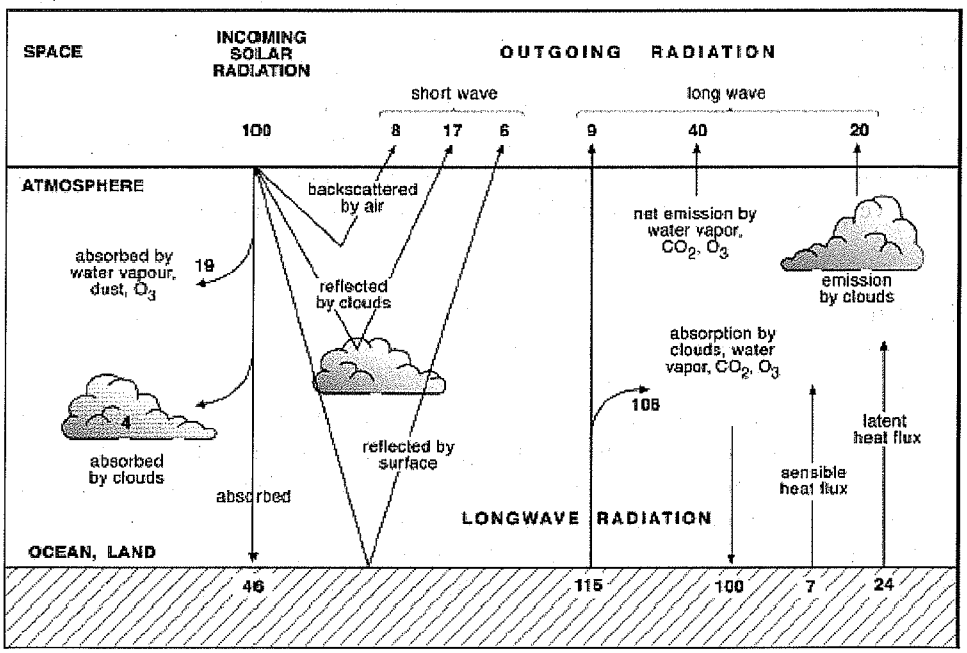

Figure 1.2 Schematic diagram of the annual mean global energy balance. Units are percentage of incoming solar radiation. The solar (short-wave) radiation fluxes are shown on the left-hand side and the terrestrial (long-wave) radiation fluxes are on the right-hand side (from Pitman, 2003).

1.2.1 Radiation balance

The surface radiation balance is defined by

$$Rn = Sd - Su + Ld - Lu = Sd(1-\alpha) + Ld - Lu \qquad (1.1)$$

where, Rn is the net radiation, Sd the downward short-wave radiation, Su the upward short-wave radiation, Ld the downward long-wave radiation, Lu the upward long-wave radiation, and α the surface albedo. Based on Figure 1.2, 31% of the total entering the global climate system is exchanged as turbulent fluxes of sensible and latent heat.

1.2.2 Heat balance

The surface heat balance is defined by

$$Rn - G - \Delta Q = H + \lambda E \qquad (1.2)$$

where, G is the soil heat flux, ΔQ the rate of change of the heat storage, H the sensible heat flux, and λE the latent heat flux. Generally the units used for

all of the elements shown in equations (1.1) and (1.2) are in W m^{-2}. Chemical energy stored during photosynthesis and released by respiration is usually omitted, and thus they are not shown in equation (1.2). The right hand side (RHS) of equation (1.2) is the total turbulent heat flux, which is important to the canopy-scale exchange process between the terrestrial ecosystem and the atmosphere. From the hydrological point of view, evapotranspiration E (kg m^{-2} s^{-1}) is a very important element but is difficult to measure regionally.

1.2.3 Water balance

The surface water balance is defined by

$$P = E + D + \Delta S \tag{1.3}$$

where, P is the precipitation, D the drainage from the surface, and ΔS the rate of change of the surface water storage. Regional scale or basin scale water balances can be checked using river runoff data. The difficulty in measurement exists for regionally distributions both in ΔS and E.

By using the atmospheric water balance, evapotranspiration E can be also calculated from a regional point of view with the following equation,

$$E = P + \frac{\partial W}{\partial t} + \nabla_H \cdot \vec{Q} \tag{1.4}$$

where, W is the precipitable water within an atmospheric column, and $\nabla_H \cdot \vec{Q}$ is the horizontal divergence of water vapor. Both W and $\nabla_H \cdot \vec{Q}$ can be evaluated using reanalysis data such as that from NCEP/NCAR (National Centers for Environmental Prediction / National Center for Atmospheric Research) (e.g. Kistler et al., 2001).

1.2.4 Carbon balance

Figure 1.3 indicates schematics of heat and carbon exchanges over terrestrial ecosystems. Because atmospheric CO_2 is absorbed during daytime photosynthesis through stomatal pores, transpiration and CO_2 transfer correlate closely. Respiration (CO_2 release) from plant bodies (surfaces of leaves, trunks, branches, and roots) is one of the sources of CO_2 from terrestrial ecosystems. Heterotrophic respiration (soil respiration or decomposition of soil organic matter, SOM) is another source of CO_2.

The surface carbon balance is defined by

$$GPP = NPP + DR \tag{1.5}$$

$$NPP = NEP + SR \tag{1.6}$$

where, GPP is the gross primary production (due to photosynthesis), NPP the net primary production, DR the dark respiration (or plant respiration), NEP the net ecosystem production, and SR the soil respiration (heterotrophic respiration).

Both *DR* and *SR* correlate with temperature, and *SR* is a function of soil moisture. Satellite remote sensing of vegetation is possible to detect chloroplast amounts or their activity through processing "vegetation indexes" (see Chapters 6 and 7). Thus, though it is difficult to estimate *NEP* directly, through some modeling *NPP* can be estimated using vegetation indexes (see Chapter 7). One of the modeling approaches is using LSMs with general circulation models (GCMs). Some important equations will be introduced in section 1.6.

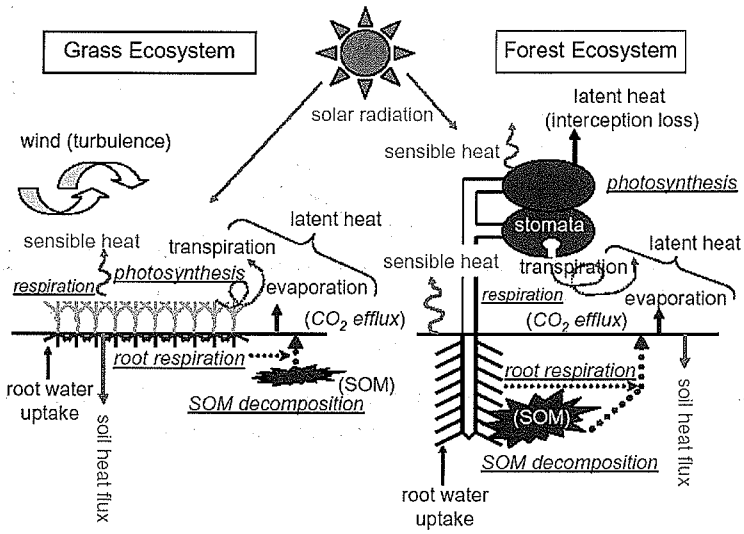

Figure 1.3 Heat and carbon exchanges over terrestrial ecosystems.

1.3 Atmospheric Boundary Layer (ABL)

ABL is the lowest part of the atmosphere. It is through the ABL that momentum, heat, water vapor, and carbon dioxide exchanges occur with the terrestrial ecosystem (or with vegetation). The most significant variation of ABL appears diurnally. Figure 1.4 shows the typical diurnal change of ABL over a land surface. In the daytime, the ABL is divided into three or four layers. From the lower to the upper part, they are called the "roughness sublayer," "surface layer," "transition layer," and "mixed layer." The most important layer for the exchanges of momentum, heat, water vapor, and carbon dioxide over the terrestrial ecosystem is the "surface layer." In this layer, vertical air motion is suppressed by the surface, and surface friction causes large differences of wind speed (wind shear) and small scale turbulence. The following sub-sections define vertical turbulent fluxes and several important variables arising within the "surface layer" in order to understand canopy-scale fluxes.

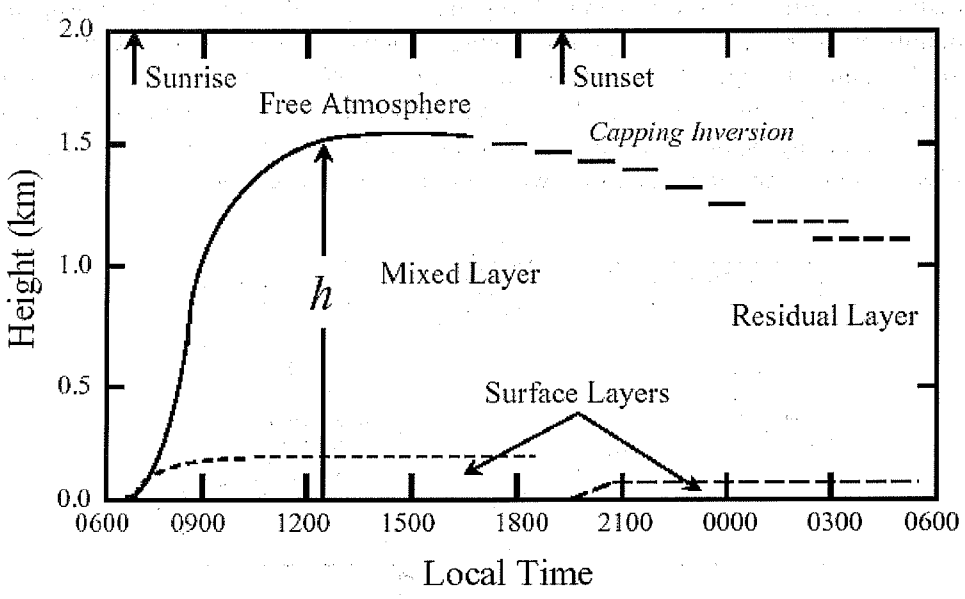

Figure 1.4 Diurnal change of the atmospheric boundary layer (ABL) over a land surface (modified from Kaimal and Finnigan, 1994).

1.3.1 Turbulence and turbulent fluxes

In the atmospheric surface layer, if the surface and flow are horizontally homogeneous, the most important exchanges in momentum, heat and mass are in the vertical direction. Vertical momentum flux τ is defined by

$$\tau = -\rho(\overline{u'w'}) \qquad (1.7)$$

where, ρ is air density, u the horizontal wind velocity, and w the vertical wind velocity. The over-bar denotes certain time averaging and prime represents the fluctuation from the mean value. τ is also referred to as Reynolds stress.

Vertical sensible heat flux H is defined by

$$H = \rho c_p(\overline{w'\theta'}) \qquad (1.8)$$

where, c_p is the specific heat of air at constant pressure (1006 $J\,kg^{-1}\,K^{-1}$), and θ the potential temperature.

Vertical latent heat flux is defined by

$$\lambda E = \rho\lambda(\overline{w'q'}) \qquad (1.9)$$

where, λ is the latent heat of vaporization of water (around 2.45×10^6 $J\,kg^{-1}$ at

20°C), E the moisture flux (evapotranspiration in units of kg m^{-2} s^{-1}), q the specific humidity. Vertical buoyancy flux H_v is also represented as

$$H_v = \rho c_p (\overline{w'\theta_v'}) \tag{1.10}$$

where, θ_v is virtual potential temperature ($\theta_v = \theta(1+0.61q)$).

Vertical flux of other scalars such as CO_2 (F_c) is similarly defined by

$$F_c = \overline{w'c'} \tag{1.11}$$

where c is the CO_2 density.

1.3.2 Turbulent scaling parameters

Besides the surface fluxes, some turbulent scaling parameters are often used to characterize surface layer turbulence. Those key parameters have frequently appeared in previous similarity theories. The Monin-Obukhov similarity theory is usually applied to the surface layer and hence is sometimes called surface layer similarity. The important turbulent scaling parameters in the theory are listed as follows.

$$u_*^2 = -(\overline{u'w'}) \tag{1.12}$$

$$\theta_* = -(\overline{w'\theta'})/u_* \tag{1.13}$$

$$\theta_{v*} = -(\overline{w'\theta_v'})/u_* \tag{1.14}$$

$$q_* = -(\overline{w'q'})/u_* \tag{1.15}$$

Here, u_* is the friction velocity, θ_* and θ_{v*} are the temperature scales, and q_* the humidity scale. The Monin-Obukhov similarity works only when the winds are not calm, and u_* is not zero.

A length scale (the Obukhov stability length) L is defined by

$$L = u_*^2 \overline{\theta_v}/(kg\theta_{v*}) \tag{1.16}$$

where, k is the von Karman constant ($\approx$ 0.4), and g the acceleration due to gravity. The Obukhov stability length L is positive for stable atmospheric conditions, negative for unstable conditions, and infinitely large for neutral conditions (Brutsaert, 1982). Originally $z = -L$ was interpreted as the height of the surface layer and it could be considered to be the height at which the shear

production is approximately equal to the buoyant energy production (see equation (1.23)).

To focus on the mixed layer turbulence, the mixed-layer similarity theory is applied. This layer is in a state of free convection, assuming calm or light winds. Mixed-layer or free convection scale for velocity w_*, which is the most important velocity scale, is defined by

$$w_*^3 = g(\overline{w'\theta_v'})h/\overline{\theta_v} \tag{1.17}$$

where h is the atmospheric boundary-layer height (Figure 1.4).

1.3.3 Conservation equations and turbulent kinetic energy

To quantitatively describe the state of the boundary layer, we should turn to the equations of fluid mechanics that describe the dynamics and thermodynamics in the atmosphere (Stull, 1988).

The set of equations governing the flow consists of four equations; those are the *conservation of momentum* (i.e. the Reynolds equation), the *conservation of mass*, the *conservation of thermal energy* (the thermodynamic or enthalpy equation), and the *equation of state* (the gas law). These equations, except for the gas law, are described by the following when the surface and flow are horizontally homogeneous.

Conservation of momentum (Reynolds equation):

$$\frac{\partial \bar{u}}{\partial t} + \bar{w}\frac{\partial \bar{u}}{\partial z} = -\frac{1}{\rho}\frac{\partial \bar{p}}{\partial x} - \frac{\partial(\overline{u'w'})}{\partial z} \tag{1.18}$$

Conservation of heat:

$$\frac{\partial \bar{\theta}}{\partial t} + \bar{w}\frac{\partial \bar{\theta}}{\partial z} = -\frac{\partial(\overline{w'\theta'})}{\partial z} \tag{1.19}$$

Conservation of water vapor:

$$\frac{\partial \bar{q}}{\partial t} + \bar{w}\frac{\partial \bar{q}}{\partial z} = -\frac{\partial(\overline{w'q'})}{\partial z} \tag{1.20}$$

Conservation of scalar such as CO_2:

$$\frac{\partial \bar{c}}{\partial t} + \bar{w}\frac{\partial \bar{c}}{\partial z} = -\frac{\partial(\overline{w'c'})}{\partial z} \tag{1.21}$$

Here t is time, p the pressure, x the horizontal position, and z the vertical position (i.e. height). In all of these equations, molecular diffusion is neglected. If we assume very simple conditions such as;

a) no horizontal variation of all turbulent variables,
b) steady state condition (the surface layer reaches equilibrium with the environment immediately), and
c) no phase change of water (evaporation and condensation) within the surface layer,

the equations from (1.18) to (1.21) can be recast as,

$$\frac{\partial(\overline{u'w'})}{\partial z} = 0 \qquad (1.18b)$$

$$\frac{\partial(\overline{w'\theta'})}{\partial z} = 0 \qquad (1.19b)$$

$$\frac{\partial(\overline{w'q'})}{\partial z} = 0 \qquad (1.20b)$$

$$\frac{\partial(\overline{w'c'})}{\partial z} = 0 \qquad (1.21b)$$

These four equations indicate the turbulent fluxes are constant in the surface layer.

In the original form of the Navier-Stokes equation (not shown here), the ratio of the inertia force to the viscous force was defined as the Reynolds number (R_e). Laboratory experiments have shown that if the value of R_e is larger than 10^4, the flow changed from laminar to turbulent. The main forces of the turbulence within the ABL are the mechanical force and buoyant force. Production, transport, and dissipation of turbulence are represented as *turbulent kinetic energy* (TKE). The relative balance of these processes determines the ability of the flow to maintain turbulence or become turbulent, and thus indicates flow stability (Stull, 1988). TKE is a measure of the turbulence within the ABL. TKE is defined by

$$e' = \frac{1}{2}(u'^2 + v'^2 + w'^2) \qquad (1.22)$$

In equation (1.22), the three-dimensional velocity components of u (longitudinal velocity component), v (transverse velocity component), and w (vertical velocity component) are considered. If we choose a coordinate system aligned with the mean wind, assume horizontal homogeneity, and neglect advection such as subsidence, then the TKE budget is shown as

$$\frac{\partial}{\partial t}\bar{e} = -\overline{u'w'}\frac{\partial \bar{u}}{\partial z} + \frac{g}{T}\overline{w'\theta'} - \frac{1}{\rho}\frac{\partial \overline{w'p'}}{\partial z} - \frac{\partial}{\partial z}\overline{w'e'} - \varepsilon \qquad (1.23)$$

(I) (II) (III) (IV) (V)

where T is the surface air temperature. The individual terms in the TKE budget

equation describe physical processes that generate turbulence (Stull, 1988). The left hand side (LHS) of equation (1.23) represents local storage of TKE. The five terms in the right hand side (RHS) of equation (1.23) are,

(I) mechanical or shear production/loss term
(II) buoyant production or consumption term
(III) pressure correlation term
(IV) turbulent transport term
(V) viscous dissipation term (conversion of TKE into heat)

The fifth term (V) of the RHS, ε, represents the rate of molecular (viscous) dissipation of TKE, and is a loss term that always exists whenever TKE is nonzero. This means that turbulence will tend to decrease and disappear with time, unless it can be generated locally or transported by mean, turbulent, or pressure processes (Stull, 1988).

1.3.4 Energy spectra and cospectra

In the ABL, and in the absence of strong thermal stratifications, the flow is generally turbulent ($R_e > 10^4$). Because the ABL is generally turbulent, a statistical approach rather than a deterministic approach is necessary (Garratt, 1992). There are several concepts that are of value when dealing with turbulence in the ABL.

a) If statistical properties are independent of time, turbulence is stationary.
b) If the flow field is statistically invariant to the horizontal direction, turbulence is homogeneous.
c) If there is no buoyancy, turbulence is isotropic at a sufficiently small scale.

Within the ABL, the spectrum of turbulent eddies extends over a wide range of sizes. Turbulent energy is gained at the expense of instabilities in a mean flow having the characteristic length scale Λ. The smallest scale is represented as viscous dissipation, and has a length scale $\eta = (\nu^3 / \varepsilon)^{1/4}$, which is called the Kolmogorov scale. Here ν is the kinematic viscosity of air, and ε is the rate of dissipation of TKE by viscosity. In 1941, Kolmogorov developed a similarity theory of turbulence (Kolmogorov two hypotheses) which is as follows.

a) At large R_e, there exists an *equilibrium range* in which the average properties of the small-scale turbulent motion are determined uniquely by ν and ε (Figure 1.5).

b) At large enough R_e, there exists an *inertial subrange*, within the *equilibrium range* in which the eddy structure is independent of energy input or viscous dissipation. In this subrange inertial transfer of energy is important and wavenumbers κ of average properties are independent of ν and determined solely by ε ($\kappa_e << \kappa << \kappa_d$; where κ_e and κ_d are the representative wavenumber scales of the energy input region and Kolmogorov scale η).

In the *inertial subrange*, the energy spectrum as a function of wavenumber (κ) is expressed as

$$E_s = a\varepsilon^{2/3}\kappa^{-5/3} \tag{1.24}$$

where a is an empirically determined constant ($\approx$ 0.5). In Figure 1.5, region (B) corresponds to the *inertial subrange*.

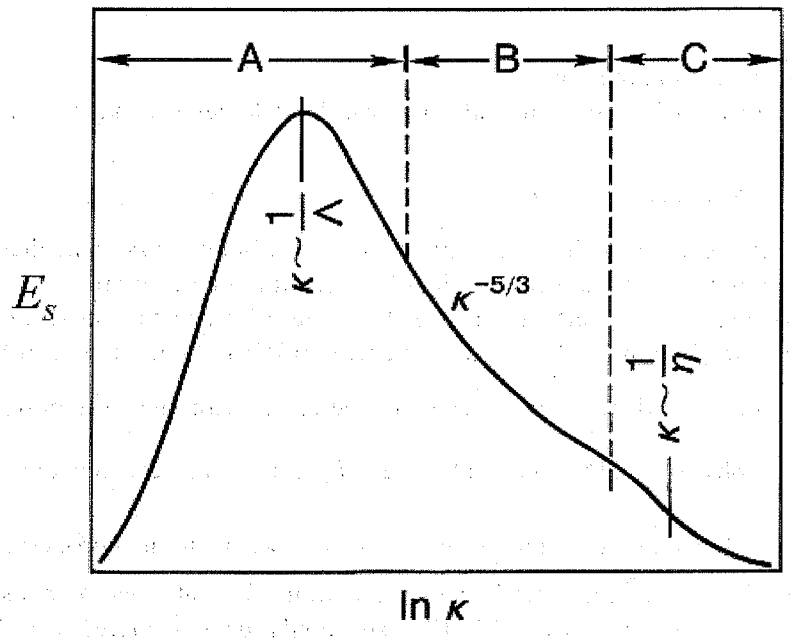

Figure 1.5 Schematic of energy spectrum in the ABL showing distinct regions of energy production (A), inertial subrange (B), and dissipation (C) (modified from Kaimal and Finnigan, 1994).

Energy spectra represent the relationship between turbulent intensity and eddy size using such as wavenumbers. On the contrary, energy cospectra are the

relationship of wavenumbers (κ) with flux densities. For example, the cospectra of sensible heat is defined by

$$\overline{w'\theta'} = \int_0^\infty S_{w\theta}(\kappa)d\kappa \qquad (1.25)$$

Namely cospectra indicate the dominant turbulent scales for the fluxes, and can be used to compare the turbulent properties in scalars (such as temperature, water vapor, and carbon dioxide) and those for turbulence similarity.

1.4 Surface flux estimations

With the knowledge of the basics on the atmospheric turbulence, we can now proceed to the application and measurement of canopy-scale fluxes. The eddy correlation method (or eddy covariance technique) is one direct method, with a few assumptions, for the determination of turbulent fluxes in atmospheric turbulence.

1.4.1 Eddy correlation method

The vertical surface flux of scalar (s) can be calculated using the following equation.

$$F_s = \overline{ws} = \overline{w's'} + \overline{w}\,\overline{s} \qquad (1.26)$$

The first term of RHS is the turbulent transport (turbulent flux) and the second term of RHS represents the mean vertical flow (mainly due to vertical advection). It is understood that the vertical surface fluxes described in the subsection 1.3.1 (equations from (1.8) to (1.11)) are the first term of RHS of equation (1.26).

If the mean vertical flow $\overline{w}$ can be neglected with the assumption from equation (1.18b) to (1.21b), the scalar flux F_s can be represented only by the first term of RHS of equation (1.26). However when $\overline{w}$ is non-zero, or the fluctuations in s are reproduced from fluctuations in water vapor density and temperature, the second term of RHS also should be considered for the flux determination (see subsection 1.4.4).

1.4.2 Measuring three-dimensional wind velocity

Ultra-sonic anemometers are often used to measure three- dimensional wind velocity with high-time response. These anemometers measure wind velocity by sensing the effect of the wind on transit times of acoustic pulses traveling in

opposite directions across a known path. The main limitation to their frequency response is the imposition of line averaging along the path. Ultra-sonic anemometers can be of either the pulse type or the continuous-wave type. The former measures transit time differences directly to compute the velocity component along the path, whereas the latter measures phase differences that can be converted to time differences. Both measurements relate directly to wind velocity (Kaimal and Finnigan, 1994).

Measurement difficulties occur when velocities or scalar fluctuations are not measured on a homogeneous flow over flat ground described in Cartesian coordinates. Two different strategies can be adopted to avoid this difficulty. One choice is to set axes of rectangular Cartesian coordinates with the z axis aligned with the geopotential gradient, x in the East - West direction and y in the North – South direction. The difficulties are those of accurately knowing the x, y, and z directions for every measurement. Another choice is to allow the flow to set the coordinate directions. In this case x may be taken in the direction of local mean wind vector. The instrument can be aligned at its optimum orientation to the prevailing wind. The mathematical transformations and detailed explanations are shown in Kaimal and Finnigan (1994).

1.4.3 Measuring H_2O and CO_2 density fluctuations

Open- and closed-path systems are generally used to measure H_2O and CO_2 density fluctuations. Both systems are similar in their use of infrared gas analyzers, but they are different in how they handle the air being sampled. These differences are crucial when applying spectral corrections and WPL corrections (see subsection 1.4.4) for the flux estimation (Lee et al., 2004).

Since sensor sensitivity changes with environmental factors such as temperature, radiation, dust and raindrops on the lens, the signal from the infrared gas analyzers should be corrected by a dynamic calibration for every measurement run using a standard hygrometer (Tsukamoto et al., 1995). This correction is more effective using the open-path system than the closed-path system. The sensor response for the H_2O fluctuation measured with the infrared gas analyzers ranges from 0.0015 to 10 Hz, while the measurement with the standard hygrometer is generally up to 0.03 Hz. The dynamic calibration should be applied within the fluctuation range at which both fluctuations have a good correlation (0.003 – 0.03 Hz). After the employment of this calibration, a correct time series for the H_2O fluctuation can be obtained, and thus those of the latent heat fluxes.

Leuning and Moncrieff (1990) pointed out that water vapor may cause errors in the measurement of CO_2 concentration, because it absorbs infrared radiation in wavebands which overlap those of CO_2. Thus the electrical signal from the infrared gas analyzers is affected by both CO_2 and H_2O densities. This issue is known as a "cross sensitivity" problem. Technically, a cross sensitivity coefficient should be determined, but with the most recently developed gas analyzers (such as LI-7500, Li-COR, USA) this calibration can be omitted.

1.4.4 WPL correction for the eddy correlation method

For the flux determination of trace gases, fluctuations in scalar s can result from fluctuations in water vapor density and temperature which are not associated with the net transport of s (Lee et al., 2004). These errors are particularly severe for trace constituents such as CO_2. In this case, the WPL correction (Webb et al., 1980) should be applied to achieve an accurate flux estimation of CO_2 as well as for water vapor itself due to temperature fluctuations. The original concept for WPL correction is as follows.

Vertical flux of dry air should be zero, thus,

$$\overline{w\rho_a} = \overline{w}\,\overline{\rho_a} + \overline{w'\rho'_a} = 0 \tag{1.27}$$

where ρ_a is the density of dry air. Based on equation (1.27), the mean vertical wind velocity can be expressed as

$$\overline{w} = -\frac{\overline{w'\rho'_a}}{\overline{\rho_a}} \tag{1.28}$$

Using the *equation of state* (the gas law), equation (1.28) recast as

$$\overline{w} = \frac{\mu}{\overline{\rho_a}}\overline{w'\rho'_v} + (1+\mu\sigma)\frac{\overline{w'\theta'}}{\overline{T}} \tag{1.29}$$

where, $\mu = m_a / m_v$, $\sigma = \rho_v / \rho_a$, m_a is the mole fraction of dry air, m_v the mole fraction of water vapor, and ρ_v the density of water vapor. When equation (1.29) is applied to equation (1.26) for the moisture flux (E), we obtain

$$E = (1+\mu\sigma)(\overline{w'\rho'_v} + \frac{\overline{\rho_v}}{\overline{T}}\overline{w'\theta'}) \tag{1.30}$$

Similarly, we obtain the following equation for CO_2 flux

$$F_c = \overline{w'c'} + \mu\frac{\overline{c}}{\overline{\rho_a}}\overline{w'\rho'_v} + (1+\mu\sigma)\frac{\overline{c}}{\overline{T}}\overline{w'\theta'} \tag{1.31}$$

Here, the first term of RHS is the measured CO_2 flux using the eddy correlation method, the second term represents the contribution from the water vapor flux, and the third term is that from the sensible heat flux.

1.5 Carbon dioxide fluxes in a terrestrial ecosystem

An observational example of seasonal and inter-annual changes in net ecosystem exchange (NEE) in a terrestrial ecosystem is presented in this section. If we can assume a horizontally homogeneous surface and that the estimated

carbon dioxide fluxes using the eddy correlation method are accurate (no advection and no horizontal sink / source), $-NEE$ equals NEP. Note that the signs of NEE and NEP are opposite, but those absolute values are the same.

1.5.1 Flux measurements in a West Siberian wetland

Around one-third of the global soil carbon (estimated to be 200 - 450 Gt C) is stored in boreal wetlands (Gorham, 1991; Schlesinger, 1996). Most global warming scenarios predict that the most distinctive temperature increases will occur in northern high latitudes (IPCC, 2001). Thus the carbon budget in northern wetlands is important to the future development of the climate. Wetlands are considered to be a sink of atmospheric CO_2 due to the presence of immense stores of carbon in the peat layer. Several studies suggest a possible changeover of the carbon budget in boreal and arctic ecosystems from a sink to a source due to global warming (Billings et al., 1982; Oechel et al., 1993, 2000). Multi-year studies show wetlands can either be sources or sinks of CO_2, depending on weather conditions (Shurpali et al., 1995; Joiner et al., 1999; Griffis et al., 2000). These results suggest that the carbon budget in boreal wetlands is very sensitive to climate change.

The target wetland in this chapter, which was characterized as a bog according to the definition of Aselmann and Crutzen (1989), is located in the southeastern portion of the West Siberian Lowland (56° 51' N, 82° 50' E) near Plotnikovo, Russia, in the Ob River basin. The annual mean temperature and annual precipitation are 1.2°C and 584 mm, respectively, based on NCEP / NCAR data obtained from 1988 to 2000 at Tomsk, 160 km east of the study bog. The dominant vegetation in the bog is *Carex* spp. (*C. rostrata* and *C. limosa*) and *Equisetum fluviatile*, which reach a height of about 60 cm in midsummer. The ground surface is covered with *Sphagnum* mosses (*S. majus*, *S. magellanicum*, *S. angustifolium*, *S. fuscum*, etc.) and underlying the *Sphagnum* moss is a peat layer that is more than 2 meters in depth.

Continuous measurements were taken from early April to late October in 1999 and 2000 (Shimoyama, 2005). The sensible heat, latent heat, and carbon dioxide fluxes were measured by the eddy correlation method 2m above the moss surface using a three-dimensional ultra-sonic anemometer (DA600, Kaijo, Japan) and an open-path infrared gas analyzer (E009B, Advanet, Inc., Japan). Both sensors have a 10-cm span length with a horizontal sensor separation of 15cm. Data were recorded at 10 Hz over 1740 s at 30-min intervals on a magneto-optical disk using a data recorder (DR-M2a, TEAC, Japan). The fluxes were calculated every 30 min.

1.5.2 Gap filling and nocturnal CO_2 flux

Missing or rejected data due to instrumental errors, rain, low wind condition, and unreliable extreme fluctuations, i.e. high amplitudes greater than three times

the average value during either the previous or following one hour, were filled in using empirical relationships between F_c and environmental variables. Diurnal F_c primarily depends on downward short-wave radiation (Sd), and the seasonal trend of light response corresponds to the phenology of vascular plants.

A methodological example is as follows. First, the missing data was interpolated by regression model using a rectangular hyperbolic curve, which was applied to the light-response relationship between instantaneous Sd and F_c. Since the daylight F_c measured with the eddy correlation method includes CO_2 assimilation by photosynthesis as well as CO_2 release by respiration, temperature changes should also be taken into consideration when estimating diurnal CO_2 flux. Thus a simple linear regulation was applied, because the error from a light response curve involves a complex physiological effect caused not only by temperature but also by other environmental restrictions. The differential error of the measured values from the fitting curve is experimentally corrected by air temperature. Those empirical parameters were determined for a total of 19 stages from mid-April (DOY 101) to mid-October (DOY 290) at 10-day periods. Missing diurnal data for each stage were, therefore, interpolated.

Nocturnal CO_2 flux was interpolated using the relationship between soil temperature (T_g) and F_c obtained for a growing period (Figure 1.6). We chose to illustrate the nocturnal F_c with mean values every 5°C because there was a large scatter in the flux. This scattering was likely caused by measurement error, due to the small amount and spatial heterogeneity of the fluxes. In both growing periods, a temperature dependency of the nocturnal F_c was apparent. A higher respiration was observed in 2000 that was statistically significant over that in 1999 during which the temperature increased more than 10°C. Therefore, the Q_{10}, the factor by which respiration increases with a rise of 10 °C in T_g, was 2.60 in 2000, slightly higher than the Q_{10} of 2.41 in 1999 (Figure 1.6). The Q_{10} in both years was in the lower range of previously established values for northern boreal wetlands, which range from 2.0 to 4.1.

Finally, a continuous, gap-filled diurnal F_c of this wetland was obtained.

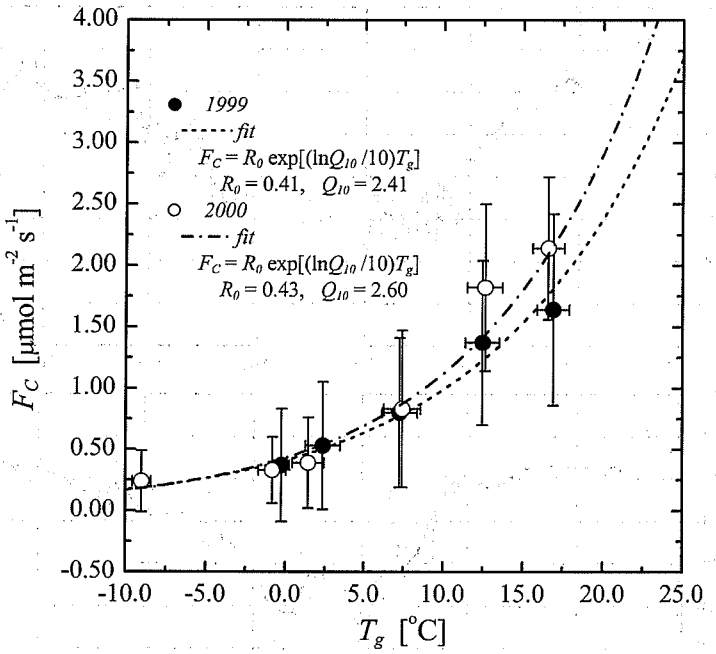

Figure 1.6 Relationship between the half-hourly nighttime CO_2 flux (F_c) and soil temperature (T_g) (Shimoyama, 2005).

1.5.3 Estimated annual *NEE*

Figure 1.7 shows the seasonal variation in the daily *NEE* with gap-filled values and 10-day running mean values. The net daily *NEE* ranged from -0.230 to +0.050 mol m^{-2} d^{-1} and -0.270 to +0.040 mol m^{-2} d^{-1} in the 1999 and 2000 growing periods, respectively. The day-to-day variation was rather obvious in summer. Nearly neutral *NEE* was observed with the highest sink rate. The data, averaged over ten days, showed that the bog was a source of CO_2 during the spring thaw. The continuous increase in uptake *NEE* started around mid-May and reached a peak sink rate in summer, approximately -0.170 mol m^{-2} d^{-1}, in both years. The *NEE* then reverted to a net loss of CO_2 at the end of September. The total duration of the CO_2 uptake stage was 145 days in 1999 and 127 days in 2000.

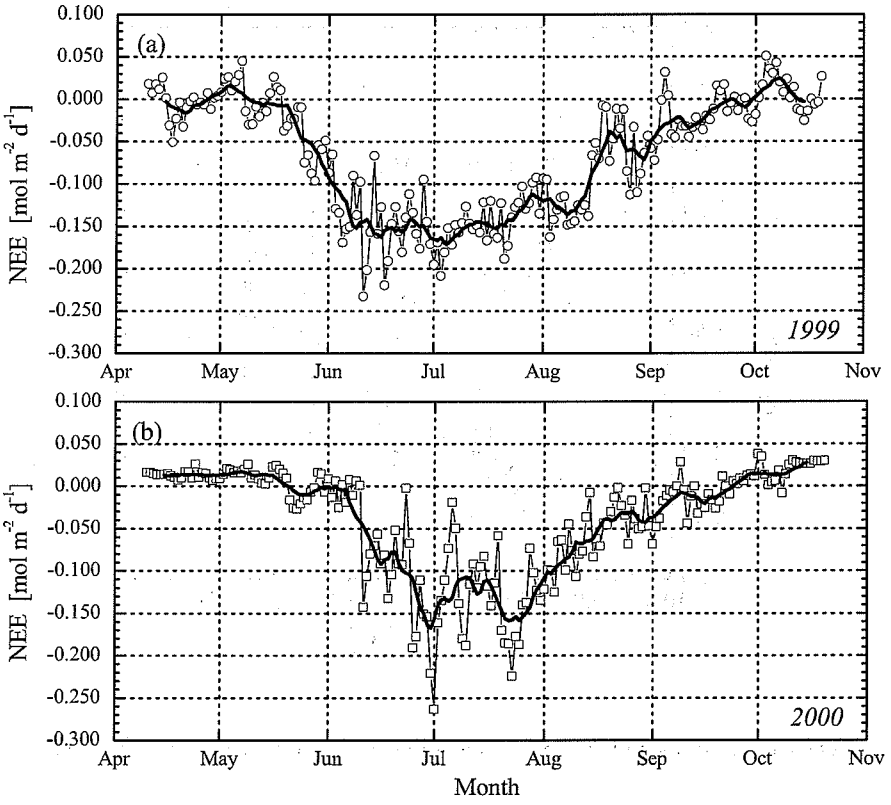

Figure 1.7 Seasonal variation in the daily net ecosystem CO_2 exchange rate (*NEE*). The solid lines indicate running mean values over ten days; (a): in 1999 and (b) in 2000 (Shimoyama, 2005).

Inter-annual variation in the seasonal trend of *NEE* was quite different between the two growing periods, although the phenology of the vascular plants was quite similar. The most distinctive difference was that the highest summer *NEE* spell appeared approximately three weeks earlier and lasted longer in 1999 than in 2000. This result can be attributed to different meteorological conditions, because the biological activity of the bog ecosystem is significantly correlated with Sd and T_g. The earlier occurrence of the peak stage in 1999 depended in part on inter-annual variation in light response of F_c, meaning that the earlier sprouting of vascular plants are a cause of inter-annual variation.

1.5.4 FLUXNET and energy imbalance issue

To better understand and determine *NEE* for each terrestrial biome, flux research networks (referred to as, "FLUXNET"; Baldocchi et al., 2001) were developed. There are more than 260 flux measurement sites all over the world, but most are concentrated in Europe, the United States of America, and East Asian countries. The following web site has more information:

http://www.fluxnet.ornl.gov/fluxnet/index.cfm

For better determination of annual & inter-annual *NEE*, better algorithms for the eddy covariance techniques are being developed in the FLUXNET. Standard correction methodologies for the flux measurements are found on the web site.

The energy imbalance of equation (1.2) is a serious issue among the FLUXNET research sites (e.g., Wilson et al., 2002). In most sites, the RHS of equation (1.2) is underestimated in comparison with LHS (i.e., available energy). There are some reasons for the energy imbalance. These include estimation errors in Rn, G, and ΔQ, estimation errors in turbulent heat fluxes H and λE (i.e., mainly high-frequency losses of turbulence), insufficient averaging periods related to nonstationarity (i.e., low-frequency losses of H and λE), and advection effects that are especially notable at night. Sakai et al., (2001) showed that turbulent eddies with periods from 4-30 min account for about 17% of low-frequency contributions to eddy fluxes over rough surfaces. Additional error sources include flux divergence between the measurement height and the surface or a non-zero mean vertical velocity (Lee, 1998), and effects of three-dimensional mean velocity fields (Finnigan, 1999; Hiyama et al., 2006). Quantitative evaluation of these contributions to the energy imbalance should be done at each flux research site.

1.6 Modeling of soil - vegetation - atmosphere transfers

In this section, physical-based approaches (modeling) of terrestrial ecosystems (or vegetation) in climate models are presented in order to aggregate the scale of the canopy-scale fluxes to longer time-scale issues such as future climate prediction. Modeling of soil – vegetation – atmosphere is crucial for future climate prediction. Evidence is now very strong that regional-scale land surface perturbations cause continental-scale changes in climate. There is also evidence that regional-scale land surface changes in key regions can cause significant changes in geographically remote areas by means of atmospheric teleconnections. Climate models appear to be sensitive to the land surface because these changes affect the exchange of water, energy, momentum and carbon (Pitman, 2003). Thus LSMs are important modules in the simulation of future climate.

The canopy-scale fluxes of sensible heat, latent heat (and momentum) are one of the important boundary conditions for the climate model. This section introduces the history and important equations regarding LSMs. Historical classification of LSMs is given by Sellers et al. (1997) and Pitman (2003). Sellers et al. (1997) defined first and second generation LSMs, and Pitman (2003) described third generation LSMs. Brief explanations of these LSMs developed since 1960s are shown below.

1.6.1 First generation land surface model

The first LSM was incorporated by Manabe (1969) into a climate model to represent the seasonal or diurnal cycle of energy balance. A simple energy balance equation ignoring heat conduction into the soil (not like equation (1.2)) was introduced using a globally constant soil depth and water-holding capacity. This parameterization of hydrology is called the "Manabe bucket model". The Manabe (1969) LSM and a generation of simpler schemes are defined as first generation LSMs (Sellers et al., 1997).

In the model, the surface sensible heat flux can be represented as

$$H = \frac{T_s - T_r}{r_a} \rho c_p \tag{1.32}$$

where T_s is the surface temperature, T_r a reference temperature above the surface, and r_a the aerodynamic resistance which represents turbulent diffusion above the surface. The latent heat flux is expressed as

$$\lambda E = \beta \left(\frac{e^*(T_s) - e_r}{r_a} \right) \frac{\rho c_p}{\gamma} \tag{1.33}$$

where β is surface moisture availability, which ranges between zero (dry) and one (saturated), $e^*(T_s)$ the saturated water vapor pressure at T_s, e_r the water vapor pressure at a reference height, and γ the psychrometric constant. In the first generation LSM, the latent heat flux is controlled only by surface moisture availability. Thus if the function of plants is modeled explicitly, this model fails to capture the complexity of the real system (Pitman, 2003).

1.6.2 Second generation land surface model

Deardorff (1978) introduced a method for simulating soil temperature and moisture in two soil layers, and that for air temperature using a single vegetation layer. Deardorff's (1978) soil model is called the "force-restore model." Sellers et

al. (1997) described those LSMs that included vegetation models of the Deardorff (1978) type as being second generation LSMs. Excellent examples of the second generation model are those developed by Sellers et al. (1986, 1992, 1994, 1996) and Dickinson et al. (1986, 1993). These models are, respectively, "the Simple Biosphere Model (SiB)" and "the Biosphere Atmosphere Transfer Scheme (BATS)."

The important characteristics of second generation LSMs are the development of micrometeorological contributions to LSMs because surface fluxes are treated explicitly and mathematically. As described by Sellers et al. (1997), second generation LSMs usually represent the vegetation - soil system interacting with the atmosphere. These models differentiate between soil and vegetation at the surface, thus albedo may vary spatially across a grid square. The second generation LSMs also explicitly represent the impact of vegetation on momentum exchange, which enhances the exchange of sensible heat and latent heat.

The canopy-level latent heat flux (λE_c) in second generation LSMs is represented as

$$\lambda E_c = \left(\frac{e^*(T_s) - e_r}{r_c + r_a} \right) \frac{\rho c_p}{\gamma} \qquad (1.34)$$

where r_c is the canopy resistance (not surface resistance) which only simulates the evaporative flux from within the leaves to the atmosphere. The second generation LSM includes two layers generating sensible and latent heat fluxes (Figure9 of Pitman, 2003). Equation (1.34) represents latent heat transfer only from a canopy to the atmosphere, and thus it does not include that from a soil surface. The canopy resistance r_c is the inverse of the canopy conductance g_c and these two terms can be obtained from the stomatal conductance g_{st} or stomatal resistance r_{st} via appropriate scaling from a stomatal-scale function to a canopy-scale function. A common method (Dickinson et al., 1998) is to use a leaf area index (*LAI*):

$$r_c = {}^{r_{st}}\!/_{LAI} \quad g_c = g_{st} \cdot LAI \qquad (1.35)$$

A relationship developed by Jarvis (1976) was used to represent g_{st} in most second-generation schemes and captures key responses of stomates to photosynthetically active radiation (*PAR*), humidity δe and temperature T. It also includes the leaf water potential ψ, which can be related to soil water content in the root zone, root distribution and evaporative demand (Pitman, 2003).

$$g_{st} = \frac{1}{r_{st}} = g_{st\max}(PAR)[f(\delta e) f(T) f(\psi)] \qquad (1.36)$$

Here $f(\delta e)$, $f(T)$, and $f(\psi)$ are known as stress functions compared to $g_{st\max}(PAR)$, which demonstrate g_{st} as a function of PAR without any other meteorological stresses. A major effort through the 1980s and 1990s was the investigation of the form of each of the stress functions in equation (1.36) (Schulze et al., 1994).

1.6.3 Third generation land surface model

The improvement in the third generation LSMs was the inclusion of carbon exchange by plants. Particularly, the major change from the second to third generation LSMs is the representation of stomatal conductance (Figure11 of Pitman, 2003).

A semi-empirical model of leaf conductance (Collatz et al., 1991) was

$$g_s = m\frac{A_n h_s}{c_s} + b \qquad (1.37)$$

where, A_n is the net leaf assimilation rate, c_s the partial pressure of CO_2 at the leaf surface, h_s the relative humidity at the leaf surface, m is an empirical coefficient ($m \approx 9$ for most C_3 plants and $m \approx 4$ for C_4 plants), and b is the minimum stomatal conductance (around 0.01 for C_3 and 0.04 for C_4 plants); see Sellers (1992) and Sellers et al. (1997). Sellers et al. (1992) derived methods to scale the leaf-level models to canopy-scale models in order to provide estimates of the canopy resistance r_c, canopy photosynthesis A_C, and canopy respiration R_D (Figure11 of Pitman, 2003).

The third generation schemes are distinguished by the method used to model carbon. Thus, they can respond to changes in climate through influences of energy and water exchange, and also respond physiologically with increasing atmospheric CO_2 through the canopy conductance. They can then also respond structurally by growing different leaves and taller trees.

1.7 Summary and future research issues

This chapter described the basic theoretical and technical approaches to canopy-scale fluxes of heat, water vapor, and carbon dioxide in terrestrial

ecosystems. Also explained was the historical background of LSM in climate modeling. Although the canopy-scale fluxes pertained mainly to time scales from seconds to hours through ABL turbulence, those accumulated outcomes appear from seasonal to inter-annual time scales. Previous LSM in climate modeling was somehow only a one-directional approach interacting with static terrestrial ecosystem and the atmosphere. However, actual interactions between terrestrial ecosystems and the atmosphere are really a dynamic feedback system. Not only human-induced disturbance but also evolution of terrestrial ecosystems themselves (or vegetation dynamics) interact with the atmosphere and thus the climate system. Therefore dynamic vegetation modeling is necessary for predicting future climate. Chapter 10 describes this research status and its issues using "dynamic global vegetation models (DGVMs)".

Acknowledgements

I would like to thank Dr. Koh Shimoyama of the National Institute for Environmental Studies (NIES), Japan, for his valuable assistance and providing us the flux observation results in the West Siberian wetland.

References

Aselmann, I, and Crutzen, P.J., (1989), Global distribution of natural freshwater wetlands and rice paddies, their net primary productivity, seasonality and possible methane emissions, Journal of Atmospheric Chemistry, 8, 307-358.

Baldocchi, D., Falge, E., Gu, L., Olson, R., Hollinger, D., Running, S., Anthoni, P., Bernhofer, Ch., Davis, K., Evans, R., Fuentes, J., Goldstein, A., Katul, G., Law, B., Lee, X., Malhi, Y., Meyers, T., Munger, W., Oechel, W., Paw, K.T., Pilegaard, K., Schmid, H.P., Valentini, R., Verma, S., Vesala, T., Wilson, K., and Wofsy, S., (2001), FLUXNET: A new tool to study the temporal and spatial variability of ecosystem-scale carbon dioxide, water vapor, and energy flux densities, Bulletin of the American Meteorological Society, 82, 2415 – 2434.

Brutsaert, W., (1982), *Evaporation into the Atmosphere, Theory, History, and Applications*, Kluwer Academic Publishers, 299pp.

Billings, W.D., Luken, J.O., Mortensen, D.A., and Peterson, K.M., (1982), Arctic Tundra: A source or sink for atmospheric carbon dioxide in a changing environment? Oecologia, 53, 7-11.

Collatz, G.J., Ball, J.T., Grivet, C., and Berry, J.A., (1991), Physiological and environmental regulation of stomatal conductance, photosynthesis and transpiration: a model that includes a laminar boundary layer, Agricultural and Forest Meteorology, 54, 107 – 136.

Deardorff, J.W., (1978), Efficient prediction of ground surface temperature and moisture with inclusion of a layer of vegetation, Journal of Geophysical

Research, 83, 1889 – 1903.
Dickinson, R.E., Henderson-Sellers, A., Kennedy, P.J., and Wilson, M.F., (1986), Biosphere–Atmosphere Transfer Scheme (BATS) for the NCAR Community Climate Model, NCAR Technical Note, NCAR, TN-275 + STR.
Dickinson, R.E., Henderson-Sellers, A., and Kennedy, P.J., (1993), Biosphere–Atmosphere Transfer Scheme (BATS) Version 1e as coupled to the NCAR Community Climate Model, NCAR Technical Note, NCAR, TN383 + STR.
Dickinson, R.E., Shaikh, M., Bryant, R., and Graumlich, L., (1998), Interactive canopies for a climate model, Journal of Climate, 11, 2823-2836.
Finnigan, J., (1999), A comment on the paper by Lee (1998): "On micrometeorological observations of surface-air exchange over tall vegetation", Agricultural and Forest Meteorology, 97, 55-64.
Garratt, J.R., (1992), *The atmospheric boundary layer*, Cambridge University Press, 316pp.
Gorham, E., (1991), Northern peatlands: Role in the carbon cycle and probable response to climatic warming, Ecological Applications, 1, 182-195.
Griffis, T.J., Rouse, W.R., and Waddington, J.M., (2000), Interannual variability of net ecosystem CO_2 exchange at a subarctic fen, Global Biogeochemical Cycles, 14, 1109-1121.
Hiyama, T., Strunin, M.A., Tanaka, H., and Ohta, T., (2006), The development of local circulations around the Lena River and their effect on tower-observed energy imbalance, Hydrological Processes, (in press).
IPCC (2001), *Climate Change*, The scientific basis, Houghton, J, T., Y, Ding, D, J, Griggs, M, Noguer, P, J, van der Linden, X, Dai, K, Maskell, and C, A, Johnson, (eds.), Cambridge Univ, Press., Cambridge; New York.
Jarvis, P.G., (1976), The interpretation of the variations in leaf water potential and stomatal conductance found in canopies in the field, Philosophical Transactions of the Royal Society of London, Series B 273, 593-610.
Joiner, D.W., Lafleur, P.M., McCaughey, J.H., and Bartlett, P.A., (1999), Interannual variability in carbon dioxide exchanges at a boreal wetland in the BOREAS northern study area, Journal of Geophysical Research, 104(D22), 27663-27672.
Kaimal, J.C., and Finnigan, J.J., (1994), *Atmospheric Boundary Layer Flows, Their Structure and Measurement*, Oxford University Press, 289pp.
Kistler *et al*, (2001), The NCEP / NCAR 50-year reanalysis: monthly means CD-ROM and documentation, Bulletin of the American Meteorological Society, 82, 247-267.
Lee, X., (1998), On micrometeorological observations of surface-air exchange over tall vegetation, Agricultural and Forest Meteorology, 91, 39-49.
Lee, X., Massman, W., and Law, B., (2004), *Handbook of Micrometeorology, A Guide for Surface Flux Measurement and Analysis*, Kluwer Academic Publishers, 250pp.
Leuning, R., and Moncrieff, J., (1990), Eddy-covariance CO_2 flux measurements

using open- and closed-path CO_2 analyzers: corrections for analyzer water vapor sensitivity and damping of fluctuations in air sampling tubes, Boundary-Layer Meteorology, 53, 63 – 76.

Manabe, S., (1969), Climate and the ocean circulation: 1, the atmospheric circulation and the hydrology of the Earth's surface, Monthly Weather Review, 97, 739 – 805.

Oechel, W.C., Hastings, S.J., Vourlitis, G.L., Jenkins, M., Riechers, G., and Grulke, N., (1993), Resent change of arctic tundra ecosystems from a net carbon dioxide sink to source, Nature, 361, 520-523.

Oechel, W.C., Vourlitis, G.L., Hastings, S.J., Zulueta, R.C., Hinzman, L., and Kane, D., (2000), Acclimation of ecosystem CO_2 exchange in the Alaskan Arctic in response to decadal climatic warming, Nature, 406, 978-981.

Pitman, A.J., (2003), The evolution of, and revolution in, land surface schemes designed for climate models, International Journal of Climatology, 23, 479 – 510.

Sakai, R.K., Fitzjarrald, D.R., and Moore, K.E., (2001), Importance of low-frequency contributions to eddy fluxes observed over rough surfaces, Journal of Applied Meteorology, 40, 2178-2192.

Schlesinger, W.H., (1996), *Biogeochemistry: An Analysis of Global Change*, 2nd ed., Academic Press, San Diego, Calif.

Schulze, E.D., Kelliher, F.M., Korner, C., and Lloyd, J., (1994), Relationships among maximum stomatal conductance, ecosystem surface conductance, carbon assimilation rate, and plant nitrogen nutrition: a global ecological scaling exercise, Annual Review of Ecology and Systematics, 25, 629 – 660.

Sellers, P.J., (1992), Biophysical models of land surface processes, In *Climate System Modelling*, Trenberth, K, E, (ed.), Cambridge University Press.

Sellers, P.J., Mintz, Y., Sud, Y.C., and Dalcher, A., (1986), A Simple Biosphere model (SiB) for use within general circulation models, Journal of the Atmospheric Sciences, 43, 505 – 531.

Sellers, P.J., Berry, J.A., Collatz, G.J., Field, C.B., and Hall, F.G., (1992), Canopy reflectance, photosynthesis and transpiration, III, A reanalysis using improved leaf models and a new canopy integration scheme, Remote Sensing of the Environment, 42, 187 – 216.

Sellers, P.J., Tucker, C.J., Collatz, G.J., Los, S.O., Justice, C.O., Dazlich, D.A., and Randall, D.A., (1994), A global 1°× 1° NDVI data set for climate studies, Part 2: the generation of global fields of terrestrial biophysical parameters from the NDVI, International Journal of Remote Sensing, 15, 3519 – 3545.

Sellers, P.J., Randall, D.A., Collatz, C.J., Berry, J.A., Field, C.B., Dazlich, D.A., Zhang, C., Collelo, G., and Bounoua, L., (1996), A revised land-surface parameterization (SiB2) for atmospheric GCMs, Part 1: model formulation, Journal of Climate, 9, 676 – 705.

Sellers, P.J., Dickinson, R.E., Randall, D.A., Betts, A.K., Hall, F.G., Berry, J.A., Collatz, G.J., Denning, A.S., Mooney, H.A., Nobre, C.A., Sato, N., Field, C.B., and Henderson-Sellers, A., (1997), Modelling the exchanges of energy, water

and carbon between continents and the atmosphere, Science, 275, 502-509.
Shimoyama, K., (2005), Seasonal and Interannual Variation in Energy and Carbon Dioxide Fluxes in a West Siberian Bog, Ph.D, dissertation, Nagoya University, 105pp.
Shurpali, N.J., Verma, S.B., Kim, J., and Arkebauer, T.J., (1995), Carbon dioxide exchange in a peatland ecosystem, Journal of Geophysical Research, 100(D7), 14319-14326.
Stull, R.B., (1988), *An Introduction to Boundary Layer Meteorology*, Kluwer Academic Publishers, 666pp.
Tsukamoto, O., Sahashi, K., and Wang, J., (1995), Heat budget and evapotranspiration at an oasis surface surrounded by desert, Journal of the Meteorological Society of Japan, 73, 925 – 935.
Webb, E.K., Pearman, G.I., and Leuning, R., (1980), Correction of flux measurements for density effects due to heat and water vapour transfer, Quarterly Journal of the Royal Meteorological Society, 106, 85 – 100.
Wilson, K., Goldstein, A., Falge, E., Aubinet, M., Baldocchi, D., Berbigier, P., Bernhofer, C., Ceulenmans, R., Dolman, H., Field, C., Grelle, A., Ibrom, A., Law, B.E., Kowalski, A., Meyers, T., Moncrieff, J., Monson, R., Oechel, W., Tenhunen, J., Valentini, R., and Verma, S., (2002), Energy balance closure at FLUXNET sites, Agricultural and Forest Meteorology, 113, 223 – 243.
Wu, J., (1999), Hierarchy and scaling: extrapolating information along a scaling ladder, Canadian Journal of Remote Sensing, 25, 367-380.

Chapter 2

The Water Cycle in Forested Areas

Takeshi Ohta
Graduate School of Bioagricultural Sciences,
Nagoya University, Nagoya 464-8601, Japan
Tel: +81-52-789-4059
Fax: +81-52-789-4059
e-mail: takeshi@agr.nagoya-u.ac.jp

2.1 Introduction

Forests cover only about 10 % of the globe, which is equal to about 30 % of the land surface; however 90 % of the global photosynthesis occurs in forest areas. Consequently, forests transpire a great deal of water associated with photosynthesis and water is evaporated from the forest canopy during and after rainfall events. Furthermore, water exchange between the atmosphere and forests occurs not only in summer but also in winter, particularly from snow-covered canopies. Thus forests represent a very important type of land surface in relation to water management and the climate system, and it is necessary to understand the effects of forests on the water cycle from the single plot scale through watershed and regional scales, and up to the global scale.

Forests are characterized by having deep canopies, deep root layers and deep and porous surface soil layers, compared to other vegetation types. These properties are important factors affecting the water cycle characteristics; forests affect both evapotranspiration and runoff. Evapotranspiration consists of interception loss from the wet canopy during and just after precipitation events, and transpiration from the dry canopy; canopy structure is an important factor in the former situation, and forest physiology in the latter. Evapotranspiration consumes much energy in the form of latent heat, and consequently affects not only the water cycle but also the energy budget and thus the general meteorological situation. The runoff system is strongly influenced by soil properties, and the flow path of water is determined by the presence or absence of soil layer. Furthermore, runoff characteristics have a marked influence on sediment discharge in watersheds.

The characteristics of the water cycle in forested areas, especially evapotranspiration, are discussed here because evapotranspiration results from an

energy exchange between the atmosphere and the forests and it affects the meteorological and climate systems. In addition, processes occurring during winter in forested areas are also described in this chapter.

2.2 Water balance in the forest

Water balance is one of the most important hydrological characteristics at every scale. The annual water balance is represented as;

$$P = Q + E + \Delta S, \qquad (2.1)$$

where P is annual precipitation, Q is annual runoff, E is the annual amount of evapotranspiration and ΔS is the change in water storage over a water year. (the term "water year" denotes a period of 365 days, sometimes different from a calendar year, which can be subdivided for hydrological analysis). It is impossible to determine the value of ΔS. It might fluctuate between positive and negative values. Over a sufficiently long period of several years, the value of ΔS converges to zero, and this value is assumed here.

Watershed experiments have been conducted to elucidate the effects of forest effects on the water balance. Two methods have been used: one is the single watershed method, and the other is the paired watershed method. The latter is more accurate. Figure 2.1 is a schematic graph of the paired watershed method. In this method, two or more watersheds that adjoin each other with the same geological and topographical features are selected. Precipitation and runoff are firstly observed for several years under forested conditions for all watersheds.

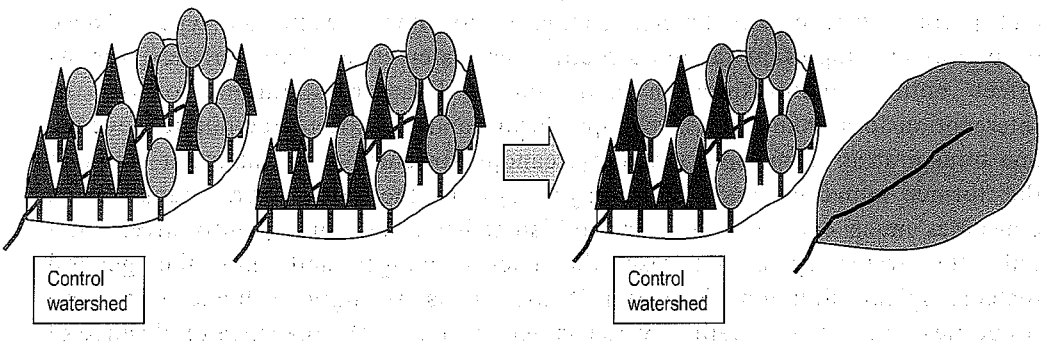

Figure 2.1 Schematic diagram of the paired watershed experiment method

Then some treatments, for example clear- or partial felling, are carried out on all the watersheds except for the one control watershed which is kept under a forested condition. The differences in runoff characteristics between the control and the treated watersheds before and after the timber cutting are analyzed.

Figure 2.2 shows the relationships between the reduction in vegetation cover and the increase in annul runoff obtained for the 94 paired catchments covering a range of meteorological conditions (Bosh and Hewlett, 1982). Annual discharge increases with a reduction in vegetation cover regardless of vegetation types. Figure 2.3 indicates the interannual variation in the increase of annual runoff after

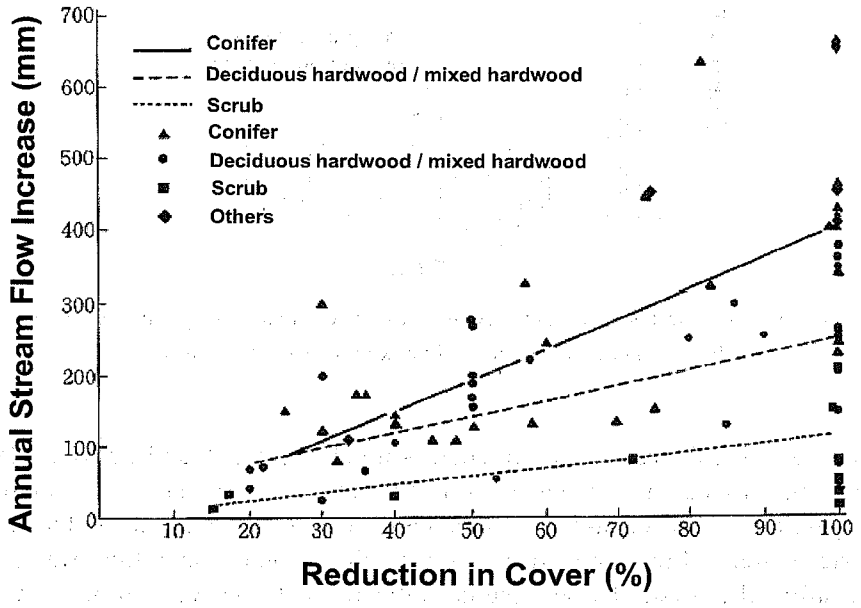

Figure 2.2 Relationship between the reduction in vegetation cover and annual stream flow increase obtained by the paired watershed mehod. (Bosh and Hewlett, 1982).

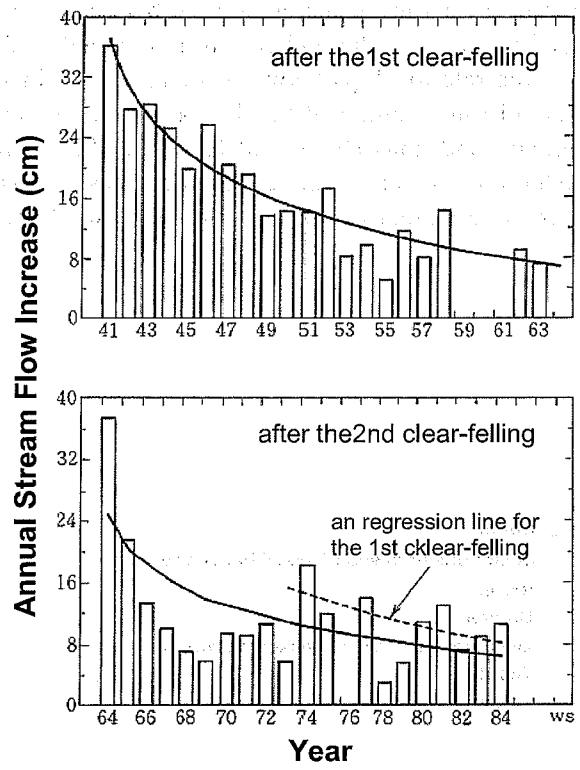

Figure 2.3 Time series of stream flow increase after clear-felling in the Coweeta Experimantal Watershed (Swank and Crossley, 1988).

clear-felling in the Coweeta Experimental Watershed (Swank and Crossley, 1988). Clear-felling was conducted twice, in 1940 and 1963. Annual runoff increased rapidly just after both clear-felling episodes, and then decreased gradually. The time series pattern of the runoff decrease after the second clear-felling was similar to that after the first. These results indicate that the vegetation consumes considerable quantity of water by evapotranspiration. Vegetation, especially forests, is a great consumer of water.

The analyses mentioned above were focused on the annual water balance in a watershed. How can we estimate the seasonal variation of water balance at the watershed scale? The same concept represented in equation (2.1) is used to analyze the seasonal variation of catchments water balance. The method is called the short-term water balance method, and indicated by the following equation:

$$\int_{t_1}^{t_2} e(t)dt = \int_{t_1}^{t_2} p(t)dt - \int_{t_1}^{t_2} q(t)dt, \qquad (2.2)$$

where $e(t)$, $p(t)$ and $q(t)$ are the time series of evapotranspiration, precipitation and discharge, respectively, and t_1 and t_2 are the start and the end times of the analysis. The $q(t_1)$ and $q(t_2)$ should be selected during base-flow stages on the hydrographs, and the differences between them should be as small as possible so that the difference in water storage at t_1 and t_2 becomes small. It is also necessary to ensure that the duration between t_1 and t_2 is adequate because the seasonal variation in evapotranspiration can not be detected if the duration is too long, and the accuracy will be inadequate if it is too short.

The results indicated in Figure 2.1 and 2.2 indicate that runoff from the watershed decreased with increasing vegetation coverage. When does the runoff decrease?, during the periods of direct runoff or base flow? Runoff changes after the killing of pine trees by the pinewood nematode were analyzed in western Japan (Abe et al., 1983; Abe and Tani, 1985). In this case, the soil layer condition was protected after the killing of pine trees in this case. Base flow in the damaged watershed increased 50 % in the winter season and 100 % in the summer season, and the annual increase was about 70 %, compared to the control watershed. The damage by the pinewood nematode also affected the direct runoff. The amount of direct runoff and the peak runoff increased about 30 and 20 %, respectively. The increase in base flow results from the decrease in transpiration, and the increase during direct runoff is caused by the decrease of interception loss of precipitation.

We see that the forests lose much water not only on clear and overcast days but also on rainy days. The existence of the forest strongly affects the water balance, and the characteristics of evapotranspiration are important in understanding the water cycle in forested areas.

2.3 Evapotranspiration from forests

2.3.1 Theory of evapotranspiration

Evapotranspiration is produced by the energy exchange between the atmosphere and the forests. Figure 2.4 shows the schematic diagram of energy flow in a forest, and the energy balance is written as;

$$Rn - G = SH + LH + Pp, \qquad (2.3)$$

where Rn is net all-wave radiation; G is the ground heat flow, including that from the canopy and trunk layers in forests; SH is sensible heat flux; LH is latent heat flux; and Pp is the energy of photosynthesis. Pp is usually negligible in energy balance analyses because it accounts for only about 3 % of the Rn.

Net all-wave radiation is expressed as

$$Rn = (1-\alpha)\cdot Sd + Ld + Lu \qquad (2.4)$$

where, α is the albedo of the surface, *Sd* is the incoming short-wave (solar) radiation (W m^{-2}), *Ld* is the atmospheric long-wave radiation (W m^{-2}) and *Lu* is the long-wave radiation emitted from the surface (W m^{-2}). The sensible and latent heat fluxes are represented by the following equations

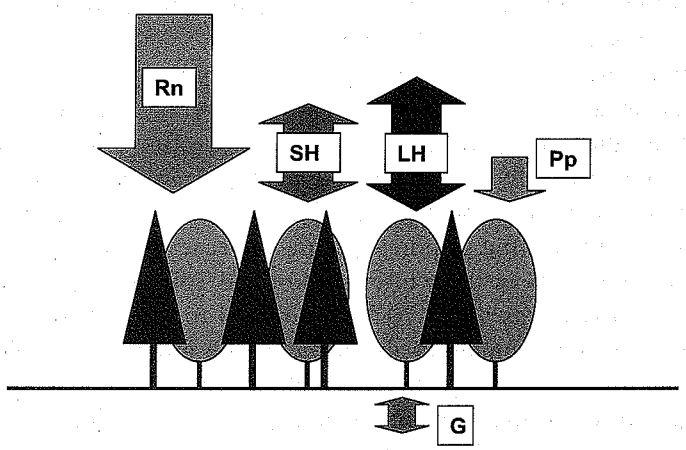

Figure 2.4 Schematic diagram of energy partitioning in forest areas.

$$SH = \rho \cdot Cp \cdot T \cdot v \qquad (2.5)$$

$$LH = \lambda \cdot \rho \cdot q \cdot v, \qquad (2.6)$$

where ρ is the air density (kg m^{-3}), *Cp* is the specific heat under constant pressure (J kg^{-1}), λ is the latent heat of water (J kg^{-1}), *T* is temperature (℃), *q* is specific humidity (kg kg^{-1}), and *v* is the mean vertical wind speed (m sec^{-1}). These fluxes are transferred by turbulence, and *T*, *q* and *v* consist of temporal mean values and fluctuations from these mean values. Thus, these variables can be written as

$$T = \overline{T} + t' \qquad (2.7)$$

$$q = \overline{q} + q' \qquad (2.8)$$

$$v = \overline{v} + v', \qquad (2.9)$$

where $\bar{}$ indicates the temporal average and ' denotes the fluctuation for each of the variables. Substituting equations (2.7) – (2.9) into equations (2.5) and (2.6), the sensible heat flux and latent heat fluxes are expressed as

$$SH = \rho \cdot Cp \cdot (\overline{\bar{T}\bar{v}'} + \overline{T'v'}) = \rho \cdot Cp \cdot \overline{T'v'} \qquad (2.10)$$

$$LH = \lambda \cdot \rho \cdot (\overline{\bar{q}\bar{v}'} + \overline{q'v'}) = \lambda \cdot \rho \cdot \overline{q'v'}. \qquad (2.11)$$

Consider an example in which land surface temperature is higher than air temperature and the upward direction is positive. The sensible heat flux is positive and upward in this case. The value of v' is positive as the vertical wind is upward and t' is also positive because warmer air is flowing up from a lower layer. However, t' is negative when v' is negative, and wind flow is downward. Thus, there is a positive correlation between t' and v', and the sensible heat flux is positive. In constant, t' and v' are negatively correlated and the sensible heat flux is downward when air temperature is higher than ground surface temperature. The values of t', q' and v' can be directly observed by ultrasonic anemometer and infrared gas analyzer.

2.3.2 Environmental variables, vegetation and evapotranspiration

The effects of environmental variables, for example, net all-wave radiation, air temperature, atmospheric water vapor and wind speed on evapotranspiration have been investigated. The Penman-Monteith formula is usually used to calculate evapotranspiration above vegetated surface and can be written as follows:

$$\lambda \cdot LH = \frac{\Delta(Rn - G) + \rho \cdot Cp \cdot (es(Ta) - e)/ra}{\Delta + \gamma \cdot (1 + rc/ra)}, \qquad (2.12)$$

where Δ is the slope in the relationship between air temperature and saturated atmospheric water vapor pressure (hPa C^{-1}) at air temperature Ta (C), es is atmospheric saturated water vapor pressure (hPa), e is atmospheric water vapor pressure (hPa), γ is the psychrometer constant, ra is the aerodynamic resistance (s m^{-1}) and rc is canopy resistance (s m^{-1}).

The aerodynamic resistance, ra, is related to the canopy structure and can be written as:

$$ra = \frac{\left(\ln \frac{z-d}{z_0}\right)^2}{\kappa^2 \cdot u(z)} \qquad (2.13)$$

where z is the observation height (m), z_0 is roughness length (m), d is the zero plane displacement (m), κ is the von Karman constant and u is wind speed at height z. The relationships between the values of z_0 and d and vegetation height h (m) are approximately represented by the following equations for coniferous forests.

$$d/h = 0.61 - 0.92 \quad \text{(average: 0.78)} \tag{2.14}$$

$$z_o/h = 0.02 - 0.14 \quad \text{(average: 0.07)} \tag{2.15}$$

For low vegetation other than forests, these relationships can be approximately expressed as

$$d/h = 0.61 - 0.83 \tag{2.16}$$

$$z_0/h = 0.03 - 0.16 \tag{2.17}$$

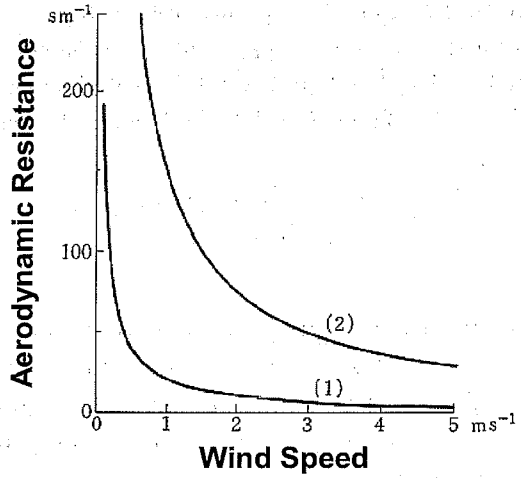

Figure 2.5 Two examples of the relationships between windspeed and the aerodynamic resistance. The lineindicates the relationship using the parametersfor a forest, and the line (2) for a grassland.

Figure 2.5 shows the relationships between wind speed at $z=h+2$ m and aerodynamic resistance for a forest (h=10 m, z_0=0.07 m, d= 7.8 m) and a grassland (h=0.1 m, z_0=0.013 m, d=0.063 m). Thc valucs of acrodynamic resistance arc smaller above a forest canopy than above a grass canopy under the same wind

speed. This is due to the difference in roughness length between the land surfaces. The roughness of a forest canopy is large, and the air is mixed well above the canopy.

The canopy resistance *rc* is influenced by plant physiological properties and controlled by environmental factors. The primary factors affecting the canopy resistance are solar radiation (more precisely PAR; photosynthetic active radiation), atmospheric water vapor content, leaf temperature, soil moisture, and atmospheric carbon dioxide concentration. Air temperature is often used instead of leaf temperature when leaf temperature cannot be measured. Figure 2.6 shows the general tendency of the resistance response for each of the five variables. The canopy resistance rapidly drops as the solar radiation increases. For soil moisture, the canopy resistance has a similar tendency. However, the resistance increases with atmospheric water vapor deficit and/or atmospheric carbon dioxide concentration. For air or leaf temperature, there is an optimal temperature, and the resistance increases in both directions away from the optimal leaf temperature.

The above discussion relates to the case of a dry canopy. Stomata will close when the canopy is wet, and interception loss occurs. The interception loss can be calculated substituting *rc*=0 into equation (2.12).

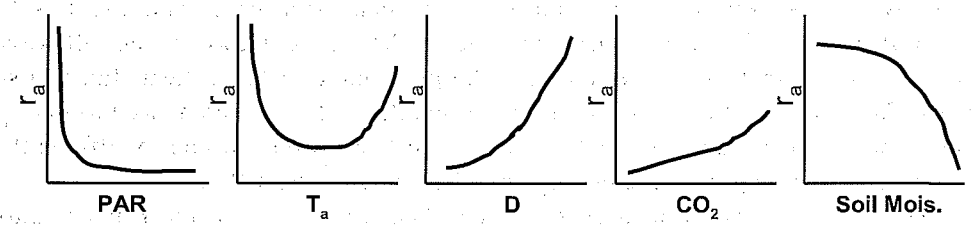

Figure 2.6 Typical responses of the canopy resistances to the five variables.

2.3.3 Characteristics of evapotranspiration from a dry forest canopy

Evapotranspiration E in equation (2.1) and latent heat flux LH in equation (2.3) are equivalent but expressed in different units; E is measured in mm hr^{-1}, and LH in W m^{-2}. Water and energy exchanges above the canopy are related to each other through evapotranspiration.

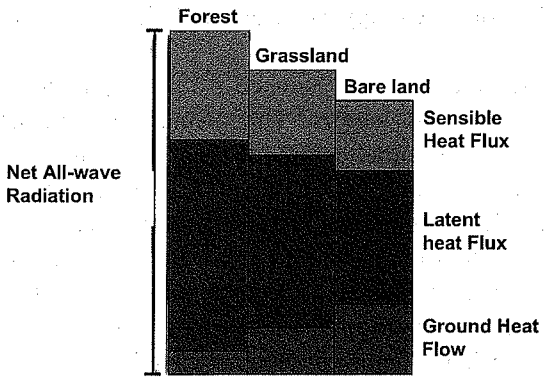

Figure 2.7 Energy partitioning in the typical landsurface types.

Forests consume a considerable amount of water as mentioned in section 2.2; the energy balance above the forest canopy is affected by evapotranspiration. Figure 2.7 shows a schematic diagram of the partitioning of energy by different land cover types. Net all-wave radiation is maximal for a forest, and about 64 % of net all-wave radiation is consumed in latent heat flux. However, net all-wave radiation is minimal over bare land and the percentage of latent heat flux is also small. The albedo of the top of the forest is smaller, 0.1 – 0.2, compared to that of other land surfaces, as shown in Table 2.1. Forests absorb solar energy efficiently, and transfer a large part of the energy absorbed to latent heat flux.

The ratio of sensible heat flux to latent heat flux is called the Bowen ratio, and described as

$$\beta = SH/LH \tag{2.18}$$

where β is the Bowen ratio.

The Bowen ration is usually less than unity in forests of humid and warm regions during the growing season, showing seasonal variation during the year inyearinthese regions.

Table 2.1 The albedo in the typical land use

Forest		Snow		Sand		Paddy field	Wheat field	Meadow
conifer	hardwood	new	old	wet	dry			
0.05-0.15	0.1-0.2	0.75-0.95	0.45-0.8	0.2-0.3	0.3-0.4	0.17-0.22	0.1-0.25	0.15-0.25

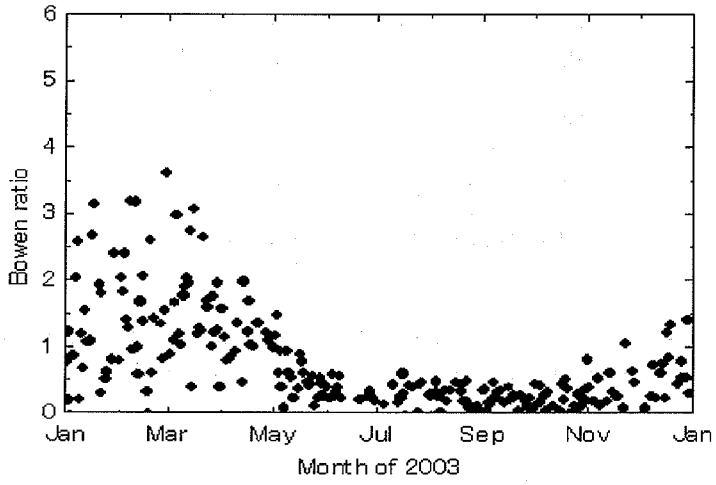

Figure2.8 Seasonal variation of the albedo above the mixed hardwood forest in Seto,central Japan

Figure 2.8 shows an example of seasonal variation in the Bowen ratio obtained at the Seto experimental site, a mixed forest in central Japan in the temperate climate zone. The seasonal variation is clearly "U-"shaped because evapotranspiration drops in winter and the energy partitioned into sensible heat flux becomes high. The opposite is true in the summer.

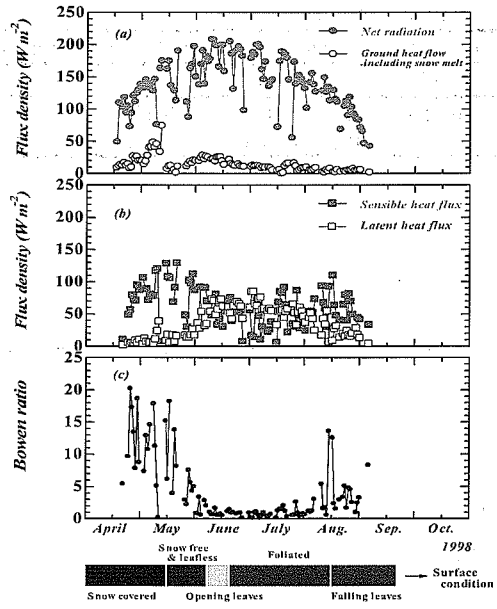

Figure 2.9 Seasonal variation of the energy flux components, the Bowen ration, and the land surface condition in the larch forest of eastern Siberia (Ohta et al., 2001)

Is the Bowen ration during the growing season less than unity in forests everywhere? Figure 2.9 shows the time series of the flux components, the Bowen ratio, and land surface condition in a larch forest in eastern Siberia (Ohta et al., 2001). The characteristics of the energy balance dramatically change after leaf emergence. Latent heat flux increases when the trees begin to foliate at the end of May. The sensible heat flux consequently drops at the same time although net all-wave radiation is increasing, and the Bowen ratio also drops to unity. This value remains close to 1.0 during the growing season and is larger than that obtained in temperate and tropical forests. For example, the Bowen ratio at Seto is about 0.3 during the growing season, and about 0.4 in an Amazonian tropical forest (Shuttleworth et al., 1984). It was previously considered that much of net all-wave radiation was consumed as latent heat flux above the forest canopy, but the magnitude of sensible heat flux is almost equal to or larger than that of latent heat flux in boreal forests (Sellers et al., 1995, Ohta et al., 2001, Hamada et al., 2004). The atmosphere and the soil are usually dry in a high latitude region and stomatal conductance becomes high in this region.

2.3.4 Characteristics of interception loss from a wet canopy

Evaporation also occurs from a wet canopy. This is interception loss, an important component of evapotranspiration; 10 – 50 % (about 20 % in many case) of precipitation evaporates from a wet canopy during and just after precipitation events. Hourly interception rates of 0.15 to 0.33 mm h^{-1} in coniferous forests and 0.37 to 0.45 mm h^{-1} in broad-leaved forests have been measured (McNaughton and Jarvis, 1983). These values are equal to transpiration rates on a clear day.

Interception loss is affected not only by meteorological variables but also by rainfall characteristics. Figure 2.10 shows the relationships between rainfall properties and the interception rate, the ratio of the amount of interception to gross rainfall (Toba and Ohta, 2005). Interception rates are distributed widely when the precipitation events are small; they converge toward an upper limit of 0.2 as precipitation events became larger. Interception loss is also affected by the

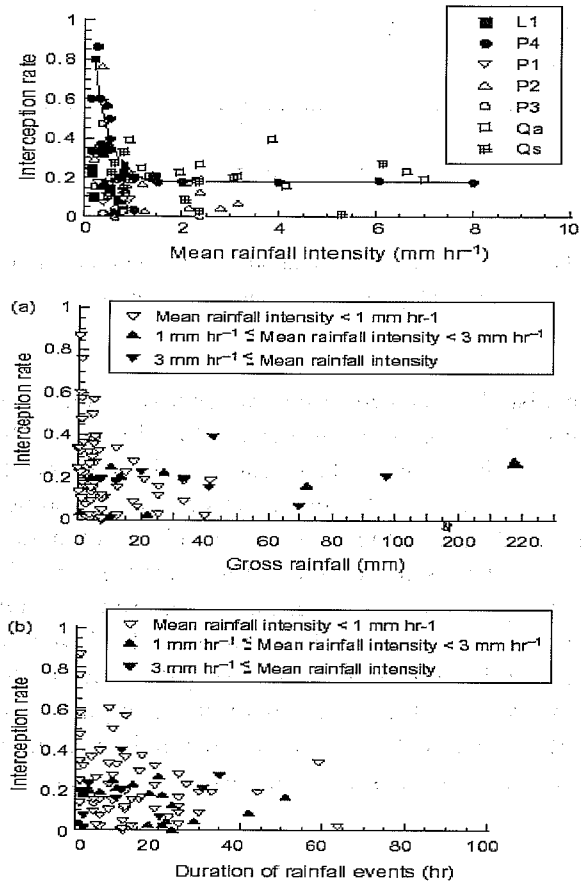

Figure 2.10 The relationships between the rainfall properties and the interception rate in temperate and boreal forests (Toba and Ohta, 2005).

canopy structure. Figure 2.11 shows the relationships between the plant area index (PAI) and the interception rate (Park et al., 2000; Toba and Ohta, 2005). The rate increases with PAI because the storage capacity is high within a dense canopy.

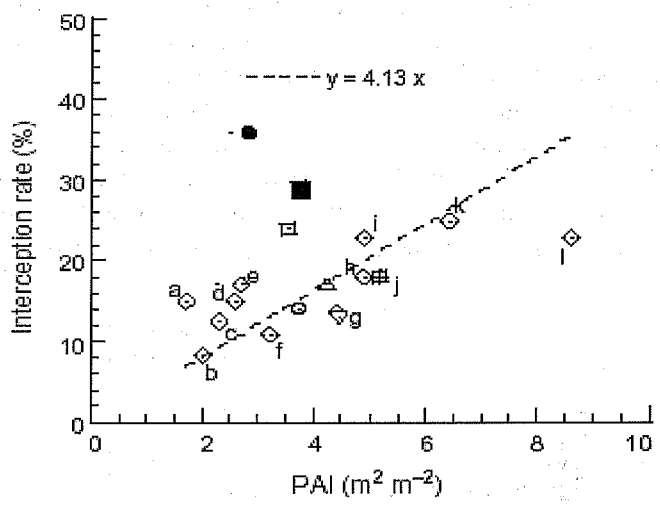

Figure 2.11 Rerlationship between the plant area index and the interception rate (Park et al., 2000; Toba and Ohta, 2005)

Interception can also be derived from the energy budget above the forest canopy during and just after precipitation events. Sensible heat flux above a wet canopy is usually upward in a temperate forest even in daytime (Shuttleworth et al., 1985; Takanashi et al., 2003). However, the opposite is sometimes true in a boreal forest. Figure 2.12 shows the time series of air temperature differences between two observation levels above the forest canopies in a boreal forest in eastern Siberia and a temperate forest in central Japan (Toba and Ohta, 2005). The air temperature is higher at the upper level than at the lower level above the temperate forests during rainfall events, even during daytime, so that sensible heat flux is downward. In contrast, the air temperature is higher at the lower level during rainfall and the sensible heat flux is upward in the boreal forest. This phenomenon may result from lower rainfall intensity in Siberia.

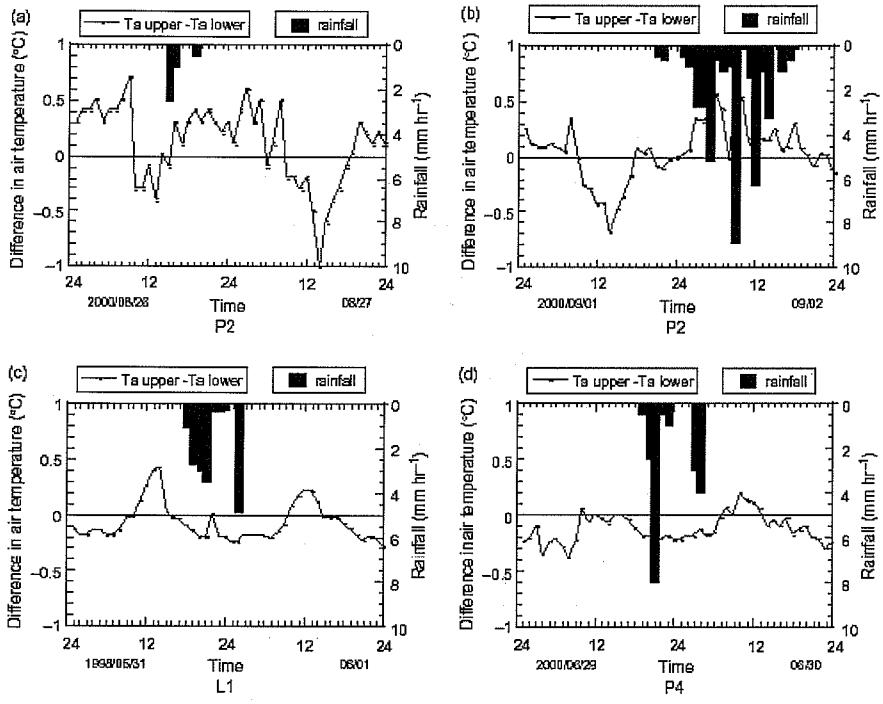

Figure 2.12 Time series of air-temperature differences observed at two levels and hourly hyetographs. Air-temperature differences were calculated by subtracting air temperature at the lower

2.4 Winter processes in forests

Evapotranspiration occurring in summer is discussed in the above sections. There are certain phenomena particular to in forests during the winter season.Forests have a low albedo but snow albedo is very high, as shown in Table 2.1. Figure 2.13 show time series of solar radiation, abledo and net all-wave radiation above a deciduous forest and an evergreen forest in a midwinter (Ohta et al., 1999). The albedo of forest floors covered with snow was more than 0.85 during this period. The albedo dropped to about 0.1 above an evergreen coniferous forest and 0.2 – 0.25 over a deciduous broad-leaved forest, respectively; this value was very low even in the deciduous forest. However, the net all-wave radiation was similar at each site. The major reasons are that the albedo is lower above the evergreen forest than the deciduous forest and thus, available short-wave radiation is higher in the evergreen forest; and total long-wave radiation emitted from the surface to atmosphere, including that from the canopy surface and the snow surface, is also higher at the evergreen forest because the canopies are closed in the evergreen forest and sparse at the deciduous forest.

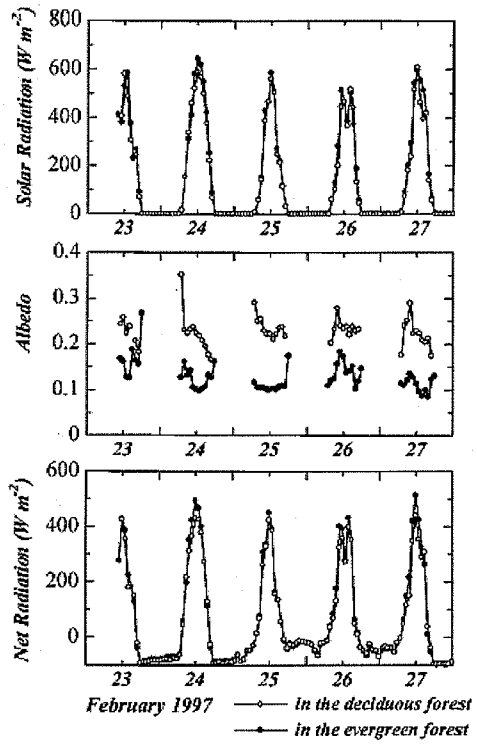

Figure 2.13 The time series for the incoming solar radiation, albedo, and net-all wave radiation above the ash (deciduous) and Sakhalin fir (evergreen) forests (Ohta et al., 1999)

The forest effects on sensible and latent heat fluxes are also substantial. The magnitude of sensible heat flux is affected by whether snow is present on the canopy. Sensible heat flux was smaller in the evergreen forest than in the deciduous forest because part of the evergreen canopy was covered with snow (Ohta et al., 1999); however the magnitudes were similar over the snow-free canopies. The direction of sensible heat flux was always upward in this study. Sensible heat flux dramatically changed when the greater part of the canopy was covered with snow. Table 2.2 shows the daily net all-wave radiation, sensible heat flux and latent heat flux above a Canadian jack pine forest and a lake (Harding and Pomeroy, 1996). Sensible heat flux was always downward on the lake, but the direction changed above the forest. The direction was upward when the canopy was snow free on 3 and 4 March, 1994 and downward above the snow covered canopy on 18 and 19 March, 1994. The combination of the effects of forests and snow cover is extremely complicate.

Table 2.2 Daily averages of energy balance for the forested and the lake site in Canada (W m^{-2}) (Harding and Pomeroy, 1996).

Date	Net radiation	Latent heat flux (HYDRA)	Sensible heat flux (HYDRA)	Sensible heat flux (Solent)
	(a) Beartrap Forest site			
3 March	30.6	16.6	27.5	32.5
4 March	30.9	18.8	46	48.3
18 March (1400–2400)	39.3	129.8	−16.3	−8.7
19 March	21.0	69.0	−11.2	−8.9
	(b) Namekus Lake			
3 March	−23.2	6.6	−29.5	
4 March	−22.7	7.9	−15.5	
18 March (1400–2400)	−9.3	20.2	−11.9	
19 March	1.1	7.7	−6.3	

Table 2.2 also indicates that latent heat flux is much greater from the canopy than from the lake. The latent heat flux of 129.8 W m-2 for 10 hours is equivalent to about 1.9 mm. This rate is about two-third of the daily evapotranspiration on a clear day in summer. Evaporation from a snow-covered canopy was also continuously observed in northern Hokkaido (Nakai et al., 1999). The average evaporation rate was 1.2 mm day^{-1} when the canopy was constantly covered with snow. This evaporation was four or more times greater than that measured at an open snow-covered site, 0.14 – 0.29 mm day^{-1} (Kojima et al., 1985). The large evaporation rate results from the high roughness length of forest canopies.

The existence of forests in the winter affects not only the radiation balance through the change of albedo but also heat and water transfer between the atmosphere and forests. However, little is known about evaporation from snow-covered canopies.

References

Abe, T., Tani, T., Kishioka, T., and Kobayashi, C., (1983), The effects of pine tree killing by the pine-wood nematode on direct runoff, Bull, Kansai Brunch, J, For, Soc., 34, 337-340. (In Japanese)

Abe, T., and Tani, T., (1985), Streamflow changes after killing of pine trees by the pine-wood nematode, J, Jap, For, Soc., 67, 261-270. (In Japanese with English summary)

Bosh, J., J.M., and Hewlwtt, J.D., (1982), A review of catchment experiments to determine the effect of vegetation changes on water yield and

evapotranspiration, J, Hydrol., 55, 3-23.
Harding, R.J., and Pomeroy, J.W., (1996), The energy balance of the winter boreal landscape, J, Climate, 9, 2778-2787.
Hamada, S., Ohta, T., Hiyama, T., Kuwada, T., Takahashi, A., and Maximov, T.C., (2004), Hydrometeorological behaviour of pine and larch forests in eastern Siberia, Hydrological Processes, 18, 23-39.
Kojima, K., Ishikawa, N., Motoyama, N., and Yamada, Y., (1985), Evaporation rate of snow at the surface of a snow cover – observation in Sapporo and Moshiri, Hokkaido, Low Temperature Science, A-44, 49-62. (In Japanese with English summary)
McNaughton, K.G., and Jarvis, P.G., (1983), Predicting effects of vegetation changes on transpiration and evaporation, In: Kozlowski (ed.), Water Deficits and Plant Grouth, Academic Press, New York, 1-47.
Nakai, Y., Sakamoto, T., Terajima, T., and Kitamura K., (1999), The effect of canopy-snow on the energy balance above a coniferous forest, Hydrological Processes, 13, 2371-2382.
Ohta, T., Suzuki, K., Kodama, Y., Kubota, J., Kominami, Y., and Nakai, Y., (1999), Characteristics of the heat balance abve the canopies of evergreen and deciduous forests during the snowy season, Hydrological Processes, 13, 2383-2394.
Ohta, T., Hiyama, T., Tanaka, H., Kuwada, T., Maximov, T.C., Ohata, T., and Fukushima Y., (2001), Seasonal variation in the energy and water exchanges above and below a larch forest in eastern Siberia, Hydrological Processes, 15, 1459-1476.
Sellers, P., Hall, F., Margolis, H., Kelly, B., Baldocchi, D., Hartog, G.D., Cihlar, J., Ryan, M.G., Goodison, B., Cril,l P., Ranson, K.J., Lettenmaier, D., and Wickland, D.E., (1995), The boreal ecosystem—atmosphere study (BOREAS), an overview and early results from the 1994 field year, Bulletin of American Meteorological Society, 76, 1549-1577.
Shuttleworth, W.J., Gash, J.H.C., Lloyd, C.R., Moore, C.J., and Roberts, J., (1984), Eddy correlation measurements of energy partition for Amazonian forest, Quart, J, R, Soc., 110, 1143-1162.
Shuttleworth, W.J., Gash, J.H., Lloyd, C.R., Moore, C.J., and Roberts, J., (1985), Daily variations of temperature and humidity within and above Amazonian forest, Weather, 40, 102-108.
Swank, W.T., and Crossley, D.A., (1988), Forest hydrology and ecology at Coweeta, Springer-Verlag, Berlin.
Takanashi, S., Kosugi, Y., Tanaka, H., and Tanaka, K., (2003), Evapotranspiration from a Japanese cypress forest during and after rainfall, J, Jpn, Soc, Hydrol, Water Resour., 16, 268-283. (In Japanese with English summary)
Toba, T., and Ohta, T., (2005), An observational study of the factors that influence interception loss in boreal and temperate forests, J, Hydrol., 313, 208-220.
Park, H., Hattori, S., and Kang, H., (2000), Seasonal and Inter-plot variations of

Stem flow, through fall and interception loss in two deciduous broad-leaves forests, J, Jpn, Soc, Hydrol, Water Resour., 13, 17-30.

Chapter 3

Biogeochemical Processes of Carbon in Forested Ecosystem

Hideaki Shibata
Field Science Center for Northern Biosphere,
Hokkaido University, 250 Tokuda, Nayoro 096-0071, Japan
Tel: +81-1654-2-4264
Fax: +81-1654-3-7522
e-mail: shiba@fsc.hokudai.ac.jp

3.1 General principle of carbon cycling in forested ecosystem

Understanding carbon cycling and budget in forest ecosystem is very important to assess the function of forest under global climate change (Schlesinger, 1997; Waring and Running, 1998; Chapin et al., 2002). In forest ecosystem, biogeochemical processes of carbon include biotic and abiotic relations and their interaction (Figure 3.1). In this chapter, the general outline and methodology of carbon biogeochemistry in forest ecosystems are introduced in the beginning part, then one of the typical example of the field study on carbon cycling and budget in forested basin located in northern Japan (Shibata et al., 2005)is presented in the letter part of the chapter.

3.1.1 Photosynthesis and respiration of vegetation

Photosynthesis of vegetation is primal process for input of carbon to vegetation and soil ecosystem (equation 3.1). Photosynthesis rate of single leaf is mainly controlled by several environmental factors including light, air CO_2 concentration, water, nutrient (mainly nitrogen) and so on (See details in Chapter 9).

$$CO_2 + 2H_2O + light\ energy \rightarrow CH_2O + H_2O + O_2 \qquad (3.1)$$

Net photosynthesis is the balance of photosynthesis and respiration from leaf, shoot, branch, trunk and roots. Plant respiration (autotrophic respiration) includes two major components, i.e. (i) maintenance and (ii) growth and synthesis respiration. To express the productivities in ecosystem, GPP (Gross primary productivity) and NPP (Net primary productivity) has been widely used (equation

3.2).

$$NPP = GPP - Rp \quad (3.2)$$

(R*p*: Respiration of plant)

NPP of terrestrial ecosystems vary with different climate and vegetation, ranging from 99 gC m^{-2} y^{-1} in tundra to 916 gC m^{-2} y^{-1} in savanna (Cramer et al., 2000, Figure 3.2)

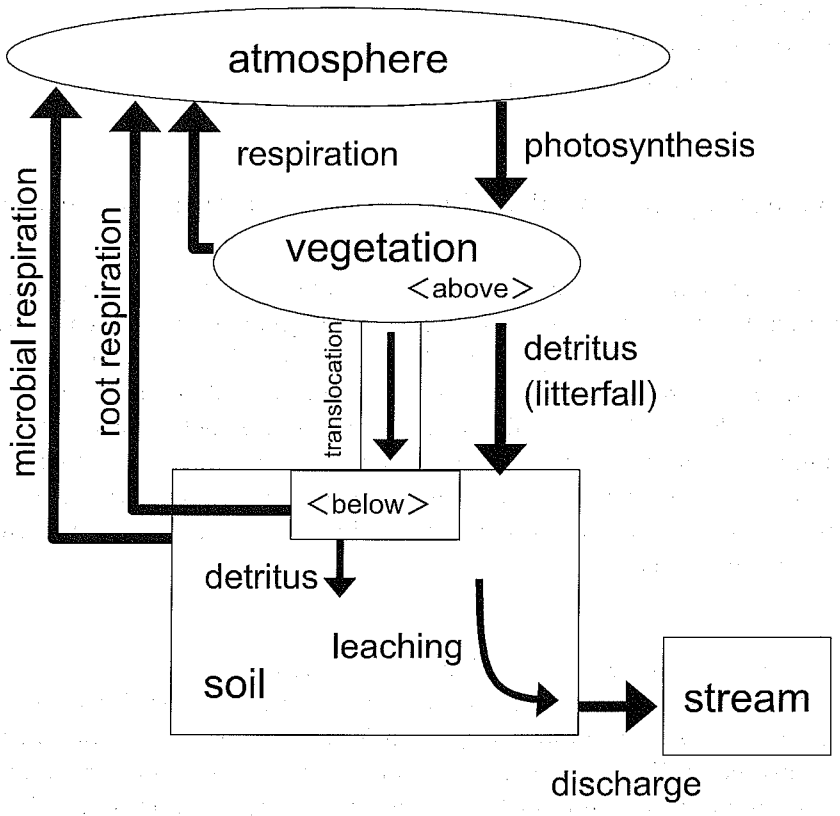

Figure 3.1 General outline of carbon budget and cycling in forest ecosystem (modified from Shibata et al., 2005).

3.1.2 Translocation of carbon from vegetation to soil

Fixed carbon through NPP is utilized to synthesize above- and belowground biomass. In aboveground vegetation, litter fall (leaf, branch and so on) from canopy to soil is important process to supply the carbon to forest floor. Detritus from above and belowground vegetation to soil was major input of carbon to soil system. In particular, mortalities of fine root and exudates from roots are major pathway for carbon supply in the soil system. Nadelhoffer et al. (1985) reported the turnover rate of fine root ranged

0.5-2.2 y^{-1} in nine forest ecosystems in southern Wisconsin, US. Reich and Bolstad, (2001) summarized that the 14 - 80 % of the NPP was produced in belowground in temperate forest, indicating that the belowground process is very important component for the ecosystem productivities.

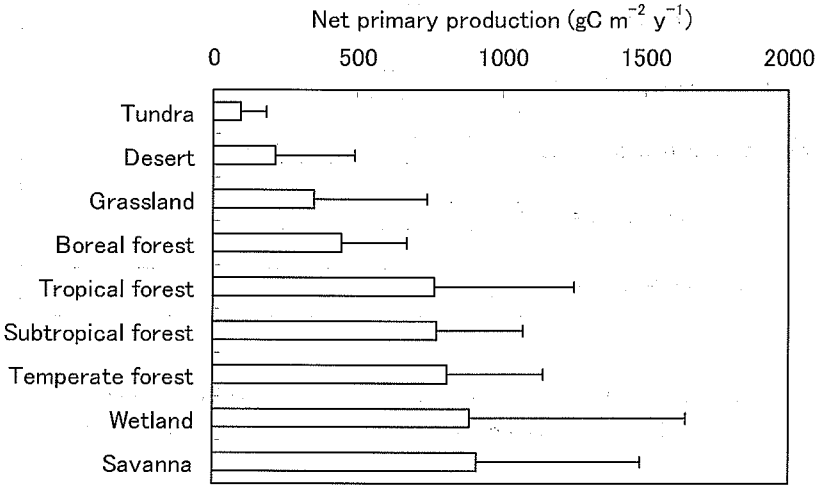

Figure 3.2 Net primary production of terrestrial ecosystem in various climate and vegetation (Cramer et al., 2001). Bar on each bar represents the standard deviation (SD).

3.1.3 Soil respiration

In soil system, CO_2 is emitted from soil surface as result of autotrophic respiration by root and heterotrophic respiration by microorganisms in soil. This emission of CO_2 is termed as soil respiration. Rate of soil respiration are generally controlled by soil temperature and moisture. In general, Q_{10} values are used to indicate the sensitivity of soil respiration to temperature. Q_{10} represents the change in the rate of respiration for a 10 °C change in temperature (equation 3.3).

$$Rs = R_0 Q_{10}^{[(T-To)/10]} \quad (3.3)$$

Rs: Soil respiration
R_0: Basal respiration
T: temperature

Raich and Schlesinger (1992) summarized the annual rate of soil respiration in various climate and vegetation, ranging from 60 gC m^{-2} y^{-1} in boreal tundra to 1260 gC m^{-2} y^{-1} in tropical moist forest (Figure 3.3).

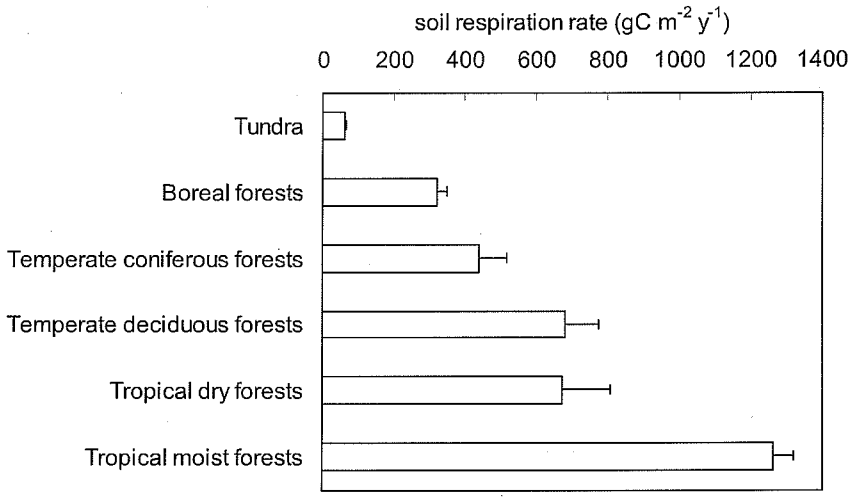

Figure 3.3 Annual rate of soil respiration in various forest ecosystems (Raich and Schlesinger, 1992). Bar on each bar represents standard error (SE).

3.1.4 Carbon storage and leaching from soil

Some part of carbon input to soil is accumulated in soil and leached from soil. Dissolved and particulate carbon is transferred in soil horizon with the movement of soil water. Dissolved carbon are consists of organic and inorganic carbon. Dissolved organic carbon (DOC) is produced during the process of mineralization of organic matter (litter, humus, detritus of microorganisms and exudates from root). Various forms and molecules exist in DOC, including humic substances, amino acids and so on. Since DOC plays a role of energy source, DOC is important not only for microorganisms in soil, but also for heterotropics organisms in aquatic ecosystem (Kaplan and Newbold, 2000). Dissolved inorganic carbon (DIC) is derived from CO_2 in soil air which originated from respiration of root and microorganism. In natural water, DIC has some forms including HCO_3^-, CO_3^{2-} and H_2CO_3 depends on pH in water. Since dissolution process of DIC produced proton, DIC in soil closely relates to silicate weathering

of parent materials.

Certain part of DOC and DIC are leached from soil to groundwater and stream water, resulting (i) important source of carbon and energy in stream ecosystem and (ii) possible source of secondary CO_2 emission through the degassing from stream surface (Jones and Mulholland, 1998).

3.2 Monitoring and analytical method of carbon dynamics

3.2.1 Net ecosystem exchange (NEE) and NPP

Observation of eddy fluxes on the forest canopy has enabled us to quantify the NEE (equation 3.4), photosynthesis and respiration between atmosphere and canopy (Baldocchi et al., 2001, See details in Chapter 1).

$$NEE = Photosynthesis - Rav - Rs \quad (3.4)$$

R*av*: Respiration of above vegetation

R*s*: Soil respiration

In general, NPP (expressed as equation 3.2) is determined measuring each component in equation (3.5).

$$NPP = Increment\ of\ woody\ tissues + Litterfall + Grazing\ by\ animal \quad (3.5)$$

Annual increment of diameter of breath height (DBH) and tree height are usually measured to estimate increment of stand volume of vegetation in a certain research area. Allometric function between DBH, tree height and biomass of each component (leaf, branch, root and so on) of vegetation are used to estimate annual increment of woody tissues (e.g. Hiura, 2005).

Litterfall of aboveground vegetation is usually measured using litter trap with a certain collecting area (e.g. circular shape of 1 m^2). It is essential for better quantification to measure at a several points as replicates in the studied area because the amount of litterfall largely varies with space.

Observation of NPP in belowground vegetation is difficult due to some methodological reasons (Smit et al., 2000a). Sequent sampling of soil core, in-growth core (Tripathi et al., 2005) and minirhizotron (Majdi et al., 2005; Smit et al., 2000b) are often used to estimate rate of production and mortalities of fine root. Disturbances during *in situ* sampling and measurement of root sometimes cause serious uncertainties for the quantification of root dynamics (Smit et al., 2000b).

3.2.2 Soil respiration and soil solution

Closed or flow-through chamber system with an infrared gas analyzer (NDIR)

is commonly used to determine the rate of CO_2 emission from soil surface (e.g. Boone et al., 1998; Dantec et al., 1999). Using temperature-respiration functions, annual soil respiration is estimated based on the continuous measurement of soil temperature.

Various lysimeters are used to obtain soil solution for chemical analysis of solute concentration in soil solution. Plate lysimeter with no suction is commonly used to collect soil water which flows by gravity water movement, while tension lysimeter with suction cup is usually utilized to collect soil matrix water retained between the soil particles (Wolt, 1994).

3.2.3 Carbon in stream water

Dissolved and particulate carbon is existed in stream water of typical natural watershed. DOC and DIC are usually analyzed after filtering using glass-fiber filter (GF/F) (e.g. Shibata et al., 2001). Since the POC has various particle sizes in stream water, different size of filter is used to separate each fraction of POC. Water discharge rate has to be measured in stream to estimate the dissolved and particulate carbon flux from the watershed.

3.2.4 Analysis of DOC, DIC and POC in water

DOC is usually analyzed using total carbon analyzer (e.g. Shimadzu TOC 5000A, Shimadzu Co. Ltd. Kyoto). In this system, water sample is combusted at high temperature (e.g. 680 °C) in the tube with catalysis and converted to CO_2 gas. Then CO_2 gas is analyzed using NDIR sensor in the analyzer. DIC is also analyzed using the total carbon analyzer without combustion. For further improvement to detect lower concentration of DOC, DIC in sample water is removed adding strong acid and degassing before the DOC analysis. Concentration of POC in the particle sample on the filter is analyzed using CN analyzer after the drying. In this system, the particle sample is oxidized in the combustion tube and converted to CO_2 gas, then detected by thermal conductivity detector (TCD) (Burrman et al., 1996)

3.3 Case study on carbon dynamics in forested basin

In this section, the example of the case study on carbon cycling and budget in forested basin is presented (Shibata et al., 2005). This study was conducted as a part of TEMA (Terrestrial Ecosystem in Monsoon Asia) program in IGBP (International Geosphere and Biosphere Program)-GCTE (Global Change of Terrestrial Ecosystem) project (Kohyama et al., 2005).

3.3.1 Background of the study

The quantification of carbon budget and cycling is a useful research tool with

which to assess the role of forest vegetation and soil on carbon accumulation in the ecosystem. Given the close relationship that exists between the carbon dynamics of forest ecosystems and productivity within the ecosystem, carbon dynamics has become a fundamental component of the research conducted by ecosystem ecologists since international biological program (IBP) that was conducted late 60s to 70s (Cole and Rapp, 1981). However, quantification of the actual carbon sequestration rate in forest ecosystems is complicated by the difficulty associated with measuring the rate of CO_2 exchange in the atmosphere and ecosystem. Eddy-correlation techniques for assessing CO_2 flux over the forest canopy provide quantitative information on net photosynthesis and respiration (for both vegetation and microorganisms), or net ecosystem exchange (NEE) (Baldocchi et al., 2001).

NEE, measured using eddy flux at the boundary between the canopy and the atmosphere corresponds with the net flux of CO_2 including photosynthesis and respiration, provides an indication of how much carbon was sequestrated in the ecosystem. However, while NEE provides useful quantitative information on ecosystem functioning associated with carbon sequestration, it cannot be used to derive the extent partitioning of this sequestrated carbon in the terrestrial ecosystem. Given that the difference in turnover time for carbon in the soil and that contained in the vegetation is markedly different (Chapin et al., 2002; Malhi et al., 1999), it is very important to assess the internal cycling and partitioning of carbon in the vegetation and soil system separately. It is thus essential to compare the carbon budget and the internal cycling in the same basin over same period.

In a previous study associated with the internal partitioning of carbon in ecosystems, Malhi et al., (1999) indicated the carbon distribution and cycling in forest ecosystems was highly dependent upon climate and vegetation type. However, studies that have integrated monitoring of the carbon budget and cycling in the same basin over the same period of time have rarely been conducted to date. In the Asian region particularly, biogeochemical assessments of eddy CO_2 flux and internal cycling and budget have been particularly limited (Yamamoto et al., 1999), despite the occurrence unique climatic and other environmental characteristics that distinguish the region from the relatively well-studied forests of the northeastern US and northwestern Europe. In addition, this studied forest has been recognized as sensitive ecosystem against environmental changes and stresses because the forest was located on the infertile volcanic young soil in transient zone from temperate to sub-boreal region.

Quantitative analysis of the carbon dynamics will not only provide fundamental information of the biogeochemical processes of ecosystems, but also contribute towards our current understanding of the impact of carbon sequestration on ecosystem functioning and the effect that this might have on global climate change. The objective of this study was therefore to 1) quantify the carbon budget and cycling, and, 2) understand the quantitative role of the vegetation and soil on carbon sequestration in a forest basin.

3.3.2 Study site

This study was conducted in the Horonai stream basin in the Tomakomai Experimental Forest (TOEF) of Hokkaido University, located in southwestern Hokkaido, northern Japan (42° 40' N, 141° 36'E). The Horonai stream is a first-order stream with a basin area of 9.4 km^2. The mean annual precipitation is approximately 1,200 mm and the mean annual temperature is 7.1 °C. Vegetation in the basin consists of cool-temperate forest, mainly dominated by secondary deciduous forests that colonized the area after a typhoon in 1954. Approximately 50 tree species are co-existed, including *Quercus mongolica* var. *crispula*, *Acer mono*, *Acer palmatum ssp. matsumurae*, and *Magnolia hyporeuca* (Hiura, 2001). The predominant soil type is volcanic regosols (Andic Udipsamments, Soil Survey Staff 1994), with the parent material of the soil consisting of clastic pumice and sand that was deposited by eruptions of Mt. Tarumae in 1667 and 1739 (Sakuma, 1987). Other detailed characteristics of the vegetation, soil and streams of the area have been described by Shibata et al. (1998, 2001), Takahashi et al. (1999) and Hiura (2001).

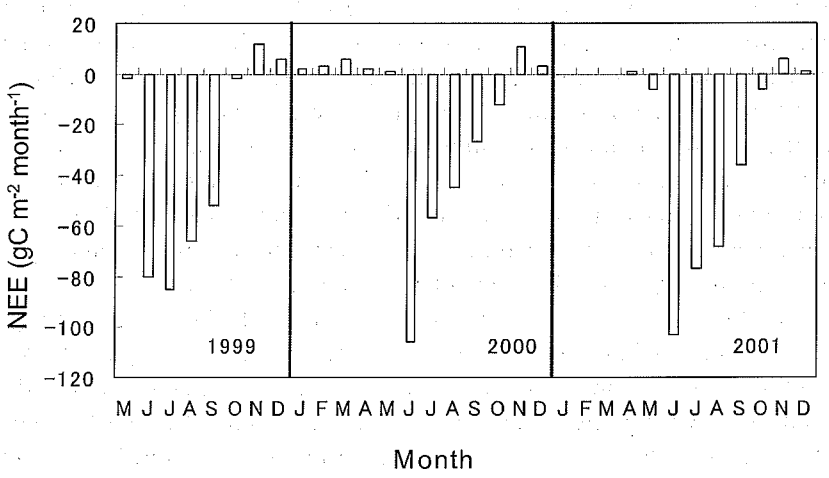

Figure 3.4 Seasonal fluctuations in monthly net ecosystem exchange (NEE) over the forest canopy from 1999 to 2001 in TOEF, northern Japan (modified from Shibata et al., 2005). Negative values represent net inflow of carbon from atmosphere to canopy.

3.3.3 Method of field observation and chemical analysis

CO_2 fluxes between atmosphere and canopy (NEE) was measured by applying the eddy correlation method above the canopy layer from a 21-meter high observation tower from 1999 to 2001 (Tanaka et al., 2001). The mean height of the vegetation around the tower is approximately 13 m. Atmospheric CO_2 concentration was measured using a NDIR (Non dispersive infrared)-CO_2 sensor

(LI-COR 6262, Li-Cor Co. Ltd.) by the closed-path system. An ultrasonic anemometer (DAT-600, Kaijo Co. Ltd.) and CO2/H2O fluctuation meter (AH-300, Kaijo Co. Ltd.) were used for the measurement of these fluxes.

Long-term inventory data collected for the Tomakomai Research Station of Hokkaido University was used to calculate the stand volume of various forest stands in the study area. The investigated plot was 1 ha in area, and the stand volume and mortality of the above-ground vegetation were measured at every one year interval. Both above- and below-ground biomass of the stand was estimated by combining the measured stand volume and applying an allometric-growth equation for each species derived from harvesting research previously conducted in the study basin (Takahashi et al., 1999). A more detailed description of the vegetation and the methods used to estimate biomass on a landscape scale was described by Hiura (2001, 2005). Litter traps (1 m^2) were used to collect litter-fall from vegetation with 25 replicates in a representative secondary stand in the study area. These samples were collected on a monthly interval, dried and weighed from 1999 to 2001 (Hiura, 2005).

Closed-chamber system and NDIR sensor (LI-6200, Licor Co Ltd.) was used to measure soil respiration (Yanagihara et al., 2000). Twelve circular chambers (71.6 cm^2) were installed in stands of forest considered representative of the study area. Soil respiration and surface soil temperature (0-10 cm) were measured using the sensor of 10 cm long at monthly intervals during periods of no snowfall from 1999 to 2000. The relationship between soil respiration and soil temperature derived empirically and used to extrapolate annual soil respiration using the continuous soil surface temperature data; one of the long-term meteorological parameters collected at the Tomakomai Experimental Forest.

The tension-free lysimeters was installed under the forest floor and in mineral soil (1.5 m deep) to collect the soil gravity water. Four lysimeters were thus installed below the forest floor and two lysimeters in the mineral soil at the bank near the middle part of the stream. Stream water was collected from the upper and lower river reaches at two-week intervals and analyzed for dissolved organic (DOC) and inorganic carbon (DIC) concentrations using a TOC analyzer (TOC 5000A, Shimadzu Co. Ltd.). Particulate organic carbon (POC) (particles > 0.7 μm) was also measured by filtering the stream water collected from the lower stream reaches (Shibata et al., 2001). Total carbon content of the particulate material was analyzed using a CN analyzer (PE 2400 II, Perkin elmer Co. Ltd.).

Stream height was measured continuously using a pressure transducer and data logger at the weir station located at the lower stream reaches. Stream discharge was calculated using an empirical relationship between stream height and observed discharge (Shibata et al., 2001). Carbon flux in the stream was calculated by multiplying the carbon concentrations for DOC, DIC and POC, with discharge. Given that this basin was located in very flat region, and on course, volcanic, gravel deposit suggesting that the groundwater inflow from the neighboring basin might affect the hydrologic budget, differences of the flux between upper and lower stream reaches were used to quantify net export of DOC

and DIC from soil to stream (Shibata et al., 2001). The influx of POC from the upper stream reaches was assumed to be negligible because most of the POC would have been derived from the riparian canopy and the riverbank. Throughfall was collected using a circular funnel (30 cm in diameter) at the riverbank and analyzed for DOC and DIC concentrations. More detailed methods for calculating the contributions of the soil and stream on carbon dynamics were reported by Shibata et al., (2001).

3.3.4 Budget calculation

All carbon flux measurements were conducted from 1999 to 2001. Mean fluxes for the three years were used in the budget analysis. We used the steady state budget for vegetation and soil as illustrated in equations (3.6) and (3.7), respectively, to analyze the carbon dynamics of the ecosystem.

$$NEE - Rs = LF + AB + AC \quad (3.6)$$

NEE: Net ecosystem exchange
Rs: Soil respiration
LF: Litterfall and mortality of above vegetation
AB: Above-ground biomass increment
AC: Allocation from above to below vegetation

$$AC - BB + LF = SR + DC + SS \quad (3.7)$$

BB: Below-ground biomass increment
DC: Discharge to stream
SS: Carbon storage in organic and mineral soil

Measured carbon fluxes were NEE, SR, LF, AB, BB and DC, while the estimated carbon fluxes based on these equations were AC and SS. Left side of equation (3.6) (=NEE – SR) correspond with gross ecosystem exchange (GEE).

3.3.5 NEE of the forest ecosystem

Figure 3.4 shows the seasonal fluctuation in monthly NEE over the canopy from 1999 to 2001. Negative values for NEE indicate net CO_2 transport from atmosphere to ecosystem. Atmospheric CO_2 was sequestrated mainly from June to October each year. Maximum estimates of carbon uptake ranged from -80 to -100 gC m^{-2} month-1 from June to July (Figure 3.4).

Annual mean NEE (-258±36 SD gC m^{-2} y^{-1}) in this basin is comparable with that reported for a growing of season similar length (about 150 days) in the worldwide CO_2 flux network (FLUXNET, Baldocci et al., 2001). However, for the eddy measurements, it should be noted that several uncertainties regarding the applicability of the techniques still remain including, (i) difficulties in measuring eddies during periods of high atmospheric stability and the irregularity of the

canopy surface, and, (ii) the drainage flow of CO_2 across the stream valley (Baldocci et al., 2001) These uncertainties might affect the estimation of the unmeasured flux; particularly the allocation of carbon from the vegetation to the soil. In addition, we used the compartment model for the carbon budget (as discussed below), which assumes a steady state on an annual basis. It should be noted that actual carbon transport sometimes fluctuates and is transient. For example, the aforementioned buffering function of the soil system against temporal fluctuations in carbon input would be attributed to the transient system.

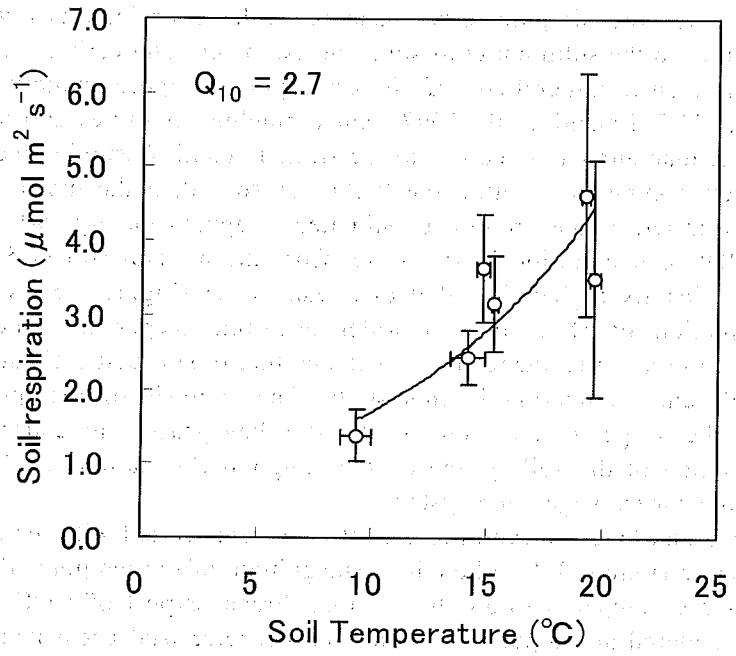

Figure 3.5 Relationship between soil respiration and soil surface temperature (0-10 cm) in TOEF, northern Japan (modified from Shibata et al., 2005). Data were obtained at different months during non-snowy period. Bars represent standard deviations.

3.3.6 Carbon dynamic in vegetation-soil-stream system

Soil respiration was observed to fluctuate with in response to changes in soil temperature (Figure 3.5). The Q_{10} value was 2.7 and the annual flux of soil respiration over three years was 592 (+55 SD) gC m^{-2} y^{-1} within the range of reported values for temperate forest (Figure 3.3). The annual flux of soil

respiration was approximately two times larger than the NEE in this studied basin. Given this relationship between respiration and NEE, gross ecosystem exchange (GEE; the net flux of photosynthesis and respiration for the above-ground vegetation) corresponded with 850 gC m^{-2} y^{-1}.

Litterfall occurred mainly in late summer and fall (October and November) of each year. The annual carbon sequestered by the vegetation was approximately 42 % of the NEE. The sum of the litterfall and mortality for above-ground vegetation was 197 gC m^{-2} y^{-1}, accounting for the organic carbon input from the above-ground vegetation to soil surface.

In the soil system, dissolved organic carbon decreased with depth of the ground (Figure 3.6), suggesting that the adsorption and/or decomposition of the DOC were the dominant mechanisms of DOC retention in ground (Shibata et al., 2001). In general, volcanic pumice is considered to have a relatively high ability to adsorb solutes to the solid phase of soil. The estimated total carbon pool in soil from the O horizon to mineral soil of 100 cm depth was approximately 5500 gC m^{-2} (Sakuma, 1987; Eguchi et al., 1997), corresponding to values approximately 38 times larger than annual net carbon sequestration in soil. Assuming most of the organic carbon accumulates within the 0-100 cm soil, then the mean residence time of sequestrated carbon in soil is estimated at approximately forty years in this basin. DOC concentration in soil water from the mineral soil (1.5 m deep) was still significantly higher than that of stream water (Figure 3.6), suggesting that the depletion of DOC in soil water occurred deeper in mineral soil. Consequently, the mean residence time of the carbon in soil that estimated above could be still underestimation in this study. The analysis of the quantitative dynamics in the deeper mineral soil would be a key process to understand the buffering function of the soil system on the temporal fluctuations of the carbon input from atmosphere-vegetation system.

DOC, DIC and POC concentrations in stream water varied with the change of stream discharge (Figure 3.7) although the magnitude of the temporal fluctuation was not so large compared to another region. Stream export of DOC, DIC and POC was considered an output of carbon from the terrestrial ecosystem. Annual mean export of dissolved and particulate carbon from soil to stream for three years was 4.1 (±1.8 SD) gC m^{-2} y^{-1} and DIC, DOC and POC accounted for 68, 13 and 19 % of the total carbon export to the stream. The total export of carbon to the stream corresponded to only 2 % of the NEE flux in this basin. DOC concentration was higher in the surface soil water, and tended to decrease with depth of ground. DIC was a major carbon forms in stream water collected from both the upper and lower stream (Figure 3.7) reflecting the soil and bedrock characteristics (young volcanic pumice).

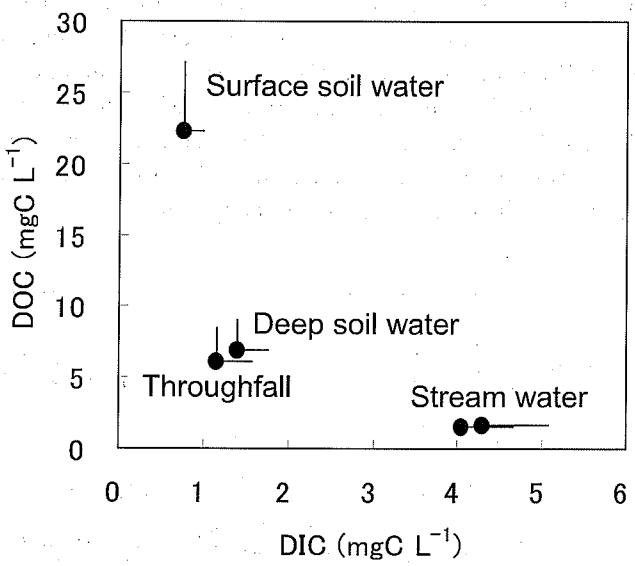

Figure 3.6 Mean concentration of DOC and DIC in throughfall, surface soil water (forest floor), deep soil water (1.5 m depth) and stream water (left; upper, right; lower) in TOEF, northern Japan (modified from Shibata et al., 2005). Bars represent standard deviations.

3.3.7 Carbon budget in the basin

Based on the NEE and export to the stream, the annual net carbon sequestration rate in this basin (=NEP; Net Ecosystem Productivity) was 254 gC m^{-2} y^{-1}. The carbon allocation from the above- to below-ground vegetation calculated using equation (3.6) was 549 gC m^{-2} y^{-1}, corresponded to 65 % of GEE. The carbon budget in the soil (equation 3.7) indicated that 146 gC m^{-2} y^{-1} was sequestrated in the soil in this basin. The annual carbon sequestration in vegetation and soil accounted for 43 and 57 % of NEP, respectively. The total input of carbon from the above- and below- ground vegetation to the soil was 730 gC m^{-2} y^{-1}, including the litterfall, mortality of above-ground vegetation, root detritus and root respiration.

In this forest basin, net carbon sequestrated in the ecosystem is partitioned between the vegetation and soil almost equally on an annual basis (Figure 3.8). The total litterfall and above-ground tree mortality accounted for 27 % of the total carbon input from the vegetation to soil. Consequently, the transport carbon through the roots into the soil was an important pathway for carbon input to the soil. Since CO_2 input via root respiration to soil would ordinarily be balanced by emission from the soil surface to the atmosphere in a annual steady-state (no net change in the storage of CO_2 in soil on annual basis), the organic carbon input via root detritus and exudates could be an important form of carbon for the net release of carbon from below-vegetation to soil. The net increment of root biomass (16 gC m^{-2} y^{-1}; estimated using the allometric-growth equation obtained from

harvesting measurements) suggested that the increment in very fine root biomass might have been underestimated in this budget. Detailed measurement and estimation methods will be required to clarify the extent of fine and very fine root production with respect to the carbon sequestration (Shutou and Nakane, 2004; Satomura et al., 2003). Reich and Bolstad (2001) reported that the net primary production of below-ground vegetation accounted for 14-80 % of the total net primary production in various temperate forest ecosystems.

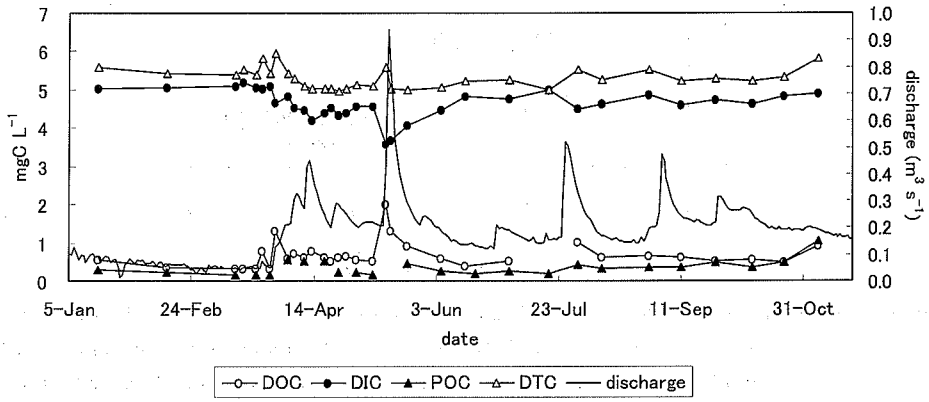

Figure 3.7 Seasonal fluctuation of water discharge, DOC, DIC, POC and DTC (dissolved total carbon = DOC + DIC + POC) concentration (2000) in Horonai river in TOEF, northern Japan.

Hiura (2005) indicated that the secondary forest that is the dominant vegetation type in this basin showed more higher net biomass increment than the mature forest also found in this basin, suggesting that the higher sequestration rate of the vegetation and soil in this basin may mean that the forest in the study area was relatively young and at an early stage of succession. Since most of the forest stands in this basin became established after a large disturbance caused by a by typhoon in 1954, the growth rate of the vegetation seems to be still increasing. The soil is also a very young regosol that developed after the recent eruption of a volcano within the last several centuries. These age characteristics of vegetation and soil would affect the NEP in the basin. Furthermore, since the study area is located near urban and industrial areas (Shibata et al., 1998), the forest ecosystem currently receives slightly elevated amounts of atmospheric nitrogen (4-5 kgN ha^{-1} y^{-1} of wet deposition, Shibata et al., 1998). The effect of nitrogen deposition as a nutrient input on carbon sequestration would need to be examined more closely to determine if the input of nitrogen nutrients from the atmosphere would enhance the uptake of carbon in the forest (Lloyd, 1999; Nadelhoffer et al., 1999). See next chapter for more information of linkage between carbon and nitrogen

biogeochemistry.

The study presented in this section suggest that the fundamental characteristics of the parent materials of soil and the chronological attributes of the vegetation and soil - including natural disturbances in the past - was an important factor affecting the current NEP and the partitioning of sequestrated carbon in the ecosystem. An integrated regional cross-site analysis of carbon biogeochemistry, including eddy measurements and budgets under the various environmental conditions would improve our understanding of the role of forest ecosystem functioning on global climate change.

3.4 Suggested literature

Several key textbooks; Chapin et al. (2002), Schlesinger (1997) and Warning and Running (1998) are recommended for further understandings of carbon biogeochemistry in forest ecosystem.

References

Baldocchi, D., Falge, E., Gu, L., Olson, R., Hollinger, D., Running, S., Anthoni, P., Bernhofer, C., Davis, K., Evans, R., Fuentes, J., Goldstein, A., Katul, G.., Law, B., Lee ,X., Malhi, Y., Meyers, T., Munger, W., Oechel, W., Paw, K.T., Pilegaard, K., Schmid, H.P., Valentini, R., Verma, S., Vesala, T., Wilson, K., and Wofsy, S., (2001), FLUXNET, A New Tool to Study the Temporal and Spatial Variability of Ecosystem-Scale Carbon Dioxide, Water Vapor, and Energy Flux Densities, Bull Am Meteorol Soc, 82, 2415-2434.

Boone, R.D., Nadelhoffer, K.J., Canary, J.D., and Kaye, J.P., (1998), Roots exert a strong influence on the temperature sensitivity of soil respiration, Nature, 396, 570-572.

Buurman, P., van Lagen, B., and Velthorst, E.J., (1996), *Manual for soil and water analysis*, Backhuys Publishers, Leiden, 314pp.

Chapin III, F.S., Matson, P.A., and Mooney, H.A., (2002), *Principles of terrestrial ecosystem ecology,* Springer, NewYork, 436pp.

Cole, D.W., and Rapp, M., (1981), Elemental cycling in forest ecosystem, in Dynamic properties of forest ecosystems, edited by Reichle E.D., pp, 341-410, Cambridge University Press, Cambridge.

Cramer, W., Olson, R.J., Prince, S.D., Scurlock, J.M.O, and Members of the Global Primary Production Data Initiative (2001), Determining present patterns of global productivity, In "Terrestrial Global Productivity", Roy, J., Sauger, B., Mooney, H.A, (Eds.), 429-448, Academic Press, San Diego.

Dantec, V.L., Epron, D., and Dufurene, E., (1999), Soil CO_2 efflux in a beech forest: comparison of two closed dynamic systems, Plant and Soil, 214, 125-132.

Eguchi, S., Sakata, T., Hatano, R., and Sakuma, T., (1997), Daily change of CO_2 efflux from the soil of a deciduous broad-leaved forest and its significance as a CO_2 source for vegetation, Jpn J Soil Sci Plant Nutr 68, 138-147. (in Japanese with English summary)

Hiura, T., (2001), Stochasticity of species assemblage of canopy trees and understory plants in a temperate secondary forest created by major disturbances, Ecol, Res., 16, 887-893.

Hiura, T., (2005), Estimation of aboveground biomass and net biomass increment in a cool temperate forest on a landscape scale, Ecol, Res., 20, 271-277.

Jones, J.J.B., and Mulholland, P.J., (1998), Carbon dioxide variation in a hardwood forest stream: an integrative measure of whole catchment soil respiration, Ecosystems, 1, 183-196.

Kaplan, L.A., and Newbold, J.D., (2000), Surface and subsurface dissolved organic carbon, In "Streams and ground waters", Jones, J.B, and Mulholland, P.J, (Eds), 237-258, Academic Press, San Diego.

Kohyama, T., Canadell, J., Ojima, D.S., and Pitelka, L.F., (2005), *Forest Ecosystems and Enviroments*, Springer-Verlag, Tokyo, 155pp.

Lloyd, J., (1999), The CO_2 dependence of photosynthesis, plant growth responses to elevated CO_2 concentrations and their interaction with soil nutrient status, II, Temperate and boreal forest productivity and the combined effects of increasing CO_2 concentrations and increased nitrogen deposition at a global scale, Functional Ecol., 13, 439-759.

Majdi, H., Pregitzer, K., Moren, A.-S., Nylund, J.-E., and Agren, G.I., (2005), Measuring Fine Root Turnover in Forest Ecosystems, Plant and Soil, 276, 1-8.

Malhi, Y., Baldocchi, D.D., and Jarvis, P.G., (1999), The carbon balance of tropical, temperate and boreal forests, Plant Cell Environ., 22,715-740.

Nadelhoffer, K.J., Aber, J.D., and Melillo, J.M., (1985), Fine roots, net primary production, and soil nitrogen availability: A new hypothesis, Ecology, 66, 1377-1390.

Nadelhoffer, K.J., Emmett, B.A., Gundersen, P., Kjonaas, O.J., Koopmans, C.J., Schleppi, P., Tietema, A., and Wright, R.F., (1999), Nitrogen deposition makes a minor contribution to carbon sequestration in temperate forests, Nature, 398, 145-148

Raich, J.W., and Schlesinger, W.H., (1992), The global carbon dioxide flux in soil respiration and its relationship to vegetation and climate, Tellus, 44B, 81-99.

Reich, P.B., and Bolstad, P., (2001), Productivity and evergreen and deciduous temperate forests, In Terrestrial global productivity, Roy, J., Saugier, B, and Mooney, H.A, eds., 245-283, Academic Press, San Diego.

Sakuma, T., (1987), Characterization of Soils in the Tomakomai Experiment Forest, Res, Bull, College Exp, For, Hokkaido Univ., 44, 749-759, (in Japanese with English summary).

Satomura, T., Nakatsubo, T., and Horikoshi, T., (2003), Estimation of the biomass of fine roots and mycorrhizal fungi: a case study in a Japanese red pine (Pinus densiflora) stand, J, For, Res., 8, 221-225.

Schelesinger, W.H., (1997), *Biogeochemistry 2nd edition*, Academic Press, San Diego, 588pp.

Shibata, H., Kirikae, M., Tanaka, Y., Sakuma, T., and Hatano, R., (1998), Proton Budgets of Forest Ecosystems on Volcanogenous Regosols in Hokkaido, northern Japan, Water Air Soil Pollut., 105, 63-72.

Shibata, H., Mitsuhashi, H., Miyake, Y., and Nakano, S., (2001), Dissolved and particulate carbon dynamics in a cool-temperate forested basin in northern Japan, Hydrological Processes, 15, 1817-1828.

Shibata, H., Hiura, T., Tanaka, Y., Takagi, K., and Koike, T., (2005), Carbon cycling and budget in a forested basin of southwestern Hokkaido, northern Japan, Ecological Research, 20, 325-331.

Shutou, K., and Nakane, K., (2004), Change in soil carbon cycling for stand development of Japanese Cedar (Cryptomeria japonica) plantations following clear-cutting, Ecol, Res., 19, 233-244.

Soil survey staff, (1994), Keys to soil taxonomy, USDA conservation service, Washington.

Smit, A.L., Bengough, A.G.., Engels, C., van Noordwijk, M., Pellerin, S., and van de Geijn, S.C., (2000a), *Root Methods: A Handbook*, Springer-Verlag, Heidelberg, 587pp.

Smit, A.L., George, E., and Groenwold, J., (2000b), Root observatino and measurements at (Tranparent) interface with soil, In Root methods: A handbook, edited by A.L, Smit, A.G, Bengough, C, Engels, M, van Noordwijk, S, Pellerin & S.C, van de Geijn, pp, 235-271, Springer-Verlag, Heidelberg.

Takahashi, K., Yoshida, K., Suzukim M., Seinom T., Tanim T., Tashiro, N., Ishii, T., Sugata, S., Fujito, E., Naniwa, A., Kudo, G., Hiura, T., and Kohyama, T., (1999), Stand biomass, net production and canopy structure in a secondary deciduous broad-leaved forest, northern Japan, Res, Bull, Hokkaido Univ, For., 56, 70-85.

Tanaka, Y., Tanaka, N., and Hatano, R., (2001), Seasonal variation of carbon dioxide and energy fluxes above a cool, temperate, broad-leaved forest, CGER-Report, M-011-2001, Proceedings of International Workshop for Advanced Flux Network and Flux Evaluation, 133-137

Tripathi, S.K., Sumida, A., Shibata, H., Uemura, S., Ono, K., and Hara, T., (2005), Growth and substrate quality of fine root and soil nitrogen availability in a young Betula ermanii forest of northern Japan: Effects of the removal of understory dwarf bamboo (Sasa kurilensis), Forest Ecol, Manag, 212, 278-290.

Warning, R.H., and Running, S.W., (1998), *Forest Ecosystems, 2nd edition*, Academic Press, San Diego, 370pp.

Wolt, J., (1994), *Soil solution chemistry*, John Wiley & Sons, New York, 345pp.

Yamamoto, S., Murayama, S., Saigusa, N., and Kondo, H., (1999), Seasonal and inter-annual variation of CO_2 flux between a temperate forest and atmosphere in Japan, Tellus, 51B, 402-413.

Yanagihara, Y., Koike, T., Matsuura, Y., Mori, S., Shibata, H., Satoh, F., Masuyagina, O.V., Zyryanova, O.A., Prokushkin, A.S., Prokushkin, S.G.., and

Abaimov, A.P., (2000), Soil respiration rate on the contrasting north- and south-facing slopes of a larch forests in central Siberia, Eurasian, J, For, Res., 1, 19-29.

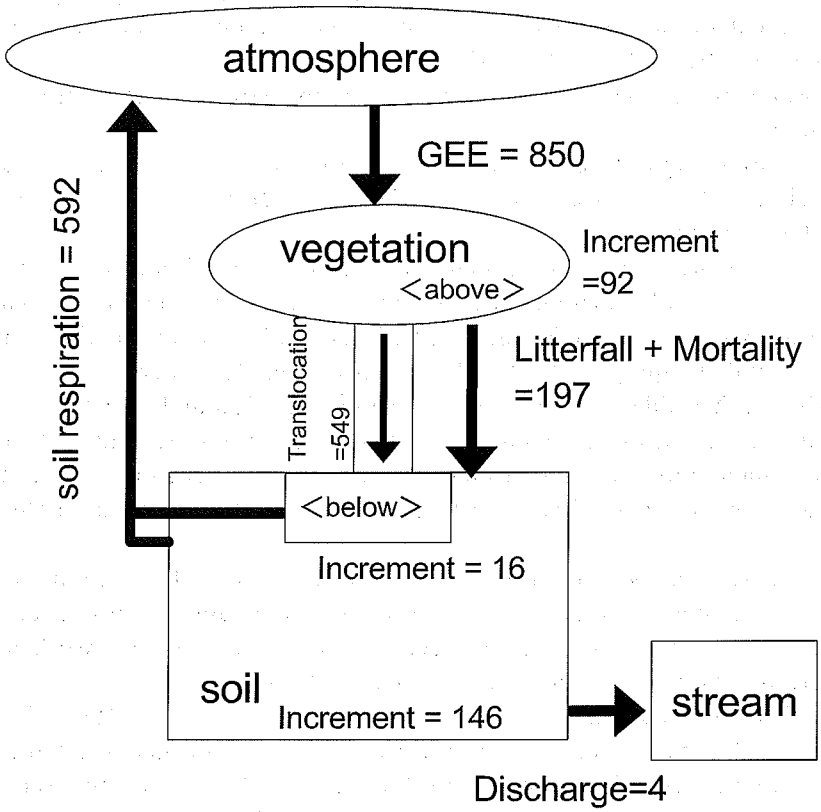

Figure 3.8 Annual carbon budget and cycling (gC m^{-2} y^{-1}) in the Horonai stream basin (1999-2001) in TOEF, northern Japan (modified from Shibata et al., 2005

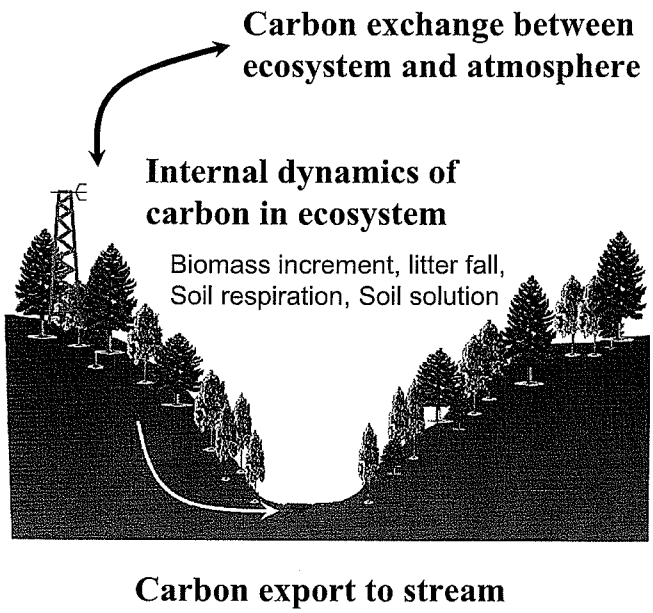

Appendix 3.1 General outline of watershed monitoring for carbon biogeochemistry

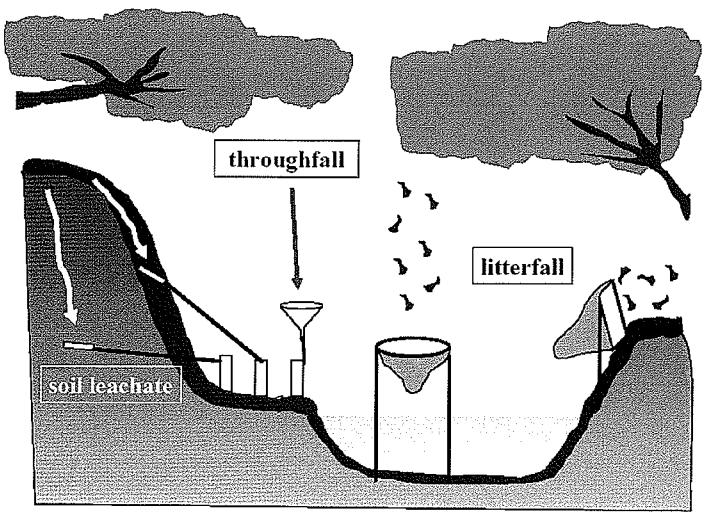

Appendix 3.2 Example of the monitoring protocol in forest-stream interface in forested basin.

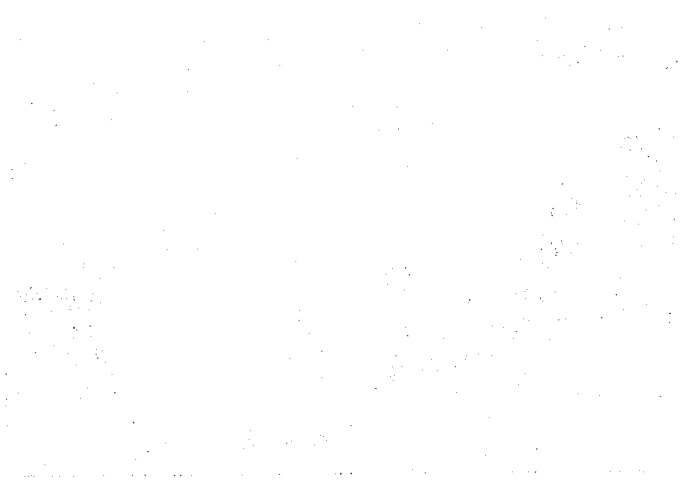

Chapter 4

Biogeochemical Processes of Nitrogen in Forested Ecosystems

Eiichi Konohira
21st Century COE Program, Dynamics of the Sun-Earth-Life interactive System, Nagoya University, Nagoya 464-8601, Japan
Present affiliation: Nonprofit Organization Morinoza, Ina, Nagano, 396-0011, Japan
Tel: +81-265-76-5915
Fax: +81-265-76-5915
e-mail: konohira@inacatv.ne.jp

4.1 General principle of nitrogen cycling in a forested ecosystem

Nitrogen is an essential nutrient for plants. Forest plants make organic matter from H_2O and CO_2 by photosynthesis, and nitrogen is not necessary for photosynthesis processes. However as plant leaf tissues where photosynthesis occurs contain nitrogen, deficits of nitrogen limit photosynthesis and control carbon cycling in a forest ecosystem. Plants do not show symptoms of nitrogen deficiency even when sufficient nitrogen is not absorbed, because they grow slowly to adapt to a nitrogen-deficit condition (Schlesinger, 1997). This nitrogen control of carbon cycling and growth rate is referred to as, "nitrogen as a limiting nutrient in a forest ecosystem." The general principle of nitrogen cycling in a forest ecosystem is summarized in this section.

Figure 4.1 illustrates nitrogen cycling in a forest ecosystem. Nitrogen is supplied from the atmosphere dissolved in rainwater. This nitrogen deposition rate depends on the atmospheric environment, and is usually very low in a clean atmosphere. In recent years, human activity has supplied a great amount of nitrogen compounds into the atmosphere which has brought about a high atmospheric nitrogen deposition rate in forests. This high atmospheric nitrogen input is thought to be very important for forest nitrogen cycling, and the next section will discuss in detail the effects of atmospheric nitrogen input on forest nitrogen cycling. Another nitrogen input to forest ecosystems is nitrogen fixation. Nitrogen fixation is a biological process by microscopic organisms which converts N_2 gas into NH_4^+. Nitrogen fixation is an important nitrogen source in the early succession stage of forests, but usually is not active in mature forests.

In a forest ecosystem, soil organic matter is decomposed and organic nitrogen is converted to NH_4^+ by soil microscopic organisms. Adequate amounts of NH_4^+ are then converted to NO_3^- by nitrification. NH_4^+ and NO_3^- produced in soil dissolve in water and up-taken by the roots of plants. NH_4^+ and NO_3^- taken up by plants are synthesized into organic matter again, and supplied to soil as litter fall. This internal cycling of nitrogen displays how nitrogen travels between plants and soil while changing to organic and inorganic forms of nitrogen. The main process for how nitrogen is output is the occurrence of stream nitrogen leaching. NO_3^- is the main form of nitrogen in such a stream, but usually the NO_3^- level is quite low in the stream. Input and output of nitrogen is quite small in comparison with the internal nitrogen cycling within a forest ecosystem. This nitrogen cycling can be characterized as a closed system.

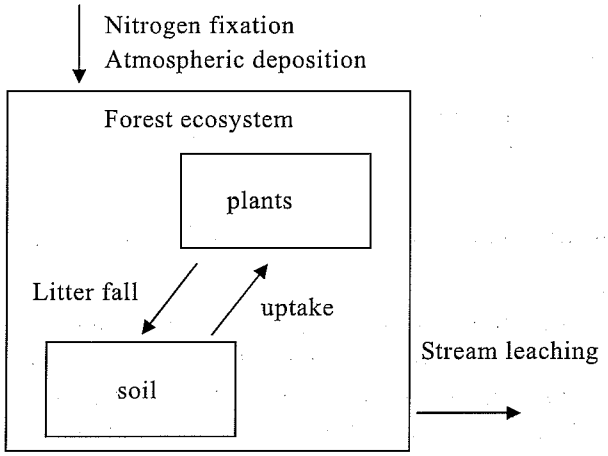

Figure 4.1 Outline of nitrogen cycling in a forest ecosystem

4.1.1 Effects of nitrogen deposition on forest ecosystems

Atmospheric pollution has an effect on forest ecosystems, and some forests in Europe and the U.S suffered from severe damage by the acidic deposition that became known as, "Acid Rain". Nitrogen oxides and sulfur oxides are oxidized, and the NO_3^- and SO_4^{2-} in rainwater causes acidification of the rainwater. Fortunately, severe damage to forests by acid rain has never been detected in Japan. In Europe and the U.S., sulfur oxides emissions have become regulated, and the problem of acid rain has improved in recent years.

Another aspect of acid rain which contains nitrogen in available form, is that nitrogen fertilizer is applied to forest ecosystems by this atmospheric pollution. Atmospheric nitrogen deposition is considered as an excess nutrient supply, and its effects on a forest ecosystem has been intensively studied since the late 80's.

Biogeochemical processes that control NO_3^- leaching from forests have been

intensively studied recently in association with "Nitrogen saturation" in forest ecosystems (Aber et al., 1989). Gundersen et al. (1998) showed that nitrogen concentrations and transformation rates in forest ecosystems were closely related with nitrogen leaching below the rooting zone and subsequently entering into streams. Increased nitrogen concentrations and nitrogen transformation rates in forests (increased nitrogen availability) were thought to be responsible for nitrogen leaching into streams. Stream water NO_3^- concentrations and nitrogen availability within the forest ecosystem correlated each other, which means that stream water chemistry can be a useful index indicating catchment environment on a macro scale.

4.2 Nitrogen in stream and forest environments

River water quality in Japan will be discussed in this section. The Japanese government conducted river water quality monitoring at over 6,000 points located mainly near river mouths, to detect human influences on river water quality. These data show that human activities (drainage from houses, paddy fields) are affecting river water chemistry as high nutrient concentrations were found around big cities (e.g. Tokyo, Nagoya and Osaka) in Japan.

The chemistry of headwaters in forested areas in Japan has been monitored by researchers and discussed in previous studies. These studies, however, covered only a limited region in Japan (eg, Yoh et al., 2001), and though the monitoring sites covered a variety of areas in Japan, the sampling density was not sufficient for discussion of the stream water chemistry on a Japanese national scale (Hirose et al., 1988, Toda et al., 2000).

Stream water chemistry was controlled by forest biogeochemical environments which include geological bedrock, topography of the catchments, soil type, tree species, climate and many other factors. When integrated, these effects can be detected from stream water chemistry, and would be a useful index for indicating forest environments at the catchment scale. However, observation data of stream water chemistry is limited in Japan and the basic knowledge about stream water chemistry is not well understood. As an example of this, the previous studies did not even provide national average values of stream water chemistry.

To understand the formation processes of stream water chemistry, Konohira et al. (2004) conducted systematic stream water sampling and chemical analyses as part of Japan-Wide Stream Monitoring (JWSM) 2003. In the following sections, an outline of the JWSM 2003 is described, and the relationship between nitrogen concentration in streams and forest environments is discussed

4.2.1 Methods for stream water chemistry observation

A total of 1,278 samples from stream headwaters were collected in the summer season of 2003 (July 1st to October 11th). Samples were collected only once from each location during the period. All catchments were covered by forest and completely free from human influences, such as houses, paddy fields and croplands. Catchment areas varied, ranging on sites from less than 1km^2 to more than 100km^2, with 5.3km^2 as the average. As stream samples were collected under different climate conditions, samples were taken as much as possible in ordinary flow conditions and not during or just after rainfall. This was to avoid direct influence of rainfall on the stream water chemistry. About 30 sampling points per prefecture were chosen before sampling to cover all areas of the 47 prefectures in Japan, and 100 points were chosen for Hokkaido Prefecture which makes up a large portion of Northern Japan. Okinawa Prefecture, consisting of many islands in south-west Japan, was excluded from this sampling and no suitable sampling sites could be found in Chiba Prefecture because of steep topography and the existence of houses in headwater areas. When locations were judged to be unsuitable for sampling due to human influences in the field, the sampling sites location was changed to a suitable one nearby or sampling was not conducted at that location.

The 1,278 samples were collected by 11 people who trained beforehand on the sampling procedure in order that it would be standardized. Samples were collected in clean polycarbonate bottles (1 or 2L, No.2015, Nalgene, Nalge Nunc International, U.S.A.) after being rinsed 3 times by the sample. For slopes near streams that were too steep to access the stream water, the water was usually collected from a bridge with a rope connected to a polyethylene hand bucket. The rope was washed several times before use to prevent it from contaminating the sample. Collected samples were kept under refrigeration and sent to a laboratory by a transport company (Yamato transport Ltd). Samples were filtrated usually within 24 hours after sampling with a Whatman GF/F filter at the laboratory. Electric conductivity (EC, Model D-25, Horiba Ltd., Japan) and pH (Model CM-14P, TOA Electronics Ltd., Japan) were measured immediately after filtration. Alkalinity was also measured for some unfiltered samples by the titration method. Filtrated samples were put in 50ml polyethylene bottles (I・BOY, As one LTD., Japan) after being rinsed 3 times, then were frozen and kept at –40°C until analysis. The defrosted samples were filtered again with a 0.22 μm membrane filter and the concentrations of Na^+, NH_4^+, K^+, Mg^{2+}, Ca^{2+}, Cl^-, NO_3^- and SO_4^{2-} were measured by ion chromatography(Model : Dionex DX500, Separation column: AS14(anion), CS14(cation), Eluent: 3.5 mM Na_2CO_3 + 1.0 mM $NaHCO_3$ (anion), 10 mM methanesulfonic acid (cation), standard solutions: 2 ppm, 10 ppm, 50 ppm)

Some samples showed much higher concentrations of some components due to the contribution of hot spring water from volcanic areas. The extreme values of

each ion were judged by the Smirnov test ($p<0.01$) and samples containing extreme values were omitted. 36 out of the 1,278 samples were omitted by the Smirnov test, meaning that 1,242 data samples were used in this analysis.

4.2.2 Stream water chemistry in Japan

Stream water chemistry averaged for Japan is shown in Table 4.1. Anion deficit equivalents (Table 4.1) were calculated by subtracting the sum of anions from the sum of cations in the equivalent. Anion deficit corresponded with the alkalinity, composed of mainly HCO_3^- with a pH range of around 7 (Figure 4.2). These results show that ion concentrations measured by ion chromatography are reliable.

The Japanese average values and concentrations of EC and pH and Cl^-, NO_3^-, SO_4^{2-}, HCO^{3-}, Na^+, NH_4^+, K^+, Mg^{2+} and Ca^{2+} were 6.94ms/m, 6.84, 119μM, 26.2μM, 62.8μM, 344μeq/L, 211μM, 6.1μM, 16.4μM, 55.8μM and 135μM, respectively. The major anion was HCO_3^-, which makes up more than half of the total anions in equivalent bases. Cl-, SO_4^{2-}, and NO_3^- follow HCO_3^-, but SO_4^{2-} was comparable with Cl^- in equivalent bases. NO_3^- was higher than Cl^- or SO_4^{2-} in some regions of Japan (e.g. Saitama Prefecture), but it is a minor anion in the overall Japanese average.

Na^+ was higher than other cations but Ca^{2+} was the highest in equivalent basis. Mg^{2+} followed by Na^+ and Ca^{2+}, NH_4^+ and K^+ showed low concentrations compared with other cations, and the NH_4^+ concentration was much lower than the other nitrogen compound, NO_3^-.

Features of these ion concentrations in Japanese streams waters are discussed in comparison with data collected in Europe. Lahermo et al. (1995) observed 1,165 streams throughout Finland and the results of that study showed higher concentrations than those of Japanese stream waters did for all ions except HCO_3^-. The NO_3^-.concentration in Finland (73μM) was especially higher than that in Japanese stream waters (26.2μM). Binkley et al. (2004) also reported stream water NO_3^- concentrations in the U.S. and reported 44μM as the average value in over 300 streams. Japanese stream waters are therefore characterized by low NO_3^- concentrations compared with those in Finland and the U.S. Other ions, excluding HCO_3^- were higher in Finland than in Japan, but differences in concentrations of Japanese and Finnish streams were nearly two times higher. The relative order of amounts in mol bases in Japan, $HCO_3^- > Cl^- > SO_4^{2-} > NO_3^-$ in anion, and $Na^+ > Ca^{2+} > Mg^{2+} > K^+$ in cation, were in the same order as Finnish streams.

Table4.1 Stream water chemistry averaged in Japan

	EC (mS m^{-1})		pH		Cl^- (μM)		NO_3^- (μM)	
n	average	SD	average	SD	average	SD	average	SD
1242	6.94	3.42	6.84	0.31	119	88.2	26.1	25.4

	SO_4^{2-} (μM)		anion deficit (μ eq)		Na^+ (μM)		NH_4^+ (μM)	
n	average	SD	average	SD	average	SD	average	SD
1242	62.8	61.1	344	235	211	115	6.1	3.8

	K^+ (μM)		Mg^{2+} (μM)		Ca^{2+} (μM)	
n	average	SD	average	SD	average	SD
1242	16.4	9.6	55.8	43.0	135	108

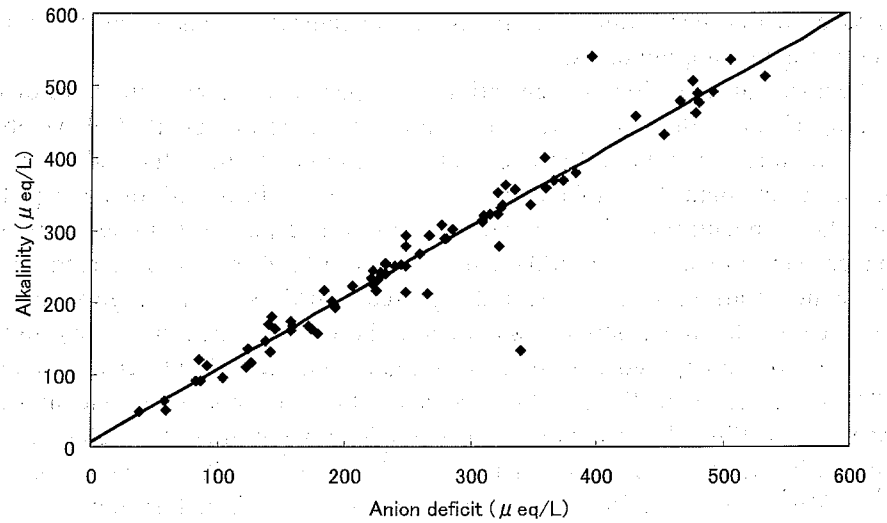

Figure 4.2 Relationship between anion deficit equivalent and alkalinity.

4.2.3 Distribution of stream water quality in Japan and its controlling factors

Stream water chemistry is quite different depending on the site, indicated that regional distribution of stream water chemistry and its controlling factors must be discussed in detail. But environmental factors controlling stream water chemistry are different depending on the substances, so detailed analysis of the controlling factors on stream water chemistry will be needed for each substance. An analysis of NO_3^- distribution and its controlling factors is conducted in this section.

Figure 4.3 shows the distribution of stream water chemistry in Japan. NO_3^-, Cl^-, SO_4^{2-} and pH distribution are selected, and shown in this figure. Cl^- distribution clearly indicates that streams near sea costs showed higher concentrations while lower concentrations were found in inland areas. Cl^- is a typical substance originating from sea salts, so the distance from the sea is the main factor controlling Cl^- in streams. SO_4^{2-} and pH distribution did not show any characteristic features at first sight. SO_4^{2-} and pH distributions are, however, believed to be related to geological features in Japan (data not shown). Geological effects will be important to understand these substances.

Streams in the northern part of Japan (Hokkaido and the Tohoku region) usually showed very low NO_3^- concentrations. Forest ecosystems in low temperature areas retained nitrates within the ecosystems and did not release NO_3^- to streams. Higher concentrations were found around the Metropolis of Tokyo and also along the Seto Inland Sea. These areas are located in the middle of Japan, and no characteristic climate conditions could be found in these areas. On the other hand, these areas

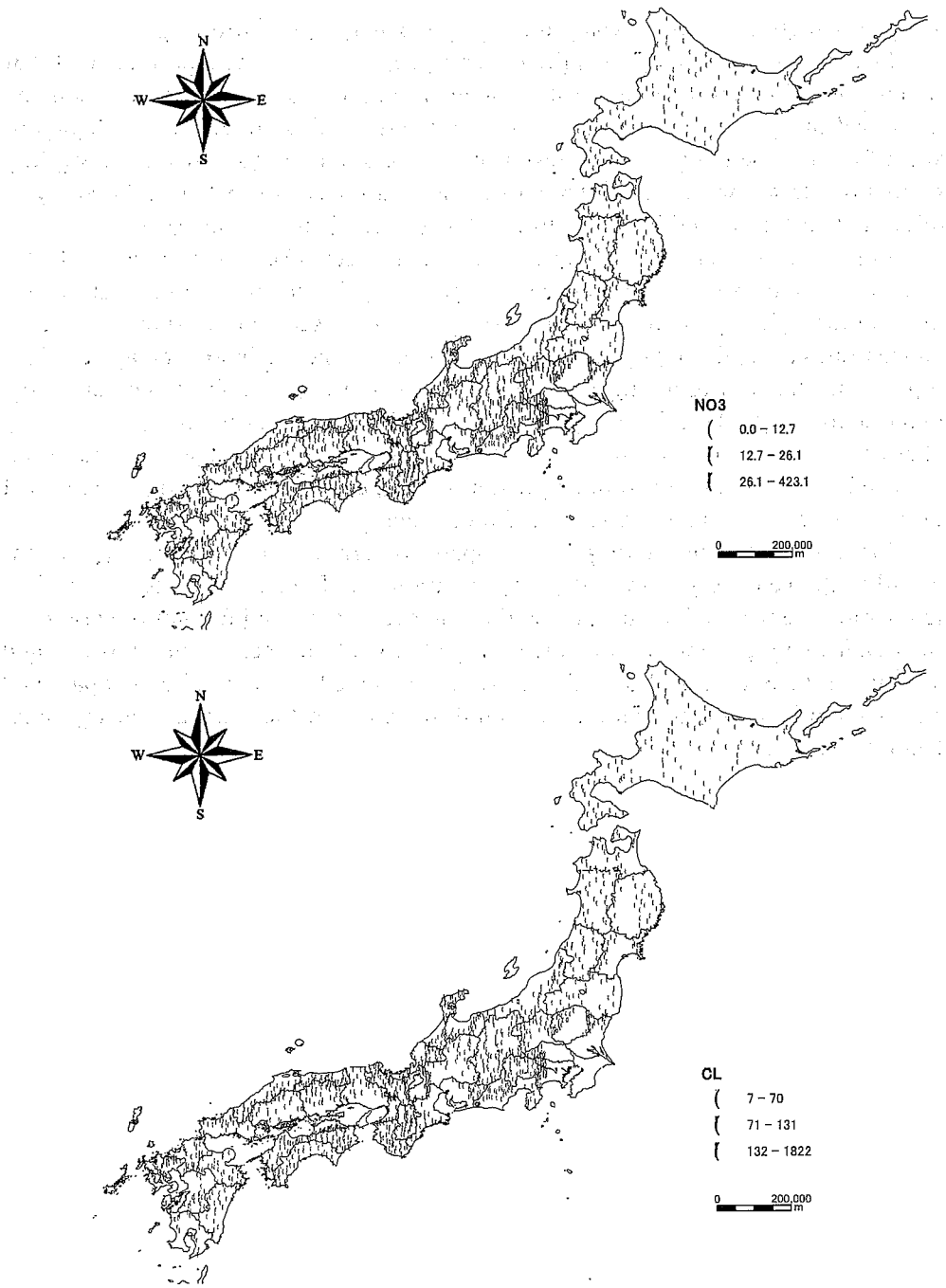

Figure 4.3 Distribution of NO_3^- and Cl^- concentrations in stream water
Unit: μM

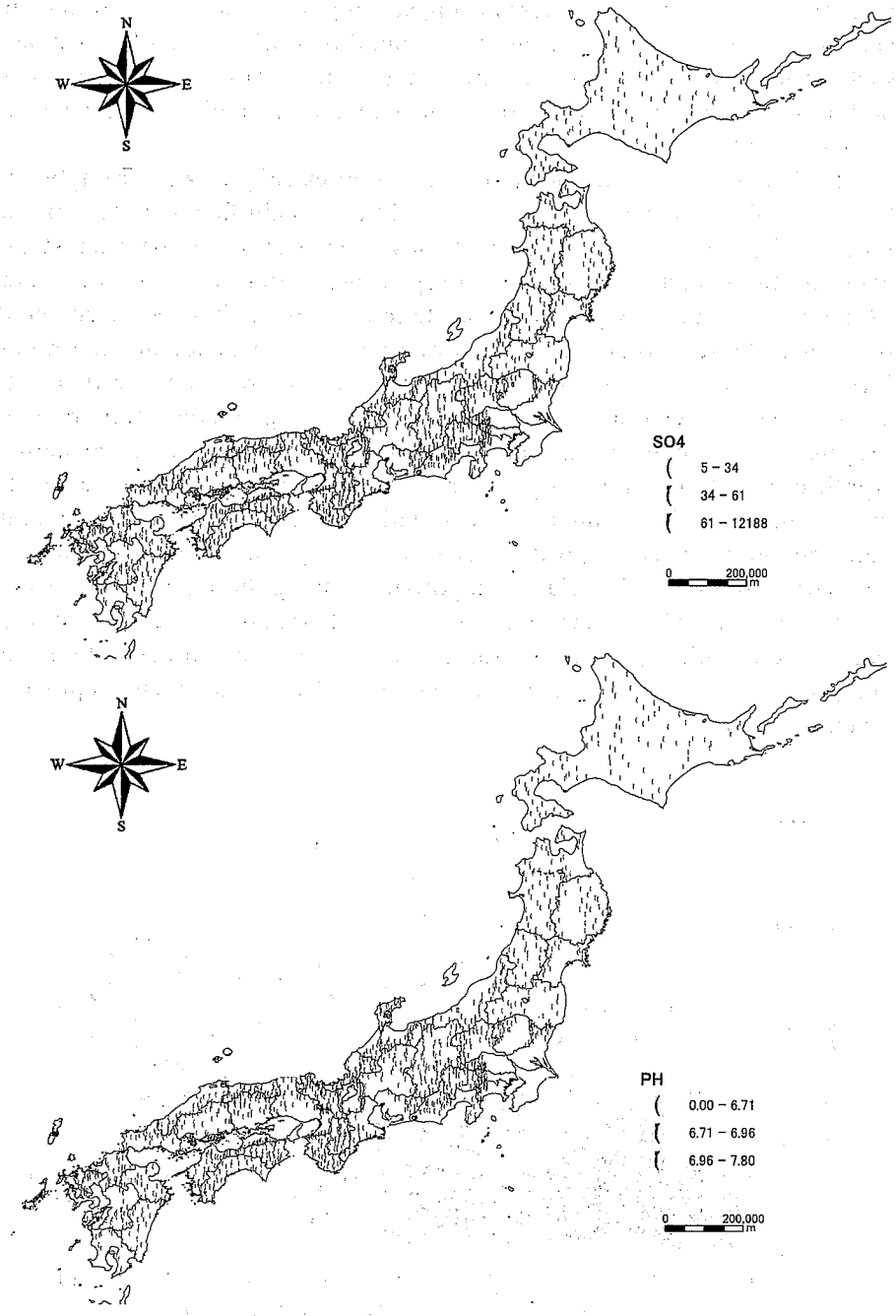

Figure 4.3 (continued) Distribution of SO_4^{2-} and pH in stream water
Unit: μM

were very close to big cities including Tokyo, Osaka, Okayama, Hiroshima and Fukuoka, suggesting that human impact highly contributes to stream NO_3^- concentrations. These streams are free from direct influences of human activities, such as houses, paddy fields or croplands. Only indirect influences of nitrogen pollution by way of atmosphere could explain the higher NO_3^- concentrations around big cities.

Higher NO_3^-.concentrations around big cities (Figure 4.3) strongly suggested that atmospheric nitrogen deposition would be a main factor in determining NO_3^- levels in Japanese streams. Figure4.4 shows the relationship between stream NO_3^- concentrations and atmospheric nitrogen deposition rates to the catchments (Shindo et al., 2005). Significant correlation was found between them, confirming that atmospheric nitrogen deposition rate was a main factor in determining NO_3^- levels in Japanese stream waters. However, the correlation coefficient between stream NO_3^- concentration and atmospheric nitrogen deposition rate was low (Figure 4.4), so other factors might contribute to NO_3^- levels in Japanese stream. Application of multiple regression analysis showed that catchment slope, catchment direction, annual precipitation, annual mean temperature and atmospheric nitrogen deposition rate were significant parameters for stream NO_3^-concentrations. The relative importance among these parameters was studied by analyzing their by normalized coefficients. Normalized coefficients were 0.501 (atmospheric nitrogen deposition), -0.275 (annual precipitation, negative correlation), 0.250 (annual mean temperature), 0.142 (catchment slope) and -0.081 (catchment direction).

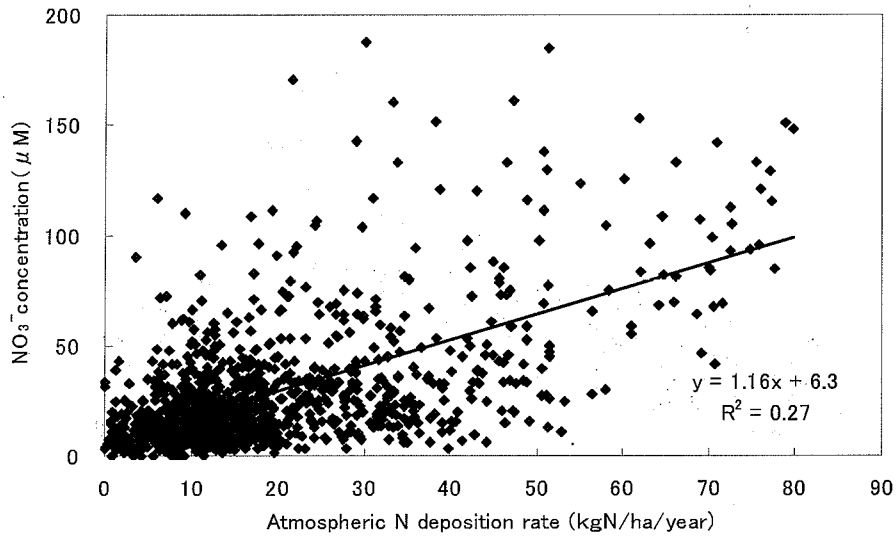

Figure 4.4 Relationship between atmospheric nitrogen deposition rates (Shindo et al., 2005) and stream NO_3^- concentrations.

4.2.4 Change in Japanese stream water chemistry over the past 50 years

JWSM 2003 was the first opportunity to investigate stream water chemistry in Japan on a national scale. But about 50 years ago (1943-1958), Kobayashi (1971) reported river Japanese water chemistry on a national scale. He mainly observed major rivers having a large catchment area and many of the observation points were located downstream in comparison to those for JWSM 2003. Though the sampling locations were different, these two observations were conducted to understand background levels of river water chemistry.The observation results by Kobayashi (1971) did include some that were directly influenced by human activities, but the observation period (1943-1958) was before the rapid economic and industrial development in Japan after 1960. The river water chemistry then might be relatively free from human influence for many substances, and it should have been close to stream water chemistry at that time. Thus it is assumed that changes in Japanese stream water chemistry over the past 50 years can be detected by these data sets. As mentioned above, sampling locations were different in the two data sets, and the average values for prefectures were used for comparison (Figure 4.5).

Figure 4.5 shows that pH decreased and HCO_3^- increased in the last 50 years. Other anions and cations usually decreased except for nitrogen compounds, NO_3^- and NH_4^+. These results suggest that stream water chemistry has changed over the past 50 years and that forest environments controlling stream water chemistry might also have changed in this period. The reasons and mechanisms which generated these changes are not clear, but clear increases in NO_3^- concentration during this time period support the conclusion that atmospheric N deposition would be a main factor in controlling NO_3^- levels in 2003. Increases in atmospheric N deposition in the last 50 years could explain the increase of NO_3^- concentration in stream water in this period.

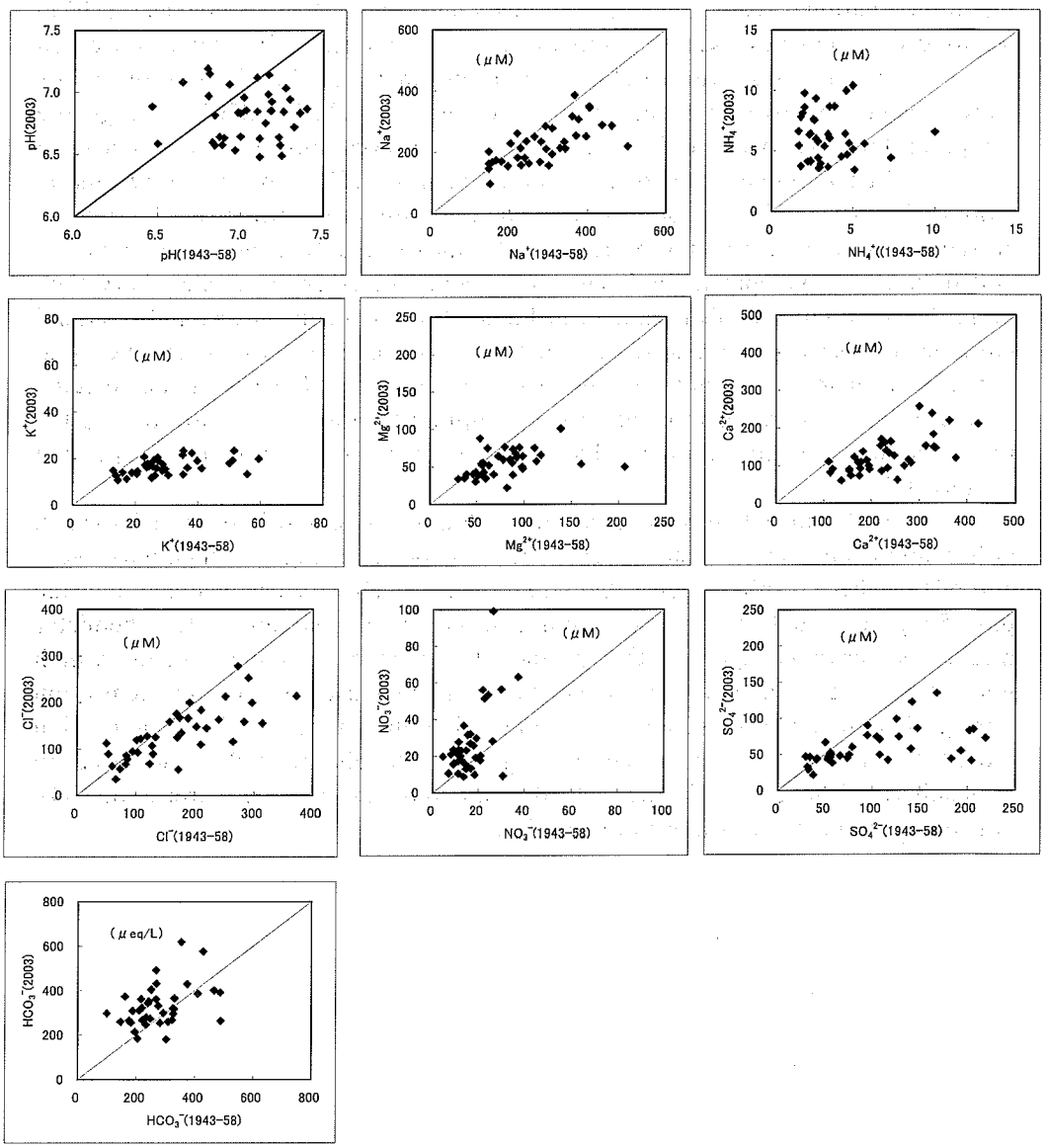

Figure 4.5 Relationships of Japanese stream water compositions between 1943-58 (data from Kobayashi, 1971) and 2003.

4.3 Implications of carbon and nitrogen dynamics in forested ecosystems

Carbon and nitrogen cycling in forested ecosystems are related to many biological processes. For example, forest plants make organic matter from CO_2 by photosynthesis, but plant leaf tissues where photosynthesis takes place require nitrogen. Organic matter contains both carbon and nitrogen and the relative amount of carbon and nitrogen (C/N ratio) regulates soil decomposition process of organic matter. Carbon and nitrogen cycling in forested ecosystems are related to and have an effect on each other. But carbon and nitrogen are related at the micro scale in biological processes, so it is very difficult to understand carbon and nitrogen relationship from field observations. As mentioned in previous sections, stream water chemistry can be an index indicating forest environment at the macro scale, so the relationship between carbon and nitrogen processes can be tested from stream water chemistry.

Dissolved organic carbon (DOC) and nitrate (NO_3^-) are important forms of carbon and nitrogen in streams. Stream DOC and NO_3^- both originate from organic matter in the soil of forested ecosystems. Aitkenhead and McDowell (2000) showed that an increase in riverine DOC flux occurs with increased soil C/N ratio on a global scale. This result suggests that DOC in rivers is controlled by both C and N biogeochemical cycling in the catchment, implying that riverine DOC concentrations are related to the NO_3- levels.

In this section, distribution of DOC and NO_3^- concentrations in streams are intensively observed in the Lake Biwa watershed in central Japan. Lake Biwa is the largest lake in Japan, and an important water resource for the Kansai region which includes Kyoto and Osaka cities. The relationship between DOC and NO_3^- concentrations in these streams is discussed along with the potential mechanisms responsible for the observed relationship.

4.3.1 Dissolved organic carbon (DOC) and NO_3^- concentrations in streams

Stream water samples were collected from the Lake Biwa watershed located in central Japan (35°10'N, 136°10'E). Annual precipitation ranged from <1600 mm in the southern region to >2400 mm in the northern region of the watershed (Lake Biwa Research Institute, 1986). Snow falls in winter, but the southern part of the watershed is usually free from snow cover. The annual average temperature is 14.1°C in Hikone city near Lake Biwa. Elevation ranges from 86 m A.S.L. at the lake surface to >1000 m in the mountainous areas. The catchment areas of the sampling sites are covered by forest and free from human interference such as houses, paddy fields and croplands. Vegetation type varies among sites, but the coniferous plantation tree species, *Cryptomeria japonica* and *Chamaecyparis obtusa* are generally predominant.

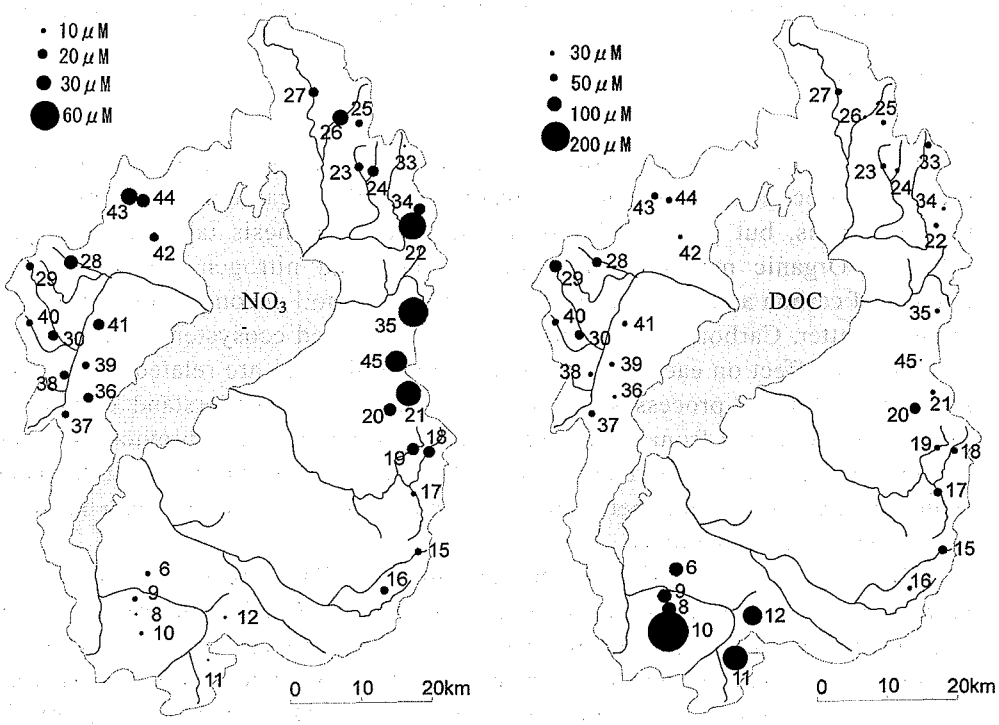

Figure 4.6 Regional distributions of NO_3^- and DOC concentrations in stream water (modified from Konohira and Yoshioka, 2005)

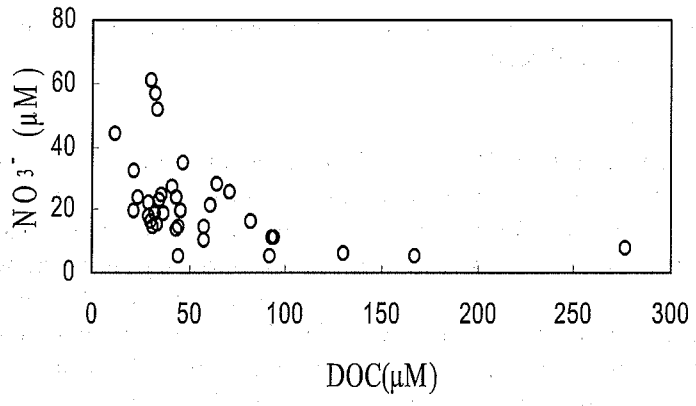

Figure 4.7 Relationship between DOC and NO_3^- concentrations in stream water in the Lake Biwa watershed (modified from Konohira and Yoshioka, 2005)

NO_3^- concentrations in stream water ranged from 4.7 to 60μM (Figure 4.6) with the average concentration of the 35 streams being 22μM. NO_3^- concentrations were high in the eastern part of the watershed (above 30μM) and low in the southern part (less than 10μM). The DOC concentration ranged from 12 to 280μM with an average concentration of 57μM (Figure.4.6). There were considerable regional variations; highs in the southern part of the watershed (above 80μM) and lows in the eastern part (less than 40 μM). As a result, an inverse relationship was found between NO_3^- and DOC concentrations in stream waters (Figure 4.7).

To examine the regional variability of DOC and NO_3^- concentrations on a larger scale in Japan, stream water samples were collected at two regions apart from the Lake Biwa watershed. One was in the Okutama region (35°50'N, 139°00'E) near Tokyo where high nitrate concentration streams have been reported by Yoh et al. (2001). The other was in the Uryu region (44°20'N, 142°10'E) in Hokkaido which is located in the northern part of Japan. This area receives much snow in winter and has a much cooler climate than either Lake Biwa watershed or the Okutama region. The streams in the Okutama and Uryu regions are also free from human activity.

Stream water in the Okutama region showed a large variation in NO_3^- concentration ranging from 2.8 – 262 μM (Figure 4.8). The maximum concentration in the Okutama region greatly exceeded that of the Lake Biwa watershed. The high NO_3^- levels in the Okutama region are mainly due to the high atmospheric N deposition from the Tokyo metropolitan area (Yoh et al., 2001).

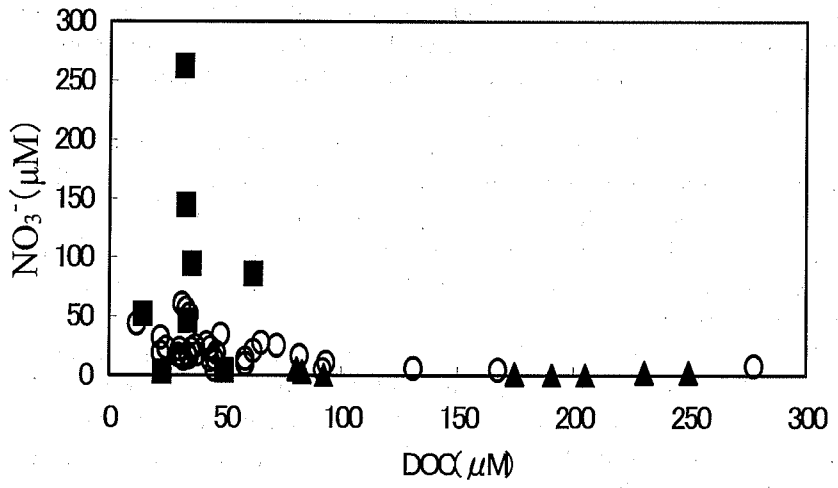

Figure 4.8 Relationship between DOC and NO_3- concentrations in stream water in Okutama, Uryu and the Lake Biwa watershed. (modified from Konohira and Yoshioka, 2005)

■ : streams in the Okutama region; ▲: streams in the Uryu region;
○: streams in the Lake Biwa watershed

Conversely, DOC concentrations in the Okutama region were low and showed small variation, ranging from 14 to 62 μM. These concentrations were in the low range of DOC found in the Lake Biwa watershed. Stream water in the Uryu region showed higher and more variable DOC concentrations ranging from 80 to 230 μM and showed a low NO_3^- concentration (less than 10 μM). Even though NO_3^- concentrations ranged much higher in the Okutama region, the inverse relationship between DOC and NO_3^- concentration in streams persisted when streams from various regions were analyzed.

4.3.2 Soil environments of different DOC and NO_3^- levels in streams

Soil and the soil organic layer at 4 catchments in the Lake Biwa watershed (Azusa, Itanago, Kakagawa, Shigaraki) were also sampled to investigate mechanisms responsible for differences in DOC and NO_3^- concentrations in streams. Soil organic layer and surface soil (0-10 cm depth) were collected from October 23 to 24, 2001. These soil sampling sites (4 to 8 places for each catchment) were located in the valley area within 100m from the streams.

Soil organic layers were dried (60°C, 2 days) and milled, and the C/N ratio was measured by an elemental analyzer (NA2500, Thermo Quest Co. Ltd., Italy). 50ml of pure water was added to the 10-gram soil samples which were then shaken for 30 minutes to extract soil solutions. These extracts were centrifuged and filtered (Whatman GF/F filters). DOC and NO_3^- concentrations in soil extracts were measured in the same way as stream waters.

Selection was made of two C-type streams (DOC concentrations in the summer of 1998 were higher than 80 μM) and two N-type streams (NO_3^- concentrations were higher than 30 μM). The C/N ratio in soil organic layers and DOC and NO_3^- concentrations in soil extracts of these catchments were measured (Figure 4.9).

C/N ratios in soil organic layers ranged from 43 to 53. Since the variation within the catchment was quite large, it was not possible to detect differences in C/N ratios between C-type and N-type catchments. Gundersen et al. (1998) showed that N leaching was mainly controlled by C/N ratios of soil organic layers, but no relationship was found between C/N ratios in the soil organic layers and stream $NO3^-$ in the Lake Biwa watershed.

DOC concentrations in soil extracts were higher in the catchemnts of C-type than those of N-type (Figure 4.9). Although the variation within a catchment was also large, differences were detected in DOC concentrations between C-type and N-type catchments ($p<0.01$, t-test). NO_3^- concentrations in soil extracts were higher in N-type catchments, and NO_3^- was not detected in Shigaraki (C-type catchment). A clear difference in NO_3^- concentrations was also observed between C-type and N-type catchments ($p<0.01$, t-test).

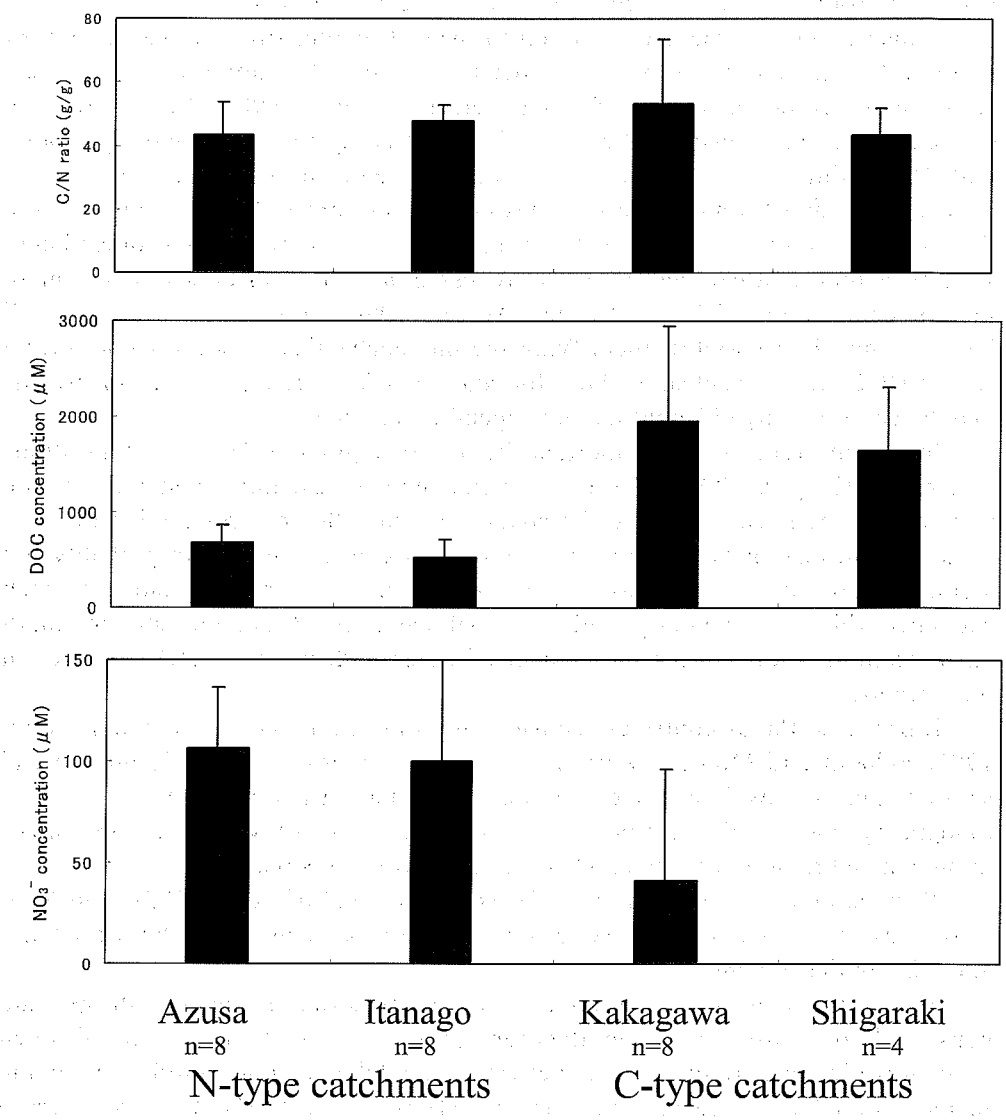

Figure 4.9 C/N ratio of soil organic matter and DOC and NO_3^- concentrations in soil extracts in the Lake Biwa watershed (modified from Konohira and Yoshioka, 2005)

4.3.3 Mechanisms responsible for DOC and NO_3^- relationship in streams

An inverse relationship between DOC and NO_3^- concentrations was found and persisted through seasonal variations in the Lake Biwa watershed. Moreover, the inverse relationship could be expected to apply to other regions of Japan. These results suggested that in Japanese streams the forest biogeochemical processes

which control DOC and NO_3^- concentrations were closely related..

Biogeochemical processes that control NO_3^- leaching from forests have been intensively studied recently in association with "N saturation" in forest ecosystems (Aber et al., 1989). Gundersen et al. (1998) showed that N concentrations and transformation rates in forest ecosystems were closely related with N leaching below the root zone and subsequently into streams. Increased N concentration and N transformation rates in forests (increased N availability) were thought to be responsible for N leaching to streams. While on the other hand, several factors in stream and riparian processes have been discussed as the main factors controlling DOC in streams (Meyer, 1990; Dillon and Molot, 1997; Ekhardt and Moore, 1990). Identifying the biogeochemical processes controlling stream DOC are not as clear as those for NO_3^-, and DOC concentrations in streams may be controlled by different factors depending on the site.

In-stream processes are important factors for regulating DOC concentrations in streams (Meyer, 1990). These processes include leaching of stored organic matter from the stream bed into the water and autochthonous production of DOC by algae and macrophytes. However, these in-stream processes are probably not significant for DOC in the Lake Biwa watershed. The very steep slope of each catchment (high flow velocity) and very small catchment area (short stream length until sampling site) reduces the contact of water with potential DOC sources in the streams.

Riparian wetlands contribute considerably to stream DOC (Dillon and Molot, 1997; Ekhardt and Moore, 1990). The steep topography resulting in no wetland area explain the low DOC concentrations in the Lake Biwa watershed. The steep topography and small catchment area in the Lake Biwa watershed minimizes in-stream and riparian effects on DOC concentrations in streams.

Whereas in-stream and riparian effects are minimal on stream DOC and NO_3^- in the Lake Biwa watershed, upland processes are likely important both for DOC and NO_3^- in the streams.

Soil inorganic nitrogen is produced by decomposition of organic nitrogen and consumed by nitrogen immobilization processes. A decrease in nitrogen immobilization generated from a deficit in available carbon could explain the increase of NO_3^- in the soil environment (Hart et al., 1994). Carbon (energy) deficit in a soil environment causes an increase in NO_3^- concentrations, and will cause DOC consumption. DOC and NO_3^- concentrations in soil extracts corresponded to those in streams (Figure 4.9). As soil environment varies depending on space and time, the measurements in this study are not sufficient to detect differences between catchments. But qualitative differences detected in soil extracts suggest that the inverse relationship in DOC and NO_3- in streams is attributable to the decomposition process of organic matter in the surface soil layer. Thus, the C (energy) deficit in the soil environment may be the best explanation for the observed inverse relationship between DOC and NO_3^- concentrations in streams.

Denitrification is another possible mechanism that affects both DOC and NO_3^-

concentrations because denitrification reduces NO_3^- to other nitrogen forms using DOC as the energy source (Hedin et al., 1998). The importance of riparian denitrification was reported in some Japanese catchments (Konohira et al., 2001; Koba et al., 1997). However, the denitrification processes can not explain the depletion of DOC with the increase in NO_3^- concentration, because it consumes both DOC and NO_3^-.

4.3.4 Stream DOC and NO_3^- as an index of forest carbon and nitrogen cycling

The inverse relationship between DOC and NO_3^- concentrations in the Lake Biwa watershed suggests an excess nitrogen availability and carbon (energy) deficit condition in the soil environment. Aber (1992) hypothesized DOC depletion in an excess nitrogen environment, and the results of this study support his hypothesis. This also implies that the stream DOC and NO_3^- concentrations could be an index indicating carbon and nitrogen availability in the catchment. This index may be applicable to other steep slope catchments where in-stream and riparian processes do not contribute to stream DOC and NO_3^- concentrations.

References

Aber, J.D., Nadelhoffer, K.J., Steudler P., and Melillo J.M., (1989), Nitrogen saturation in northern forest ecosystems, Bioscience, 39, 378-386.

Aber, J.D., (1992), Nitrogen cycling and nitrogen saturation in temperate forest ecosystems, Tree 7, 220-224.

Aitkenhead, J.A., and McDowell, W.H., (2000), Soil C:N ratio as a predictor of annual riverine DOC flux at local and global scale, Global Biogeochem, Cycles 14, 127-138.

Buffam, I., Galloway, J.N., Blum, L.K., and McGlathery K.J., (2001), A stormflow / baseflow comparison of dissolved organic matter concentrations and bioavailability in an Appalachian stream, Biogeochem, 53, 269-306.

Binkley, D., Ice, G..G., Kaye, J., and Williams C.A., (2004), Nitrogen and phosphorus concentrations in forest streams of the United States, Journal of the American Water Resources Association, 40 (5), 1277-1291.

Dillon, P.J, and Molot, L.A, (1997), Effect of landscape form on export of dissolved organic carbon, iron, and phosphorus from forested stream catchments, Water Resour, Res, 33, 2591-2600.

Eckhardt, B.W., and Moore T.R., (1990), Controls on dissolved organic carbon in streams, Southern Quebec, Can, J, Fish, Aquat, Sci, 47,1537-1544.

Gundersen, P., Emmett, B.A., Kjonaas, J., Koopmans, C.J., and Tietema A., (1998), Impact of nitrogen deposition on nitrogen cycling in forests: a synthesis of NITREX data, For, Ecol, Manage., 101, 37-55.

Hart, S.C., Nason, G.E., Myrold, D.D., and Perry, D.A., (1994), Dynamics of gross nitrogen transformation in an old-growth forest: The carbon connection,

Ecology, 75, 880-891.
Hedin, L.O., Fischer, J.C., Ostrom, N.E., Kennedy, M.G., Brown, B.P., and Robertson, G.P., (1998), Thermodynamic constraints on nitrogen transformations and other biogeochemical processes at soil-stream interfaces, Ecology, 79, 684-703.
Hirose, K., Iwatsubo, G, and Tsutsumi, T., (1988), Study on run-off water chemistry in Japanese forest (1), Bull, Kyoto university forests, 60, 162-173. (in Japanese with English Abstract)
Koba, K., Tokuchi, N., Wada, E., Nakajima, T., and Iwatsubo, G., (1997), Intermittent denitrification:the application of a 15N natural abundance method to a forested ecosystem, Geochimica et Cosmochimica Acta, 61, 5043-5050.
Kobatashi, J., (1971), *Health diagnosis of water, Iwanami shinnsho No.777*, Iwanami shoten, Tokyo, 207pp. (in Japanese)
Konohira, E., Yoh, M., Kubota, J., Yagi, K., and Akiyama, H., (2001), Effects of riparian denitrification on stream nitrate –evidence from isotope analysis and extreme nitrate leaching during rainfall-, Water, Air, Soil Pollut, 130, 667-672.
Konohira, E., and Yoshioka, T., (2005), Dissolved organic carbon and nitrate concentrations in stream -A useful index indicating carbon and nitrogen availability in catchments -, Ecological Research 20, 359-365, 2005.
Lahermo, P., Jaakko, M. J., and Tarvainen, T., (1995), The hydrogeochemical comparison of streams and lakes in Finland, Applied Geochemistry, 10, 45-64.
Lake Biwa Research Institute (1986), Shiga prefecture regional environmental atlas, Lake Biwa Research Institute, Ohtsu, Shiga, Japan.. (in Japanese)
Meyer, J.L., (1990), Production and utilization of dissolved organic carbon in riverine ecosystems, In: Perdue EM, Gjessing ET (eds) Organic acids in aquatic ecosystems, John Wiley and Sons, 281-299.
Ozawa, M., Shibata, H., Satoh, F., and Sasa, K., (2001), Annual element budget of soil in snow-dominated forested ecosystem, Water, Air, Soil Pollut, 130, 703-708.
Shindo, J., Konohira, E., Yoshioka, T., Okamoto, K., and Kawashima, H., (2005), Nationwide estimation of nitrogen load and nitrogen concentration in natural catchments, Journal of environmental science, 18(4), 455-464.
Toda, H., and other 46 authors (2000), Stream water chemistry of university forests over Japan, Journal of Japanese Forestry Society, 82, 308-312 (in Japanese with English Abstract).
Yoh, M., Konohira, E., and Yagi, K., (2001), Regional distribution of natural stream nitrate in central Japan, Water, Air, Soil Pollut, 130, 655-660.

Chapter 5

Assessment of Plant-Water Relations using Stable Isotope Tracers

Tsutomu Yamanaka
Terrestrial Environment Research Center (TERC),
University of Tsukuba, Ibaraki 305-8577, Japan
Tel: +81-29-853-2538
Fax: +81-29-853-2530
e-mail: tyam@suiri.tsukuba.ac.jp

5.1 Introduction

Plants play an important role in the hydrological cycle as a "regulator" of water flux. At the same time, however, hydrological conditions inversely control plant growth, geographical distribution, and water use patterns. The water relations to plants is also closely associated with agricultural production and the carbon cycle of terrestrial ecosystems because the pattern of photosynthesis and respiration of plants depends on moisture conditions of the soil and the atmosphere through stomata closure. Therefore, this subject has attracted widespread interest from fields as diverse as hydrology, ecology, agronomy and climatology, including global warming research.

The plant-water relations has been studied since the 18^{th} century (Kramer and Boyer, 1995), and since then the plant physiological basis from a mechanistic aspect has been established and improved by means of more sensitive physical measurement and numerical modeling. Recently, an approach using stable isotopes as a tracer is revealing new insights into this subject. This approach does not quantify fluxes, but instead provides some important parameters or indices to diagnose the plant-water relations. In addition, the isotopic approach gives a real picture of ecosystem dynamics with respect to water/carbon cycles on wide-ranging scales from a single leaf to the globe.

This chapter introduces an isotope-geochemical basis followed by methodology in practice. Recent research trends and some case studies are then presented. The following texts are recommended for further reading: Clark and Fritz (1997) and Kendall and McDonnell (1998) for isotope-hydrology, Ehleringer et al. (1993) and Griffiths (1998) for isotope-ecology.

5.2 Fundamentals of stable isotopes

Most elements have two or more stable isotopic forms, and light isotopes are usually far more abundant than heavy ones. For instance, hydrogen has two stable isotopes: abundant H (^{1}H) and rare D (deuterium; ^{2}H). Similarly, oxygen has three stable isotopes and carbon, two (Table 5.1). However ^{17}O is extremely rare and usually negligible except for special interest in atmospheric circulation. Combining the two hydrogen isotopes and two oxygen isotopes results in six types of water molecules: $H_2{}^{16}O$, $HD^{16}O$, $H_2{}^{18}O$, $HD^{18}O$, $DD^{16}O$, and $DD^{18}O$. Since combinations including two or three rare isotopes in one molecule hardly ever occur, usually only $H_2{}^{16}O$, $HD^{16}O$ and $H_2{}^{18}O$ need to be considered. These water molecules comprised of different isotopes have slightly different properties, so temporal and spatial variations in their abundance are created during the hydrological cycle.

Table 5.1: Stable isotopes of hydrogen, carbon and oxygen.

Element	Isotope	Abundance (%)	Standard isotope ratio
Hydrogen	^{1}H	99.985	^{2}H/^{1}H = 0.00015576 (SMOW)
	^{2}H (D)	0.015	
Carbon	^{12}C	98.89	^{13}C/^{12}C = 0.0112372 (PDB)
	^{13}C	1.11	
Oxygen	^{16}O	99.759	^{18}O/^{16}O = 0.0020671 (SMOW)
	^{17}O	0.037	
	^{18}O	0.204	

Isotopic abundance can be represented also as the molar ratios of the heavy-to-light isotopes (isotope ratio; R = [D/H] = [$HDO/H_2{}^{16}O$] or [^{18}O/^{16}O] = [$H_2{}^{18}O/H_2{}^{16}O$]), while it is common to use the δ notation, as in

$$\delta = \left(\frac{R_A}{R_S} - 1 \right) \times 1000 \ (‰) \qquad (5.1)$$

where R_A and R_S are the isotope ratios of a sample and an international standard, respectively. The reference standards are Standard Mean Ocean Water (SMOW or V-SMOW) for δD and δ^{18}O and Pee Dee Belemnite (PDB) for δ^{13}C.

Isotopically heavy water (i.e., HDO or $H_2{}^{18}O$) has a lower saturation vapor pressure and less molecular diffusivity than those for light water (i.e., $H_2{}^{16}O$). Due to the difference in saturation vapor pressure, heavier isotopes become more abundant in a liquid phase than in a gas phase under thermodynamically equilibrium conditions between the two phases. This effect is called, equilibrium fractionation, and its magnitude is represented by the equilibrium fractionation

factor, α, defined as the following:

$$\alpha = \frac{R_l}{R_v} \tag{5.2}$$

where R_l and R_v are the isotope ratios in liquid and vapor phases, respectively. It should be noticed that there have been other definitions in which the numerator and denominator replaced each other. This parameter depends on temperature and the α-temperature relationship has been experimentally determined. One of the most common equations is that of Majoube (1971),

$$\alpha_D = \exp\left(24844T^{-2} - 76.248T^{-1} + 0.05261\right) \tag{5.3}$$

$$\alpha_{18} = \exp\left(1137T^{-2} - 0.4156T^{-1} - 0.00207\right) \tag{5.4}$$

where T is the temperature in K, and α_D and α_{18} are the factors for hydrogen and oxygen, respectively. As shown in Table 5.2, for normal temperature ranges the value of α increases with decrease in temperature.

Table 5.2: Temperature dependence of equilibrium fractionation factor α.

Temperature (°C)	α_D	α_{18}
25	1.0793	1.00937
20	1.0850	1.00979
15	1.0911	1.01023
10	1.0977	1.01070
5	1.1047	1.01119

Conversely, differences in molecular diffusivity induce other isotopic fractionation during vapor movement after evaporation. This effect is called, kinetic fractionation. Although the ratio of δD change against $\delta^{18}O$ change is approximately 8 during equilibrium fractionation, it normally becomes from 3 to 5 for kinetic fractionation. Therefore, isotopic signals due to the two fractionation effects are distinguishable by delta-diagram, which takes δD as the vertical axis and $\delta^{18}O$ as the horizontal axis. Since in hydrological cycles the equilibrium fractionation effect is dominant over the kinetic effect, plots of meteoric water generally distribute along a line with a slope of 8. Craig (1961) originally called this line the "meteoric water line," but now it is referred to as the global meteoric water line (GMWL) to distinguish from local ones. However, the intercept of

GMWL is not zero and some samples (especially from arid regions) plot apart from GMWL. Such deviations are due to the kinetic effect during evaporation from oceans, lakes, rivers, soil and falling raindrops.

5.3 Methods for water sampling, extraction and analysis

5.3.1 Water sampling and extraction

As mentioned above, evaporation causes isotopic fractionation, so prevention of evaporative enrichment is one of the primary concerns when collecting and storing water samples. Precipitation can be simply collected by a dense-polyethylene tank with a funnel with some oil often added into the tank to prevent evaporation of the stored water. Silicone oil or paraffin oil is suitable, and its depth should be a few centimeters or more. It is important that the oils be removed from the water using paraffin wax in advance of isotopic analysis. Paraffin wax can adsorb oil when it melted and then solidified. To avoid the procedure for removing oil from becoming complicated, an attachment using a ping-pong ball is often utilized. The ping-pong ball allows precipitated water to drop into the tank by floating up but prevents evaporated water vapor from escaping. Collected water should be sealed in a glass vial or dense-polyethylene bottle. It is desirable to fill the vial and to keep it at a cold temperature (e.g., 5°C).

Surface waters (e.g., lake water, river water and ocean water) can be directly collected by a glass vial or dense-polyethylene bottle. A completely dry vial or bottle should be used to prevent contamination, and the sampling location and time must be considered to get representative samples. Sampling from well water is usually a good proxy for groundwater, and it is best to avoid stagnant water.

There are several methods for collecting soil water: (1) the suction lysimeter method, (2) centrifugation method, and (3) distillation method including vacuum distillation, azeotropic distillation, and normal temperature distillation. The suction lysimeter method is the most convenient though it is applicable only in relatively moist conditions (e.g., matric potential > -80 kPa). The centrifugation method can be used for dryness up to -1000 kPa. While the distillation methods have no limitation in moisture conditions, there is some risk of evaporative enrichment or contamination from crystallized water contained in clay minerals.

To extract xylem water, samples of plant bodies are collected by cutting off twigs or extracting small wood cores from trunks. When collecting plant body samples, representative sampling should be considered. When identifying source water for plants, leaves and greenish parts should not be selected as they may be affected by evaporative enrichment. Sampled plant bodies should be peeled, cut into small pieces, and sealed in a glass tube with a double rubber stopcock as quickly as possible. The tube should be kept at sub-zero temperatures until the extraction procedure to avoid changes in the chemical compositions of the plant tissue. In the laboratory, xylem water is then extracted from the plant bodies by

cryogenic vacuum distillation. In this procedure, glass tube A, containing the plant body samples, is connected by a short glass line with another glass tube, B, (Figure 5.1), and then submerged into liquid nitrogen. After completely freezing the plant samples, the entire system is evacuated down to approximately 0.13 Pa (10^{-3} torr) or less. Cooling tube B by liquid nitrogen and heating tube A to 80°C, transfers the xylem water contained in plant tissue into tube B and traps it. It takes approximately 1.5 hours until the water is completely extracted. The extracted frozen water is melted, transferred into a glass vial, and stored as with other water samples.

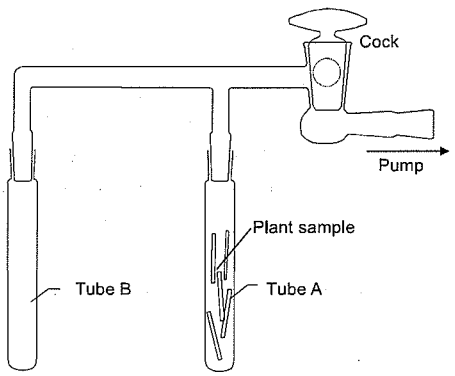

Figure 5.1: Schematic illustration of cryogenic distillation equipment.

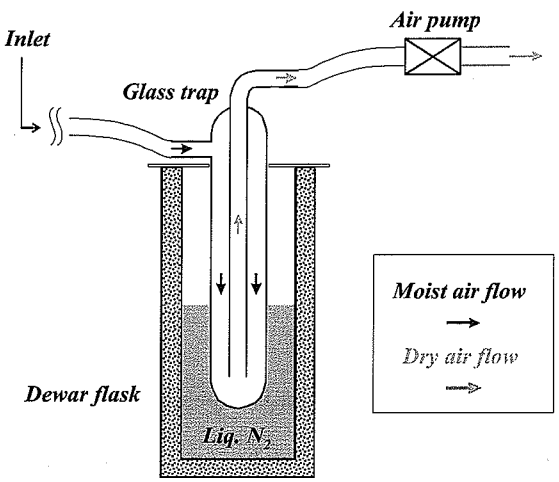

Figure 5.2: Schematic illustration of cryogenic trapping of atmospheric water vapor.

Atmospheric water vapor can be collected by the cryogenic trapping method. One of the simplest types of the equipment is illustrated in Figure 5.2. Moist air is sucked by an air pump and water vapor is completely trapped in a glass trap. If part of the water vapor was not trapped, the collected water will be enriched with more heavy isotopes than the original water vapor. To prevent water vapor escaping, it is effective to fill the trap with a porous media (e.g., aluminum or glass beads). In that case, however, trapped water vapor must be transferred from the trap into another glass tube by the cryogenic distillation method.

5.3.2 Mass spectrometry and sample preparation

Isotopic composition is determined by isotope ratio mass spectrometry. To measure the hydrogen isotopic composition, H_2 gas is prepared by reducing a water sample using zinc as a reducing agent or by isotopically equilibrating the sample using a platinum catalyst. For an oxygen isotope, CO_2 gas is prepared by equilibrating the water sample. Given the measured isotopic ratio of these gases, the isotopic ratio of original water sample can be obtained by mathematical conversion.

Figure 5.3 schematically illustrates the principal features of an isotope ratio mass spectrometer. H_2 gas or CO_2 gas is introduced into a chamber under very low

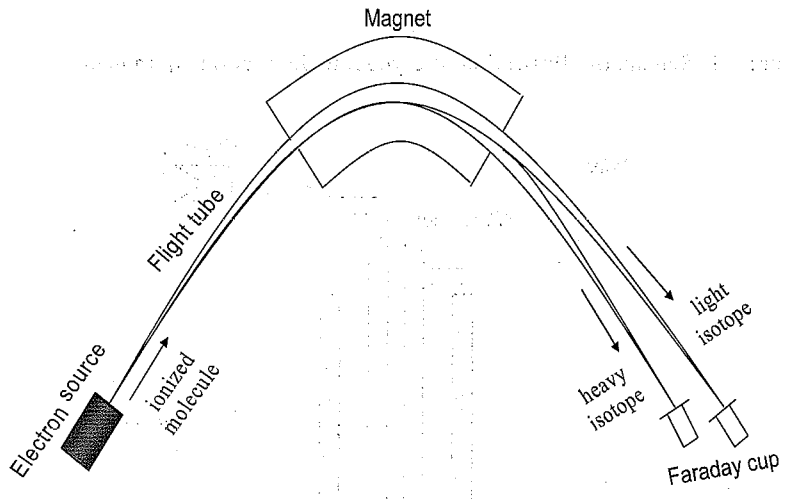

Figure 5.3: Schematic illustration of isotope ratio mass spectrometer.

pressure ($< 10^{-6}$ torr) and bombarded by an electron source to produce ionized molecules. The charged ions are accelerated and pass along a flight tube with a magnet attached to its center point. The flight trajectory of the molecules made up of heavy isotopes is deflected more than that of molecules consisting of light isotopes, so Faraday cups positioned at the terminal of the trajectory can detect molecules with different masses and measure the isotope ratio.

There are two approaches to introduce a sample gas into the chamber. The traditional one is the dual inlet mode; a sample gas and standard gas are introduced 6 to 12 times alternately from different bellows with variable volumes. The isotope ratio is calculated from the average of these 6 to 12 individual measurements. The error of measurement including that due to sample preparation is typically ±1‰ for δD and ±0.1‰ for $\delta^{18}O$. Another approach called the continuous flow mode yields lower precision but is more convenient.

5.4 Water sources of plants and interspecific interactions

5.4.1 Identifying water use pattern

In general, the processes of root water uptake and water transfer within plant bodies induce no isotopic fractionation, so xylem water preserves the isotopic signature of the source water. In other words, comparing the isotopic compositions of xylem water and various source waters enable the identification of the water resources actually utilized by each plant species or individual. There are many good examples based on this idea (reviewed in Ehleringer and Dawson, 1992; Dawson, 1993a; Dawson and Ehleringer, 1998).

White et al. (1985) were among the first to demonstrate that the water use pattern of trees (white pine; *Pinus strobes*) changes depending on the environmental conditions of their habitat. Trees in upland dry sites always utilized rain water, while trees in relatively wet lowlands mainly used groundwater except for days just after rainfall. Dawson and Ehleringer (1991) discovered that mature trees inhabiting a riparian zone in a semiarid region had an isotopic composition that was identical to the groundwater rather than stream water, demonstrating that the streamside trees were not using stream water. According to their interpretation, the trees sought groundwater as the most stable water source in the region in order to ensure a greater probability of survival during droughts, or when stream channels changed due to major floods (see also Dawson, 1993).

In a similar manner, Flanagan et al. (1992) clarified the differential water use among co-occurring plant species in a semi-arid climate. Two shrub species were highly depended on groundwater, but two tree species had a higher uptake of summer precipitation. Ehleringer et al. (1991) showed the relationships of water sources of various plant species in a desert shrub community to their life form and root system.

5.4.2 Quantitative evaluation of water source contribution

If only two water sources (e.g., rainwater and groundwater) are available for a plant, the relative contribution from each source can be quantitatively evaluated using the following equations based on a simple two-component mixing model.

$$F_1 = \frac{\delta_x - \delta_2}{\delta_1 - \delta_2} \tag{5.5}$$

$$F_2 = 1 - F_1 \tag{5.6}$$

where F is the relative contribution ratio, and subscripts x, 1 and 2 denote the values of xylem water, sources 1 and 2, respectively. This approach requires different isotopic signature between the two sources. In general, the higher the altitude, the lower the δ value of precipitation (e.g., Clark and Fritz, 1997). Thus, mountain foot regions, where groundwater is recharged at sites higher than the region, are one of the most suitable locations for evaluating contributions from groundwater and on-site precipitation.

If variations of δD and $\delta^{18}O$ are independent of each other, contributions from three sources can be evaluated by a three-component mixing model. Solving simultaneously mass conservation equations for water, hydrogen isotopes and oxygen isotopes, the following equations are given.

$$F_1 = \frac{(\delta D_x - \delta D_3)(\delta^{18}O - \delta^{18}O_3) - (\delta^{18}O_x - \delta^{18}O_3)(\delta D_2 - \delta D_3)}{(\delta D_1 - \delta D_3)(\delta^{18}O_2 - \delta^{18}O_3) - (\delta^{18}O_1 - \delta^{18}O_3)(\delta D_2 - \delta D_3)} \tag{5.7}$$

$$F_2 = \frac{(\delta D_x - \delta D_3)(\delta^{18}O_1 - \delta^{18}O_3) - (\delta^{18}O_x - \delta^{18}O_3)(\delta D_1 - \delta D_3)}{(\delta D_2 - \delta D_3)(\delta^{18}O_1 - \delta^{18}O_3) - (\delta^{18}O_2 - \delta^{18}O_3)(\delta D_1 - \delta D_3)} \tag{5.8}$$

$$F_3 = 1 - F_1 - F_2 \tag{5.9}$$

For instance, in addition to hydrograph separation (e.g., Ogunkoya and Jenkins, 1993; see section 5.6.2), it is possible to separately evaluate the contribution ratios of rainwater, groundwater and soil water that exist before the rain event and the effect of kinetic fractionation. In practice, however, it is not often valid to assume only one representative value of isotopic composition in soil water, because soil water δ values are highly variable by depth. In addition, it is difficult to evaluate contributions from different depth-zones, because (1) isotopic signatures do not always change monotonically with depth and thus the signatures of two separate depth-zones may become identical at times, and (2) even though the signatures monotonically changed, it is not distinguishable as to whether the plant takes up water from two separate depth-zones or only one intermediate depth-zone. Therefore, it seems not to be promising to evaluate quantitatively the

contributions of waters from each layer in the soil profile.

When there is no or minor advection of groundwater from higher altitude regions as well as no or minor evaporative enrichment, the δ value of groundwater nearly equals the long-term mean δ of precipitation weighted by the precipitation amount, so that soil water can be treated as a mixture of two sources: groundwater, which is a good proxy of the accumulated precipitation, and recent rain water. Based on this idea, White et al. (1985) proposed a model assuming that the recent rain component linearly reduces with time. In the simplest case of a single rainfall, δ of xylem water after the event can be described as,

$$\delta_x = \left[F_g' \cdot \delta_g + \left(1 - F_g'\right) \cdot \delta_r\right] \cdot \left(1 - t/d\right) + \delta_g \cdot t/d \qquad (5.10)$$

where F'_g is the initial fraction of groundwater, t is the time after the rain event, d is the decay time constant for rain in the xylem water, and δ_g and δ_r are isotopic compositions of groundwater and rainwater, respectively. The quantity in brackets is the initial (i.e., $t = 0$) isotopic mixture of rain and groundwater as measured in the xylem water. At time $t = d$, the xylem water δ is equal to that of groundwater. It should be noted and taken into consideration that a time lag occurs until the isotopic signal of rain appears in δ_x. Though this model is somewhat too simple, it successfully reproduces the observation results by White et al. (1985). Rearranging equation (5.10), the temporal change in the contribution ratio of groundwater, F_g, and recent rain water, F_r, are expressed as,

$$F_g = \frac{1 - F_g'}{d} \cdot t + F_g' \qquad (5.11)$$

$$F_r = \frac{F_g' - 1}{d} \cdot t - F_g' + 1. \qquad (5.12)$$

This model can be expanded to consider multiple, overlapping rain events (see White et al. (1985) for more details), whereas its usefulness under various conditions has not yet been clarified.

5.4.3 Diagnoses of interspecific interaction

To diagnose competition for water between a crop and windbreak trees in the Sahel region, Smith et al. (1997) identified their water sources using $\delta^{18}O$. According to their results, for a deep (> 35m) water table, both the crop and trees extracted water from the top 2-3 m of the soil. While for a shallower (6-8 m) water table, the crop still used the top soil moisture while the trees extracted groundwater or deep soil water rather than top soil moisture. This indicates that competition for water is likely reduced by water source separation at such

locations where groundwater is accessible.

Water source separation among co-occurring plants occurs under not only in arid climates, but also in relatively humid climates. Yamanaka et al. (2004) reported that in a suburban pine forest undergoing succession in Central Japan, pioneering pine (*Pinus densiflora*) trees took up deep soil water or groundwater (approximately 1.3 m in depth), while invading oak (*Quercus myrsinaefolia*) extracted shallower (< 0.4 m) soil water, and understory plants (mainly bamboo grass) depended on soil water from the intermediate depth-zone (Figures 5.4 and 5.5). The general feature of this water source separation was almost invariant throughout growing season and likely insensitive to soil dryness. Excavation investigation conducted in the same forest (Yamanaka et al., 2005) revealed that the pine tree had not only deep roots, but also many shallow roots, though the adjacent bamboo grasses had much more shallow roots. In contrast, the root systems of oak trees enriched from a shallow zone while those of the adjacent bamboo grasses dominated in a zone

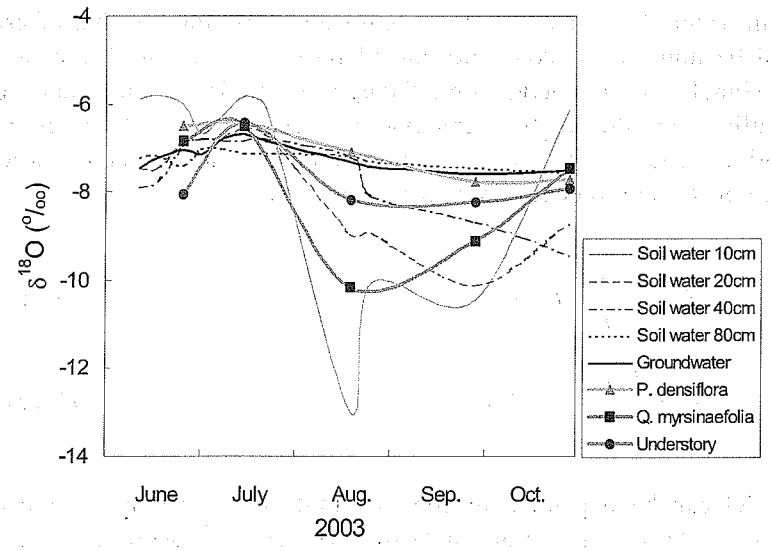

Figure 5.4: Isotopic variation of sap, soil and ground waters at a forest under succession.

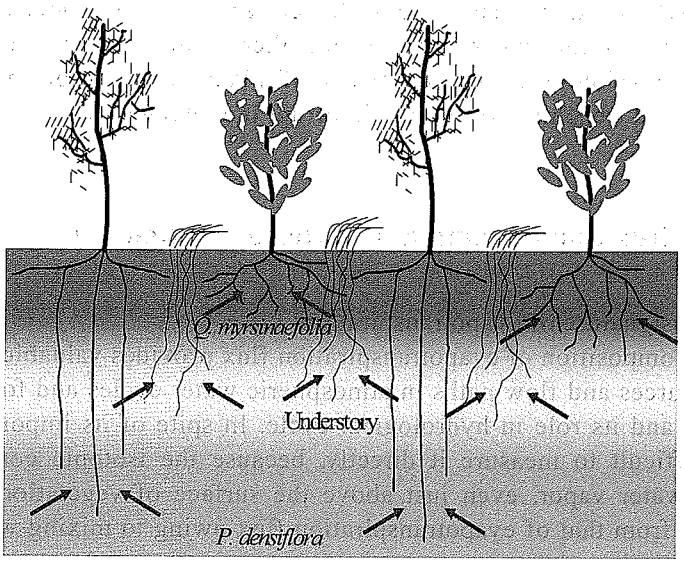

Figure 5.5: Schematic illustration of water source separation among plants.

deeper than the oak's root zone. These facts may suggest that an ability to compete for shallow soil water is highest in oak and lowest in pine. In other words, it is likely that pine trees and bamboo grasses seek other water sources in deeper depths to avoid competition with oak. In fact, pine trees take up shallow soil water in pure pine forest (i.e., without competitors) even very near to the forest mentioned above.

In the context of interspecific interaction, there is an interesting phenomenon called as "hydraulic lift" (Richards and Caldwell, 1987; Caldwell and Richards, 1989). At night, some species of trees and shrubs release water, which was adsorbed by deep roots, into upper soil layers. In New York State during a severe drought, Dawson (1993b) observed that the δD of shallow soil water (ranging from -25 to -57‰) was closer to that of groundwater (-59±2.7‰) and xylem water (-54±6.1‰) in large sugar maples (*Acer saccharum*) and decreased with distance from the maple trees, indicating the existence of hydraulic lift. Surprisingly, δD values of xylem water in herbaceous plants decreased from -25‰ as their distance from that maples grew shorter. Herbaceous plants adjacent to the maple trees generally had higher leaf-water potential and leaf conductance than that of plants far away from the trees. These facts demonstrate that herbaceous plants that grow in close proximity to a maple tree utilize hydraulically lifted water and benefit from that tree. However, this may be a somewhat special case that occurs only during periodic or chronic drought events. Recent studies using isotopic approach together with trenching treatment report that benefits from hydraulic lift can be overwhelmed by competition for water between large trees and adjacent grasses

(Ludwig, 2004). In ether case, isotopic tracers are powerful tools for assessing interspecific interaction when utilized together with other approaches (e.g., physical and physiological measurements of plant status, root morphological investigation, and trenching to forcibly interrupt the interaction).

5.5 Canopy flux partitioning and water use efficiency

5.5.1 Isotopic signature of evapotranspiration

Isotopic composition of evapotranspiration flux provides valuable information for tracing sources and flow paths in atmospheric water cycles and for diagnosing plant activity and its role in hydrological cycle. In spite of its importance, it has long been difficult to measure it directly, because the isotopic composition of atmospheric water vapor, even just above the surface of vegetation canopy, no longer differs from that of evapotranspiration flux owing to mixing with advected water vapors.

Yakir and Wang (1996) have proposed a method to estimate the isotopic signature of evapotranspiration flux using a set of isotopic compositions and concentrations (i.e., absolute humidity or mixing ratio) of water vapor. The method is essentially identical to the Keeling plot approach, which was first used by Keeling (1958, 1961) to identify plant-originated contributions to atmospheric CO_2 and is now commonly used to study carbon cycles (for a review, see Pataki et al., 2003).

The basis of the Keeling plot approach is the mass balance of a substance (i.e., water, carbon dioxide, or others) and its isotope. Consider an air parcel in which the water vapor is a mixture of that produced by evapotranspiration and the preexisting mix of the background atmosphere. The mass balance equations for water and its isotope are given as,

$$Q_v = Q_{ET} + Q_{bg} \tag{5.13}$$

$$Q_v \cdot \delta_v = Q_{ET} \cdot \delta_{ET} + Q_{bg} \cdot \delta_{bg} \tag{5.14}$$

where Q is the water vapor mixing ratio, and subscripts v, ET and bg represent the whole water vapor, evapotranspiration component and background component, respectively. Simultaneously solving these equations for δ_v gives

$$\delta_v = a \cdot (1/Q_v) + \delta_{bg} \tag{5.15}$$

where $a = Q_{bg} \cdot (\delta_{bg} - \delta_{ET})$. If we assume that the background atmosphere is uniform in time and space (i.e., Q_{bg} and δ_{bg} are constant) and the isotopic

signature of evapotranspiration does not change (i.e., δ_{ET} is constant), then a is constant. Thus, in a plot of δ_v versus $1/Q_v$, an estimate of δ_{ET} can be obtained as the interception of the regression line. The validity of the assumptions can be checked by referring the determination coefficient of the linear regression, in which is found to fit well with the results of many researches. However, the limitations of this approach are not always explicit.

On the other hand, He and Smith (1999a) derived the same approach by another method. They defined the isotope ratio of water vapor flux as the ratio of the isotopically heavy water flux to that of the light (i.e., normal) water flux, that is,

$$R_{ET} = j^{-1}\frac{f^i}{f} \tag{5.16}$$

where j=19/18 (20/18) is the ratio of the molecular weights of $HD^{16}O$ and $H_2{}^{16}O$ ($H_2{}^{18}O$ and $H_2{}^{16}O$), f and f^i are the fluxes of light water vapor and heavy water vapor, respectively (hereafter superscript i denotes the quantity for the heavy isotope). The water vapor flux in the atmospheric boundary layer can be expressed by flux-gradient relation (e.g., Garratt, 1992, p.28)

$$f = -K\frac{d\overline{Q}}{dz} \tag{5.17}$$

where K is the eddy diffusivity, z is the height, and the overbar denotes the temporal mean value in a certain period. In the same manner, heavy isotope flux is expressed as,

$$f^i = -K^i\frac{d\overline{Q^i}}{dz} \tag{5.18}$$

Substituting equations (5.17) and (5.18) into (5.16) and assuming $K = K^i$ just like in the derivation of the Bowen ratio, the following equation is given.

$$R_{ET} = j^{-1}\frac{d\overline{Q^i}}{d\overline{Q}} \tag{5.19}$$

If we have measured values of water vapor δ and Q at two levels, equation (5.19) can be rewritten in delta notation as follows,

$$\delta_{ET} = \frac{Q_l \delta_{vl} - Q_u \delta_{vu}}{Q_l - Q_u} \tag{5.20}$$

where subscripts u and l represent upper and lower sampling levels, respectively. This equation indicates that δ_{ET} is identical to the intercept of the regression line in the δ - $1/Q$ diagram (see also Appendices A & B of He and Smith, 1999a).

As compared to a derivation based on isotopic mass balance, the derivation from the flux-gradient relation has the advantage of defining the clear limitations of this approach as to its application. For instance, because the assumptions in deriving equation (5.20) are the same as in the energy balance/Bowen ratio method for evaluating evapotranspiration flux, the same order of fetch length (e.g., 100-300 times greater than measurement/sampling height; Brutsaert, 1982, p.166) is required. Thus, the Keeling plot approach holds if isotopic measurement of water vapor is done simultaneously at two or more levels while taking the fetch requirement into consideration.

5.5.2 Flux partitioning

For vegetated surfaces, evapotranspiration flux can be partitioned into two components: transpiration and soil evaporation,

$$ET = T + E \tag{5.21}$$

As well as for normal water flux, isotope flux can be also distinguished between its transpiration component and soil evaporation component,

$$ET \cdot \delta_{ET} = T \cdot \delta_T + E \cdot \delta_E \tag{5.22}$$

where δ_T and δ_E are the isotopic compositions of transpiration flux and soil evaporation flux, respectively.

Solving equations (5.21) and (5.22) simultaneously, gives the following equation

$$\frac{T}{ET} = \frac{\delta_{ET} - \delta_E}{\delta_T - \delta_E} \tag{5.23}$$

Consequently, the transpiration fraction T/ET can be evaluated if we obtain the values of δ_T and δ_E in addition to δ_{ET}.

As mentioned in section 5.4, no isotopic fractionation occurs during water uptake and transport to the leaves inside the plant body. Although leaf water becomes isotopically enriched due to evaporation, the isotopic composition of transpiring water vapor, which is in isotopical equilibrium with the leaf water, is

the same as that of soil water absorbed by root system and transported into the leaves if under a steady-state condition (White, 1989, p.148; Flanagan et al., 1991). Therefore, δ_T can be obtained by the isotopic composition of the soil water in the active root zone.

For extremely dry soils, evaporation and thus water isotopic enrichment occurs not at the soil surface, but at the bottom boundary of the dry surface layer as well (Allison and Barnes, 1983; Yamanaka and Yonetani, 1999), and kinetic fractionation is strongly enhanced by molecular diffusion of water vapor through the layer (Barnes and Allison, 1983). However, soils covered by vegetation are hardly ever in such a condition. Therefore, the Craig-Gordon model can be utilized (Craig and Gordon, 1965) or other alternatives (e.g., Flanagan et al., 1991; He and Smith, 1999b) to estimate dE.

An arranged form of Craig-Gordon model is expressed as (Merlivat and Jouzel, 1979: He and Smith, 1999b),

$$\delta_E = \left\{ K \frac{(1/\alpha_{eq})(10^{-3}\delta_s + 1) - h^*(10^{-3}\delta_v + 1)}{1 - h^*} - 1 \right\} \times 10^3 \qquad (5.24)$$

where K (= 0.9723 for oxygen or 0.9755 for hydrogen; Gat, 1996) is the ratio of molecular diffusivities of isotopic water to normal water in the air, α_{eq} is the equilibrium fractionation factor, δ_s is the isotopic composition of surface soil water, and h^* is the relative humidity defined as the ratio of the actual water vapor pressure e of the air to the saturation vapor pressure e_{sat} at the soil surface temperature. This model incorporates not only the effects of equilibrium and kinetic fractionations but also the effect of isotope back flux from the atmosphere (He and Smith, 1999b).

Using the Keeling plot (Figure 5.6), Moreira et al. (1997) showed that transpiration was far greater than soil evaporation in eastern and central Amazon forests. Yakir and Sternberg (2000) recalculated *T/ET* based on the data from Moreira et al. (1997) using Eq. (5.23) with the value of *T/ET* ranging from 76 to 100%. In a similar manner, Wang and Yakir (2000) estimated *T/ET* for wheat fields to be in the range of 96-98%. Combining measurements within tree and understory canopies in semiarid savanna woodland, Yepez et al. (2003) evaluated the relative contribution to total evapotranspiration from tree transpiration (70%), understory transpiration (15%) and soil evaporation (15%). Yamanaka et al. (2005) conducted observations in a temperate grassland throughout a growing season and revealed there is unity. The variations in *T/ET* correlated closely with the leaf area index (LAI) and energy flux partitioning (Figure 5.7). These results demonstrate the great importance of vegetation status in affecting water and energy balances of vegetated land surfaces, as well as the usefulness of isotopic tracers in studying such subjects.

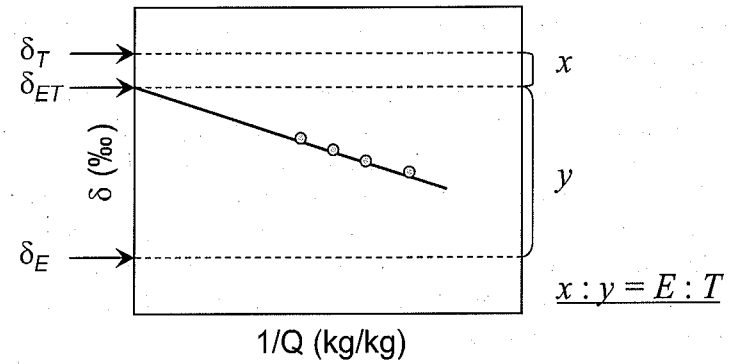

Figure 5.6: Schematic illustration of Keeling plot and its use for flux partitioning.

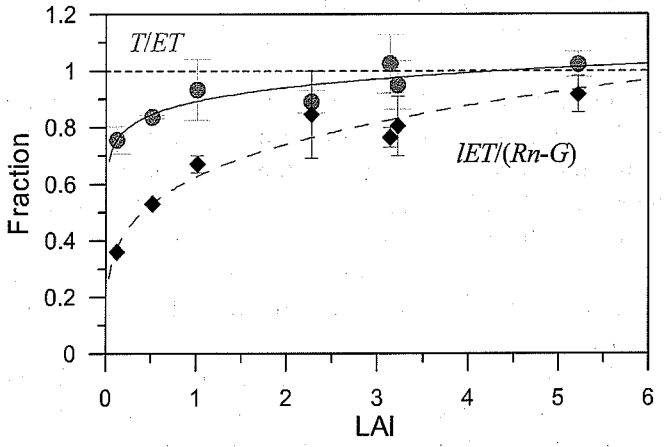

Figure 5.7: Transpiration fraction (*T*/*ET*) and evaporative fraction (*lET*/(*Rn*-*G*))as a function of leaf area index (LAI); *T* is the transpiration rate, *ET* is the evapotranspiration rate, *l* is the latent heat for vaporization, *Rn* is the net radiation and *G* is the soil heat flux.

5.5.3 Water use efficiency

Carbon isotope discrimination, Δ, is defined as (Farquahar and Lloyd, 1993)

$$\Delta \equiv \frac{\delta^{13}C_a - {}^{13}C\delta_p}{1+\delta^{13}C_p} \qquad (5.25)$$

where subscripts *a* and *p* denote the values for atmospheric CO_2 and plant material,

respectively. These parameters correlate with the ratio of intercellular CO_2 concentration to that of the atmospheric and thus are linked to stomata closure. Because the water-use efficiency, which is the ratio of carbon fixed to water transpired, is dependent of stomata closure, Δ is a good proxy for water-use efficiency, as schematically illustrated in Figure 5.8.

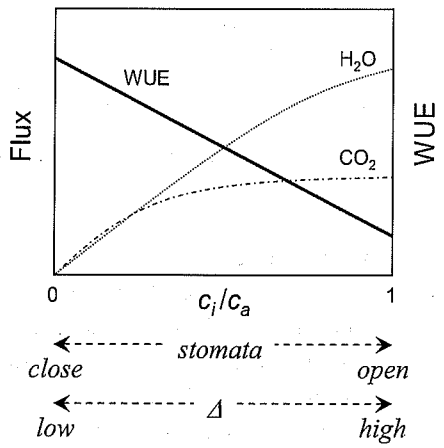

Figure 5.8: Schematic illustration of the relationship between carbon isotope discrimination (Δ) and water use efficiency (WUE); c_i and c_a are the intercellular and atmospheric CO_2 concentrations, respectively.

Using the Keeling plot for $\delta^{13}C$, it is possible to obtain isotopic signatures of ecosystem carbon sinks (i.e., photosynthesis minus respiration) in daytime and carbon sources (i.e., respiration) at nighttime (Figure 5.9). Considering the δ of a carbon sink as δ_p, one can obtain Δ from isotopic measurements of atmospheric CO_2 within and/or around a vegetation canopy to assess instantaneous water-use efficiency.

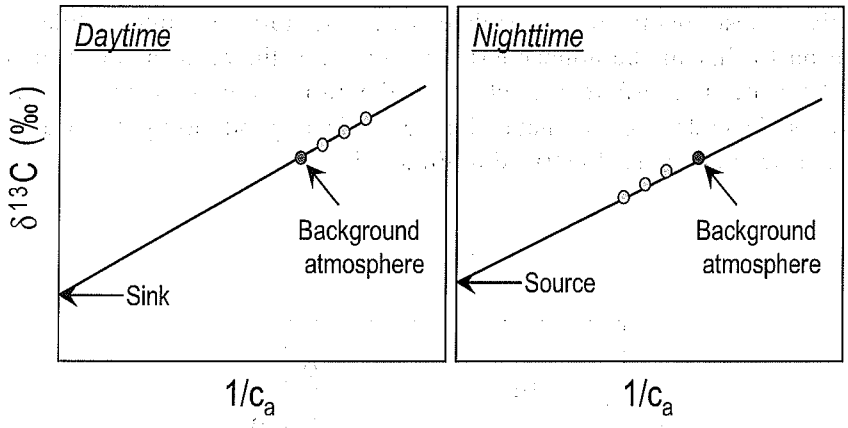

Figure 5.9: Schematic illustration of Keeling plot for atmospheric CO_2

To diagnose long-term water-use efficiency, direct measurement of carbon isotopes in plant dry matter (for methods, see Ehleringer et al., 2000) is possible and commonly used. Ehleringer (1993) showed that plants inhabiting arid land had low Δ values (i.e., high water-use efficiency), suggesting that stomata are very nearly closed during the main periods of carbon gain. They also demonstrated that longer-lived plants had lower Δ and such a tendency is more dominant in warmer desert regions. These facts support the idea that higher water-use efficiency is of great advantage to survival through extended, severe drought periods. Flanagan et al. (1992) found a relationship between water-use efficiency and water source in which shrub species that mainly take up groundwater have a lower water-use efficiency than tree species that are highly dependant on summer precipitation. This may be a indication that the use of groundwater as a stable resource helps to avoid suffering water stress.

5.6 Catchment water balance and ecosystem dynamics

5.6.1 Plant-water relations on a catchment scale

Changes in terrestrial ecosystems (e.g., deforestation, reforestation and natural vegetation succession) can affect catchment water balance and thus river discharge. For instance, clear cutting of forests in a mountainous headwater catchment apparently increases streamflow (e.g., Swank et al., 2001). For the case of a catchment overlaid by a native eucalyptus forest in Australia, a bushfire similarly increased streamflow for a few years just after the event, which then declined to levels below those before the fire (Roberts, 2000). This may be because old trees were replaced by young trees that have higher transpiration-activity. On the other hand, changes in catchment water balance can

affect forest health. Jolly et al. (1993) demonstrated that changes in river manipulation induced rises in groundwater, higher evaporation, and salt accumulation, and inferred that the use of such highly saline water was detrimental to tree health.

Such plant-water relations on a catchment scale can be assessed by the approach mentioned in previous sections of this chapter. In particular, since the processes of transpiration and root water uptake are less independent of spatial scale, scaling up from an individual or plot scale to the catchment scale is relatively easy. The runoff process is, however, highly dependent on the scale. The following two subsections describe isotopic tracer approach for assessing catchment hydrological processes.

5.6.2 Identifying flowpath

Typically, stream water during and after storm events has been regarded as a mixture of new water that was added directly into stream by rainfall or surface runoff and old water that was recharged by exfiltration of soil water and/or groundwater. In recent studies, old water is explicitly divided into a soil water component having a shallow flowpath and a groundwater component having a deep flowpath. Changes in the terrestrial ecosystem affect not only water flux from forest canopy but also the surface/subsurface flowpaths of water in the catchment through modification of moisture distribution and hydraulic properties of the soil (e.g., infiltration capacity, porosity and hydraulic conductivity). The changes in water flowpath are closely related to the carbon/nitrogen cycle and buffering ability against acid rain in the catchment.

Separation into two or three components can be achieved using equations. (5.5)-(5.9). Besides water isotopes, alternative tracers (e.g., anions) are often utilized. In principle, four or more flowpaths can be identified if three or more tracers are used. However, the behaviors of tracers are not independent of each other, so end-member mixing analysis (EMMA) is utilized for the selection of isotopic and chemical tracers. According to a review of hydrograph separation around the world (Buttle, 1994), in many fields a peak discharge of 50% or more is maintained by old water, and the percentage tends to be smaller in non-forested catchments than in forested catchments. This demonstrates that the existence of vegetation increases water loss from land surface via transpiration but also has a role in retaining water in the catchment.

5.6.3 Estimating residence time

Change in the water balance throughout the catchment is indicated by the residence time of stream water. Because residence time is difficult to evaluate in spite of its importance, its relationship to ecosystem dynamics has not yet been clarified. However, isotopic variations in precipitation and stream water aid in estimating residence time if the variations can be approximated by sinusoidal

curves (Maloszewski et al., 1983).

Assuming adequate mixing in a reservoir, residence time τ is expressed as

$$\tau = \omega^{-1}\left((B/A)^{-2} - 1\right)^{1/2} \qquad (5.26)$$

where ω is the angular frequency (= $2\pi/C$), C is the period of isotopic variation in precipitation and stream water (normally, one year), A and B are the amplitudes of a sine curves describing the isotopic variations in precipitation and stream water, respectively. This model is called the exponential model (EM) because residence time distribution is expressed by exponential function.

An alternative modelcalled the dispersive model (DM), can be given by

$$\tau = \omega^{-1}\left(\frac{-\ln(B/A)}{D_p}\right)^{1/2} \qquad (5.27)$$

where D_p is the dispersion parameter. This model is derived by solving the dispersion equation. Stewart and McDonnel (1991) applied the two models and found that DM yields more accurate residence times. However, there remains uncertainty in determining D_p. Further studies are required to improve this technique and assess the interaction between ecosystem dynamics and catchment hydrology.

References

Allison, G.B., and Barnes, C.J., (1983), Estimation of evaporation from non-vegetated surfaces using natural deuterium, Nature, 301, 143-145.

Barnes, C.J., and Allison, G.B., (1983), The distribution of deuterium and oxygen-18 in dry soils: 1, theory, J, Hydrol., 60, 141-156.

Brutsaert, W., (1982), *Evaporation into the Atmosphere: Theory, History and Applications*, Kluwer Academic Pub., Boston, 299pp.

Buttle, J.M., (1994), Isotope hydrograph separations and rapid delivery of pre-event water from drainage basins, Progress in Physical Geography, 18, 16-41.

Caldwell, M.M., and Richards, J.R., (1989), Hydraulic lift: water efflux from upper roots improves effectiveness of water uptake by deep roots, Oecologia, 79, 1-5.

Clark, I.D., and Fritz, P., (1997), *Environmental Isotopes in Hydrogeology*, Lewis Pub., New York, 311pp.

Craig, H., (1961), Isotopic variation in meteoric waters, Science, 133, 1702-1703.

Craig, H., and Gordon, L.I., (1965), Deuterium and oxygen 18 variations in the ocean and the marine atmosphere, in Stable Isotopes in Oceanographic Studies

and Paleotemperatures, edited by E, Tongiorgi, pp, 9-130, Spoleto, Italy.
Dawson, T.E., (1993a), Water sources of plants as determined from xylem-water isotopic composition: perspectives on plant competition, distribution, and water relations, in Stable Isotopes and Plant Carbon-Water Relations, edited by J, R, Ehleringer et al., pp, 465-496, Academic Press, San Diego.
Dawson, T.E., (1993b), Hydraulic lift and water use by plants: implications for performance, water balance and plant-plant interactions, Oecologia, 95, 565-574.
Dawson, T.E, and Ehleringer, J.R., (1991), Stream side trees that do not use stream water, Nature, 350, 335-337.
Dawson, T.E., and Ehleringer, J.R., (1998), Plants, isotopes and water use: a catchment-scale perspective, in Isotope Tracers in Catchment Hydrology, edited by C, Kendall and J, J, McDonnell, 165-202, Elsevier, New York.
Ehleringer, J.R., (1993), Carbon and water relations in desert plants: an isotopic perspective, in Stable Isotopes and Plant Carbon-Water Relations, edited by J, R, Ehleringer et al., pp, 155-172, Academic Press, San Diego.
Ehleringer, J.R., and Dawson, T.E., (1992), Water uptake by plants: perspectives from stable isotope composition, Plant Cell Environ., 15, 1073-1082.
Ehleringer, J.R., Philips, S.L., Schuster, W.F.S., and Sandquist D.R., (1991), Differential utilization of summer rains by desert plants: implications for competition and climate change, Oecologia, 88, 430-434.
Ehleringer, J.R.J., Roden, and Dawson, T.E., (2000), Assessing ecosystem-level water relations trough stable isotope ratio analyses, in Methods in Ecosystem Science, edited by O, E, Sala et al., pp, 181-198, Springer, New York.
Farquhar, G.D., and Lloyd, J., (1993), Carbon and oxygen isotope effects in the exchange of carbon dioxide between terrestrial plants and the atmosphere, in Stable Isotopes and Plant Carbon-Water Relations, edited by J, R, Ehleringer et al., pp, 47-70, Academic Press, San Diego.
Flanagan, L.B., Comstock, J.P., and Ehleringer, J.R., (1991), Comparison of modeled and observed environmental influences on the stable oxygen and hydrogen isotope composition of leaf water in Phaseolus vulgaris L., Plant Physiol., 96, 588-596.
Flanagan, L.B., Ehleringer, J.R., and Marshall, J.D., (1992), Differential uptake of summer precipitation among co-occurring trees and shrubs in a pinyon-juniper woodland, Plant Cell Env., 15, 831-836.
Garratt, J.R., (1992), *The Atmospheric Boundary Layer*, Cambridge Univ, Press, New York, 316pp.
Gat, J.R., (1996), Oxygen and hydrogen isotopes in the hydrologic cycle, Annu, Rev, Earth Planet, Sci., 24, 255-262.
Griffiths, H., (ed.) (1998), *Stable Isotopes: Integration of Biological, Ecological and Geochemical Processes*, BIOS Scientific, Oxford, 438pp.
He, H., Smith., R.B., (1999a), Stable isotope composition of water vapor in the atmospheric boundary layer above the forests of New England, J, Geophys, Res., 104, 11657-11673.

He, H., Smith., R.B., (1999b), An advective-diffusive isotopic evaporation-condensation model, J, Geophys, Res., 104, 18619-18630.
Jolley, I.D., Walker, G.R., and Thorburn, P.J., (1993), Salt accumulation in semi-arid floodplain soils with implications for forest health, J, Hydrol., 150, 589-614.
Keeling, C.D., (1958), The concentration and isotopic abundance of atmospheric carbon dioxide in rural areas, Geochim, Cosmochim, Acta, 13, 322-334.
Keeling, C.D., (1961), The concentration and isotopic abundance of carbon dioxide in rural and marine air, Geochim, Cosmochim, Acta, 24, 277-298.
Kendall, C., and McDonnell, J.J., (1998), *Isotope Tracers in Catchment Hydrology*, Elsevier, New York, 839pp.
Kramer, P.J., and Boyer, J.S., (1995), *Water Relations of Plants and Soils*, Academic Press, San Diego, 495pp.
Ludwig, F., Dawson, T.E., Prins, H.H.T., Berendse, F., and de Kroon, H., (2004), Below-ground competition between trees and grasses may overwhelm the facilitative effects of hydraulic lift, Ecol, Lett., 7, 623-631.
Majoube, M., (1971), Fractionnement en oxygene-18 et en deuterium entre l'eau et sa vapeur, J, Chem, Phys., 197, 1423-1436.
Maloszewski, P., Rauert, W., Stichler, W., and Herrmann, A., (1983), Application of flow models in an alpine catchment area using tritium and deuterium data, J, Hydrol., 66, 319-330.
Merlivat, L., and Jouzel, J., (1979), Global climatic interpretation of the deuterium-oxygen 18 relationship for precipitation, J, Geophys, Res., 84, 5029-5033.
Moreira, M.Z., Sternberg, L.S.L., Martinelli, L.A., Victoria, R.L., Barbosa, E.M., Bonates, L.C.M., and Napstad, D.C., (1997), Contribution of transpiration to forest ambient vapour based on isotopic measurements, Global Change Biol., 3, 439-450.
Ogunkoya, O.O., and Jenkins, A., (1993), Analysis of storm hydrograph and flow pathways using a three-component hydrograph separation model, J, Hydrol., 142, 71-88.
Pataki, D.E., Ehleringer, J.R., Flanagan, L.B., Yakir, D., Bowling, D.R., Still, C.J., Buchmann, N., Kaplan, J.O., and Berry J.A., (2003), The application and interpretation of Keeling plots in terrestrial carbon cycle research, Global Biogeochem, Cycles, 17(1), 1022, doi:10.1029/2001GB001850.
Richards, J.H., and Caldwell, M.M., (1987), Hydraulic lift: substantial nocturnal water transport between soil layers by Artemisia tridentate roots, Oecologia, 73, 486-489.
Roberts, J., (2000), The influence of physical and physiological characteristics of vegetation on their hydrological response, Hydrol, Processes, 14, 2885-2901,
Stewart, M.K., and McDonnell, J.J., (1991), Modeling base flow soil water residence times from deuterium concentrations, Water Resour, Res., 27, 2681-2693.
Smith, D.M., Jarvis, P.G., and Odongo, J.C.W., (1997), Sources of water used by

trees and millet in Sahelian windbreak systems, J, Hydrol., 198, 140-153.
Swank, W.T., Vose, J.M., and Elliott, K.J., (2001), Long-term hydrologic and water quality responses following commercial clearcutting of mixed hardwoods on a southern Appalachian catchment, For, Ecol, Manage., 143, 163-178.
Wang, X.-F., and Yakir, D., (2000), Using stable isotopes of water in evapotranspiration studies, Hydrol, Processes, 14, 1407-1421.
White, J.W.C., (1989), Stable hydrogen isotope ratios in plants: a review of current theory and some potential applications, in Stable Isotopes in Ecological Research, edited by P, W, Rundel et al., pp, 142-162, Springer-Verlag, New York.
White, J.W.C., Cook, E.R., Lawrence, J.R., and Broecker, W.S., (1985), The D/H ratios of sap in trees: implications of water sources and tree ring D/H ratios, Geochim, Cosmochim, Acta, 49, 237-246.
Yakir, D., and Sternberg, L.S.L., (2000), The use of stable isotopes to study ecosystem gas exchange, Oecologia, 123, 297-311.
Yakir, D., and Wang, X.-F., (1996), Fluxes of CO_2 and water between terrestrial vegetation and the atmosphere estimated from isotope measurements, Nature, 380, 515-517.
Yamanaka, T., and Yonetani, T., (1999), Dynamics of the evaporation zone in dry sandy soils, J, Hydrol., 217, 135-148.
Yamanaka, T., Iizuka, S., and Tanaka, T., (2004), An isotope-ecohydrological study on water use strategy of plants in a suburban secondary forest, EOS Trans, AGU, 85 (28), West, Pac, Geophys, Meet, Suppl., Abstract B12A-05.
Yamanaka, T., Matsuo, D., Yano, M., Kakubari, J., Iida, S., Wakui, H., Shimizu, R., and Tanaka, T., (2005), Difference in Root System among Co-occurring Plants in a Secondary Pine Forest Undergoing Succession, Bull, Terrestrial Environ, Res, Center, Univ, Tsukuba, 6, 39-44. (in Japanese)
Yamanaka, T., Tsunakawa, A., and Smith, R.B., (2005), Isotopic measurement of evapotranspiration flux and its use for partitioning evaporation/transpiration components, Proceedings of 2005 Annual Conference, Japan Society of Hydrology and Water Resources, 78-79. (in Japanese)
Yepez, E.A., Williams, D.G., Scott, R.L., and Lin, G., (2003), Partitioning overstory and understory evapotranspiration in a semiarid savanna woodland from the isotopic composition of water vapor, Agric, For, Meteorol., 119, 53-68.

Chapter 6

Integrated use of vegetation indices and surface temperature space obtained from Earth observation satellite dataset

Atsushi Higuchi
Center for Environmental Remote Sensing (CEReS),
Chiba University, Chiba 263-8522, Japan
Tel: +81-43-290-3858
Fax: +81-43-290-3857
e-mail: higu@faculty.chiba-u.jp

For more than three decades, humans have had access to advanced "eyes" from the space. Observations from spaceborne sensors have several advantages such as "repeatability," "uniformity," and "wide-range scanning of the Earth." Despite the difficulties and uncertainties in interpreting or retrieving satellite dataset (e.g., for surface physical characteristics), these sensors detect "real" targets or objects. This chapter focuses on vegetation indices and surface temperature, both of which are widely applied to environmental studies. In particular, temperature is not only used in the monitoring of terrestrial ecosystems, but it also widely and practically applied to meteorological and climatological purposes (as in the form of brightness temperature or outgoing longwave radiation [OLR]).

6.1 Introduction

"Remote sensing" is defined as acquisition of information about the condition and/or the state of a target by a sensor that is not in direct physical contact with it (Asrar, 1989). The spaceborne sensors currently used for Earth observations are divided into two groups: active and passive systems. Only the fundamental basis for passive systems observing wavelengths from optical to thermal-infrared is described here. For information on microwave sensors both active and passive, please refer to Ulaby et al. (1981).

6.1.1 Fundamental basis for measurement by spaceborne optical and thermal sensors

a). Basic quantities

All of the information received by a satellite sensor about the Earth and its atmosphere comes in the form of electromagnetic radiation. It is necessary to understand the mechanisms by which this radiation is generated and how it interacts with the atmosphere (Kidder and Haar, 1995). Electromagnetic radiation consists of alternating electric and magnetic fields. The electric field vector is perpendicular to the magnetic field vector, and the direction of propagation is perpendicular to both.

Radiation is often specified by its wavelength, which is the distance between crests of the electric or magnetic field. A broad range of wavelengths from the ultraviolet (ranged from 0.1 micrometer) to the microwave (more than 1 millimeter) is useful for the observation of the Earth, including the atmosphere. A fundamental property of electromagnetic radiation is that it can transport energy. The basic unit of radiant energy is the joule. Radiant flux is radiant energy per unit of time, measured in watts [W], the same as electric power. Radiant flux density is radiant flux crossing a unit area (W m^{-2}). This is generally referred to simply as, radiation (see Chapter 1 for the radiation budget on the surface).

In nature, radiation is a function of direction. The directional dependence is taken into account by employing the solid angle. Radiant flux density per unit solid angle is known as, radiance (W m^{-2} sr^{-1}). In addition, the most fundamental radiation unit for satellite measurement is monochromatic radiance, which is the energy per unit time per unit wavelength per unit solid angle crossing a unit area perpendicular to the beam. The aircraft- or satellite-borne instrument, the radiometer, has a detector of a certain area (field of view [FOV]), whose output is proportional to the energy per unit time striking it.

b). Blackbody radiation

All material above the temperature of absolute zero emits radiation. If one looks at two different kinds of material, both at the same temperature, one finds that the radiation being emitted by them is different. Such a characteristic led physicists to invent the perfect emitter, known as a blackbody, which emits the maximum amount of radiation at each wavelength. Even though some materials come very close to being perfect emitters in some wavelengths, there are no natural materials that are a perfect blackbody. Fortunately, however, the radiation inside a cavity whose walls are think enough to prevent any radiation from passing directly through them can be regarded to be radiation that would be emitted by a blackbody. There is an empirical relationship between blackbody radiation and the two variables on which it depends: temperature and wavelength (Kidder and Haar, 1995).

c). The Planck Function

Max Planck, physicist (1858-1947), made the revolutionary assumption that an oscillating atom in the wall of a cavity can exchange energy with the radiation field inside a cavity only in discrete bundles called quanta given by $\Delta E = h\nu$, where ν is frequency and h is what is known as Planck's constant (6.6260744×10^{-34} [J s]). With the above assumption, Planck showed that the radiance emitted by a blackbody is as follows:

$$B_\lambda(T) = \frac{2hc^2\lambda^{-5}}{\exp\left(\frac{hc}{\lambda kT}\right)-1} \qquad (6.1)$$

where k is Boltzmann's constant (1.380658×10^{-23} [J K^{-1}]), λ is the wavelength, c is the speed of light (2.99792458×10^{8} [m s^{-1}]), and T is the absolute temperature. Equation (6.1) is known as the Planck function. The Planck function is more conveniently written as

$$B_\lambda(T) = \frac{c_1\lambda^{-5}}{\exp\left(\frac{c_2}{\lambda T}\right)-1} \qquad (6.2)$$

where c_1 and c_2 are the first and second radiation constants ($c_1 = 1.1910439 \times 10^{-16}$ [W m^{-2} sr^{-1}], $c_2 = 1.438769 \times 10^{-2}$ [m K]).

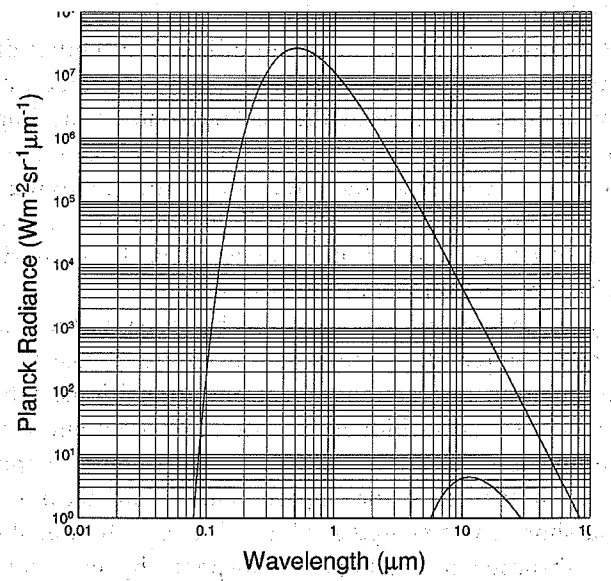

Figure 6.1 The Planck function. Planck radiance versus wavelength for the blackbody temperature of 5800 K (corresponding to Sun) and of 250 K (corresponding to Earth). Lines are estimated from equation (6.2).

Since the radiance from a blackbody is independent of direction, the radiant exitance from a blackbody is simply integrated as all angles πB_λ. Figure 6.1 shows the Planck function for the blackbodies of the temperature 5800 K (Sun) and of 250 K (radiometric equivalent temperature of the Earth), respectively. There are two important points in Figure 6.1. First, $B_\lambda(T)$ is monotonically increasing as a function of T and second, $B_\lambda(T)$ has a single maximum at wavelength (for a blackbody temperature of 5800K, around 0.4 micrometers and around 10 micrometers for 250K) that may be determined by setting the partial derivative of $B_\lambda(T)$ (known as Wein's displacement law; not shown here).

Another important aspect of the Planck function is its integral wavelength. The total radiant exitance from a blackbody is

$$M_{bb} = \int_0^\infty \pi B_\lambda(T) d_\lambda = \frac{\pi^5}{15} c_1 C_2^{-4} T^4 = \sigma T^4 \qquad (6.3)$$

where σ is called the Stefan-Boltzmann constant (5.67051×10^{-8} W m^{-2} K^{-4}). Equation (6.3) is called the Stefan-Boltmann law (Kidder and Haar, 1995).

d). Atmospheric gases absorptions

If the effect of polarization is not taken into account, four processes can change radiance as it passes through a volume:

a. Radiation from the beam can be absorbed by the material.
b. Radiation can be emitted by the material.
c. Radiation can be scattered out of beam into other directions.
d. Radiation from other directions can be scattered into the beam.

When considering radiance at the surface, one of the important components mentioned above is absorption in the atmosphere by gases. It should be noted that scattering does not consume radiance, only the changing its direction. For example, the Rayleigh scattering of the light from the sun, which is the reason why the sky looks blue (0.4-0.5 micrometers), is the scattering process of light from the sun by the components of the atmosphere.

The study of absorption and emission by gases is the field of spectroscopy. Radiation can interact with atmospheric gases in five ways: ionization-dissociation interactions, electronic transitions, vibrational transitions, rotational transitions, and forbidden transitions (Kidder and Haar, 1995).

In ionization-dissociation interactions, an electron is stripped from an atom or molecule, or a molecule is torn apart. These interactions occur primarily at ultraviolet and shorter wavelengths. Most of solar radiation shorter than about 0.1 micrometer is absorbed in the upper atmosphere by ionizing atmospheric gases, particularly oxygen. Short wavelengths within a range between 0.1 and 0.3 micrometers are absorbed by oxygen and ozone (O_3). Such interactions in the atmosphere make solar radiation at the surface relatively free from ultraviolet light from the sun. In electronic transitions, an orbital election jumps between quantized energy levels. In vibrational transitions, a molecule changes vibrational

energy states. In rotational transitions, a molecule changes rotational energy states. Finally, forbidden transitions are those transitions which are not caused by the interaction between the electric field of radiation and the electric dipole moment of a molecule. Some forbidden transitions, in fact, occur. Such transitions depend on the number of molecules, the characteristics of each molecule in the atmosphere, and so on. In the Earth's atmosphere, whose components are mainly N_2, O_2, CO_2 and H_2O [vapor, liquid, solid], absorption bands by the above processes concentrate on infrared wavelengths . Thus the atmosphere is relatively clear to the solar radiation (see Figure 6.1) but not a clear pathway for the Earth's radiation (Figure 6.2). This is what fills the gap of the radiometric equivalent temperature and actual temperature of the Earth. This important function of the atmosphere is well known as the "green house effect."

As shown in Figure 6.2, visible wavelength (0.4 to 0.7 micrometer) is close to 1 in transmittance. In combination with the basics such as the center wavelength of solar radiation (Figure 6.1), our eyes are optimized for wavelengths that reach the maximum radiance with the least absorption by the atmosphere. Indeed, observed short-wave spectral radiance at the land surface (Figure 6.3) has a peak of around 0.45 in micrometers. In addition, several absorption bands by molecules (listed in Figure 6.2) show a rapid decrease in some spectral radiances. Fortunately, to take care of the infrared, the peak wavelengths of Earth radiation (centered in 11 micrometers, Figure 6.1), have relatively high transmittances (i.e., relatively do not become trapped by the atmosphere). This is what is known as the "window of the atmosphere" for this wavelength.

Table 6.1 shows the specifications of major spaceborne radiometers for the purpose of the Earth observation. As described before, observed wavelengths adopted by sensors are optimized to see the surface and/or make efforts to avoid the interference of the atmosphere (but are not completely free from atmospheric effects).

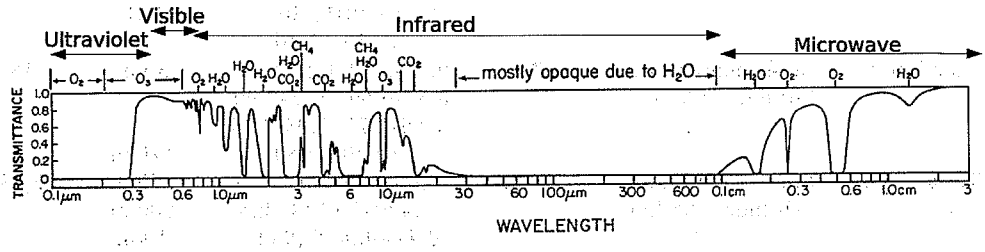

Figure 6.2 Spectrum of the Earth's atmosphere (after Kidder and Harr, 1995, but slightly modified. Original figure was from Goody and Yung, 1989).

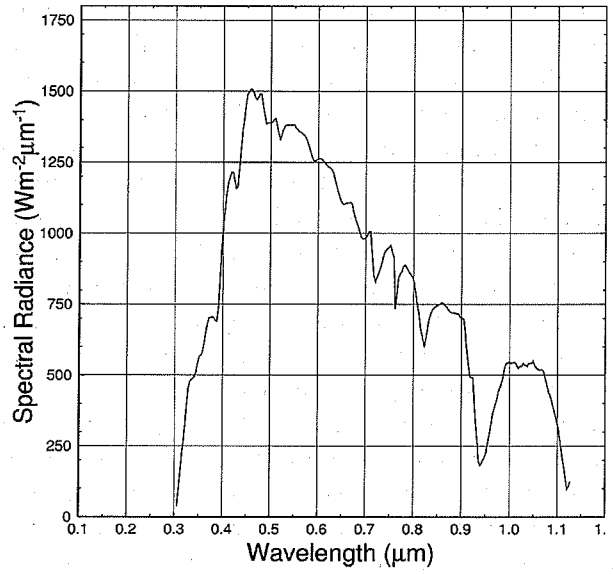

Figure 6.3 Observed downward spectral radiance for short-wave (solar) radiation. Measured by a hyper-spectral radiometer (MS-700, EKO, Japan) installed at Changwu experimental field, located on Loess Plateau, China. Captured time was 12:00 BST, 1 May, 2005. Several absorption bands byO_3, H_2O, O_2, were also observed (please compare with Figure 6.2).

Table 6.1 Specifications of major spaceborne optical & thermal sensors (radiometers)

Platforms	Orbit Information	Sensor Name	Channels (micro-m)	Spatial Resolution	Swath
NOAA Series(-14)	Sun-synchronous, Altitude: 833 km or 870 km,	AVHRR or AVHRR/2	0.58-68, 0.725-1.10, 3.55-3.93, 10.30-11.30, 11.50-12.50	1.1km at nadir	2,700 km
(15-18)	-	AVHRR/3	0.58-0.68, 0.725-1.0, (1.58-1.61 or 3.55-3.93) 10.30-11.30, 11.50-12.40	**1.1km at nadir**	2,700 km
Landsat-5	Sun-synchronous, Altitude: 705 km	TM	0.45-0.52, 0.52-0.60, 0.63-0.69, 0.75-0.90, 1.55-1.75, 2.08-2.35 10.40-12.50	30 m 120 m	185 km
Terra, Aqua	Sun-synchronous, Altitude: 705 km	MODIS	0.659-0.875 (2 ch.) 0.470-2.13 (4 ch.) 0.414-0.865 (9 ch.) 0.905-0.940 (3 ch.) 3.75-14.24 (17 ch.)	250 m 500 m 1 km 1 km 1 km	2,330 km

6.1.2 Basics of optics for monitoring vegetation activity

As described in 6.1.1, solar radiation, i.e., short-wave radiation, has a peak in visible wavelengths. These wavelengths are also suitable for the growth of plants. In the field of plant physiology, visible wavelengths are defined as PAR (photosynthetically active radiation; but slightly different wavelengths are used by some researchers). To be more specific, chlorophyll a and b in a living leaf have absorption peaks around blue and red wavelengths. In addition, there are far-red light absorbing and red light absorbing forms of phytochrome, while riboflavin mainly absorbs blue wavelength light (Jones, 1992). As these functions are combined, the human eye detects living leaves as green. On the other hand, beams of light longer than visible wavelengths, defined as near infrared (near-IR) which cannot be seen by the human eye, are also not suitable for plants as one of driving forces for photosynthesis. Thus, plant leaves reflect well in the wavelength of near-IR to avoid the leaf temperature rising. Figure 6.4 shows examples of observed spectral reflectance of winter wheat on different days. It should be noted that the results in Figure 6.4 are not essentially the same as those in previous studies derived from field-spec^{R} type measurements. These results are governed by integrated spectral radiance in all direction by radiometer (thus no units in sr^{-1} in Figure 6.3), however, as most of the field measurements are variables of hyper-spectral reflectance, which are based on a fiber type with a narrow FOV which takes into account the effect of direction and of FOV.

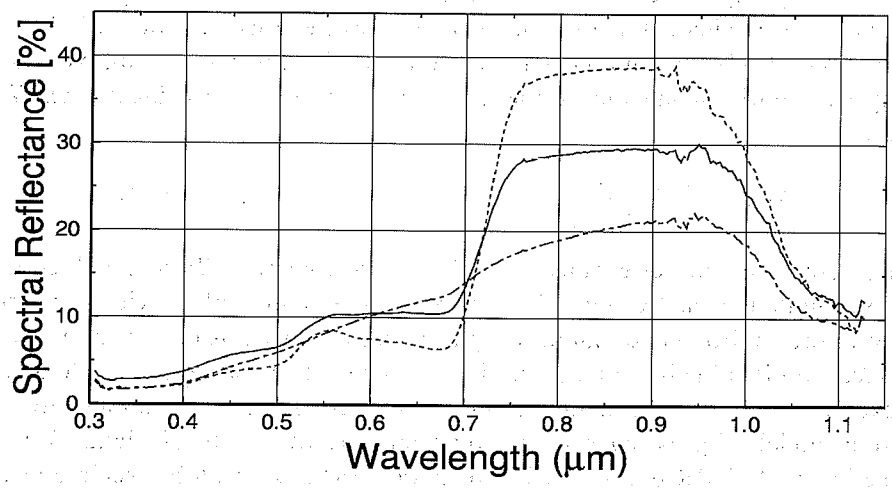

Figure 6.4 Examples of the spectral reflectance observed by two spectral-radiometers (downward & upward looking), same location and equipments as that of Figure 6.3 over winter wheat. The solid line represents the reflectance on April 1, 2005 (growing season), the dashed line shows that of mature season (May 1, 2005), and the dash-dots line represents the day before harvesting the wheat (June 19, 2005).

Features of spectral reflectance, as displayed in Figure. 6.4, vary with the conditions of the target vegetation such as thickness, leaf age, water content, surface morphology, orientation, and so on. Briefly, spectral reflectance in near-IR is proportional to the number of leaves, or in other words, the number of "effective reflectors" within a target. However, visible wavelength is absorbed well by the leaves. From the point of view of the seasonal march, i.e., in terms of phenology, the values of spectral reflectance in near-IR reach a maximum in the mature season (a dashed line in Figure 6.4). In addition, a peak in green (0.55 micrometers) wavelength and a depression in red (0.65 micrometers) were observed. Just before the harvesting the wheat (June 19, 2005, the dash-dots line), the wheat plant had already stopped the activity of photosynthesis, thus spectral reflectance of that day represented the state of dead wheat (no appearance of definite "red edge", and a rapid increase of the spectral reflectance around 0.7 micrometers). Spectral reflectance of the plants, or actually the canopy (essentially satellite sensors observe the status of the canopy, not individual leaves and plants), represents the status of vegetation activity.

Analysis of spectral reflectance over surfaces is not limited to vegetated surfaces. Analysis of surfaces such as soil as a background factor, materials from the field of geology, and so on, has been conducted on the basis of in-situ measurements. It is currently not possible for satellites observations to cover the whole wavelength with fine spectral resolution (see Table 6.1). To explore and/or fill the gaps, some indices which represent the status of vegetation activity have been used as proxy indicators since the mid-70's. In the initial stage to develop the index, researchers focused on visible wavelengths. In the 1980's, the combination of visible and near-IR became useful for monitoring vegetation activity by satellite using the normalized vegetation difference index (*NDVI*) as follows:

$$NDVI = \frac{\rho_{NIR} - \rho_{red}}{\rho_{NIR} + \rho_{red}} \tag{6.4}$$

where ρ represents the reflectance of each band or channel, *NIR* and *red* represent the wavelength as near-IR and red or visible, respectively. *NDVI* widely has been applied to the environmental monitoring of terrestrial systems on the spatial scales from local to global (Figure 6.5), and in time scales from seasonal to interannual. For example, on the continental scale, White et al. (1997) demonstrated the detection model of growing season length and the life cycle of plants from the time series of AVHRR-derived *NDVI* over the USA. On a global scale and over long-term in time (ten years), Myneni et al. (1997) found the increasing trends at high latitude zones maybe associated with global warming (more detail in studies using vegetation indices will be described in Chapter 7).

Several factors have influence on the vegetation indices (a lot of vegetation indices have been developed and published), which may cause them to not represent actual vegetation status or activity. These kinds of noise or additional information are listed below.

- Angle dependency both in incoming radiation (represented as solar angles) and view angle of the sensor
  Such effects are known as the bidirectional reflectance distribution function (BRDF). Some researchers are focusing on the BRDF both for the purpose of angle correction and its usage to produce additional information from optical sensors.
- Background effect
  Satellite sensors do not only detect the reflected light from the vegetation, but also the "background reflected" light such as from soil or understories, etc. Some vegetation indices such as *SAVI* (soil adjusted vegetation index; Huete, 1988) account for the effect of the background based on the analysis of the soil line.
- Atmospheric effects
  Even though the atmosphere is relatively clear in the wavelengths of visible and near-IR in comparison to other wavelengths (see Figure 6.2), atmospheric correction is required for better estimation of vegetation indices or more accurate monitoring of the terrestrial environment. In addition, aerosols (including biomass burning) and dust flows influence the shorter wavelengths in visible light. Some researchers are developing indices relatively resistant to aerosol interference, including that on the mid-IR channel.

These should all be kept in mind when dealing with the dataset of vegetation indices.

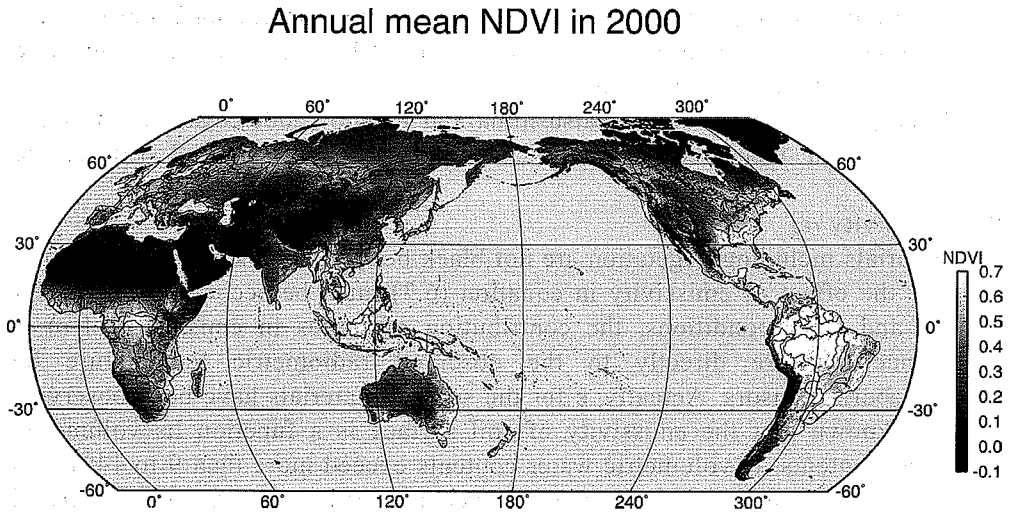

Figure 6.5 Global distribution of annual mean *NDVI* derived from pathfinder AVHRR land (PAL; Price and Goward, 1996) in 2000. Original spatial resolution is 8km both in latitude and longitude (original dataset coordinated as Goode Projection), but re-sampling into 0.1 degrees both in latitude and longitude has been conducted.

6.1.3 Basics of thermal infrared channels

Thanks to the window of the atmosphere, satellites can also observe radiometric temperature. However, the radiometric temperature of each thermal channel is not directly connected to the surface temperature. Several factors (mainly based on measurement physics) influence the estimation of surface temperatures from the radiometric temperature(s) derived from satellite observation (based on Seguin et al., 1999; though modified). These factors are as follows.

- Atmospheric effects

  Easily visualized in Figure 6.2, despite the window of the atmosphere phenomena, contamination by components of the atmosphere affect detected signals by satellites. Several algorithms or packages for atmospheric correction of targeted wavelengths, which can optimize the operational radiometer, such as AVHRR, have been developed. Additionally, split window techniques described later have also been developed.

- View angle dependencies

  Infrared radiometric temperatures observed by spaceborne sensors vary with view-angle, particularly over vegetated surfaces. Vegetated surfaces have a three dimensional structure such as that of forests (trees and understory) and even crop fields (consisting of plants and underlying soil). In general, radiometric temperatures at nadir seem higher than actual surface temperatures for sensible heat flux (aerodynamic temperature; expressed as *Ts* in the bulk formula for sensible heat flux in Chapter 1). This is due to the contribution of the radiometric temperature from the soil surface. Matsushima and Kondo (2000) demonstrated correction methods including a sensor view angle correction proposed by Troufleau et al. (1997) to estimate the sensible heat flux over the paddy fields.

  After the corrections from Matsushima and Kondo (2000), estimation errors with in-situ measured radiometric temperature were around 1.0 degree Celsius.

- Emissivity *(ε)*

  Materials including vegetation are not black body (i.e., ε is not equal to one), thus the effect of emissivity in equation (6.3) must be accounted for. Under dry and clear conditions, the contribution of losses in emissivity (1-ε) is connected more directly to the observed radiometric temperature by spaceborne sensors. Actually, ε for the several materials have been observed. It is known that the emissivity of soil surface is a function its volumetric water contents. If volumetric water contents exceed more than 9 to 14%, ε is close to that of over open water (Matsushima et al., 2003). Over vegetated surfaces, ε is larger for a canopy than that for a leaf. For example, ε of a leaf is about 0.95, but for a canopy, ε ranges from 0.98 to 0.99. In addition, emissivity is also dependent on the view angle. Until recently, the combination of emissivity and view angle of satellites has imposed complex functions on the estimation of surface temperatures.

There are additional problems in the estimation methods for heat fluxes based on thermal-IR remote sensing as described in Matsushima et al. (2003). To estimate surface temperatures more accurately, atmospheric information such as the vertical profiles of air temperature, water vapor and other absorption gases that have influence on the wavelength of spaceborne radiometer will be required for the atmospheric correction.

Otherwise, split window techniques can be applied to small differences of absorption by water vapor in the atmosphere over two (or more) narrow wavelengths. For example, AVHRR has two thermal-IR channels (see Table 6.1), the differences of radiometric temperature between thermal-IR at 10 micrometers and that at 11 micrometers are proportional to the amount of water vapor. Because, in the 10 to 13-micrometer window, aerosol scattering may be neglected except under hazy conditions, and clouds render this treatment inapplicable. The dominant effect results from absorption and reemission of radiation by water vapor (Price, 1984). Application of several split window technique was conducted to estimate surface temperatures without vertical profiling of the atmosphere. One of widely applied equations, Price's equation for AVHRR, is as follows (Price, 1984):

$$Ts = Tbb_{ch4[10.5]} + 3.3\,(Tbb_{ch4[10.5]} - Tbb_{ch5[11.5]}) \qquad (6.5)$$

Where Tbb is the radiometric temperature for each observed channel (wavelength), ch4 and ch5 are channels 4 and 5 in AVHRR, respectively. It should be noted that the present situation with the use of NOAA-AVHRR leads to an overall precision on the order of 2 to 3 degrees Kelvin in the derivation of Ts (Seguin et al., 1999). This is partly due to the errors related to surface emissivity and atmospheric correction procedures as mentioned above. Thus surface temperatures based on the split window technique, particularly those obtained from AVHRR, represent a kind of proxy indicator of thermal information on the surface, rather than accurate, "real" surface temperatures.

6.2 Combination usage of vegetation indices (VIs) and surface temperature (Ts) space

Before describing the combination usage of VIs and Ts, in general, satellite images need to undergo several procedures in addition to the atmospheric correction mentioned before. They are as follows.

- Radiometric correction or conversion
  Initially, sensors detect a signal as an analog beam, within a spaceborne instrument and the received signal is converted to digital form. Bit resolution depends on the specifications of the sensors and transmission systems. For example, for TM, the bit resolution is 8-bit (i.e., ranged from 0 to 255), while for AVHRR it is 10-bit (0 to 1024). Conversion or correction from digital data into physical variables (radiance or reflectance) is called as "radiometric correction." For AVHRR, pre-flight calibration was conducted, results are based on the calibration table (for more detail, see Kidwell, 1997).
- Geometric correction
  Geometric correction is defined as the correction from an original orbital image into a targeted, geographical coordination system (e.g., UTM projection, latitude-longitude perpendicular coordination). To conduct geometric correction, several methods are applied both manually and automatically. Manual correction is based on ground control points (GCPs) selected by eye, with targeted maps or images. After the selection of GCPs, conversion functions are determined. Automatic correction is mainly based on the orbital information of the platform or auto-detection algorithms of GCPs (mainly for the detection of coastlines).

Figure 6.6 shows an example of an AVHRR channel 2 image already corrected both radiometrically and geometrically as received with corrected products released by CEReS.

Recently, the data format of satellite dataset is based on, and distributed in the Hierarchical Data Format (HDF). Examples are MODIS and ETM+ boarded on Landsat 7.

Figure 6.7 shows the images of *NDVI* (left) and surface temperature (Ts) (right) for the same snapshot as Figure 6.6. When comparing the two images, several features are observed. First, high *NDVI* areas correspond to low Ts (and the opposite is also true). For example Northeast China has a high Ts, but significant *NDVI* values do not appear. Second, images of *NDVI* and Ts are NOT mirror sets. This is one reason motivating the development of the combined usage of VIs and Ts space.

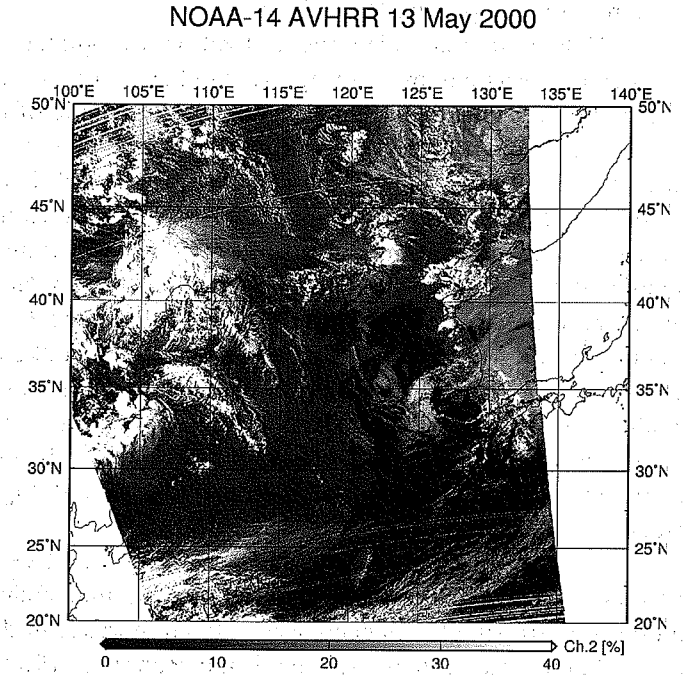

Figure 6.6 A NOAA-14 AVHRR channel 2 (near-IR) image received at CEReS, Chiba University, Japan, on May 13, 2000.

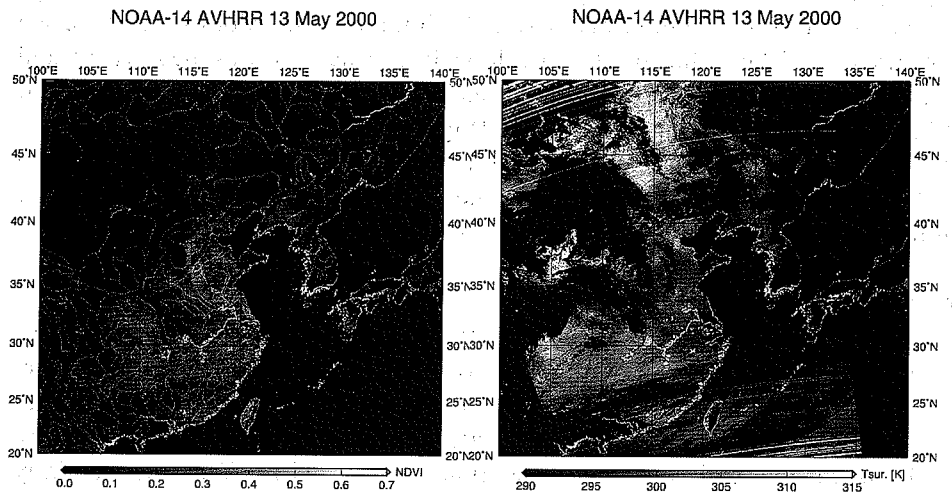

Figure 6.7 Images of *NDVI* (left) and surface temperature (right). Base image is same as that of Figure 6.6.

6.2.1 Simple principle for interpreting VIs – Ts space

Since the mid-1980's, to maximize the utilization of optical and thermal sensors for terrestrial ecosystem monitoring, researchers have focused on the methodologies to combine VIs and Ts. Sampling taken of a couple of the pixels of VIs and Ts for an area and plotted as a scatter diagram usually resulted in distributions like Figure 6.8. This manner of pixels of VIs and Ts is defined here as VI-Ts space. It should be noted that, the name of methodologies using VIs-Ts space, is not fixed. Several definitions have appeared in past studies (Ts-*NDVI* curve; in Nemani and Running, 1989; Ts/*NDVI* relationship; in Nemani et al., 1993; the temperature-vegetation index scatterplot; in Gillies and Carlson, 1995; temperature-vegetation index (TVX) (contextual) approach; Prihodko and Goward, 1997; Goward et al., 2002; Ts/*NDVI* space and TVX method; in Sandholt et al., 2002; VI-Ts method; Nishida et al., 2003a, however in Nishida et al., 2003b, it was described as the vegetation index-surface temperature (VI-Ts) approach). Thus some confusion has arisen in the naming of methodologies for the combination usage of VIs and Ts.

Initially, Goward et al. (1985) demonstrated a strong negative relationship between VIs and Ts as mentioned before (Figure 6.7). The underlying principles and background physics are simple. Ts decreases with an increase in the density of vegetation through latent heat transfer (Nemani and Running, 1989). When the surface condition became drier, highly vegetated areas (pixels) maintain transpiration (thus no significant increasing in Ts appears) however poorly vegetated locations are sensible in Ts due to the shortage of evaporative water.

Applications and/or investigations based on VIs-Ts space are divided into three groups, but mainly two categories: The former is focused on the envelope line (sometimes referred to in terms of slope) within a scatter plot of VIs-Ts space (Figure 6.8 left). The value of the envelope line usually forms negatively and becomes steeper under dry surface conditions. The latter focuses on the manner of plotted pixel members within VIs-Ts space (Figure 6.8 right).

According to an explanation of Sandholt et al. (2002) for interpretation based on findings in literature, the following mechanisms were suggested as those determining the location of a pixel in the VIs-Ts space.

- Fractional vegetation cover
  The fractional vegetation cover can be related to vegetation indices, through a simple, yet not necessarily linear transformation. Likewise, fractional vegetation cover influences the amount of bare soil and vegetation visible to a sensor and differences in radiometric temperature between the soil and the vegetation canopy will affect the spatially integrated Ts.

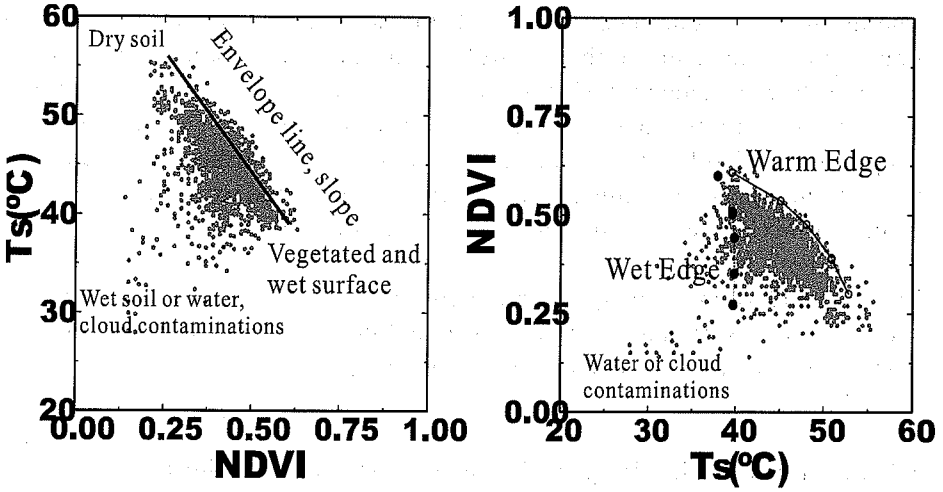

Figure 6.8 Schematic illustrations of scatter plots of *NDVI* with surface temperature (Ts). Applications using vegetation indices and surface temperature space, are divided into two methodologies. One focuses on the envelope line (usually referred to as "slope," left), the value of the slope becomes steeper under the dry conditions. The other focuses on the distributions of the pixels themselves, which sometimes define the "edges" (defined here as "warm edge", similar to slope in the right, and wet edge; left). Dotted pixels are raw data within a window size of 50 pixels and 50 lines (i.e., 2500 samples).

- Evapotranspiration
  Evapotranspiration can largely control the surface temperature through the energy balance of the surface. The lower the evapotranspiration, the greater the energy available for sensible heating of the surface. Stomatal resistance to transpiration is a key factor, which is partly controlled by soil moisture availability or its status.
- Thermal properties of the surface
  Heat capacity and conductivity, and thus the thermal inertia, influence Ts for of partly vegetated surfaces. These thermal properties are a function of the soil type, and change with surface soil moisture.
- Net radiation
  The available energy incident at the surface affects Ts. The radiative control of surface temperature implies that areas with a lower net shortwave radiation balance (e.g., due to a high albedo) will have a lower temperature, all else being equal. Albedo is controlled by soil type, surface soil moisture and vegetation cover. Incident radiation also affects the stomatal resistance to transpiration, which factors into the partitioning of net radiation into sensible and latent heat.

- Atmospheric forcing and surface roughness

The ability to conduct heat away from the surface into the atmosphere is an important component in the control of surface temperature. In part, this explains how vegetated surfaces with higher roughness have lower surface temperatures (all else being equal) compared to bare soil. This influences the shape of the VIs-Ts space. Similarly, homogeneous surfaces with unlimited water supply may have higher surface temperatures than expected, due to poor turbulent mixing between the surface and the atmosphere.

At first, the underlying principle for the formation of the locations of pixels in VIs-Ts space seems simple, however in actuality, complex functions related to both the biosphere and atmosphere make them complex.

6.2.2 Applications of VIs –Ts space for the environmental monitoring.

a). Focus on the envelope line (slope)

One remarkable work, Nemani and Running (1989; hereafter referred to as NR89) tested the hypothesis that seasonal trends in the relationship between vegetation density (*NDVI* as proxy indicator) and surface temperature derived from a NOAA-AVHRR dataset can represent seasonal changes in canopy resistance of a conifer forest located in the Experimental Forest of the University of Montana, USA. Initially, they focused on the behavior of VIs-Ts space on the different observation dates. After that, NR89 detected the envelope line (in NR89, expressed as σ) from a time series of AVHRR images manually (the data was extracted in the dimension of a 20 by 25 pixel matrix enclosing the Experimental Forest). As a reference, canopy resistance as defined by the Penman-Monteith equation was calculated as an inverse estimation of the process ecosystem model of canopy CO_2 and H_2O exchange, FOREST-BGC (here updated as Biome-BGC), with forcing of the micrometeorological dataset at the Experimental Forest. NR89 shows a clear inverse relationship in the time series between the slope of VIs-Ts space (Figure 6.9, lower) and canopy resistance (Figure 6.9, upper). The results in NR89 demonstrated that the slope of VIs-Ts space represents an indicator of canopy resistance over a regional scale. In fact, the regression relationship between the simulated canopy resistance and the slope of VIs-Ts space was in good agreement with the determination coefficient, R^2, as 0.92.

After NR89, several researchers applied and developed the methodology of the slope of VIs-Ts space. Nemani et al. (1993) developed an auto-detection algorithm for the determination of slope in VIs-Ts space. In addition, Nemani et al. (1993) discussed the scale effect of window size which is proportional to the number of pixels used to determine the slope in VI-Ts space. Nemani et al. (1993) showed that the difference in slope ranged between captured pixels at 10×10 (i.e., 100 pixel members), 30×30 (900) and 50×50 (2500). In the case of mountainous regions, "two" slopes appear in a window size of 50 x 50 (Figure 5 in Nemani et al., 1993; not shown). Window size effect will be described later.

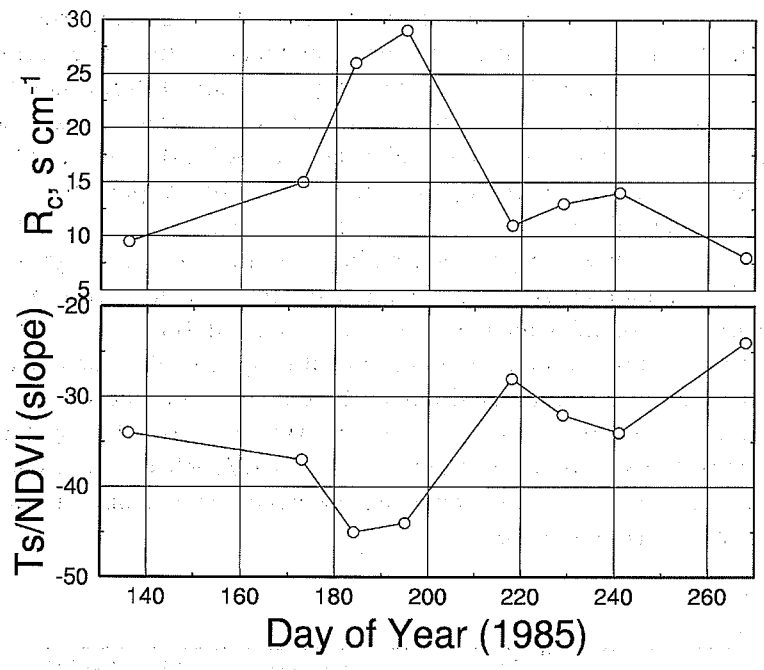

Figure 6.9 Relationship between simulated canopy resistance (Rc) at 14:30 local time from FOREST-BGC (currently updated as Biome-BGC; upper) and the slope of surface temperature and *NDVI* derived from NOAA AVHRR on eight days in 1985 (re-plotted from the Table 6.1 in Nemani and Running, 1989).

Anther aspect that applies to the slope of VIs-Ts space is the estimation of air temperature. Prihodko and Goward (1997) assumed and tested the hypothesis of that air temperature correlates with the radiometric temperature on the envelope line (slope) on "saturated, full canopy" *NDVI*. In the case of FIFE sites (First ISLSCP [International Satellite Land Surface Climatology Project] Field Experiment, carried out in northern Kansas, USA), full caopy *NDVI* was 0.86. Inferring the value of air temperature by the regression line expressed as Tair = a +b**NDVI*(here 0.86), where b is the value of the slope of VIs-Ts space, correlated well (r = 0.93) with a mean error of 2.92 degrees Celsius. However, a following study (Lakshmi et al., 2001) suggested that estimation of air temperature based on the slope of AVHRR was not good based on retrieved estimations of TOVS (TIROS Operational Vertical Sounder).

Applications into other climatological regions have been conducted. Kondoh et al. (1998) applied a modified auto-determination algorithm to the slope into the Huaihe river basin which is sandwiched between the Yellow river basin and the Yanzi river basin in China. They demonstrated that the time series of estimated slopes derived from the Global Area Coverage (GAC) version of AVHRR images

corresponded well with those of antecedent precipitation indices (API) based on in-situ operational observation network dataset. This feature supported the possibility of using the slope in relatively wet environments in temperate regions. Boegh et al. (1999) also focused on whether slopes obtained from satellites snapshots were a good indicator as to the status of water stress on sparsely vegetated surfaces over semi-arid regions (Sahel region, Africa). They used the slope as a diagnostic tool for inferring diurnal patterns of evapotranspiration based on the idea that if the surface condition becomes drier, a peak in evapotranspiration rate is observed pre-noon mainly due to water shortage. Over tropical regions, Hashimoto et al. (2001) demonstrated seasonal variations in slope and *NDVI* over Thailand which is characterized by definite wet and dry seasons under control of monsoon circulation in the atmosphere. They showed the date of "onset" (the date of changing environment) from several aspects (from the viewpoint of rainfall, based on the operational observation network, vegetation growth and surface wetness as revealed from time series AVHRR dataset). On the continental scale, Higuchi et al. (2006) revealed the behavior of slope in VIs-Ts space over monsoon Asia (Figure 6.10).

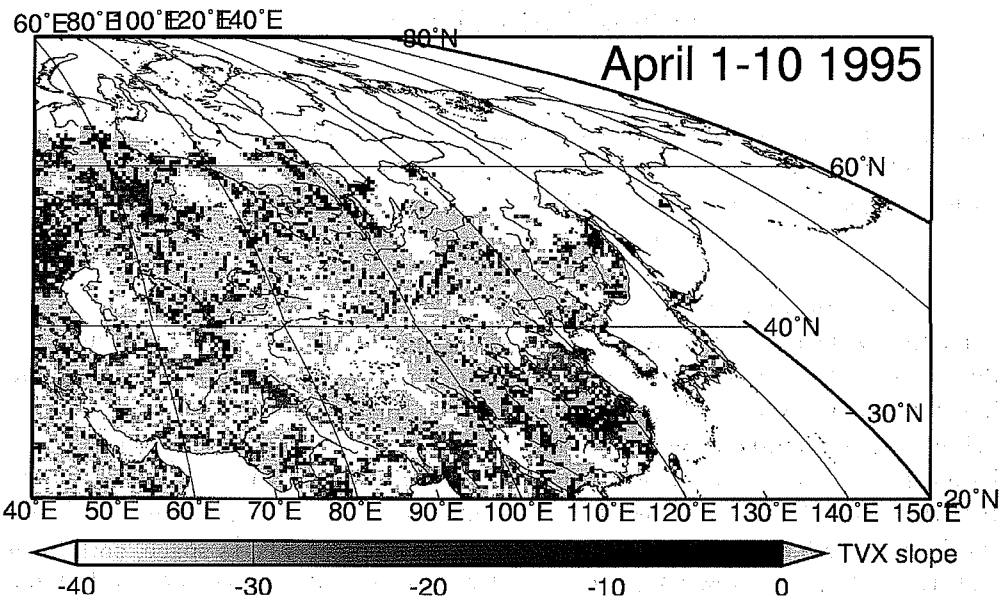

Figure 6.10 An example image of the slope of surface temperature and *NDVI* (TVX slope) over monsoon Asia. The dataset is based on a 10-day composite 1-km AVHRR dataset provided by USGS, composite period was April 1 to 10, 1995. High bright values indicate that the slope was steep (regarded as dry). Note that non-calculated areas due to snow cover at high latitudes or errors in calculation are also colored white (Higuchi et al., 2006, but modified).

One of the important advantages of applications using the slope in VIs-Ts space is the easy understanding of the results. However, several disadvantages are also recognized as in the following.

1) Spatial resolution: Spatial resolution of slope in VIs-Ts space is larger than the original pixel footprint which strongly influences how to determine the size of window.
2) Lack of base on the physical: The behavior of slope is sometimes validated quantitatively, but based on correlation or its relationship with other variables (e.g., model output [NR89], indices based on in-situ observations network).
3) Effect of window size (Nemani et al., 1993): Efficient window size, or the method of obtaining relatively heterogeneous samples without contamination from different climatological aspects (e.g., topography), is largely dependant on the environment of the land surface.

b). Focus on the distribution itself within a VIs-Ts space

Another way of application is to focus on the manner of pixel distribution itself. Based on the right side of Figure 6.8, the scatter plot of pixels in the VIs-Ts space (usually the axes are changed from a depiction of the "slope" in the VIs-Ts space as shown in the figure) forms a "warm edge." The warm edge, according to Gilles and Calson (1995), is presumed to exist when the warm side of the distribution in the scatter plot is both sharply defined and smoothly varying. Gilles and Calson (1995) focused on this warm edge by applying polynomial fitting as illustrated in the right side of Figure 6.8, and then tried to generate a reference table for the estimation algorithm of the surface soil water contents using the SVAT (soil-vegetation transfer) model.

Similarly, the concept of VITT (Vegetation-Index/Temperature Trapezoid; Moran et al., 1994) is another application to infer the evapotranspiration rate. This assumes that the warm edge is a line (in the Moran et al., 1994, assumed the edge as a line) of zero evaporation. In addition, the wet edge is a line of maximum evaporation plotted as in Figure 6.8. The four points to necessary to determine the "trapezoid" are ideally defined as: 1). Wet vegetation (top of the wet edge), 2). Wet soil (bottom of the wet edge), 3). Dry soil (bottom of the warm edge) and 4). Dry vegetation (top of the warm edge). After defining the locations of the four points and two edges, evapotranspiration rate of a given pixel within a trapezoid can be estimated by the distance between the two edges. Similar estimation methodologies have been applied for the estimation of the dryness (surface moisture status) using the analogy of a triangle (Temperature-Vegetation Dryness Index, TVDI; Sandholt et al., 2002), scale issues for surface fluxes (Brunsell and Gillies, 2003), and so on. In addition, as a prototype algorithm for the product of MODIS, Nishida et al. (2003a, b) developed an estimation algorithm for the

evaporative fraction (EF; defined as the ratio of latent heat flux to available energy, EF=LE/Qn) without referring to any in-situ measured dataset. In Nisida et al.'s algorithm, some parts of the modules were applied to the VIs-Ts space.

One of the advantages of applying the distribution of VIs-Ts space is that the estimated variables, such as evaporation rate and/or surface wetness, are equivalent in spatial scale with the original pixels.

c). Other applications

For the purpose of classification of land cover and use, VIs-Ts space applications are valid for improving the accuracy of classification (e.g., Lambin and Ehrlich, 1995; 1996). Nemani and Running (1997) focused on the seasonal transect of a location to classify land cover using two thresholds in *NDVI* (0.4) and Ts (35 degrees Celsius) according to the physical bases as follows:

- Ts (35 degrees Celsius)
  1). Ts over well-watered, dense canopies does not exceed 32 degrees Celsius under a wide range of net radiation conditions. 2). No short-term water shortages exceed the 32-degree Celsius Ts by more than 2 – 3 degrees Celsius. 3). Ts derived from satellites is a complex function of several uncertain measurements. 4). The theoretical threshold of Ts approaches 35 degree Celsius as an upper limit.
- NDVI (0.4)
  This is based on experimental results that suggest many vegetation types absorb greater than 75% of incident PAR.

Several land cover maps based on satellite observations are applied as the bases of VI-Ts space for decision trees.

Another combination usage of VIs and Ts is simple. The ratios of *NDVI* with Ts or Ts by *NDVI* are sometimes given the status of land-related indicators. For example, McVicar and Bierwirth (2001) monitored an abrupt drought over Papua New Guinea by using the integrated values of *Ts/NDVI* for composite AVHRR. Such a simple process greatly assists interpretation of the condition of land surfaces.

6.2.3 Limitations and/or uncertainties in the combination usage of VIs and Ts

Combination usage of VIs and Ts (VIs-Ts space) is based on the simple principle already described that states, higher NDVI correlates with lower Ts within a scatter plot of VIs-Ts space. However, recently, several researchers pointed out limitations in the usage of VIs-Ts space. Nishida et al. (2003b) noted that that higher NDVI correlated with increasing Ts (i.e. formed a positive slope in a scatter plot of VIs-Ts space) in areas where permafrost did not restrict vegetation growth. In addition, Goward et al. (2002) noted that ground temperatures (Tg) and canopy temperatures (Tc) were quite similar under cold conditions. This similarity in temperature results in poor estimation of slope

and/or warm edges within the VIs-Ts space during winter. Higuchi et al. (2006) presents a scatter diagram of VIs-Ts space over an arid region with oasis pixels. In such a case, the majority of land cover within the VIs-Ts space is desert, but in the determination of slope (or warm edge), the oasis pixels are the dominant factor due to wide distribution in *NDVI*. It should be keep in mind that such limitations and/or uncertainties still remain in VIs-Ts space applications.

6.3 Concluding remarks

Despite the limitations or uncertainties of integrated usage of VIs and Ts already mentioned, VIs and Ts continue to be widely applied in environmental monitoring, particularly for terrestrial dynamics. Combination usage of VIs and Ts also operates as the simplest "data fusion" of visible-near-IR and thermal-IR observation.

Several future prospects are anticipated for the maximum utilizations of huge satellite observation dataset. One is the movement to process as forcing data the initial conditions or parameterization of multi-spatial scale modeling, from GCM (General Circulation Model) to Cloud Resolving Model. Another is to couple and/or assimilate terra-dynamic models, such as the Dynamic Global Vegetation Model (DGVM; Chapter 10; Chapter 7, the connection of satellites data to the estimation of NPP), which is a natural way to use grid-physical converted (both well corrected in radiometric and geometric) satellite dataset (product). Still another way of maximum utilization is, perhaps, to improve skills in the technology to speculate on individual images. As mentioned in the beginning, satellite sensors detect real objects despite the difficulties and uncertainties in the correction processes or retrieving algorithms. In fact, new Earth observation satellites will be lunched and are in planning under an international umbrella, such as GEOSS (Global Earth Observation System of Systems). Indeed, output derived from satellites is becoming bigger and bigger. This means that despite the great progress achieved in computer technologies especially those in the fields of storage, processing time and archiving systems there will still need to be more in the future. We can easily image the day when the time required to check each image will be reduced. It must always be kept in mind that, sometimes a single image derived from satellite can play a crucial role in detecting changes in the terrestrial environment, such as that of a forest fire. Beyond the scope of this Chapter, it is necessity to pay attention the directions and/or future prospects of the satellites observation, because satellites detect what is real.

References

Asrar, G., Introduction, (1989), In "Theory and applications of optical remote sensing", edited by G, Asrar, pp, 1-13, Wiley, New York.

Boegh, E., Soegaard, H., Hanan, N., Kabat, P., and Lesch, L., (1999), A remote sensing study of the NDVI-Ts relationship and the transpiration from sparse vegetation in the Sahel base of high-resolution satellite data, Remote Sens, Environ., 69, 224-240.

Brunsell, N.A., and Gillies, R.R., (2003), Scale issues in land-atmosphere interactions: implications for remote sensing of the surface energy balance, Agric, For, Meteor., 117, 203-221.

Gillies, R.R., and Carlson, T.N., (1995), Thermal remote sensing of surface soil water content with partial vegetation cover for incorporation into climate model, J Appl, Meteor., 34, 745-756.

Goody, R.M., and Yung, Y.L., (1989), Atmospheric Radiation: Theoretical Basis, 2nd ed, Oxford University Press, Oxford and New York.

Goward, S.N., Cruickshanks, G.D., and Hope, A.S., (1985), Observed relation between thermal emission and reflected spectral radiance of a complex vegetated landscape, Remote Sens, Environ., 18, 137-146.

Goward, S.N., Xue, Y., and Czajkowski, K.P., (2002), Evaluating land surface moisture conditions from the remotely sensed temperature/vegetation index measurements: An exploration with the simplified simple biosphere model, Remote Sens, Environ., 79, 225-242.

Hashimoto, H., Suzuki, M., and Higuchi, A., (2001), Analysis of soil moisture and phenology in Thailand using NOAA/AVHRR, J, Japan Soc, Hydrol, & Water Resour., 14, 277-288. (in Japanese with English abstract)

Higuchi, A., Hiyama, T., Fukuta, Y., Suzuki, R., and Fukushima, Y., (2006), The behavior of a surface temperature/vegetation (TVX) matrix derived from 10-day composite AVHRR images over monsoon Asia, Hydrological Processes, (in press).

Huete, A.R., (1988), A soil-adjusted vegetation index, Remote Sens, Environ., 25, 295-309.

Kidder, S.Q., and Haar, T.H.V., (1995), Satellite meteorology; An introduction, Academic Press, San Diego, Calfornia, p, 466.

Jones, H.G., (1992), *Plants and microclimate, 2nd ed*, Cambridge University Press, New York, 428pp.

Kidwell, K., (1997), NOAA Polar Orbiter Data Users Guide, NOAA.

Kondoh, A., Higuchi, A., Kishi, S., Fukuzono, T., and Li, J., (1998), The use of multi-temporal NOAA/AVHRR data to monitor surface moisture status in Huaihe River Basin, Adv, Space Res., 22, 645-654.

Lakshmi, V., Czajkoowski, K., Dubayah R., and Susskind J., (2001), Land surface air temperature mapping using TOVS and AVHRR, Int, J, Remote Sens., 22, 643-662.

Lambin, E.F., and Ehrlich, D., (1995), Combining vegetation indices and surface

temperature for land-cover mapping at broad spatial scales, Int, J, Remote Sens., 16, 573-579.

Lambin, E, F., and Ehrlich, D., (1996), The temperature-vegetation index space for land cover and land-cover change analysis, Int, J, Remote Sens., 17, 463-487.

Matsushima, D., and Kondo, J., (2000), Estimating regional distribution of sensible heat flux over vegetation using satellite infrared temperature with view angle correction, J, Meteor, Soc, Japan, 78, 753-763.

Matsushima, D., Asanuma, J., Hiyama, T., and Tamagawa, I., (2003), Estimation methods for heat fluxes over vegetated surfaces based on thermal-infrared remote sensing combined with heat budget method, J, Japan Soc, Hydrol, & Water Resour., 16, 170-182. (in Japanese with English abstract)

McVicar, T.R., and Bierwirth, P.N., (2001), Rapidly assessing the 1997 drought in Papua New Guinea using composite AVHRR imagery, Int, J, Remote Sens, 22, 2109-2128.

Moran, M.S., Clarke, T.R., Inoue, Y., and Vidal, A., (1994), Estimating crop water deficit using the relation between surface-air temperature and spectral vegetation index, Remote Sens, Environ., 49, 246-263.

Myneni, R.B., Keeling, C.D., and Tucker, C.J., (1997), Asrar, G., and Nemani, R.R., Increased plant growth in the northern high latitudes from 1981 to 1991, Nature, 386, 698-702.

Nemani, R.R., and Running, S., (1989), Estimation of surface resistance to evapotranspiration from NDVI and thermal-IR AVHRR data, J, Appl, Meteor., 28, 276-284.

Nemani, R.R., Pierce, L., Running, S., and Goward, S., (1993), Developing satellite-derived estimates of surface moisture status, J, Appl, Meteor., 32, 548-557.

Nemani, R.R., and Running, S., (1997), Land cover characterization using multitemporal red, near-IR, and thermal-IR data from NOAA/AVHRR, Ecological Applications, 7, 79-90.

Nishida, K., Higuchi, A., Kondoh, A., and Matsuda, S., (2000), Remote sensing of land surface process based on spectral vegetation index and surface radiation temperature, J, Japan Soc, Hydrol, & Water Resour., 13, 304-312. (in Japanese with English abstract)

Nishida, K., Nemani, R., Running, S., and Glassy, J.M., (2003a), An operational remote sensing algorithm of land surface evaporation, J, Geophys, Res., 108, D9, 4270, doi:10.1029/2002JD002062.

Nishida, K., Nemani, R., Running, S., and Glassy, J.M., (2003b), Development of an evapotranspiration index from Aqua/MODIS for monitoring surface moisture status, IEEE Trans, Geos, Remote Sens., 41, 493-501.

Price, J.C., (1984), Land surface temperature measurements from the split window channels of the NOAA 7 Advanced Very High Resolution Radiometer, J, Geophys, Res., 89, D5, 7231-7237.

Price, S.D., and Goward, S.N., (1996), Evaluation of the NOAA/NASA pathfinder

AVHRR land data set for global primary production modeling, Int, J, Remote Sens., 17, 217-221.
Prihodko, L., and Goward, S.N., (1997), Estimation of air temperature from remotely sensed surface observations, Remote Sens, Environ., 60, 335-346.
Sandholt, I., Rasmussen, K., and Andersen, J., (2002), A simple interpretation of the surface temperature/vegetation index space for assessment of surface moisture status, Remote Sens, Environ., 79, 213-224.
Seguin, B., Becker, F., Phulpin, T., Gu, X.F., Guyot, G., Kerr, Y., King, C., Lagouarde, J.P., Ottlé, C., Stoll, M.P., Tabbagh, A., and Vidal, A., (1999), IRSUTE: A minisatellite project for land surface heat flux estimation from field to regional scale, Remote Sens, Environ., 68, 357-369.
Troufleau, D., Lhomme, J.P., Monteny, B., and Videl, A., (1997), Sensible heat flux and radiometric surface temperature over sparse Sahelian vegetation, I, An experimental analysis of the kB-1 parameter, J, Hydrol., 188-189, 815-838.
Ulaby, F.T., Moore, R.K., and Fung, A.K., (1981), Volume I: Microwave remote sensing fundamentals and radiometry, In the series of "Microwave remote sensing: Active and passive", Artech House, London, UK, p, 456.
White, M.A., Thornton, P.E., and Running, S.W., (1997), A continental phenology model for monitoring vegetation response to Interannual climatic variability, Global Biogeochemical Cycles, 11, 217-234.

Chapter 7

Observation of Global Vegetation Variations by Satellite Remote Sensing

Yasushi Yamaguchi
Graduate School of Environmental Studies,
Nagoya University, Nagoya 464-8601, Japan
Tel: +81-52-789-3017
Fax: +81-52-789-3017
e-mail: yasushi@nagoya-u.jp

7.1 Introduction

Global warming resulting from an increase in atmospheric CO_2 concentration is one of the most significant problems on the Earth recently. It is very important to understand the global carbon cycle in order to predict the future atmospheric CO_2 concentration that controls global warming. Terrestrial vegetation is an important carbon reserve in the global carbon cycle. Particularly, photosynthetic activity by vegetation, which fixes carbon as biomass in the biosphere, plays a key role in the global carbon cycle (Schimel et al., 1995).

Many attempts have been made to quantitatively estimate carbon uptake by terrestrial vegetation based upon precise ground measurements at selected flux sites around the world. However, it is difficult to know spatial distribution of carbon fluxes in regional to global scales by ground measurements. Satellite remote sensing is a powerful tool to monitor vegetation in local, regional, and global scales, and can extrapolate / compensate the ground measurements. Particularly multi-spectral remote sensing data are useful to assess terrestrial vegetation activities, and thus to estimate carbon fluxes.

This chapter explains fundamentals of multi-spectral remote sensing data analysis. A recent study on relationships between global vegetation variations and climate is shown as an example of utilizing a vegetation index, and is followed by estimation of terrestrial carbon fluxes by using remotely sensed data and a simple carbon flux model. Finally the author introduces Advanced Spaceborne Thermal Emission and Reflection Radiometer (ASTER) as an example of a high resolution remote sensor, which is useful for assessing local to regional vegetation.

7.2 Fundamentals of multi-spectral remote sensing data analysis

7.2.1 Color composite image

For discriminating and mapping surface types, we need techniques to visualize, enhance, and/or quantify the different spectral response patterns of surface materials. Many previous studies have proposed various approaches for this purpose by using remotely sensed multi-spectral data based upon the spectral signatures of surface materials. For instance, band ratios, principal component analysis (PCA), and multi-band classification are typical techniques. This chapter explains the fundamental concept of multi-spectral data analysis, and shows examples of discriminating surface materials. A variety of techniques have been developed for discriminating rock types, since minerals and rocks exhibit characteristic absorption features in the visible to near-infrared region.

A simple method to visualize different spectral response patterns is to generate a color composite image by assigining three spectral bands to three color primitives of blue, green, and red respectively. If the response of the three bands are equal, the resultant color is gray (between white to black). If there is an unequal response in the three bands, we can see color. For instance, we often use a false color composite that assigns data obtained in the visible green region to color primitive blue, visible red to green, and near-infrared to red. This color combination is similar to infrared color photography, in which vegetation appears red because of its high reflectance in the near-infrared region and low reflectance in the visible region due to chlorophyll absorptions. In a false color composite image, the areas of dense vegetation appear in reddish color as well. If you would like to express vegetation in green, you can use another color combination so called a natural color composite that assigns the visible green region to color primitive blue, visible red to red, and near-infrared to green. But please note that the greeninsh color of vegetation in this color combination is due to high reflectance in the near infrared region, and is not the same as the green color that human eyes are seeing.

7.2.2 Band ratios

Band ratios are the most widely employed and computationally simple method of data processing to evaluate multispectral data. Previous studies have described many ratio-based image processing techniques. For instance, a band ratio between the near infrared and visible red bands is useful for vegetation mapping as explained as Ratio Vegetation Index (RVI) in the section 7.3.2. For rock type discrimination, Rowan et al. [1974] employed Landsat MSS band ratios to enhance sensor response patterns and successfully demonstrated that a color composite image of the band ratios could delineate distribution of iron-oxide minerals associated with hydrothermally altered areas in Goldfield, Nevada, U.S.A.

A combination of band ratios and a color composite is a popular method to provide useful information for visual image interpretation. ASTER (see the chapter 7.6) has 14 spectral bands in the visible and near infrared (VNIR), short-wave infrared (SWIR), and thermal infrared (TIR) regions, and its multi-spectral data are widely used for surface mapping (Yamaguchi et al., 1998). For instance, a color composite image assigning the ASTER band ratios 4/7 to red, 7/6 to green and 6/7 to blue is useful to delineate hydrothermal alteration zones, which often contain minerals such as alunite, a sort of phyllosilicate minerals. Alunite has a spectral response of high in band 4, moderate in band 7, and low in band 6, so that the band ratios of 4/7 and 7/6 are high, while 6/7 is low. As a result, the areas containing alunite appear yellow in this color composite image. There are many other combinations of the ASTER band ratios. In this approach, it is important to know the spectral response pattern of a target mineral. By combining expected band responses and knowledge of additive color mixing, we can easily predict color of the target mineral on a color composite image. We can also design and propose a new combination of band ratios in this way.

7.2.3 Relative absorption-Band Depth (RBD)

A more advanced band ratio technique called Relative Absorption-Band Depth (RBD) was proposed by Crowley et al. (1989) for discriminating rock types that contain phyllosilicate and carbonate minerals. The numerator is the sum of the bands representing the shoulders (bands i and j), and the denominator is the band located nearest the absorption feature minimum (band k) as shown in Figure 7.1;

$$RBD = (band\ i + band\ j) / band\ k \qquad (7.1)$$

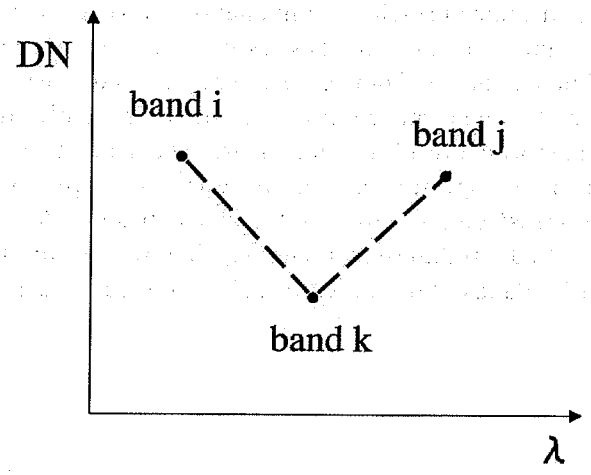

Figure 7.1 Concept of Relative Absorption-band Depth (RBD).

If there is an absorption in band k, RBD shows a larger value compared with a case where a response of band k is similar or larger than those of bands i and j. RBD was proposed to distinguish areas containing minerals with diagnostic absorption features. Below are three typical RBD examples for the ASTER SWIR bands.

$$Ca\text{-}CO_3\ RBD : (band\ 7 + band\ 9) / band\ 8 \quad (7.2)$$

$$Ca,\ Mg\text{-}CO_3\ (dolomite)\ RBD: (band\ 6 + band\ 8) / band\ 7 \quad (7.3)$$

$$Al\text{-}O\text{-}H\ RBD: (band\ 5 + band\ 7) / band\ 6 \quad (7.4)$$

The RBD technique was applied to the actual ASTER data, and was proven to be useful for lithologic mapping (Rowan et al., 2005).

7.2.4 Spectral Indices and Tasseled Cap Transformation

A spectral index is one of the techniques to quantify multi-spectral sensor response patterns, and is similar to principal component analysis (PCA) in the sense that both are orthogonal transformations of multi-spectral data. A fundamental difference between these two methods is that the spectral indices define the transform axes to represent specific spectral patterns of interest (Figure 7.2), while the PCA determines the transform axes mathematically to maximize variance of multi-spectral data. The PCA is useful to reduce dimensionality of multi-spectral data without significant information loss. Visual interpretation for discrimination and mapping of surface materials may be enhanced by a color composite image of major principal components. However, it is often difficult to know physical meanings of PCA images, as PCA results are scene dependent, i.e. transform coefficients change from scene to scene. In contrast, as spectral indices use pre-determined transform coefficients, it is possible to know physical meanings of a transformed result to some degrees (Crist and Cicone, 1984).

The concept of the spectral indices for assessing vegetation was initiated as the Tasseled Cap transformation by Kauth and Thomas (1976), who proposed four spectral indices called Brightness, Greenness, Yellowness, and Nonsuch using the four Landsat MSS bands. For more details on Greenness, please see the section 7.3.7.

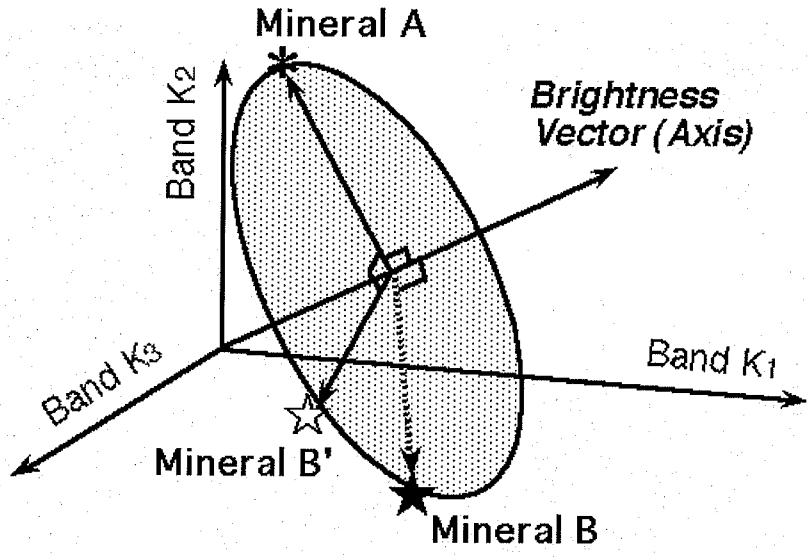

Figure 7.2 Concept of spectral indices proposed by *Yamaguchi and Naito* (2003). The second and higher order axes were determined so as to represent spectral responses of the minerals of interest in the plane orthogonal to the Brightness, the first transform axis.

In general, spectral indices in n-space can be defined as values measured by projecting data points onto axes with appropriate unit vector directions. It is a kind of orthogonal transformations, and the transform axes are determined to represent specific spectral patterns (Jackson, 1983). The m-th spectral index in n -space ($m \leq n$) for the i-th pixel ($_mY_i$) can be given by the following formula;

$$_mY_i = {}_mA_1 \times X_{1i} + {}_mA_2 \times X_{2i} + \ldots\ldots\ldots + {}_mA_n \times X_{ni} \qquad (7.5)$$

where n is the total number of the spectral bands, $_mA_n$ is the transform coefficient of n-th band data for the m-th spectral index, and X_{ni} is n-th band data of an i-th pixel. We can produce a spectral index image by simply applying the transform coefficients to a surface reflectance data set.

Figure 7.3 is examples of the spectral index images (Yamaguchi and Takeda, 2003). The bright areas show high spectral index values, and indicate relatively higher concentration of the specific mineral.

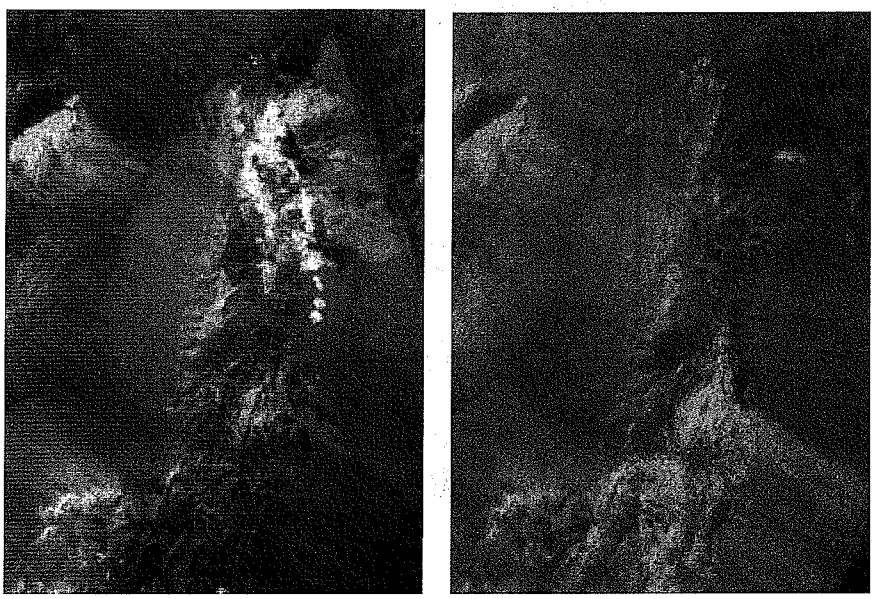

Figure 7.3 Examples of the spectral index images; Alunite index (left) and calcite index (right) images of Cuprite, Nevada (Yamaguchi and Takeda, 2003).

7.2.5 Spectral Angle Mapper (SAM)

Spectral Angle Mapper (SAM) technique is a tool that permits rapid mapping of the spectral similarity of image spectra to reference spectra. The reference spectra can be either laboratory or field spectra or extracted from the image. As shown in Figure 7.4, the algorithm determines the spectral similarity between two spectra by calculating the angle between the two spectra, treating them as vectors in a space with dimensionality equal to the number of bands (Kruse et al., 1993). The calculation consists of taking the arccosine of the dot product of the spectra as show in the equations (7.6) to (7.9).

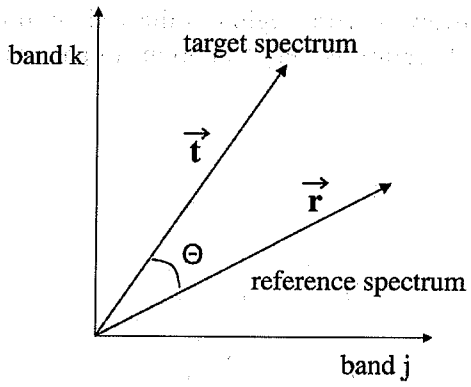

Figure 7.4 Concept of Spectral Angle Mapper (SAM).

$$\Theta = \cos^{-1}\left(\frac{\vec{t} \bullet \vec{r}}{\|\vec{t}\| \bullet \|\vec{r}\|}\right) \tag{7.6}$$

$$\vec{t} \bullet \vec{r} = \sum_{i=1}^{n} t_i r_i \tag{7.7}$$

$$\|\vec{t}\| = \sum_{i=1}^{n} t_i^2 \tag{7.8}$$

$$\|\vec{r}\| = \sum_{i=1}^{n} r_i^2 \tag{7.9}$$

7.3 Vegetation indices

7.3.1 Spectral properties of vegetation

Characteristic spectral features of green vegetation in the visible to near infrared (NIR) regions are useful to distinguish vegetation from the other materials, and are applicable to remote sensing (Figure7.5). In the visible region, chlorophyll-a has strong absorptions centered at 432nm and 663nm, and chlorophyll-b has absorptions at 467nm and 653nm, respectively. Chlorophyll utilizes solar radiation energy in these wavelenght regions for the phtosysnthesis activity. As a result, the reflectance of vegetation in the visible region is generally low. Green light in solar radiation is reflected relatively stronger than blue and red lights, so that plant leaves containing chrolophyll look greenish to human eyes.
In the NIR region, cellular structures of plant strongly reflect solar radiation. Thus, there is a steep slope between the red and NIR regions, and this slope is callled as the red edge. On the earth surface, only vegeatation has such an abrupt reflcetance

change in relatively narrow spectral region in the visible to near infrared regions. This diagnostic spectral feature is very important to analyze vegetation by using remotely sensed data.

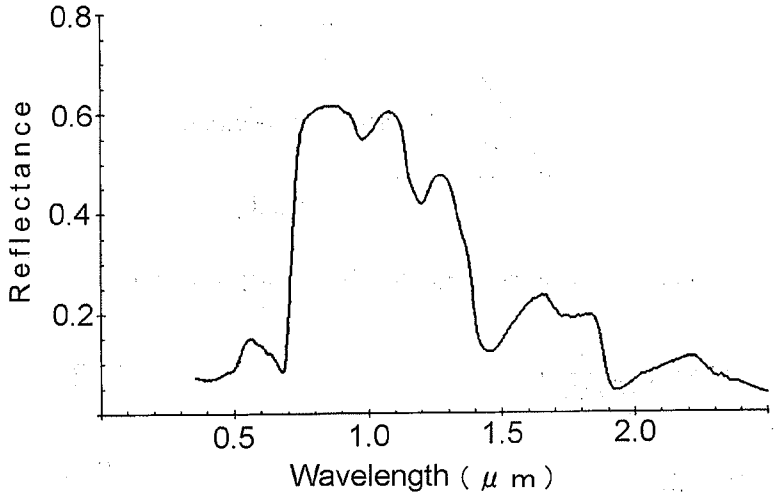

Figure 7.5 A typical reflectance spectrum of a green leaf.

7.3.2 Ratio Vegetation Index (RVI) and Difference Vegetation Index (DVI)

Ratio Vegetation Index (RVI) and Difference Vegetation Index (DVI) are simple indices to quantify the spectral contrast between the NIR and Red, and are widely used to assess vegetation. Higher RVI or DVI means denser vegetation. In general, RVI shows a better linearity to vegetation amount for sparse vegetation areas, while DVI is better for dense vegetation areas.

It is known that RVI is proportional to Leaf Area Index (LAI), which is a dimensionless parameter, and is defined as a total area of leaves (one side) in a unit area.

$$RVI = NIR / Red \tag{7.10}$$

$$DVI = NIR - Red \tag{7.11}$$

7.3.3 Perpendicular Vegetation Index (PVI)

Richardson and Wiegand (1977) developed a two-dimensional perpendicular vegetation index (PVI) using two bands of the Landsat MSS. PVI is similar to DVI, but measures a Euclidean distance from the soil line to be established by

picking up digital numbers (DNs) or reflectance of pure soil pixels, usually dark and bright ones (Figure 7.6). If the soil line coincides 1:1 line (NIR = Red) in the NIR and Red scatter plot, PVI is identical to DVI. If the soil line does not pass the origin, DVI may give an error in estimating vegetation amount. In this sense, PVI is better than DVI, if we can define the soil line properly. In the following equation, the coefficients a and b are the slope and intercept of the soil line.

$$PVI = \sin a \cdot (NIR - b) - \cos a \cdot Red \qquad (7.12)$$

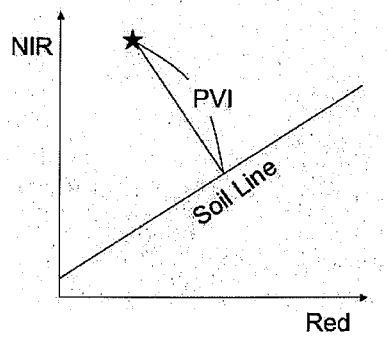

Figure 7.6 Concept of Perpendicular Vegetation Index (PVI).

7.3.4 Normalized Difference Vegetation Index (NDVI)

Normalized Difference Vegetation Index (NDVI) is the most popular and widely used vegetation index. It is calculated as a ratio between difference and sum of NIR and Red as shown below;

$$NDVI = (NIR - Red) / (NIR + Red) \qquad (7.13)$$

As the range of NDVI is fixed from -1 to +1, it is easy to use in various calculations. Usually NDVI saturates at about 0.7 for dense vegetation, and rarely exceeds it. The NDVI image around Nagoya City is shown in Figure 7.7. Please note that the urban areas show low NDVI values, while the northern and eastern mountainous areas exhibit high NDVI values.

Figure 7.7 NDVI image around Nagoya City generated from ASTER data of July 10, 2000.

NDVI seems to be a kind of difference vegetation indices, but is actually a ratio type vegetation index as shown in equation (7.14);

$$NDVI = (1 - NIR / Red) / (1 + NIR / Red)$$
$$= (1 - RVI) / (1 + RVI) \quad (7.14)$$

NOAA has edited global cloud free AVHRR mosaics on a weekly basis since April of 1982 (http://www.ncdc.noaa.gov/oa/ncdc.html), and is providing rescaled NDVI as Global Vegetation Index (GVI). This data product is very useful to study interannual variations of global vegetation, and is being widely used. Similar cloud free NDVI data is also available as a MODIS standard data product (http://daac.gsfc.nasa.gov/), e.g., 18 days or monthly NDVI composite image data as shown in Figure 7.18.

Figure 7.8 Global NDVI distribution. MODIS 18 days NDVI composite image.

7.3.5 Soil Adjusted Vegetation Index (SAVI) and its successors

Soil Adjusted Vegetation Index (SAVI) was developed by Huete (1988) in order to suppress the effect of reflectance change of soil background beneath vegetation cover. If the soil reflectance changes, NDVI also changes, since the equal-NDVI-value lines do not go through the origin. SAVI moves the origin to solve this problem. SAVI works particularly well for sparse vegetation.

$$SAVI = \{(NIR - Red) / (NIR + Red + L)\} \cdot (1 + L) \qquad (7.15)$$

where L is a correction factor in order to reduce soil influence. L=1 for very low vegetation densities, L=0.5 for intermediate densities, and L=0 to 0.25 for higher densities. We may use L=0.5 as a default, if vegetation density is unknown.
SAVI requires a rough estimation of vegetation density in advance to choose an appropriate L value that us sometimes difficult. Modified Soil Adjusted Vegetation Index (MSAVI) is proposed to provide an appropriate L value automatically based upon a NDVI value (Qi et al., 1994).

$$MSAVI = \{(NIR - Red) / (NIR + Red + L)\} \cdot (1 + L) \qquad (7.16)$$

$$L = 1 - 2 \cdot a \cdot NDVI \cdot (NIR - a \cdot Red) \qquad (7.17)$$

where a is the slope of the soil line that passes the origin.

Second Modified Soil Adjusted Vegetation Index (MSAVI2) was proposed later. MSAVI2 does not require to determine the soil line.

$$MSAVI2 = 0.5 \cdot [2 \cdot NIR + 1 - \{(2 \cdot NIR + 1)^2 - 8 \cdot (NIR - Red)\}^{1/2}] \quad (7.18)$$

Transformed Soil Adjusted Vegetation Index (TSAVI) was developed by Baret and Guyot (1991). SAVI, MSAVI, and MSAVI2 use the soil line passing the origin, but TSAVI uses a soil line that does not necessarily pass the origin and has an arbitrary intersect and slope.

$$TSAVI = \{a \cdot (NIR - a \cdot Red - b)\} / \{a \cdot NIR + Red - a \cdot b + X \cdot (1 + a^2)\} \quad (7.19)$$

where a = 1.2, b = 0.04, and X = 0.08 in Baret and Guyot (1991). These indices are useful to suppress the background soil effect particularly in relatively sparse vegetation areas. However, they are still not as popular as NDVI due to their calculation complexities.

7.3.6 Enhanced Vegetation Index (EVI)

Enhanced Vegetation Index (EVI) was developed to generate the MODIS standard data product (Justice et al., 1998) and can minimize the both soil background and aerosol effects.

$$EVI = G \cdot (NIR - Red) / (L + NIR + C_1 \cdot R - C_2 \cdot Blue) \quad (7.20)$$

Blue is reflectance in visible blue region, G is a gain factor, L is soil adjustment factor, and C_1 and C_2 are coefficients. In the actual calculation, the following values were used; G = 2.5, L = 1, C_1 = 6, and C_2 = 7.5.

7.3.7 Greenness

Greenness is the second index of the tasseled cap transformation, a sort of orthogonal transformation in multi-dimensional space, which us explained in the section 7.2.4. The following equations have been proposed as greenness for the sensors onboard the Landsat series (Kauth and Thomas, 1976; Crist and Cicone, 1984; Crist et al., 1986; Huang et al., 2002). To calculate the greenness values, simply put DNs of each band to the equation. Greenness is a simple and useful method, but it sometimes includes error as this method does not consider radiance changes due to the atmospheric and solar radiation conditions.

$$Greenness\ (MSS) = -0.29 \cdot MSS4 - 0.56 \cdot MSS5 + 0.60 \cdot MSS6 + 0.49 \cdot MSS7 \quad (7.21)$$

$$Greenness\ (Landsat\ 4\ TM) = -0.2848 \cdot TM1 - 0.2435 \cdot TM2 - 0.5436 \cdot TM3 + 0.7243 \cdot TM4 + 0.0840 \cdot TM5 - 0.1800 \cdot TM7 \quad (7.22)$$

$$Greenness\ (Landsat\ 5\ TM) = -0.2728 \cdot TM1 - 0.2174 \cdot TM2 - 0.5508 \cdot TM3 + 0.7221 \cdot TM4 + 0.0733 \cdot TM5 - 0.1648 \cdot TM7 - 0.7310 \quad (7.23)$$

$$Greenness\ (Landsat\ 7\ ETM+) = -0.3344 \cdot ETM1 - 0.3544 \cdot ETM2 - 0.4556 \cdot ETM3 + 0.6966 \cdot ETM4 + 0.0242 \cdot ETM5 - 0.2630 \cdot ETM7 \quad (7.24)$$

7.4 Relationships between global vegetation variations and climate

7.4.1 Data correction and analysis methods

Relationship between global vegetation variations and climate was investigated by using satellite remote sensing data (Kawabata et al., 2001). Photosynthetic activity by vegetation, which fixes carbon as biomass in the biosphere, plays a key role in the global carbon cycle (Schimel et al., 1995), and can be inferred using a satellite-derived vegetation index (Goward et al., 1985) such as NDVI. For example, interannual increase in NDVI associated with lengthened plant growing season in the northern high latitudes has been pointed out (Myneni et al., 1998). Climate effects are expected as one of the factors of interannual variations in vegetation activities, and relationships between NDVI and climate data have been investigated on regional (e.g., Li and Kafatos, 2000) and global (Schultz et al., 1995) scales. Although Schultz et al. (1995) reported that interannual NDVI data were not highly correlated with climate data, it might be inappropriate to utilise satellite-sensed land surface temperature data and NDVI data without proper corrections when comparing NDVI and climate variables.

Interannual trends in NDVI were investigated seasonally and annually on a global scale using the Pathfinder AVHRR (Advanced Very High Resolution Radiometer) Land NDVI data set from 1982 to 1990, which was corrected utilising desert and high NDVI areas (James and Kalluri, 1994; Ichii et al., 2002). In addition, climate effects on NDVI variations over this period were examined using land air temperature and precipitation data obtained at ground meteorological stations.

The Pathfinder AVHRR Land NDVI data set was produced from data observed by the National Oceanic and Atmospheric Administration (NOAA) meteorological satellites; NOAA-7, -9, and -11, and covers the periods from July 1981 to September 1994 at 8 km spatial and ten days or one month temporal resolutions. The monthly data from December 1981 to December 1990 were used in the present study, because the eruption of Mt. Pinatubo in June 1991 might affect the data obtained since then [Myneni et al., 1998]. This data set was originally corrected for various factors such as intra-sensor degradation; however, some residual errors have still been found to exist due to incomplete atmospheric correction resulting from lack of appropriate water vapour and aerosol data, and so on [Myneni et al., 1998]. To eliminate these errors, the authors applied further correction to the data set by utilising two targets that were expected to be time-invariant in NDVI, namely, desert (no photosynthetic activity) and dense forest (saturated NDVI; *Carlson and Ripley*, 1997) areas. In addition, geometric resampling was performed in order to reduce original spatial resolution by 8 km, to 1° latitude by longitude gridding, so as to suppress noise. These monthly NDVI data for consecutive three and twelve months were averaged to generate seasonal and annual NDVIs for each year at each grid.

The seasonal and annual NDVIs for nine years at each cell were regressed linearly as a function of time to estimate their change rates except for areas of insufficient data (n<5) or low mean NDVI (<0.05), and areas with statistical significant tendencies (>10%) were extracted. In the regions where distinct NDVI trends existed, correlations between NDVI and land air temperature or precipitation were examined to investigate climate effects on interannual variations in vegetation activities. The climate data sets were constructed from stational observations at 5° spatial resolution and one month time intervals, and the temperature data were expressed as anomalies from 1961 to 1990 [*Jones*, 1994; Hulme et al., 1998].

7.4.2 Results and discussion

Global distribution of statistically significant trends in annual NDVI from 1982 to 1990 is shown in Figure 7.9 [Kawabata et al., 2001]. Areas showing statistically significant (>10%) NDVI trends are indicated in colour from green to red. Grey regions indicate areas of insufficient data (n<5) or low mean NDVI (<0.05). White regions indicate areas in which statistically significant NDVI trends were not found. Rectangles indicate representative areas examined for correlation between NDVI and climate data. In the Northern Hemisphere, NDVI increasing trends were found broadly from the high latitudes to the equatorial regions, including north-western America, Europe, northern China, western Africa, and south-eastern Asia. On the other hand, NDVI decreased in some parts of the Southern Hemisphere, especially in arid and semi-arid regions such as northern Australia and Argentina. Most of extracted pixels with significant NDVI trends were satisfied with n=9.

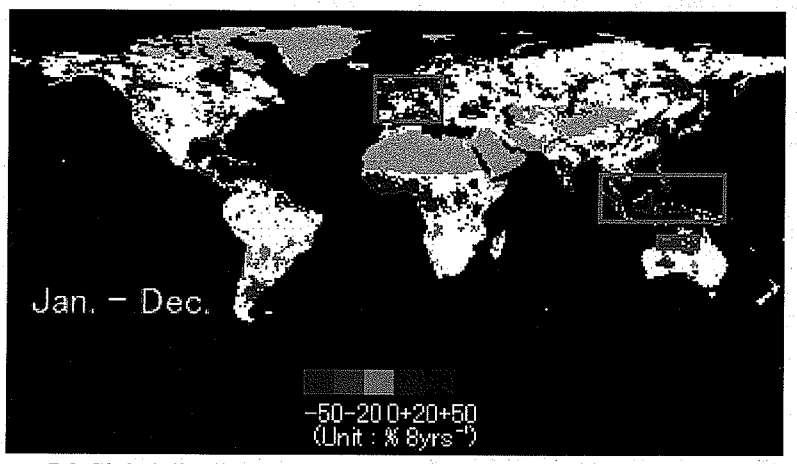

Figure 7.9 Global distribution of interannual changes in annual NDVI from 1982 to 1990.

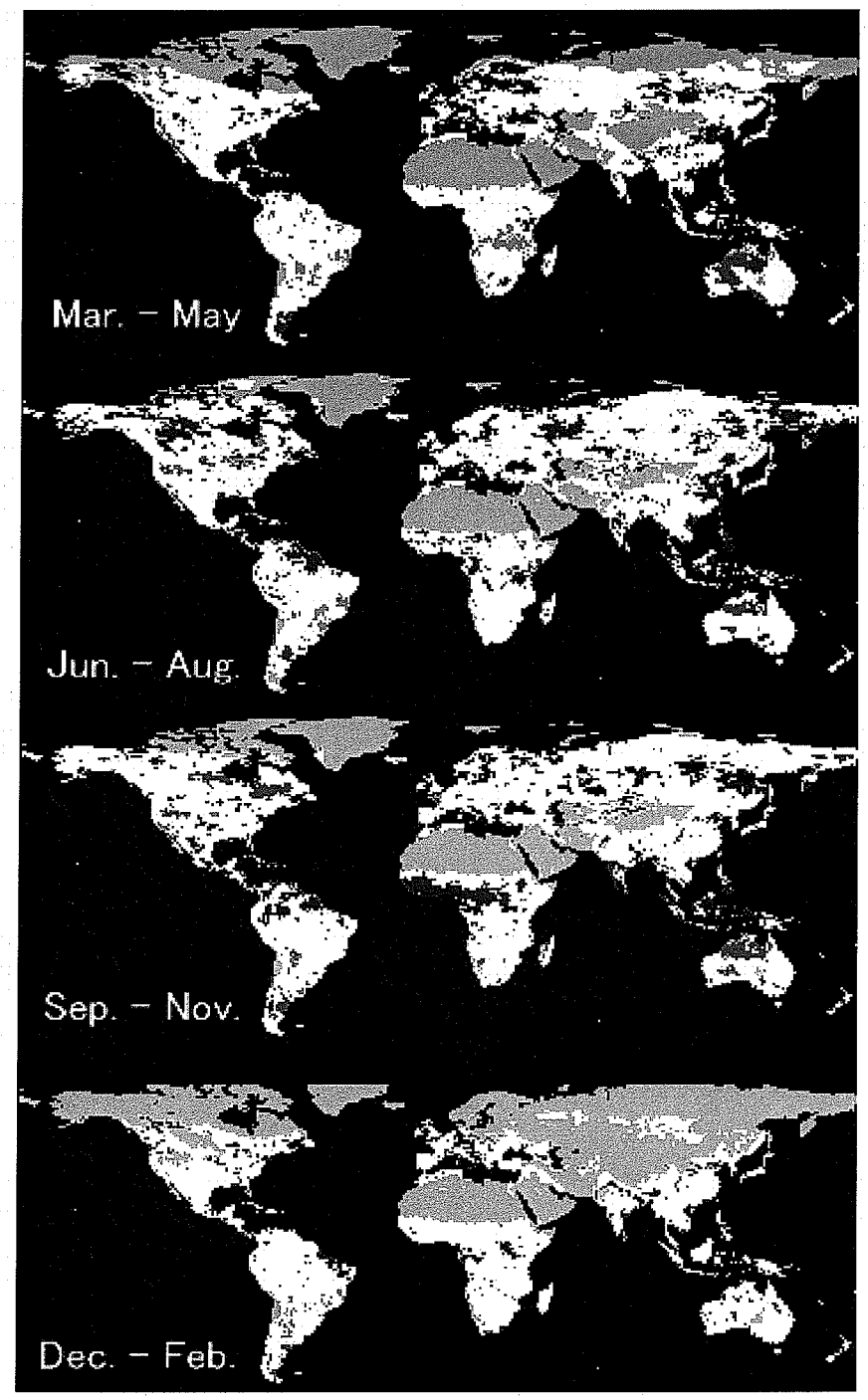

Figure 7.10 Global distribution of interannual changes in seasonal NDVI from 1982 to 1990. Details are as same as in figure 1 (Kawabata et al., 2001).

Figure 7.10 also indicates statistically significant changes in NDVI on a global scale for each season. In the northern middle-high latitudes, NDVI increased in several regions, especially between March and November, and the rates of increase were particularly high in spring and autumn, which probably corresponds to lengthened growing season of vegetation [Myneni et al., 1998]. Although NDVI increased mainly from June to November over the tropical regions, NDVI decreased almost throughout the entire year in some arid and semi-arid areas in the Southern Hemisphere.

The areas that showed significant trends can be divided into three categories: northern middle-high latitudes, tropical regions, and arid and semi-arid areas in the Southern Hemisphere. Then, relationships between NDVI and climate variables were examined for NDVI increase/decrease areas, as shown in figure 1, of these three categories.

In the northern middle-high latitudes, annual and seasonal NDVIs and temperature were positively correlated (R^2=0.3-0.7) in most of extracted areas (e.g. Figure 7.11), whereas correlation between NDVI and precipitation was not significant. Therefore, interannual rise in temperature is expected to have brought about an NDVI increase in these regions. In the tropical zone, the correlation between NDVI and climate variables was not strong (R^2<0.2), and therefore effects of temperature and precipitation on the interannual NDVI increase are small. Although possible reasons for increased NDVI might include accelerated vegetation activities due to CO_2 fertilisation, further analysis is necessary because a significant change in NDVI did not appear in the Amazon area, where anthropogenic deforestation and its regrowth are expected to be complicatedly affecting NDVI variations. Figure 7.12 indicates interannual variations in annual NDVI and precipitation in northern Australia and shows a linear correlation between them (R^2=0.75). A similar correlation was also found in Argentina (R^2=0.54). This relationship between annual NDVI and rainfall agrees with result of a previous study performed for the Sahel region [*Malo and Nicholson*, 1990]. Therefore, the interannual decrease in plant activities was due to a decrease in precipitation in these arid and semi-arid areas.

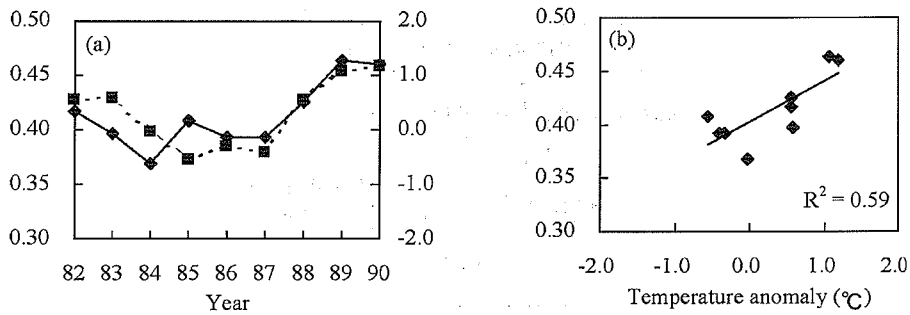

Figure 7.11 (a) Interannual variations in annual NDVI (solid line) and temperature anomaly (dotted line) in Europe (40°N-60°N, 10°W-20°E) from 1982 to 1990. (b) Correlation between NDVI and temperature anomaly (Kawabata et al., 2001).

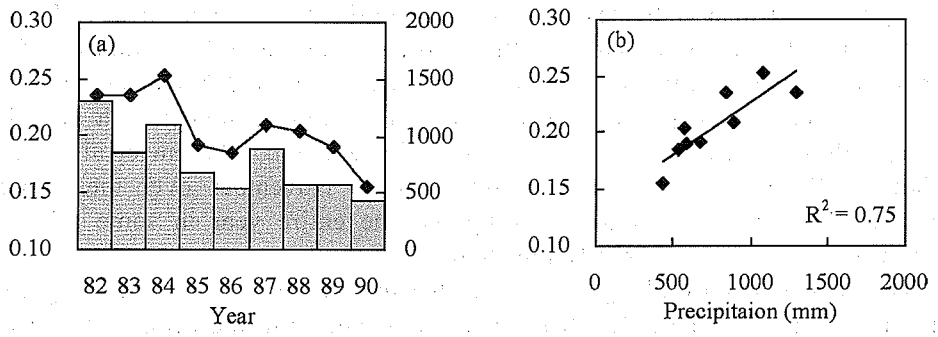

Figure 7.12 (a) Interannual variations in annual NDVI (solid line) and precipitation (grey bar) in northern Australia (15°S-20°S, 120°E-140°E) from 1982 to 1990. (b) Correlation between NDVI and precipitation (Kawabata et al., 2001).

7.5 Estimation of terrestrial carbon fluxes

7.5.1 Definitions of carbon fluxes

Gross Primary Production (GPP) is the carbon uptake by plan photosynthesis activity from the atmosphere. Net Primary Production (NPP) indicates the net carbon uptake by vegetation, and is given by subtracting Autotrophic Respiration (Ra) from GPP (Eq. 7.25). Ra is carbon emission from vegetation through plant respiration. Net Ecosystem Production (NEP) is the net carbon uptake by an ecosystem, e.g., a forest ecosystem as an example of a terrestrial ecosystem. NEP can be given by subtracting carbon emission due to soil organic matter decomposition by soil microbe (SD) from NPP (Eq. 7.26).

$$NPP = GPP - Ra \tag{7.25}$$

$$NEP = NPP - SD \tag{7.26}$$

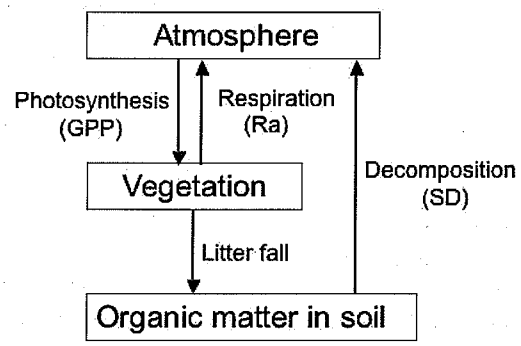

Figure 7.13 Carbon cycle processes in terrestrial ecosystem.

7.5.2 Estimation of GPP

GPP is the most fundamental carbon uptake by terrestrial vegetation, and its accurate estimation is indispensable for estimating NPP and NEP. Ra and SD are generally estimated by a model using inputs of meteorological parameters such as air temperature and precipitation, and surface condition parameters such as vegetation and soil types [e.g., Sasai et al., 2005]. Based upon estimated GPP, Ra, and SD, we usually can calculate NPP and NEP.

In order to estimate GPP, many previous studies have been using an approach called the Production Efficiency Model (PEM) concept, which assumes that carbon uptake by photosynthesis is proportional to solar light absorbed by vegetation [e.g., Myneni et al., 2002; Potter et al., 1993]. GPP is assumed to be a product of Light Use Efficiency (LUE) and Absorbed Photosynthetically Active Radiation (APAR);

$$GPP = LUE \cdot APAR \tag{7.27}$$

$$GPP = LUE \cdot FPAR \cdot PAR \tag{7.28}$$

APAR is a product of Fraction of Photosynthetically Active Radiation (FPAR), and Photosynthetically Active Radiation (PAR). PAR is a part of solar radiation that can be used for photosynthesis by vegetation, that is, visible light whose wavelength is from 400 to 700 nm. In estimation of GPP, the PAR is given by actual solar radiation measurements, or is derived from solar irradiance by assuming that PAR is about 45 to 50 % of solar irradiance. FPAR is a fraction of PAR by vegetation for photosynthesis. FPAR is a function of vegetation density, so that it can be estimated by NDVI, which has a systematic relation to vegetation density such as Leaf Area Index (LAI).

Many approaches have been proposed to estimate LUE. The simplest method is to use a constant LUE value, but later many studies use different LUE values for different vegetation types. Moreover, recent studies assume that LUE is a function of environmental parameters such as air temperature and precipitation. Thus LUE is defined by a product of the maximum Light Use Efficiency (LUEmax) under the optimum condition and stress factor which ranges from 0 to 1.

$$LUE = LUEmax \cdot Stress \tag{7.29}$$

Sasai et al. [2005] defined Stress as the ratio of actual to maximum photosynthesis based upon a photosynthesis rate, which accounts for the biochemical responses of temperature, relative humidity, and soil water content. They also proposed to calculate Stress from the three parameters of soil water, vapor pressure, and air temperature. Figure 7.14 shows the global Stress distributions as estimated by BEAMS, CASA, and MOD17. All stress results are averaged for the period 1982 to 2000. A high Stress value indicates that plants are under suitable temperature and wetness conditions, while a low value indicates

inappropriately low or high temperatures and/or dry conditions (Sasai et al., 2005).

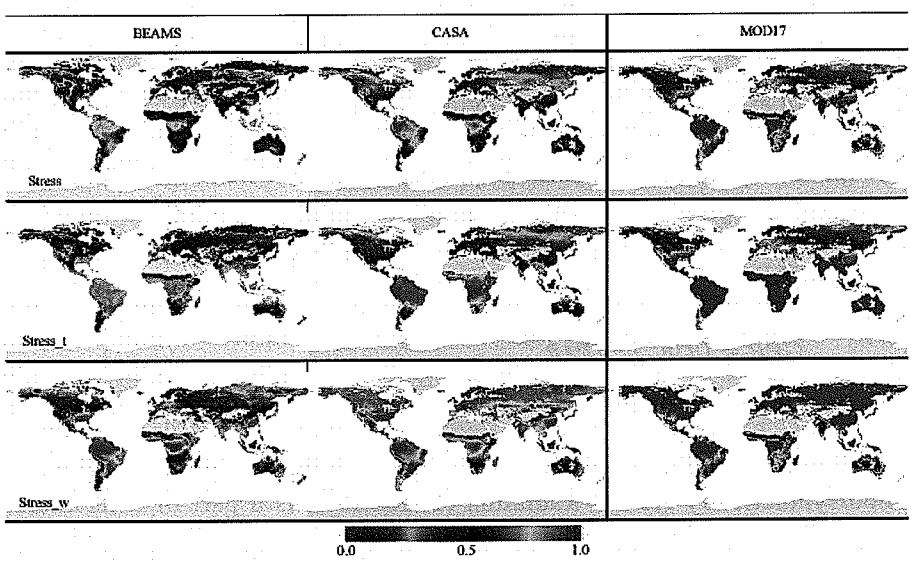

Figure 7.14 Global Stress distributions as estimated by BEAMS, CASA, and MOD17 (Sasai et al., 2005).

An example of calculation flow of estimating NPP of terrestrial vegetation from remote sensing data is summarized in Figure 7.15. NDVI calculated by remote sensing data will be used to estimate FPAR, which will be used to estimate APAR. On the other hand, surface vegetation types derived from remote sensing data is used to choose an appropriate LUEmax value. LUE will be calculated by LUEmax and meteorological parameters such as temperature and precipitation. Finally, APAR and LUE are used to estimate GPP, which will be then converted NPP by assuming Ra from meteorological data and surface types. Figure 7.16 shows Spatial variation in annual NPP averaged for the period 1982 to 2000 (Sasai et al., 2005).

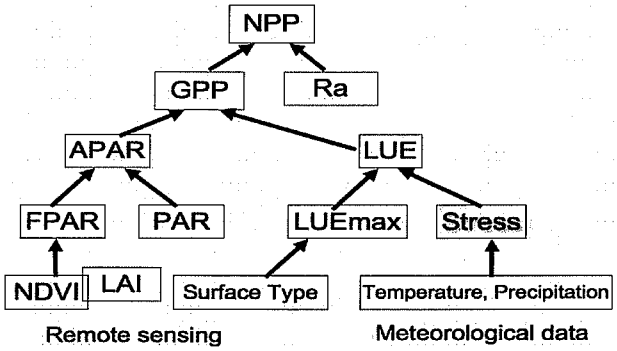

Figure 7.15 Flow of estimating NPP of terrestrial vegetation from remote sensing data.

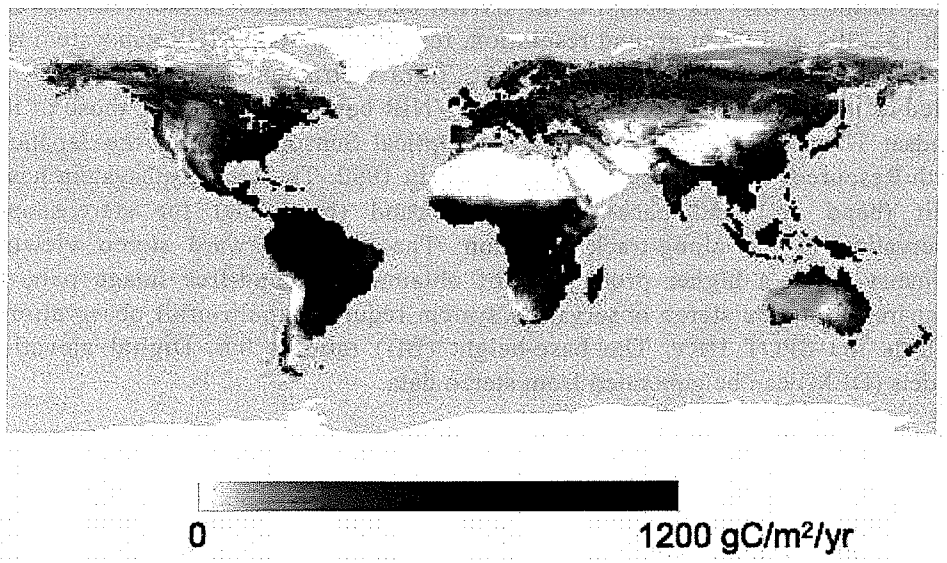

Figure 7.16 Spatial variation in annual NPP averaged for the period 1982 to 2000 (Sasai et al., 2005).

7.6 An example of a high resolution remote sensor; Advanced Spaceborne Thermal Emission and Reflection Radiometer (ASTER)

7.6.1 ASTER instrument characteristics

The Advanced Spaceborne Thermal Emission and Reflection Radiometer (ASTER) is a high spatial resolution multi-spectral imaging radiometer onboard the NASA's Terra spacecraft launched in December, 1999 [Yamaguchi et al., 1998]. The primary science objective of the ASTER mission is to improve understanding of the local and regional processes occurring on or near the Earth's surface and lower atmosphere. ASTER data can be used to help establish a baseline for long-term monitoring of local and regional changes on the Earth's surface, which either lead to, or are in response to, global climate change.

The ASTER instrument has three separate optical subsystems; the visible and near-infrared (VNIR) radiometer, short-wave-infrared (SWIR) radiometer, and thermal infrared (TIR) radiometer, as shown in Table 7.1. There are three spectral bands in the VNIR, six bands in the SWIR, and five bands in the TIR regions, with 15-, 30-, and 90-m ground resolution, respectively. The VNIR subsystem has the highest spatial resolution among the Terra instruments, so that ASTER is called as the zoom lens of Terra. The three VNIR bands are similar to those of the Landsat Thematic Mapper (TM) and the Optical Sensor (OPS) of the Japanese Earth Resources Satellite (JERS-1) launched in 1992. The VNIR subsystem has a nadir (band 3N) and backward-viewing band (band 3B) for stereoscopic observation in the along-track direction. The nadir-backward stereo viewing geometry gives a higher probability of obtaining a cloud-free image pair, as compared to a side stereo observation system requiring multi-orbit observations, such as the SPOT HRV. The base-height (BH) ratio is 0.6. Digital elevation models (DEM) can be generated from stereo data.

Table 7.1 ASTER baseline performance requirements.

	Band No.	Spectral Range (μm)	Radiometric Resolution	Absolute Accuracy (σ)	Spatial Resolution	Signal Quantization
VNIR	1	0.52 - 0.60	NEΔρ ≤ 0.5 %	≤ ± 4 %	15 m	8 bits
	2	0.63 - 0.69				
	3N	0.78 - 0.86				
	3B	0.78 -0.86				
SWIR	4	1.600 - 1.700	NEΔρ ≤ 0.5 %	≤ ± 4 %	30 m	8 bits
	5	2.145 - 2.185	NEΔρ ≤ 1.3 %			
	6	2.185 - 2.225	NEΔρ ≤ 1.3 %			
	7	2.235 - 2.285	NEΔρ ≤ 1.3 %			
	8	2.295 - 2.365	NEΔρ ≤ 1.0 %			
	9	2.360 - 2.430	NEΔρ ≤ 1.3 %			
TIR	10	8.125 - 8.475	NEΔT ≤ 0.3 K	≤ 1K - 3K	90 m	12 bits
	11	8.475 - 8.825				
	12	8.925 - 9.275				
	13	10.25 - 10.95				
	14	10.95 - 11.65				

Stereo Base-to-Height Ratio	0.6 (along-track)
Swath Width	60 km
Total Coverage in Cross-Track Direction	232 km
MTF at Nyquist Frequency	0.25 (cross-track), 0.20 (along-track)
Band-to-Band Registration	0.2 pixels (intra-telescope) 0.3 pixels (inter-telescope)
Peak Data Rate	89.2 Mbps
Mass	406 kg
Peak Power	726 W

The spectral bandpasses of the SWIR bands were selected mainly for the purpose of surface soil and mineral mapping (Figure 7.17). The ASTER permits more detailed surface soil and lithologic mapping than Landsat TM and JERS-1 OPS. The ASTER TIR subsystem has five bands in the thermal infrared region. For the first time, ASTER is providing high-spatial resolution multi-spectral TIR data from orbit. Having multi-spectral TIR data allows for a more accurate determination of the variable spectral emissivity of the land surface, and hence a more accurate determination of the land surface temperature. The ASTER Science Team developed algorithms to separate temperature and emissivity of the surface materials [Gillespie et al., 1998]. Emissivity patterns derived from the five TIR bands are useful for distinguishing silicate and carbonate rocks.

Characterization of the ASTER instrument has proven to us that the ASTER has excellent radiometric, geometric, and spectral performances, and that they meet the observation performance requirements given by the ASTER Science

Team. In order to maintain and monitor the observation performances, periodical in-flight calibration activities are being carried out by the ASTER Science Team and Instrument Team.

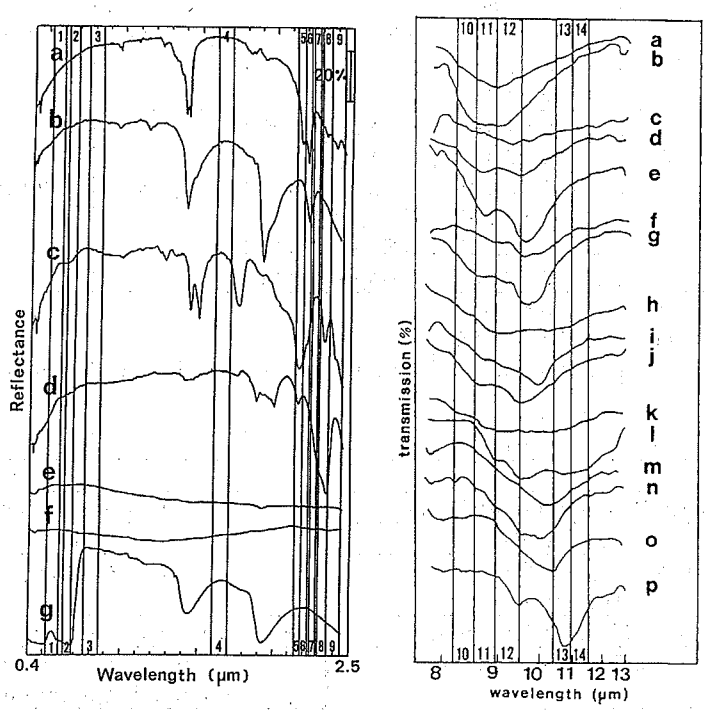

Figure 7.17 Left ; Spectral bandpasses of the ASTER VNIR and SWIR (numbers in the figure indicate ASTER bands), and the reflectance spectra of typical minerals, rocks, and vegetation: (a) kaolinite, (b) montmorillonite, (c) alunite, (d) calcite, (e) andesite, (f) granite, and (g) green leaves. Right ; Spectral bandpasses of the ASTER TIR, and the emissivity (transmission) spectra of typical rocks [modified from *Vickers & Lyon*, 1967]: (a) dacite, (b) granite, (c) pumice, (d) trachyte, (e) quartz syenite, (f) andesite, (g) nephelene syenite, (h) hyperthene andesite, (i) quartz diorite, (j) augite, (k) basalt, (l) plagioclase basalt, (m) peridotite, (n) serpentinite, (o) limburgite, and (p) dunite.

7.6.2 ASTER operation and data distribution

The three ASTER subsystems can be operated independently. Combined with multiple gain settings and pointing angles, there are many possible combinations of observation modes. However, several nominal modes have been defined. The nominal daytime mode is simultaneous data acquisition using the three subsystems looking at the same 60 km imaging swath. The nominal nighttime mode is TIR-only operation.

The primary limitation on ASTER data collection is the data volume allocated

to the instrument in Terra's memory (solid state recorder) and in the communications link with TDRSS and ground stations. The maximum average data rate allocated to ASTER, based on a two-orbit average, is 8.3 Mbps, which roughly corresponds to 8 minutes of full-mode daytime operation plus 8 minutes of night time TIR operation per orbit. The single orbit maximum data acquisition time is 16 minutes, if no data is acquired in both previous and following orbits. The peak data rate and peak power consumption are 89.2 Mbps and 726 W respectively. Currently ASTER is acquiring approximately 600 scenes per day as an average. As of September 26, 2005, ASTER had acquired 1,045,498 scenes, of which 424,025 scenes had been assessed as less than 20% cloud cover. Figure 7.18 shows a global mosaic of the ASTER level 1A browse images as of March 30, 2005.

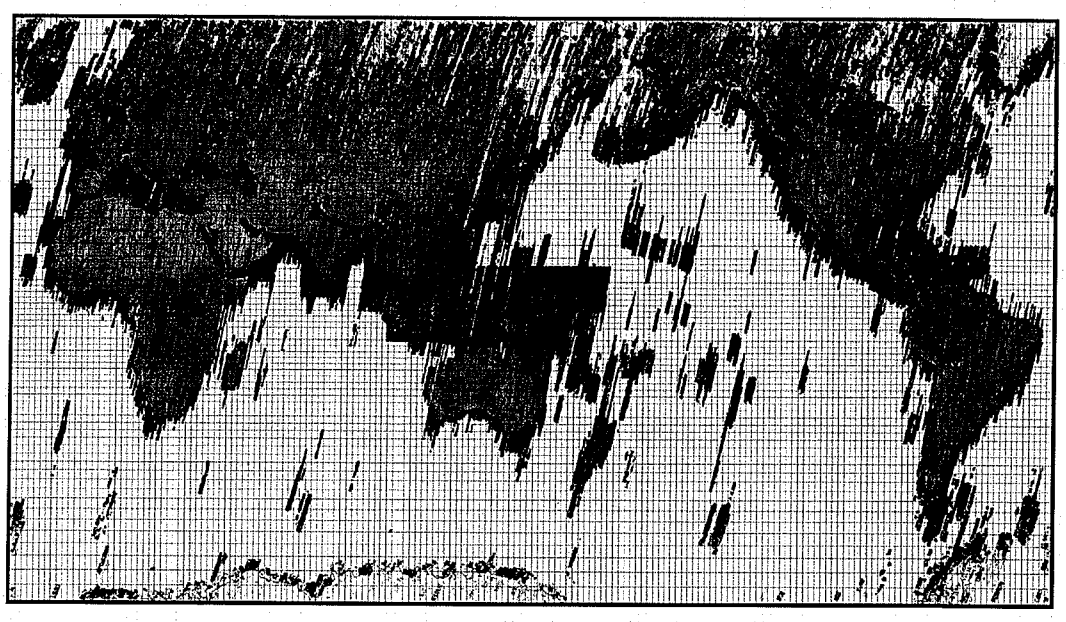

Figure 7.18 A global mosaic of the ASTER level 1A browse images as of March 30, 2005.

Fundamentally ASTER obtains data by target observation based upon data acquisition requests by users. The scheduler automatically generates a One-Day-Schedule (ODS) for ASTER observation every day using the prioritization function in order to maximize the science return. ASTER is useful to observe and monitor geohazards such as floods, tsunami attacks, volcanic eruptions, or fires. Since requests for urgent observations of such phenomena must be fulfilled in short time periods, these requests receive special handling. As soon as an ASTER user becomes aware of such a phenomenon, he/she submits a request

for an urgent observation. The ASTER Science Team reviews the request and judges whether the request should be accepted or not in a timely manner. Once accepted, the prioritization function will increase the priorities of urgent observations to increase the likelihood that they will be successfully acquired within the lifetime of the relevant event.

ASTER Ground Data System (GDS) of Earth Remote Sensing Data Analysis Center (ERSDAC) in Japan and the U.S. Geological Survey Land Processes Distributed Active Archive Center (LPDAAC) in U.S.A. provide user access to all the ASTER standard data products. In addition to the level 1A and 1B products, the ASTER GDS and LPDAAC generates the higher level standard and semi-standard data products including surface radiance, surface reflectance, surface temperature, surface emissivity, DEM, and ortho-rectified radiance at sensor. The elevation accuracy of the ASTER DEM is better than 15 m, while the horizontal geolocation accuracy is about 50 m that is consistent with the reported spacecraft positioning accuracy [Fujisada et al., 2001]. The ASTER GDS and EDC provide user access to all the ASTER standard data products, and distribute requested subsets of them to users either electronically or on appropriate media. For more details and updates, please visit the following web sites; http://www.ersdac.or.jp/eng/index.E.html or http://asterweb.jpl.nasa.gov/.

ASTER data are being used for a variety of applications including surface geological mapping, quick observations of geohazards such as glacier disasters, tsunami attacks, and volcanic eruptions, long-term monitoring of natural vegetation. Land use, glaciers, volcanoes, and coral reefs, and regional surface heat balance analysis, because of its high data qualities and reasonable data price (about 10,000 Japanese Yen per scene). The number of ASTER scenes ordered to the GDS and EDC is increasing steadily. We are very pleased to see that ASTER data are becoming more and more popular in the remote sensing and earth science communities in the world.

7.7 Concluding remarks

Remote sensing is a practical tool to observe vegetation variations on local, regional, and global scales. Particularly multi-spectral data are useful to discriminate and map surface materials including vegetation. As explained in this article, several techniques have been developed to process multi-spectral data, but there is still room to propose a new technique. Remote sensing data can also be used to estimate terrestrial carbon fluxes by combining a ecosystem model. The algorithm development is still going on. In addition, development of a new observation sensor such as ASTER can greatly contribute to give us more information on terrestrial vegetation.

References

Baret, F., and Guyot, G., (1991), Potentials and limits of vegetation indices for LAI and APAR assessment, Remote Sens, Environ., 35, 161-173.

Carlson, T.N, and Ripley, D.A., (1997), On the relation between NDVI, fractional vegetation cover, and leaf area index, Remote Sens, Environ., 62, 241-252.

Crist, E.P, and Cicone, R.C., (1984), A physically-based transformation of Thematic Mapper data –the TM tasseled cap, IEEE Trans, Geosci, Remote Sens., GE-22, 256-263.

Crist, E.P., Laurin, R., and Cicone, R.C., (1986), Vegetation and soils information contained in transformed Thematic Mapper data, Proc, IGARSS '86, European Space Agency, Paris, 1465-1470.

Crowley, J.K., Brickey, D.W., and Rowan, L.C., (1989), Airborne imaging spectrometer data of the Ruby Mountains, Montana: mineral discrimination using relative absorption band-depth images, Remote Sens, Environ., 29, 121-134.

Fujisada, H., Iwasaki, A., and Hara, S., (2001), ASTER stereo system performance, Proc, SPIE, 4540, 39-49.

Gillespie, A., Rokugawa, S., Matsunaga, T., Cothern, J.S., Hook, S., and Kahle, A.B., (1998), A temperature and emissivity separation algorithm for Advanced Spaceborne Thermal Emission and Reflection Radiometer (ASTER) images, IEEE Trans, Geosci, Remote Sens., 36 (4), 1113-1126.

Goward, S.N., Tucker, C.J., and Dye, D.G., (1985), North American vegetation patterns observed with the NOAA-7 advanced very high resolution radiometer, Vegetatio, 64, 3-14.

Huang, C., Wylie, B., Homer, C., Yang, L., and Vogelman, J., (2002), A tasseled cap transformation for Landsat 7 ETM+ at satellite reflectance, Inter, Jour, Remote Sens., 23 (8), 1741-1748.

Huete, A.R., (1988), A soil-adjusted vegetation index (SAVI), Remote Sens, Environ., 25, 295-309.

Hulme, M., Osborn, T.J., and Johns, T.C., (1998), Precipitation sensitivity to global warming: comparison of observations with HadCM2 simulations, Geophy, Res, Letters, 25, 3379-3382.

Ichii, K., Kawabata, A., and Yamaguchi, Y., (2002), Global correlation analysis for NDVI and climatic variables and NDVI trends: 1982 to 1990, Inter, Jour, Remote Sens., 23 (18), 3873-3878.

Jackson, R.D., (1983), Spectral indices in n-space, Remote Sens, Environ., 13, 409-421.

James, M.E., and Kalluri, S.N.V., (1994), The Pathfinder AVHRR land data set; an improved coarse-resolution data set for terrestrial monitoring, Inter, Jour, Remote Sens., 15, 3347-3364.

Jones, P.D., (1994), Hemispheric surface air temperature variations: a reanalysis and an update to 1993, Jour, Climate, 7, 1794-1802.

Justice, C.O., Vermote, E., Townshend, J.R.G., DeFries, R., Roy, R., Roy, D., Hall, D.K., Salomonson, V.V., Privette, J.L., Riggs, G., Strahler, A., Lucht, W., Myneni, R.B., Knyazikhin, Y., Running, S.W., Nemani, R., Wan, R.M., Huete, A.R., Leeuwen, van W., Wolfe, R.E., Giglio, L., Muller, J.P., Lewis, P., and Barnsley, M., (1998), The Moderate Resolution Imaging Spectroradiometer (MODIS): Land remote sensing for global change research, IEEE Trans, Geosci, Remote Sens., 36 (4), 1228-1249.

Kauth, R.J., and Thomas, G.S., (1976), The tasseled cap –A graphic description of the spectral-temporal development of agricultural crops as seen by Landsat, Proc, Symp, Machine Process, Remotely Sensed Data, Purdue Univ., West Lafayette, 41-51.

Kawabata, A., Ichii, K., and Yamaguchi, Y., (2001), Global monitoring of interannual changes in vegetation activities using NDVI and its relationships to temperature and precipitation, Inter, Jour, Remote Sens., 22 (7), 1377-1382.

Kruse, F.A., Letkoff, A.B., Boardman, J.W., Heidebrecht, K.B., Shapiro, A.T., Barloon, P.J., and Goetz, A.F.H., (1993), The spectral image processing system (SIPS) – Interactive visualization and analysis of imaging spectrometer data, Remote Sens, Environ., 44, 145-163.

Li, Z., and Kafatos, M., (2000), Interannual variability of vegetation in the United States and its relation to El Nino/Southern Oscillation, Remote Sens, Environ., 71, 239-247.

Malo, A.R., and Nicholson, S.N., (1990), A study of rainfall and vegetation dynamics in the African Sahel using normalized difference vegetation index, Jour, Arid Environ., 19, 1-24.

Myneni, R.B., Tucker, C.J., Asrar, G., and Keeling, C.D., (1998), Interannual variations in satellite-sensed vegetation index data from 1981 to 1991, Jour, Geophy, Res., 103, 6145-6160.

Myneni, R.B., Hoffman, S., Knyazikhin, Y., Privette, J.L., Glassy, J., Tian, Y., Wang, Y., Song, X., Zhang, Y., Smith, G.R., Lotsch, A., Friedl, M., Morisette, J.T., Votava, P., Nemani, R., and Running, S.W., (2002), Global products of vegetation leaf area and fraction absorbed PAR from year one of MODIS data, Remote Sens, Environ., 83 (1), 214-231.

Potter, C.S., Randerson, J.T., Field, C.B., Matson, P.A., Vitousek, P.M., Mooney, H.A., and Klooster, S.A., (1993), Terrestrial ecosystem production: a process model based on global satellite and surface data, Global Biogeochem, Cycles, 7 (4), 811-841.

Qi, J., Chehbouni, A., Huete, A.R., and Kerr, Y.H., (1994), Modified soil adjusted vegetation index (MSAVI), Remote Sens, Environ., 48, 119-126.

Richardson, A.J., and Wiegand, C.L., (1977), Distinguishing vegetation from soil background information, Photogram, Eng, Remote Sens., 43, 1541-1552.

Rowan, L.C., Wetlaufer, P.H., Goetz, A.F.H., Billingsley, F.C., and Stewart, J.H., (1974), *Discrimination of rock types and detection of hydrothermally altered areas in south-central Nevada by use of computer-enhanced ERTS images*, U.S, Geological Survey Professional Paper, 883, 35pp.

Rowan, L.C., Mars, J.C., and Simpson, C.T., (2005), Lithologic mapping of the Mordor, NT, Australia ultramafic complex by using the Advanced Spaceborne Thermal Emission and Reflection Radiometer (ASTER), Remote Sens, Environ., 99, 105-126.

Sasai, T., Ichii, K., Yamaguchi, Y., and Nemani, R., (2005), Simulating terrestrial carbon fluxes using the new biosphere model "biosphere model integrating eco-physioloical and mechnistic approaches using satellite data" (BEAMS), Jour, Geophy, Res., 110, G02014, doi:10.1029/2005JG000045.

Schimel, D.S., Enting, I.G., Heimann, M., Wigley, T.M.L., Raynaud, D., Alves, D., and Siegenthaler, U., (1995), CO_2 and the carbon cycle, In Climate Change 1994: Radiative Forcing of Climate Change and an Evaluation of the IPCC 1992 Scenarios, edited by J, T, Houghton et al., Cambridge University Press, Cambridge, 35-71.

Schultz, P.A., and Halpert, M.S., (1995), Global analysis of the relationships among a vegetation index, precipitation and land surface temperature, Inter, Jour, Remote Sens., 16, 2755-2777.

Vickers, R.S., and Lyon, R.J.P., (1967), Infrared sensing from spacecraft – A geologic interpretation, Proc, Thermophysics Special Conf., Amer, Inst, Astron., paper 67-284.

Yamaguchi, Y., Kahle, A.B., Tsu, H., Kawakami, T., and Pniel, M., (1998), Overview of Advanced Spaceborne Thermal Emission and Reflection Radiometer (ASTER), IEEE Trans, Geosci, Remote Sens., 36 (4), 1062-1071.

Yamaguchi, Y., and Naito, C., (2003), Spectral indices for lithologic discrimination and mapping by using the ASTER SWIR bands, Inter, Jour, Remote Sens., 24 (22), 4311-4323.

Yamaguchi, Y., and Takeda, I., (2003), Mineralogical mapping by ASTER in Cuprite, Nevada, U.S.A., Asian Jour, Geoinform., 3 (3), 17-24.

Chapter 8

Role of Vegetation in the Earth Climate System

Tetsuzo Yasunari
Hydrospheric Atmospheric Research Center (HyARC),
Nagoya University, Nagoya 464-8601, Japan
Tel: +81-52-789-3465
Fax: +81-52-789-3436
e-mail: yasunari@hyarc.nagoya-u.ac.jp

8.1 Fundamental processes for the seasonal cycle of surface climate

8.1.1 Land-atmosphere-ocean interaction

The climate of the earth surface is manifested as a land-atmosphere-ocean interaction between continents and oceans in the seasonal cycle. The ocean has large heat content with longer climate memory of more than a year, but the land has small heat content and its climate memory is believed to be short (of less than a season). Some previous studies emphasized relative importance of the ocean-atmosphere interaction (OAI) compared to land-atmosphere interaction (L-AI), particularly focusing on the strong impact of large-scale sea surface temperature (SST) anomalies in the tropical oceans nearby the continent. It should be noted, however, that to specify or distinguish the roles of L-AI from those of OAI and vice versa is very difficult, particularly in the Asian-Australian monsoon system and the tropical land areas, because these two processes are strongly coupled to each other. In other words, the L-AI (or OAI) in the monsoon system should, in any case, be understood as part of the full land-atmosphere-ocean interaction.

The land shows strong and rapid heating (and cooling) in the seasonal cycle which in turn has a large impact on seasonal atmospheric differential heating (and cooling) processes between land and ocean. The land surface processes which modulate the seasonal heating, therefore, are likely to be responsible, to some extent, for interannual variability of the hydro-climate or monsoons. For example, the snow cover and soil moisture anomalies over the Eurasian continent in the pre-monsoon seasons have been thought to have large impact on the Asian summer monsoon variability. This chapter mainly focuses on the land-atmosphere interaction with particular emphasis on the role of vegetation on the continental

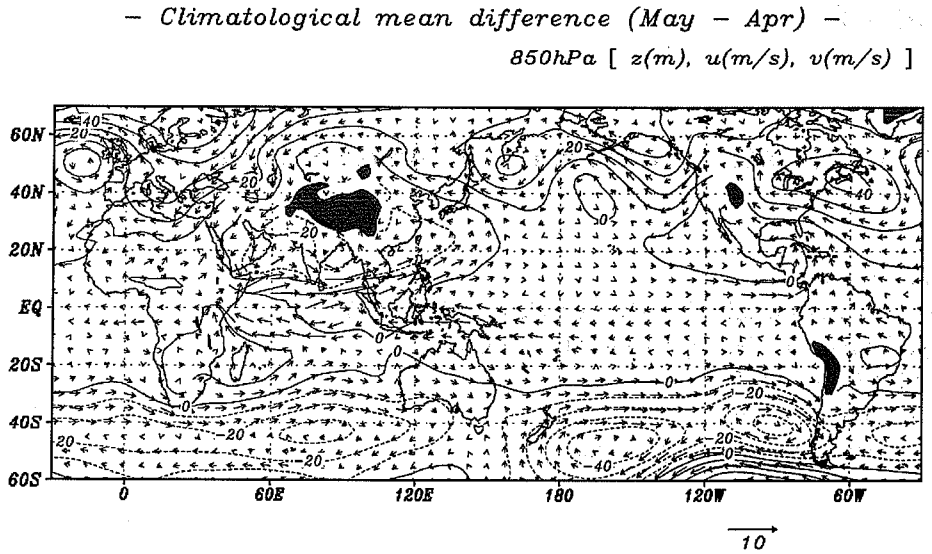

Figure 8.1 Difference of climatological mean height and U, V field for May minus April. Blue colour shows negative values.

and regional-scale climate system over Asia and Eurasian continent. Discussions focusing on the Asian monsoon system are made in Yasunari (2006).

8.1.2 Role of large-scale orography (Tibetan Plateau)

Seasonal land surface heating and resultant atmospheric heating over Eurasia manifest itself in the surface or lower tropospheric pressure field. Figure 8.1 shows difference of monthly mean geopotential field at 850hPa from April to May. A remarkable decrease of pressure is seen over southern Eurasia centered over India/Tibetan plateau area. Similar patterns of pressure change are seen over Eurasia from month to month for the period of March through July. In contrast, the pressure change over the tropical and sub-tropical oceans are very small and positive (increase of pressure). The large decrease of pressure change over Eurasia indicates seasonal heating of land, presumably centered over the Tibetan Plateau and Mongolia. The decrease of pressure over north America centered over the Rockies is very small, suggesting smaller heating over there compared to the Tibetan Plateau area.

The low-pressure area over the southern Eurasia (called the "monsoon trough") at the surface and lower troposphere induces moist southwesterly wind from the Indian Ocean (the southwest monsoon flow) toward India, southeast Asia and cast Asia, and dry northerly wind from the interior of the Eurasian continent.

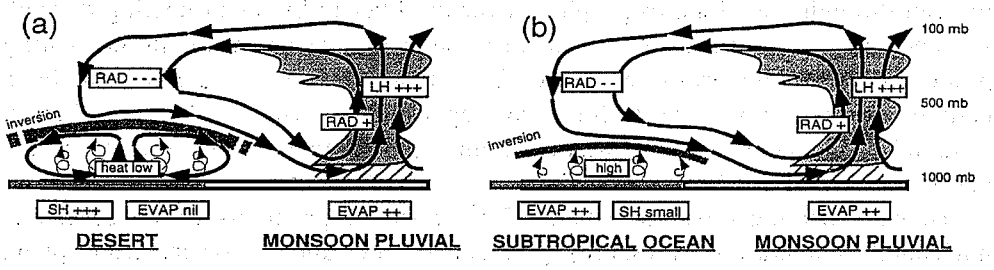

Figure 8.2 Schematic of the circulation between (a) the desert region of North Africa and the Near East; and, (b) the subtropical ocean regions and the precipitating (pluvial) part of the monsoon circulation, respectively. The components of the monsoon match the transverse and lateral monsoon components shown in Figure 8.9. The dominant heating or cooling terms are shown in the boxes. "SH" and "LH" refer to sensible and latent heating. "RAD" and "EVAP" refer to radiational heating and evaporation, respectively. The pluses and minuses represent the sign of the processes and their relative intensity.(Webster et al., 1998)

The moist monsoon flow, in turn, induces convection and precipitation over the southeastern part of the continent, which plays a dominant role of atmospheric latent heating as a "moist L-AI" during the monsoon season.

An important issue may be how this moist L-AI starts in the interior of the continent. The sensible heating over the Tibetan Plateau may be one of the important factors for triggering this process. In other continents, dry L-AI based only on sensible heating from the land surface cannot produce the continental-scale monsoons. Figure 8.2 shows a schematic diagram of this dry and shallow L-AI. This process is dominated over the Australian continent and the west Africa (to the north of west African monsoon) where desert area prevails and large-scale downward motion is dominated. The existence of the desert and the downward motion is self-perpetuating through a positive feedback of surface albedo and radiation balance (Otterman, 1974; Charney, 1975; Webster et al., 1998). This dry L-AI cannot induce deep atmospheric heating in the interior of the continents, but can trigger shallow coastal monsoon circulation along the periphery of the continent. This shallow monsoon circulation is, however, likely to trigger deep convection when the continents are surrounded by warm tropical oceans, e.g., the warm water pool of Arafura and Timor seas neighboring to the Australian continent (Kawamura et al., 2002). The land heating process over the Australian continent is thus important for triggering the Indonesia-Australian monsoon.

Over the elevated land surface of the Tibetan Plateau, in contrast, sensible heating plays a dominant role of atmospheric diabatic heating of the whole

troposphere particularly in the onset phase of the Asian monsoon. Ueda et al. (2003) showed that the strong diabatic heating rate in May over the Tibetan Plateau through the whole troposphere over the Plateau by latent heating through shallow convection in the pre-monsoon season also plays some role in the heating process even in the pre-onset phase. The simulation of Asian monsoon by a coupled ocean-atmosphere GCM also suggest that without Tibetan Plateau orography the monsoon precipitation cannot penetrate into the interior of the continent (Abe et al., 2003).

Diabatic heating over the Tibetan Plateau in the pre-monsoon phase causes horizontal temperature (pressure) gradient in the upper (lower) troposphere between the surrounding the Indian and Pacific Oceans and the interior of the continent, which facilitate large-scale convective activity over the South China Sea through the strengthening of the southwest monsoon flow intrusion (Ueda and Yasunari, 1998). Very recently, Jiang et al. (2004) and Wang et al. (2005) also pointed out an important role of the existence of strong vertical easterly wind shear over south Asia to the south of the Tibetan Plateau in the northward migration of convective zone with intraseasonal time-scales (including the monsoon onset phase) from the equatorial Indian Ocean toward the Himalayas. This may imply that the atmospheric diabatic heating over and around the Tibetan Plateau (which is primarily responsible for producing the meridional thermal contrast and the vertical easterly shear over south Asia) is one of the essential elements, which characterize the variability as well as the mean state of the Asian summer monsoon system.

8.2 Land surface quantities controlling surface climate

The physical quantities of land surface which may posses anomalous atmospheric forcing or climate memory effect can be 1) snow cover, 2) soil moisture, and 3) vegetation. The land surface layer is generally thought to have small heat capacity compared to the ocean surface layer, the non-linear processes of these quantities in the seasonal and interannual variations effectively produce relatively longer memory effect, even compatible to that of SST as shown in Figure 8.3 (Walsh et al., 1985; Shinoda and Gamo, 2000). The seasonal and interannual variability of these quantities play significant role in land-atmosphere interaction by producing anomalous surface and atmospheric heating or cooling, which in turn affects the monsoon circulation and convection. One should keep in mind that these quantities are interactive with the atmospheric conditions so that detection of simple cause-result relation is sometimes difficult. However, due to lack of the adequate observational data, and lack of understanding of actual physical processes particularly relevant to the climate studies, large uncertainties

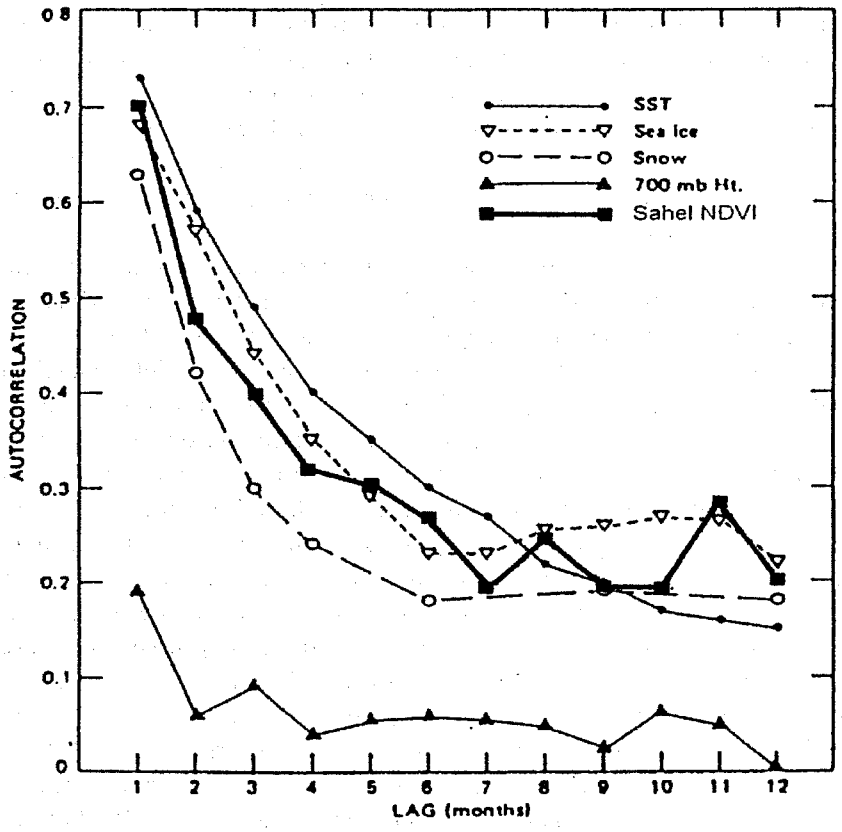

Figure 8.3 Autocorrelations of monthly anomaly of SST in the northern Pacific, sea ice in the Arctic Sea, snow cover over Eurasia, geopotential height at 700hPa depicted from Walsh et al. (1985) and NDVI in Sahel region, North Africa obtained from Shinoda and Gamo (2000). (Shinoda et al., 2003).

still exist in the relation between variabilities of these quantities and monsoon activity. Comprehensive and interactive observation and modeling strategy is really important for this study. Here we discuss the roles of soil moisture and vegetation which are important surface parameters in the earth surface climate except in high-latitude and high-atlitude regions where snow cover is also an important parameters.

8.2.1. Role of soil moisture

The soil moisture is a key parameter for L-AI in the climate system. The anomaly of surface and near-surface soil moisture is likely to have persistence of several days to several months, which may cause climate memory through

anomalous surface energy and moisture fluxes. However, this quantity is very difficult to measure adequately. The long-term in-situ measurement of soil moisture is very limited both in time and space (Robock et al., 1998; 2000). The recent satellite-based indirect measurement using microwave sensors is a promising method for large-scale soil moisture monitoring, but it has still been limited for soil moisture or wetness of very-near surface soil layer. The climate memory effect of soil moisture has, therefore, been discussed basically based upon climate model experiments.

Delworth and Manabe (1988,1989) for the first time assessed the climate memory effect of soil moisture in GCMs using the so-call bucket model (Manabe, 1969) interacting with the atmosphere through surface water balance. Their bucket model consists of one soil layer with 15cm water holding capacity (field capacity). They noticed that the persistency (measured by auto-correlation) of soil moisture anomaly is small whereas in higher latitudes this value is large, depending upon the ratio of P/Ep (P: Precipitation, Ep: Potential Evapo-transpiration)as shown in Figure 8.4. In the humid tropics or monsoon regions where P is large enough to saturate the soil layer, soil moisture anomaly does not make sense as a climate memory. The distribution of persistency in Fig. x can be generally described in the form $1/\lambda = W^*/Ep$, where λ is e-folding time of exponential decay of soil moisture anomaly, and W^* field capacity. Though their definition of soil moisture and assumption of soil layer model were so simple, this relation between soil moisture anomaly persistency, field capacity of soil layer and Ep was partly proved in the observation in central Eurasia (Vinnikov and Yeserkepova, 1991).

In the recent years, more realistic and sophisticated land surface models (LSMs) have been developed, and many sensitivity experiments with GCMs have been conducted using different types of LSMs under different experimental designs. For example, Douville et al. (2001) and Douville (2002) assessed the influence of soil moisture on seasonal and interannual variability of Asian and African monsoons. Through some ensemble experiments with and without an interactive LSM (named ISBA; Interaction between Soil Biosphere and Atmosphere model), they found that the impact of soil moisture anomaly through the land-atmosphere interactive process is significant in relatively dry monsoon regions (e.g., Indian subcontinent and northeast Asia) but not in the humid monsoon regions (e.g., southeast Asia). They also noticed that in the significant impact regions soil moisture anomaly primarily plays a role as an initial condition (at the monsoon onset phase) rather than the boundary condition. Kanae et al. (2004) also performed a set of hindcast GCM simulation (with prescribed sea surface temperature) on boreal summer hydro-climate for about 40 years (1951-1998), with and without realistic soil moisture anomalies, and noticed that only semi-arid regions in the peripheries of monsoon regions showed reasonably good simulated precipitation with the observed ones. It is interesting to note that all the GCM experiments, though the LCM performance and simulation design are quite different from each other, have shown relatively high impact of soil moisture anomaly in dry or semi-arid regions. This general tendency of soil-precipitation

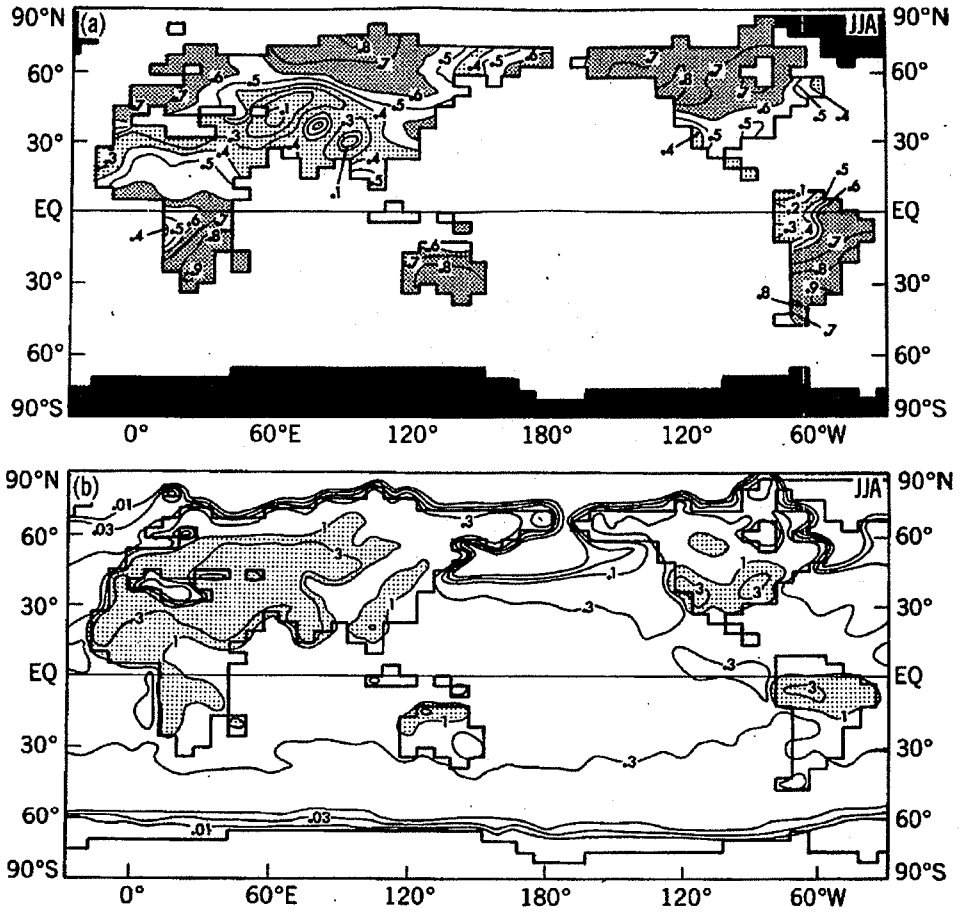

Figure 8.4 (a) Lag one autocorrelation values of soil moisture for the months of June, July and August(JJA) for SMI. At each grid point, deviations of monthly mean soil moisture from the long-term mean for that month were correlated with data from the same grid point, but lagged one month. Coefficients greater than 0.16(0.3) are significantly different from zero at the 95%(99.9%) confidence level (see Chatfield, 1984, p.63). Values greater than 0.6 are densely stippled, while value less than 0.4 are lightly stippled. Permanently ice-covered region are black. (b)Potential evaporation (cm d^{-1}) for JJA in SMI. (Delworth and Manabe, 1989)

feedback has comprehensively been confirmed by the recent Global Land Atmosphere Coupling Experiment (GLACE) (Koster et al., 2004), where twelve GCMs with different LCMs participated. For example, in the Asian monsoon region, the sensitivity of precipitation change to soil moisture condition is large only in relatively dry areas, e.g., Indian subcontinent and the Yellow-river/inner Mongolia in China as shown in Figure 8.5. In humid monsoon and tropical

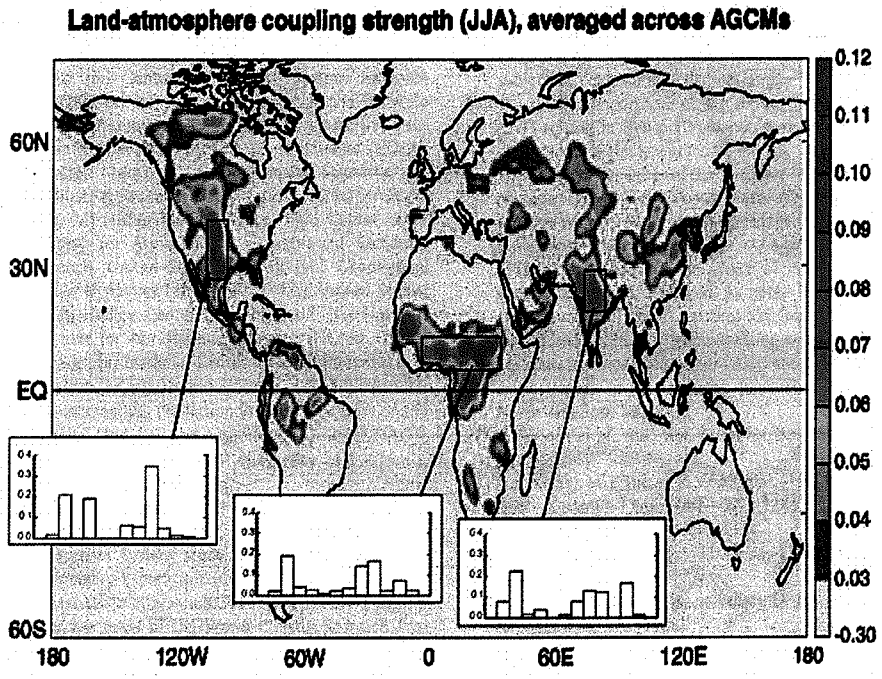

Figure 8.5 The land-atmosphere coupling strength diagnostic for boreal summer (the Ω difference, dimensionless, describing the impact of soil moisture on precipitation), averaged across the 12 models participating in GLACE. (Insets) Area-averaged coupling strengths for the 12 individual models over the outlined, representative hotspot region. No signal appears in southern South America or at the southern tip of Africa. (Koster et al., 2004)

regions, the impact seems to be small or insignificant primarily due to already-saturated soil moisture condition. However, this characteristic nature of weak soil moisture memory effect in the humid tropics may, to some extent, counteract with the relatively long memory effect in the humid tropics (Wu and Dickinson, 2004). In addition, the soil moisture anomaly may be important as an initial condition to switch on the interaction with precipitation in these relatively dry regions.

8.2.2. Role of vegetation and land use/land cover changes

a). Some new aspects from observational studies

Another important aspect of land-atmosphere interaction in addition to soil moisture (and snow cover) may be a role of vegetation. In the Asian monsoon region and topical land regions, most of the areas are heavily covered by

vegetation, including tropical rain and monsoon forests, water-fed paddy field, grass land and boreal forest etc. The roles of vegetation in land-atmosphere interaction may be classified as follows;

1) control of radiation and energy fluxes through albedo and roughness
2) control of transpiration through stomatal resistance
3) control of substantial field capacity of soil with root depth and structure

Due to lack of observations particularly in the large-scale vegetation and its impact on climate and water cycle, this aspect has been noted only in the recent years. LSMs including these vegetation processes have also been developed and improved in the recent few decades or so (e.g., Dickinson and Henderson-Sellers, 1988, Sellers et al., 1986), though these models need numerous number of tuning parameters. To improve and fully utilize these sophisticated models, however, observational studies are also essential, including optimal determination of these parameter values. In the Asian monsoon region, intensive field campaigns related to some international projects such as GAME have been conducted, and have revealed new aspects of the role of vegetation in terms of energy and water cycle processes.

In the evergreen tropical forest in Thailand, energy and water flux measurements at several sites with different types of vegetation were conducted for more than two years as part of GAME-Tropics. The evapotranspiration estimated by a multi-layer model forced by the observed radiation, leaf area index (LAI) and other realistic parameters revealed that a seasonally maximum evapo-transpiration appeared in the late dry season (Figure 8.6) just before the monsoon onset when the ground surface was driest in the year (Tanaka et al., 2003). A LSM study including the effect of root depth to pump up water in deep soil layer could well simulate this seasonal feature when the mean root depth was set at 6m (Tanaka et al., 2004). This implies that effective field capacity must be set at an extremely large value in this case. In the deciduous monsoon forest in Thailand, in contrast, the seasonal maximum of evapo-transpiration appeared in late monsoon season, associated with seasonal photosynthetic activity and water availability (Toda et al., 2002). These dependencies of the seasonal variation of evapo-transpiration (i.e., latent heating) on dominant vegetation types may have a great impact on modeling of regional and large-scale climate and water cycle, particularly in the tropics.

In the boreal forest in Siberia, similar long-term flux measurements were made in Lena river basin as part of GAME-Siberia (Ohta et al., 2001) as shown in Figure 8.7. Here, surface energy partition (sensible vs. latent energy) is strongly controlled by phenology of the (larch) forest coupled with seasonal melting (and

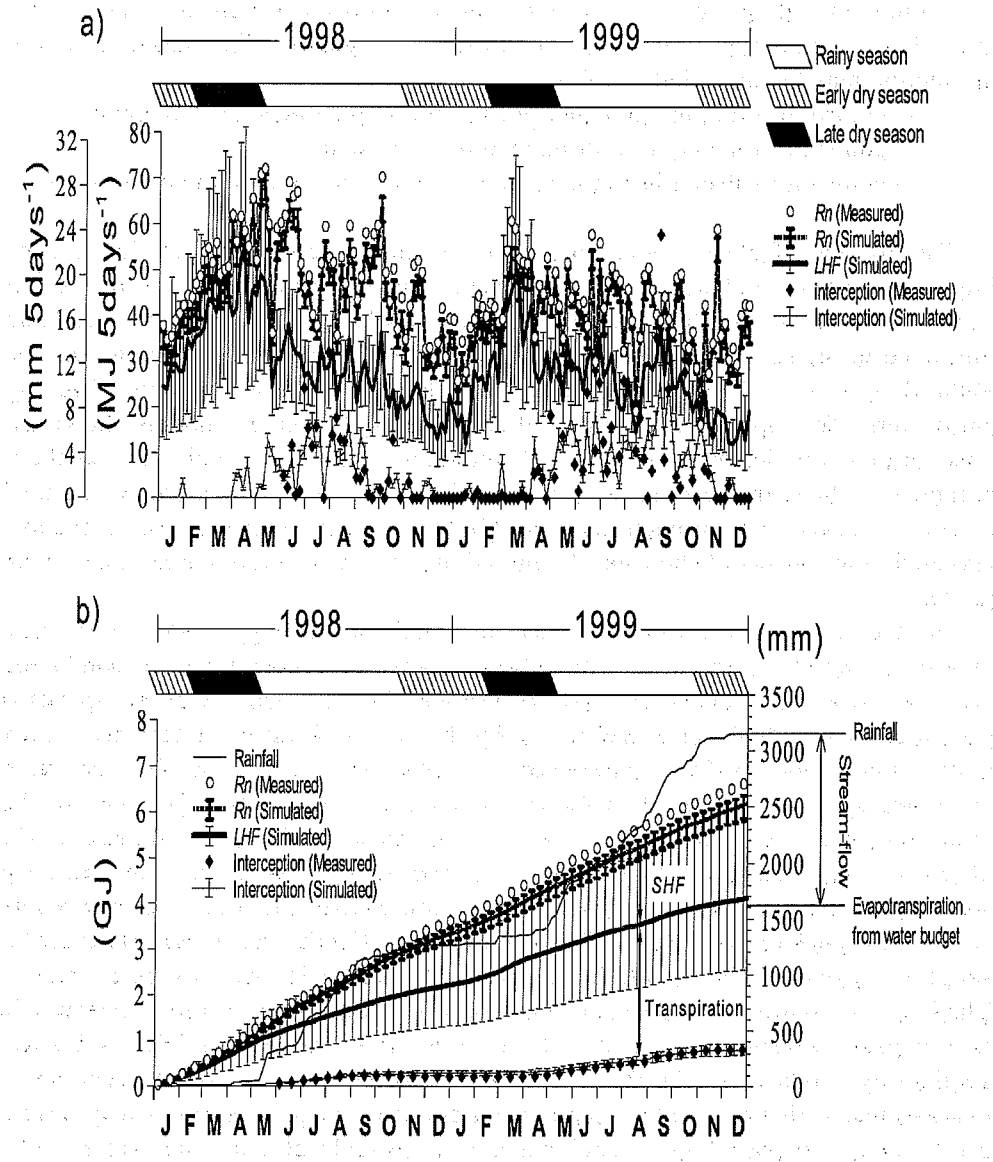

Figure 8.6 (a) Simulation of the seasonal variation in the net radiation and latent heat over an evergreen forest and rainfall interception in 1998 and 1999. (b) The cumulative result. In the figure the top and bottom of the vertical bar indicates the maximum and minimum, respectively, of the 32 simulated values. The line in between shows the average. (Tanaka et al., 2003)

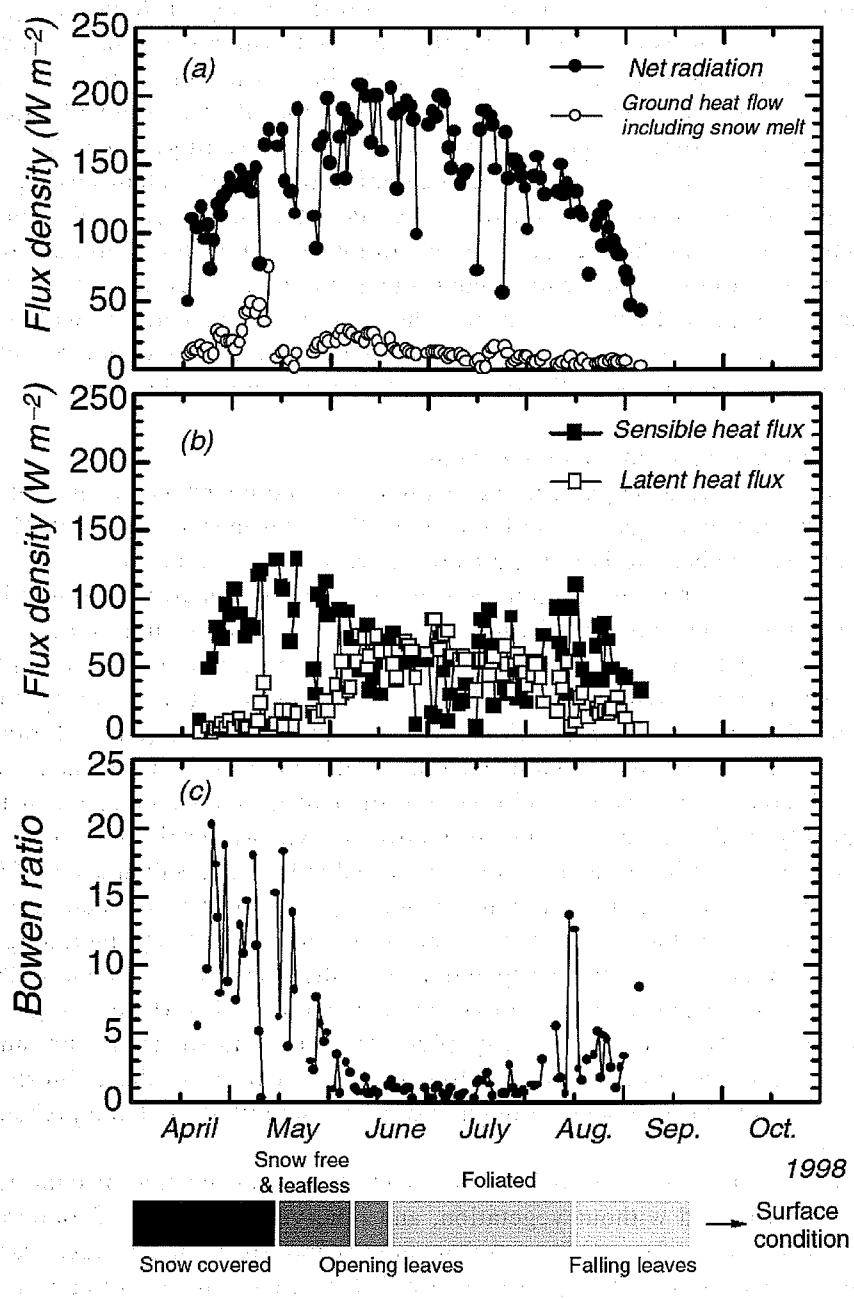

Figure 8.7 Time-series for the daily net all-wave radiation and the ground heat flow (a), the sensible heat flux and the latent heat flux (b), and the Bowen ratio (c). The energy balance components and the Bowen ratio indicated in this figure are for a dry canopy only (Ohta et al., 2001)

freezing) condition of permafrost beneath the forest. Namely, in May during and after the snow melt sensible heating greatly increased, which was mostly used for melting the frozen ground. At the beginning of June when the melted layer of ground reaches about 20 cm depth or so, the foliation of trees suddenly started which at the same time triggered transpiration (latent heating) from the trees. During mid-summer (June, July and the beginning of August) latent heating rate was comparable or more than sensible heating rate, and most of the annual precipitation occurs in this period. This condition prevailed for a broad area of Siberian boreal forest zone, which contributes to water recycling as well as maintenance of permafrost, by limiting the melting of permafrost within the near-surface layer. Thus, the boreal forest and permafrost of this region are likely to co-exist as a symbiotic eco-climate system through energy and water cycle.

b). Some new aspects from modeling studies

The potential role of large-scale vegetation and land cover on Asian monsoon has recently been investigated also by some GCM experiments. Xue et al. (2004) showed that some characteristic features of the east Asian summer monsoon, e.g., abrupt northward jump of rainfall belt in the seasonal march and low-level monsoon circulation, are far better simulated when they introduced more sophisticated vegetation scheme of SSiB with realistic vegetation distribution than a simple vegetation scheme without physiological processes (i.e., photosynthesis and stomatal control of transpiration). The abrupt northward jump of rainfall could occur due to strong sensible heating in the interior of East Asia which induced horizontal temperature and pressure gradient in the pre-monsoon season. This probably wad related to stomatal control of evapo-transpiration in the dry and hot season, resulting in enhancement of sensible heating. Suh and Lee (2004) also showed in the regional climate model experiment that temperature and rainfall biases over East Asia have improved considerably by including the biospheric processes of realistic vegetation over the east Asian landmass. These experiments have suggested that physiological control of surface energy flux partitioning (i.e., Bowen ratio) greatly affect pressure gradient over land, and in turn, circulation and rain systems. However, the reality of these biospheric processes needs to be validated through in-situ and satellite-based comprehensive observations.

We conducted a series of GCM experiments assessing the role of continental land surface with and without vegetation, and relative importance of topography and vegetation on the formation of Asian summer monsoon. In this case, various vegetation types are simply represented by difference in albedo, roughness and field capacity of surface soil layer (Yasunari et al., 2006; Saito et al., 2006). These experiments do not explicitly include the physiological processes of vegetation in the model, but the difference in field capacity of soil layer is expected to hold an important nature of vegetated or non-vegetated surface since the soil layer is basically produced by vegetation itself. The results suggest the role of vegetation is generally very large to produce strong monsoon as it is, and

relative roles of albedo and field capacity of soil have appeared to be different from region to region. In East Asia both the Tibetan plateau topography and vegetation are important for penetration of moist monsoon flow and precipitation. In addition, relative importance of albedo vs. field capacity seems to be different from region to region. In the East Asia the albedo effect of vegetation is more important, but in the south/southeast Asia the role of large field capacity has proved to be more important to produce the stronger monsoon particularly in the mid monsoon season, as shown in Figure 8.8. These numerical experiments have strongly suggested that in the Asian monsoon region the role of vegetation is essential for the formation of monsoon circulation and precipitation through strong latent heating of the atmosphere. The evapo-transpiration from vegetated surface plays a crucial role in forming thick moist boundary layer and convection for the latent heating, as will be described in the next session.

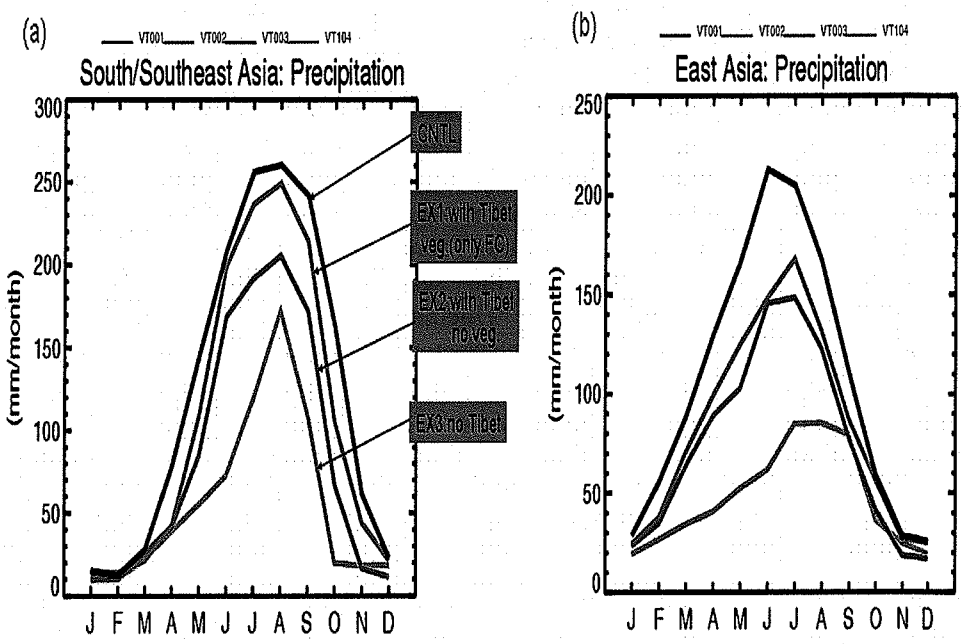

Figure 8.8 Changes of seasonal precipitation for (a) south/southeast Asia and (b) east Asia for different boundary conditions of (1) no Tibetan Plateau, no vegetation (bared surface with rock albedo and roughness) (blue) (2) with Tibetan Plateau, but no vegetation (red), (3) with Tibetan Plateau and vegetation (soil only) (green), and (4) with Tibetan Plateau with full vegetation (with soil and realistic vegetation albedo and roughness) (black).
Yasunari et al. (2005)

8.3 Coupling of land-surface, ABL and cloud/precipitation processes

Impacts of land surface processes to the atmosphere are brought about through modification of the atmospheric boundary layer (ABL), and relevant cloud processes at or above the ABL. Betts et al. (1998) reviewed the overall possible interactive processes between land surface conditions and the ABL, and emphasized the importance of vegetation and related land cover/use differences on the ABL structure and cloud/precipitation process. In the monsoon region, the advection or inflow of moist flow from oceans to the land is sometimes emphasized to produce monsoon rainfall in the in the interior of the land area. However, through some continental-scale experiments (CSEs) under GEWEX (e.g., GAME in Asian monsoon region, LBA in Amazon basin) moisture supply from wet land surface has also been proved to be important particularly in the late monsoon season when the surface becomes wetter than the earlier stage of the monsoon season. Shinoda and Uyeda (2002) examined a possible impact of water-fed paddy field in East Asia, using cloud-resolving atmospheric model. They forced the model using latent and sensible heat fluxes over the paddy field observed in GAME-Huaihe Basin Experiment (HUBEX) , and found that meso-scale cloud systems embedded in the Meiyu (Baiu) front developed through moisture supply to ABL and change of moist static stability of the lower troposphere. This change of land-atmosphere interaction and its impact on cloud/precipitation systems through the seasonal change of soil moisture condition was also observed over the Tibetan Plateau during the GAME-Tibet (Yamada et al., 2004). In fact, these characteristic changes of water balance or recycling process of water vapor between land surface and atmosphere through the seasonal march of the summer monsoon have been noticed in various part of the continent (Yasunari and Kozawa, 2005). Understanding of these non-linear feedbacks from precipitation to land surface condition may have some clue for prediction of seasonal as well interannual variation of precipitation in the Asian monsoon region.

8.4 Possible impact of anthropogenic land use/cover changes on Asian monsoon climate

The Asian monsoon region is heavily populated with nearly 60% of the people on the earth are living. Therefore, the anthropogenic land use and land cover changes have been one of the largest in the world. These land use/cover changes from the original vegetation has a high possibility to have changed regional climate and water cycle of this region. Fu (2003) investigated potential impacts of human-induced land cover change on the East Asian monsoon,assuming the present and the potential vegetation (Ojima, 2000). Using a regional model (MM5) with a land surface scheme (BATS), he noticed that the land cover change occurred in the history of China may have weakened the East Asian summer monsoon and strengthened the winter monsoon. The weakened monsoon trough in the interior of the continent presumably induced by decreased latent heating is responsible for the weakened summer monsoon.

Xue (1996) focused on the impact of desertification in the Mongolian and the inner Mongolian grassland on East Asian monsoon climate, by changing the area of desertification in the GCM. He found that the desertification is further intensified by altering from the grassland-type to the desert-type land surface due to the reduction in evaporation and convective latent heating above the surface layer. This process seems to be contrastive to the positive feedback of desertification in the Sahel, west Africa where enhanced radiative cooling and associated sinking motion induced by increased albedo is likely to be a main mechanism (Charney, 1975).

In the Indo-china peninsula, a decreasing trend of monsoon rainfall has been remarkably seen only in September during the past several decades. Kanae et al. (2001) tried to explain this feature as a result of deforestation in the central part of the peninsula using a regional climate model (RAMS). They noticed that the effect of deforestation by changing albedo, roughness and soil moisture condition significantly reduced rainfall only in September when the monsoon westerly flow seasonally became weak considerably as shown in Figure 8.9. In other monsoon months, the effect of the deforestation was negligible because the effect of strong inflow and convergence of moist monsoon flow was dominated over this region. These results suggested that the impact of land surface condition, i.e., vegetation cover, soil moisture etc., changes depending upon the atmospheric conditions including large-scale wind field, thermal stability etc.

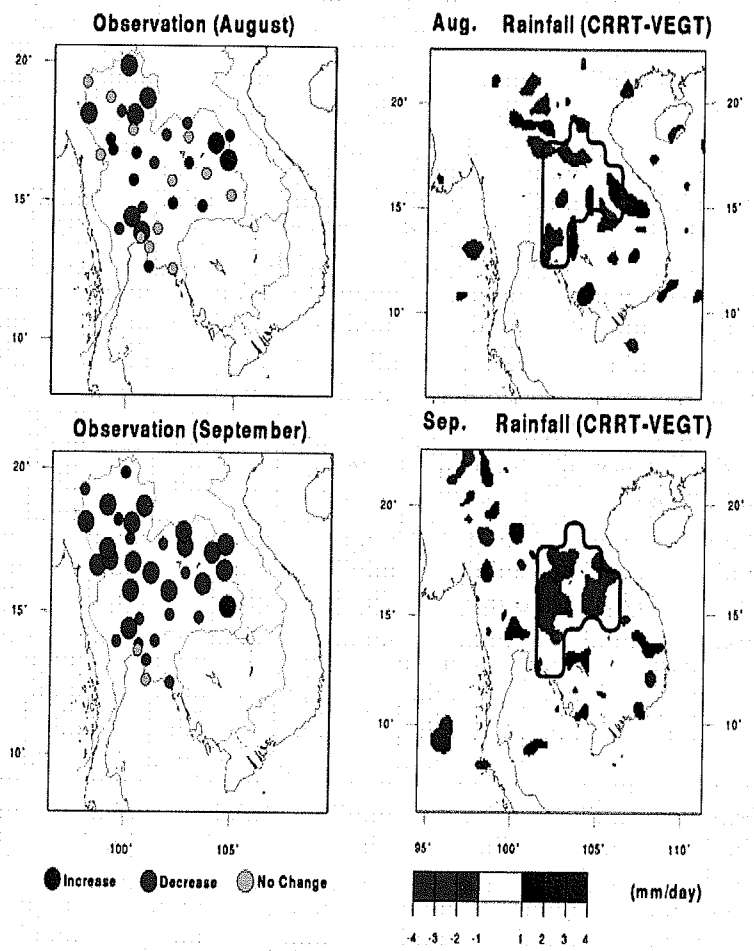

Figure 8.9 Observed Rainfall trend during 1950-1990 in August (left, upper) and September (left, lower) and rainfall difference in August (right, upper) and September (right, lower) computed between vegetated condition and deforested condition. Blue (red) colour shows increasing trend or positive values, and size of circles in the left column shows trend values (Kanae et al., 2001).

8.5 Feedback processes through energy and water cycle

A key process of regional climate and water cycle change by the land use/cover change including deforestation may be how the land surface change does induce changes of moisture convergence (C) and in-situ evapotranspiration (E)

which result in change of precipitation (P). This issue can be more generally interpreted as a fundamental energy and water cycle process of an interaction between an area-limited land surface condition and large-scale atmospheric environment or circulation. This issue was discussed in terms of deforestation in the Amazon basin by Zeng et al. (1996) and Zeng (1998). Figure 8.10 shows a schematic diagram of the two feedback loops in the perturbed land surface area in the atmospheric water cycle. Change in P is controlled by two mechanisms: C feedback (right hand side) and E feedback (left hand side). In the first mechanism, an increase in P releases latent heat that drives large-scale upward motion (w), which causes more moisture convergence, leading to more P. In the E feedback, higher P leads to a wetter surface and more evaporation, which in turn contributes to even more P. If these two positive feedbacks overlap and work at the same time, a higher sensitivity of P to land surface change appears. However, if the P increase causes decrease in radiation through, for example, cloud cover increase, the increase of C is partially compensated by decrease of E due to decrease of radiation. An essential issue in the C feedback may be how P increase contributes to increase of large-scale upward motion (w).

Assuming the thermodynamic balance neglecting the horizontal temperature advection, radiative heating approximated by Newtonian cooling, convective latent heating proportional to P, the moisture closure (i.e., P = E + C), and C proportional to w and humidity q in the boundary layer, the P change (ΔP) can be approximated as a simple equation as follows (Zeng et al., 1996; Zeng, 1998):

$$\Delta P = q \epsilon \Delta T^* / (1-q-\beta) \qquad (8.1)$$

where q is a measure of moist static stability (unstable if $q > 1$), T^* is an atmospheric equilibrium temperature, β($\equiv Ep/P_0$) is a ratio of potential evaporation Ep to a threshold precipitation rate P_0, above which soil is saturated. ϵ is a constant relevant to radiation relaxation and atmospheric latent heat profile.

In the tropics near the equator, this positive C feedback roughly depends upon whether the horizontal scale of the perturbed area is larger than the equatorial radius of deformation (Zeng, 1998). In the off-equatorial monsoon region, however, the influence of large-scale moisture advection is dominated and the feedback loops (as shown in Figure 8.10) may not be so simple. The impact of deforestation may be apparent through the two positive feedback loops when the environmental monsoon flow is weak, as is demonstrated in September case of Thailand (Kanae et al., 2001). In the relatively dry or marginal-monsoon region (e.g., the north-west part of Indian subcontinent, the Mongolia and northern China) where the sensitivity of P to soil moisture anomaly is large as discussed in 4.2.2, the positive feedback loops as shown in Figure 8.10 may be strong mostly due to large β under relatively dry condition. We should keep in mind that relatively humid regions under the Asian summer monsoon climate, the atmospheric boundary layer and the lower troposphere are close to be saturated, that is, q is relatively large. This condition also increases the sensitivity of P under

the slight change of the surface condition (e.g., albedo) and in turn change of radiational forcing. The large impact of water-fed paddy field in China on development of cloud/precipitation system in the Meiyu frontal zone may correspond to this situation.

This simple model of energy and water balance can be applied in understanding the role of land atmosphere interaction of large-scale Asian monsoon system. For example, when we compare the pre-onset phase and the mature phase of the monsoon season, we notice that Δ P between the two season is basically due to change of T* derived from seasonal change of solar radiation, but the enhancement of the P change is due to change of q and β, derived from moisture convergence and *in situ* evaporation, respectively (Yasunari and Kozawa, 2006). Without these moist processes, the large Asian monsoon system with huge P particularly over land area may not be formed as it is.

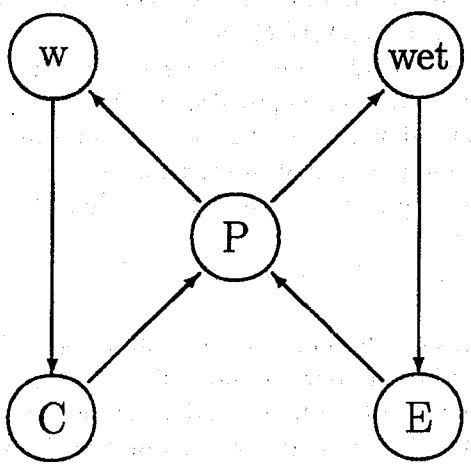

Figure 8.10 The two major feedback loops in the perturbed region: moisture convergence feedback and evaporation feedback. Here, P is precipitation, w is large-scale upward motion, C is large-scale moisture convergence, wet is surface wetness, and E is evapotranspiration. (Zeng, 1998).

8.6 Concluding remarks

This chapter has discussed the role of land-atmosphere interaction in the Asian monsoon system and tropical land areas. Particular emphasis and focus has been put on roles of large-scale orography (e.g., Tibetan Plateau) and continental or regional-scale soil moisture and vegetation.

The role of the Tibetan Plateau is emphasized to trigger the atmospheric heating over the continent. At the onset or pre-monsoon phase of the monsoon, sensible heating over the elevated land surface plays an important role to form the continental-scale heat low in the lower troposphere. This circulation system in turn produces moist southwesterly flow penetrating into the south, southeast and East Asia. This moist monsoon flow induces convection and precipitation over the southeastern part of the continent, which further intensifies atmospheric diabatic heating through latent heat release.

Another parameter, vegetation, has been noted as an important variable for the formation of moist monsoon flow over the continent. Vegetation has several functions for controlling atmospheric energy and water vapor conditions, such as albedo, roughness, stomatal conductance and water-holding capacity of root/soil structure. In fact, through the recent observations and modeling studies, the atmospheric latent heating over land has been noticed fundamentally through vegetation control of evapo-transpiration. The anthropogenically-induced change of land cover/use including the deforestation has a great impact on regional precipitation and water cycle of the monsoon region by changing some characteristics of vegetation control of energy and water cycle, which in turn affect ABL and cloud/precipitation processes in regional-scale.

Finally, a general discussion has been made on how the land surface changes could induce change of precipitation through feedback processes of moisture convergence and in-situ evapo-transpiration processes. In this simple discussion the critical role of moisture amount near surface and in the ABL is emphasized, to induce positive feedback to change of precipitation over land in the monsoon region.

In the Asian monsoon system, the fundamental heating centers are located over the warm oceans near the continent, which has also proved to be resulted from the strong thermal and thermo-dynamical effect of the Tibetan Plateau (Kitoh, 2002; Abe et al., 2004). In addition, we could emphasize that the moist land surface could play an important role for the penetration of precipitation deep interior of the continent. This moist land surface process has proved to be attributed essentially to the existence of vegetation. Thus, it has strongly been suggested that the heavily vegetated land surface in the Asian monsoon region and the humid tropics (e.g., the Amazonia) play a key role for maintaining the humid climate itself.

References

Abe, M., Kitoh, A., and Yasunari, T., (2003), An evolution of the Asian summer monsoon associated with mountain uplift —Simulation with the MRI atmosphere-ocean coupled GCM— J, Meteor, Soc, Japan, 81, 909-933.

Abe, M., Yasunari, T., and Kitoh, A., (2004), Effects of large-scale orography on the coupled atmosphere-ocean system in the tropical Indian and pacific oceans in boreal summer J, Meteor, Soc, Japan, 82, 745–759.

Betts, A.K., Viterbo, P., Beljaars, A., Pan, H.-L., Hong, S.-Y., Goulden, M., and Wofsy, S., (1998), Evaluation of land-surface interaction in ECMWF and NCEP/NCAR reanalysis models over grassland (FIFE) and boreal forest (BOREAS), J, Geophys, Res., 103, 23079-23086.

Charney, J.G., (1975), Dynamics of deserts and droughts in Sahel, Quart, J, Roy, Meteor, Soc.,.101, 193-202.

Delworth, T., and Manabe, S., (1988), The influence of potential evaporation on the variabilities of simulated soil wetness and climate, J, Climate, 1, 523–547.

Delworth, T., and Manabe, S., (1989), The influence of soil wetness on near-surface atmospheric variability, J, Climate, 2, 1447–1462.

Dickinson, R.E, and Henderson-Sellers, A., (1988), Modeling tropical deforestation: A study of GCM land-surface parameterizations, Quart, J, Roy, Meteor, Soc., 114, 439-462.

Douville, H., Chauvin, F., and Broqua, H., (2001), Influence of soil moisture on the Asian and African monsoons, Part I, Mean monsoon and daily precipitation, J.Climate, 14, 2381-2403.

Douville, H., (2002), Influence of soil moisture on the Asian and African monsoon, Part II, Interannual variability, J.Climate, 15, 701-720.

Fu, C.-B., (2003), Potential impacts of human-induced land cover change on east Asian monsoon, Global Planetary Change, 37, 219-229.

Jiang, X., Li T., and Wang, B., (2004), Structure and mechanisms of the northward propagating boreal summer intraseasonal oscillation, J, Climate, 17, 1022-1039.

Kanae, S., Hirabayashi, Y., Yamada, T., and Oki, T., (2006), Influence of "realistic" land-surface wetness on predictability of seasonal precipitation in boreal summer, J, Climate, 19, 1450-1460.

Kanae, S., Oki, T., and Musiake, K., (2001), Impact of Deforestation on Regional Precipitation over the Indochina Peninsula, J, Hydrometeorol., 2, 51-70.

Kawamura, R., (1998), A possible mechanism of the Asian summer monsoon-ENSO coupling, J, Meteor, Soc, Japan, 76, 1009-1027.

Kawamura, R., Fukuta, Y., Ueda, H., Matsuura, T., and Iizuka, S., (2002), A mechanism of the onset of the Australian summer monsoon, J, Geophys, Res., 107 (D14), doi:10.1029/2001JD001070.

Kitoh, A., (2002), Effects of Large-Scale Mountains on Surface Climate —A Coupled Ocean-Atmosphere General Circulation Model Study, J, Meteor, Soc, Japan, 80, 1165-1181.

Koster et al., (The GLACE Team) (2004), Regions of strong coupling between soil

moisture and precipitation, Science, 305, 1138-1140.
Manabe, S., (1969), Climate and the Ocean circulation, I, The atmospheric circulation and the hydrology of the earth's surface, Mon.Wea, Rev., 97, 739-774.
Ohta, T., Hiyama, T., Tanaka, H., Kuwada, T., Maximov, T.C., Ohata, T., and Fukushima, Y., (2001), Seasonal variation in the energy and water exchanges above and below a larch forest in eastern Siberia, Hydrological Processes, 15(8), 1,459-1,476.
Ojima, D., (2000), *Land use/lane cover change in temperate East Asia: current status and future trend*, International START Secretariat, Washington DC, USA, 228pp.
Otterman, J., (1974), Baring high-albedo soils by overgrazing, a hypothesized desertification mechanism, Science, 186, 426-427.
Robock A., Schlosser, C.A., Vinnikov, K.Y., Speranskaya, N.A., Entin, J.K., and Qiu, S., (1998), Evaluation of the AMIP soil moisture simulations, Global Planetary Change, 19, 181-208.
Robock, A., Vinnikov, K.Y., Srinivasan, G., Entin, J.K., Hollinger, S.E., Speranskaya, N.A., Liu, S., and Namkhai, A., (2000), The Global Soil Moisture Data Bank, Bull, Amer, Meteor, Soc., 81, 1281-1299.
Robock, A., Mu, M., Vinnikov, K., and Robinson, D., (2003), Land surface conditions over Eurasia and Indian summer monsoon rainfall, J, Geophy, Res., 108, 4131.
Saito, K., Yasunari, T., and Takata, K., (2006), Relative roles of large-scale orography and land surface prcesses on global hydro-climate, Part, II, Impacts on hydro-climate over the Eurasian continent, J, Hydrometeoroly (in press).
Sellers, P.J., Mintz, Y., Sud, Y.C., and Dalcher, A., (1986), A simple biosphere model (SiB) for use within general circulation models, J, Atmos.Sci., 43, 505-531.
Shankar-Rao, P., Lau, K.M., and Yang, S., (1996), On the relationship between Eurasian snow cover and the Asian summer monsoon, Int, J, Climatol., 16, 605-616.
Shen, X., Kimoto, M., and Sumi, A., (1998), Role of land surface processes associated with interannual variability of broad-scale Asian summer monsoon as simulated by the CCSR/NIES AGCM, J, Meteor, Soc, Japan, 76, 217-236.
Shinoda, M., and Gamo, M., (2000), Interannual variations of boundary layer temperature over the African Sahel associated with vegetation and upper-troposphere, J, Goeph, Res., 105, 12317-12327.
Shinoda, M., Morinaga, Y., and Yasunari, T., (2003), The forefront of monsoon researches, Kisho kenkyu note (edi., by R, Kawamura), 204, 69-114 (in Japanese).
Shinoda, T., and Uyeda, H., (2002), Effective Factors in the Development of Deep Convective Clouds over the Wet Region of Eastern China during the Summer Monsoon Season, J, Meteor, Soc, Japan, 80, 1395-1414.
Suh, M.-S., and Lee, D.-K., (2004), Impact of land use/cover changes on surface

climate over east Asia for extreme climate cases using RegCM2, J, Geophys, Res., 109, D020108, doi:10.1029/2003JD003681.
Tanaka, K., Takizawa, H., Tanaka, N., Kosaka, I., Yoshifuji, N., Tantasirin, C., Piman, S., Suzuki, M., and Tangtham, N., (2003), Transpiration peak over a hill evergreen forest in northern Thailand in the late dry season: Assessing the seasonal changes in evapotranspiration using a multilayer model, J, Geophys, Res., 108(D17), 4533, doi:10.1029/2002JD003028.
Tanaka, K., Takizawa, H., Kume, T., Xu, J., Tantasirin, C., and Suzuki, M., (2004), Impact of rooting depth and soil hydraulic properties on the transpiration peak of an evergreen forest in northern Thailand in the late dry season, J, Geophys, Res., 109, D23107, doi:10.1029/2004JD004865.
Toda, M., Nishida, K., Ohte, N., Tani, M., and Musiake, K., (2002), Observation of Energy Fluxes and Evapotranspiration over Terrestrial Complex Land Covers in the Tropical Monsoon Region, J, Meteorol, Soc, Jpn., 80(3), 465-484.
Ueda, H., Kamahori, H., and Yamazaki, N., (2003), Seasonal contrasting features of heat and moisture budgets between the eastern and western Tibetan Plateau during the GAME IOP, J, Climate, 16, 2309–2324.
Ueda, H., and Yasunari, T., (1998), Role of warming over the Tibetan Plateau in early onset of the summer monsoon over the Bay of Bengal and the South China Sea, J, Meteor, Soc, Japan, 76, 1-12.
Vinnikov, K.Y, and Yeserkepova, I.B., (1991), Soil moisture: Empirical data and model results, J, Climate, 4, 66-79.
Walsh J.E., Jasperson, W.H., and Ross, B., (1985), Influence of snow cover and soil moisture on monthly air temperature, Mon, Wea, Rev., 113, 756-768
Wang, B., Webster, P.J., Kikuchi, K., Yasunari, T., and Qi, Y., (2006), Quasi-monthly monsoon oscillation: A satellite perspective and mechanisms, Submitted to J, Climate.
Webster, P.J., Magaña, V.O., Palmer, T.N., Shukla, J., Thomas, R.A., Yanai, M., and Yasunari, T., (1998), Monsoons: Processes, predictability, and the prospects for prediction, J, Geophys, Res., 103(C7), 14451-14510.
Wu, W., and Dickinson, R.E., (2004), Time scales of layered soil moisture memory in the context of land-atmosphere interaction, J, Climate, 2752-2764.
Xue, Y., Juang, H.-M.H., Li, W.-P., Prince, S., DeFries, R., Jiao, Y., Vasic, R., (2004) Role of land surface processes in monsoon development: East Asia and West Africa, J, Geophys, Res., 109, D03105, doi:10.1029/2003JD003556.
Xue, Y., (1996), The impact of desertification in the Mongolian and the Inner Mongolian Grassland on the regional climate, J, Climate, 9, 2173-2189.
Yamada, H., and Uyeda, H., (2004),, Transition of the Precipitation Process over the Central Tibetan Plateau during the Summer of 1998, submitted to Mon, Wea, Rev.
Yasunari, T., (1991), The monsoon year —A new concept of the climatic year in the tropics, Bull, American.Meteorol, Soc., 72, 1131-1138.
Yasunari, T., Saito, K., and Takata, K., (2006), Relative Roles of large-scale orography and land surface processes on global hydro-climate, Part I, Impacts

on monsoon systems and tropics, J, Hydrometeorology (in press).
Yasunari, T., and Kozawa, A., (2006), Time-space characteristics of atmospheric water balance over Eurasia, To be submitted.
Yasunari, T., (2006), Land-atmosphere interaction, Chap.11, In The Asian monsoon, Ed, By B, Wang, Praxis, Springer Berlin Heidelberg, 459-478.
Zeng, N., Dickinson, R., and Zeng, X., (1996), Climatic impact of Amazon deforestation—A mechanistic model study, J, Climate, 9, 859–883.
Zeng, N., (1998), Understanding climate sensitivity to tropical deforestation in a mechanistic model, J, Climate, 11, 1969–1975.

Chapter 9

Plant responses to elevated CO_2 concentration at different scales: leaf, whole plant, canopy, and population

Kouki Hikosaka
Graduate School of Life Sciences,
Tohoku University, Aoba, Sendai 980-8578, Japan
Tel: +81-22-795-7735
+81-22-795-6698
Fax: +81-22-795-6699
e-mail: hikosaka@mail.tains.tohoku.ac.jp

9.1 Abstract

Elevated CO_2 enhances photosynthesis and growth of plants, but the enhancement is strongly influenced by the availability of nitrogen. In this article, we summarise our studies on the plant response to elevated CO_2.

Photosynthetic capacity of leaves depends not only on leaf nitrogen content but also on nitrogen partitioning within a leaf. In *Polygonum cuspidatum*, nitrogen partitioning in the photosynthetic apparatus was not influenced by elevated CO_2 but changed with seasons. Since the alteration in nitrogen partitioning resulted in different CO_2 dependence of photosynthetic rates, enhancement of photosynthesis by elevated CO_2 was greater in autumn than in summer.

Enhancement of reproductive yield by elevated CO_2 is often smaller than that expected from vegetative growth. In *Xanthium canadense*, elevated CO_2 did not increase seed production, though the vegetative growth increased by 53%. As nitrogen concentration of seed remained constant at CO_2 levels, we suggested that the availability of nitrogen limited seed production at elevated CO_2.

Does elevated CO_2 increase leaf area index (LAI, leaf area per unit ground area) of the canopy? We found that leaf area development was strongly constrained by the availability of nitrogen rather than CO_2 levels. In a rice field cultivated at free-air CO_2 enrichment, LAI increased with an increase in nitrogen availability but did not change with CO_2 elevation. We determined optimal LAI to maximize canopy photosynthesis and demonstrated that enhancement of canopy photosynthesis by elevated CO_2 was larger at high nitrogen availability.

We also studied competitive asymmetry among individuals in an even-aged

monospecific stand at elevated CO_2. Light acquisition (acquired light per unit aboveground mass) and utilisation (photosynthesis per unit acquired light) were calculated for each individual in the stand. Elevated CO_2 enhanced photosynthesis and growth of tall dominants, which reduce the light availability for shorter subordinates and consequently increased size inequality in the stand.

9.2 Introduction

In these 200 years, the atmospheric CO_2 concentration increased from a pre-industrial level 280 μmol mol^{-1} to 370 μmol mol^{-1} (2004). It is still increasing at the rate of 1.5 μmol mol^{-1} per year and may reach 700 μmol mol^{-1} at the end of this century (IPCC 2001). Because CO_2 is a substrate for photosynthesis, an increase in atmospheric CO_2 concentration stimulates photosynthetic rates in C_3 plants (Kimball, 1983; Cure and Acock, 1986; Bazzaz, 1990; Poorter, 1993; Sage, 1994; Curtis, 1996; Ward and Strain, 1999). However, the effect of elevated CO_2 on growth and reproduction is often much weaker than that predicted by the photosynthetic response. It also differs considerably between species and between plants grown under different conditions (Bazzaz, 1990; Arp, 1991; McConnaughay et al., 1993; Sage, 1994; Farnsworth and Bazzaz, 1995; Makino and Mae, 1999; Ward and Strain, 1999; Jablonski et al., 2002). Nutrient availability has been considered as one of key factors for the variation in plant responses to elevated CO_2 (e.g. Ziska et al., 1996; Lutze and Gifford, 1998; Kim et al., 2001; Stitt and Krapp, 1999; Kimball et al., 2002).

Of soil nutrients, nitrogen is one of the most important elements that limit plant growth in many natural and managed ecosystems (Aerts and Chapin 2000). Since a large fraction of leaf nitrogen is in the photosynthetic apparatus, a strong correlation holds between photosynthetic capacity and nitrogen content of leaves (Evans, 1989; Hikosaka 2004). Higher photosynthetic rates at high CO_2 concentrations may lead to an imbalance of carbon and nitrogen in the plant body because carbon acquisition is stimulated relative to nitrogen uptake at elevated CO_2. Accumulated carbohydrates sometimes cause a feedback limitation of photosynthesis (Peterson et al., 1999; Medlyn et al., 1999; Stitt and Krapp, 1999).

Plants respond to the availability of limited resources by altering their physiological and morphological characteristics to ameliorate the resource imbalance. At low nutrient availability, for example, plants allocate more biomass to roots, which compensate for low nutrient uptake rates per unit root mass (Brouwer, 1962). This contributes to balancing carbon and nitrogen uptake and to the maximisation of relative growth rates (Hirose, 1987, 1988; Hilbert, 1990). CO_2 responses of plants may also involve adaptive acclimation, which potentially increases plant growth and reproduction at elevated CO_2. Optimality models may be useful to assess adaptability of plant responses (Anten et al., 2000).

In the GCTE-TEMA program, we studied plant responses to elevated CO_2 at different scales: leaf, whole-plant, canopy, and population. Nitrogen was considered as a key factor to analyse the variation in the CO_2 responses. Here we summarise our findings (Hikosaka et al., 2005).

9.3 Leaf

Leaf is a photosynthetic organ. Photosynthetic rate of a leaf is determined by the quantity and quality of leaf nitrogen. Not only the amount of nitrogen, but also partitioning of nitrogen between photosynthetic and non-photosynthetic proteins, and partitioning between photosynthetic components potentially affects photosynthetic rate (Hikosaka and Terashima, 1995). We studied nitrogen use in leaves grown at elevated CO_2 both theoretically and experimentally.

9.3.1 Nitrogen partitioning in the photosynthetic apparatus in leaves grown at elevated CO_2 concentrations: Importance of seasonal acclimation

Light-saturated rates of photosynthesis are limited either by Rubisco (ribulose-1,5-bisphosphate carboxylase/oxygenase) activity or by the RuBP regeneration process (Farquhar et al., 1980). The former tends to limit photosynthesis at lower CO_2 concentrations while the latter does so at higher CO_2 concentrations. The capacity of the two processes is considered to co-limit at around the current CO_2 concentration (Wullschleger, 1993). Therefore, under future higher CO_2 concentrations photosynthesis may be limited solely by the RuBP regeneration process. Both RuBP carboxylation and RuBP regeneration processes need a substantial amount of nitrogen to maintain high photosynthetic capacity (Evans and Seemann, 1989; Hikosaka, 1997). To use nitrogen efficiently, nitrogen should be reallocated from non-limiting to limiting process (Evans, 1989; Hikosaka and Terashima, 1995). It was suggested that nitrogen reallocation from RuBP carboxylation to the RuBP regeneration process would increase photosynthetic nitrogen use efficiency at elevated CO_2 (Sage, 1994; Webber et al., 1994; Medlyn, 1996). Using a theoretical model of nitrogen partitioning in the photosynthetic apparatus, Hikosaka and Hirose (1998) suggested that nitrogen reallocation in doubled CO_2 would increase photosynthesis by 20%. This prediction was supported by an experimental study with a transgenic rice plant with the reduced amount of Rubisco (Makino et al., 1997, 2000). When compared at the same nitrogen content, the transgenic rice had greater amounts of proteins in the RuBP regeneration process and higher photosynthetic rates at high CO_2 concentration than the wild type. In normal plants, however, nitrogen allocation between RuBP carboxylation and regeneration processes does not seem to be influenced by CO_2 concentrations at which plants are grown (Medlyn et al., 1999).

Recent studies, however, found that growth temperature affects the balance between RuBPCase and the RuBP regeneration process. Hikosaka et al. (1999)

demonstrated that *Quercus myrsinaefolia* leaves grown at a low temperature had a higher ratio of RuBP regeneration capacity (expressed as the maximum electron transport rate, J_{max}) to carboxylation capacity (V_{cmax}) than those grown at a high temperature, and consequently that photosynthesis was more sensitive to CO_2 in plants acclimated to low temperature. A similar trend was found by Wilson et al. (2000), who reported that autumn leaves had a higher ratio of J_{max}/V_{cmax} than summer leaves in several deciduous tree species of temperate forests. These results suggest that seasonal change in temperature alters the balance between RuBP carboxylation and RuBP regeneration, which will affect the extent of CO_2 stimulation of photosynthesis.

We tested the hypothesis that seasonal change in air temperature affects the balance and modulate the CO_2 response of photosynthesis (Onoda et al., 2005). V_{cmax} and J_{max} were determined in summer and autumn for leaves of *Polygonum cuspidatum* grown at two CO_2 concentrations. Elevated CO_2 concentration reduced both V_{cmax} and J_{max} without change in the J_{max}/V_{cmax} ratio. Seasonal environment, on the other hand, altered the ratio such that the J_{max}/V_{cmax} ratio was higher in autumn than summer leaves. This alteration made the photosynthetic rate more dependent on CO_2 concentration in autumn leaves (Figure 9.1). Therefore, when photosynthetic rates were compared at growth CO_2 concentration, the stimulation in photosynthetic rate was larger in autumn than summer leaves. Across the two seasons and the two CO_2 concentrations, V_{cmax} was strongly correlated with RuBPCase and J_{max} with cytochrome *f* content. These results suggest that seasonal change in climate influences the relative amount of photosynthetic proteins, which in turn affects the CO_2 response of photosynthesis.

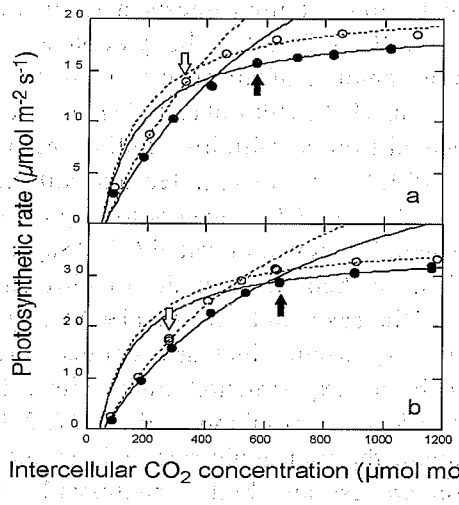

Figure 9.1 Photosynthetic rate versus intercellular CO_2 concentrations of *Polygonum cuspidatum* grown either at ambient CO_2 (370 μmol mol^{-1}, open symbols) or at elevated CO_2 (700 μmol mol^{-1}, closed symbols) in August (a) and October (b). The model of Farquhar et al. (1980) was fitted to the observations. Arrows indicate photosynthetic rate at growth CO_2 concentration.

9.4 Whole plant

Photosynthates acquired by leaves are allocated for growth of leaves, stems, roots, and reproductive organs. Increase in allocation to the leaf would be beneficial for photosynthesis, but may reduce other functions such as nutrient uptake and reproduction. We studied changes in biomass allocation with CO_2 elevation with respect to the balance between enhanced photosynthesis and other functions.

9.4.1 Reproductive growth at elevated CO_2

Although vegetative growth is enhanced by elevated CO_2, it is not always reflected by an increase in reproductive yield (final mass of the reproductive part). From more than 150 reports on the effect of elevated CO_2 on the reproductive yield of both crop and wild species, Jablonski et al. (2002) found a mean relative yield increase of 12% in fruits and 25% in seeds. These responses were smaller than the response of total plant mass (31%). In some cases, elevated CO_2 even reduced reproductive yield, though vegetative mass was increased (Larigauderie et al., 1988; Fajer et al., 1991; Farnsworth and Bazzaz, 1995). Thus, the increase in reproductive yield is not parallel to that in plant growth, and the enhancement of vegetative growth is not a reliable predictor of that of reproductive yield (Ackerly and Bazzaz, 1995).

The difference in responses to elevated CO_2 between vegetative growth and reproductive yield should be explained by factors involved in the process of reproductive growth. Reproductive growth is determined not only by biomass production but also by biomass allocation to the reproductive part. We analysed reproductive growth under elevated CO_2 using a simple growth model (Kinugasa et al., 2003). Reproductive mass was expressed as the product of (1) the duration of the reproductive period, (2) the rate of biomass acquisition in the reproductive period, and (3) the fraction of acquired biomass allocated to the reproductive part (Sugiyama and Hirose, 1991; Shitaka and Hirose, 1998). We raised *Xanthium canadense*, an annual, under ambient and elevated CO_2 concentration with two nitrogen availabilities. Elevated CO_2 increased reproductive yield at high nitrogen availability, but this increase was caused by increased capsule mass without a significant increase in seed production (Figure 9.2). The increase in total reproductive mass was due mainly to an increase in the rate of biomass acquisition in the reproductive period with a delay in leaf senescence. This positive effect was partly offset by a reduction in biomass allocation to the reproductive part at elevated CO_2. The duration of the reproductive period was not affected by elevated CO_2.

Seed production was strongly constrained by the availability of nitrogen for seed growth. The nitrogen concentration in seeds was very high in *X. canadense* and did not decrease at elevated CO_2 (Figure 9.2). On the other hand, capsule

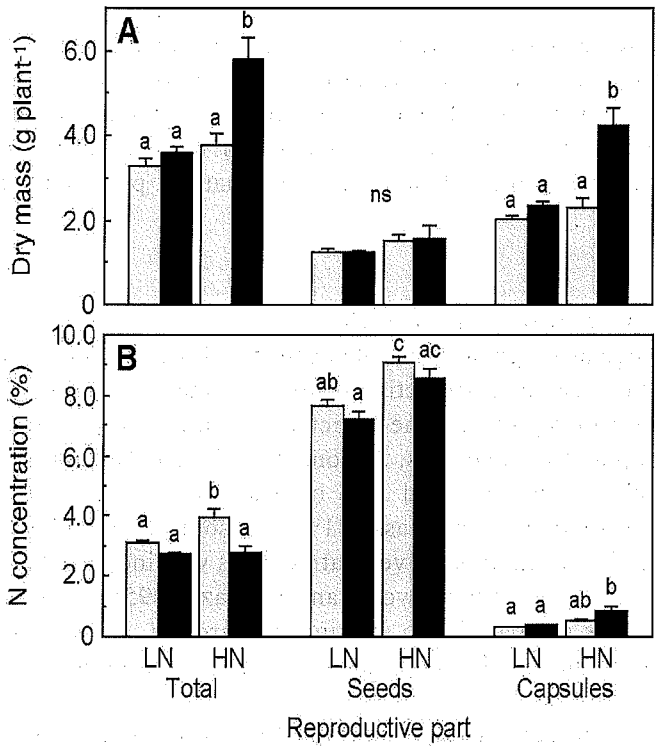

Figure 9.2 Dry mass (a) and N concentration (b) of the reproductive part (total, seeds and capsules) of *X. canadense*. Different letters above columns indicate a significant difference between treatments ($P < 0.05$, Tukey-Kramer method). White bars 360 μmol mol^{-1}, black bars 700 μmol mol^{-1} CO_2. LN and HN represent low and high nutrient availability (12 and 24 mM N), respectively. Redrawn from Kinugasa et al. (2003).

production seems to be less constrained by nitrogen availability. Capsules had very low nitrogen concentration and elevated CO_2 increased capsule mass at high nitrogen availability. Interestingly Kimball et al. (2002) reported that the boll (seed + lint) yield of cotton was increased 40% by elevated CO_2 while the lint fibre portion of the yield increased even more, by about 54%. In soybean, elevated CO_2 increased the pod wall mass more than seed yield (Allen et al., 1988). It seems that elevated CO_2 leads to a greater increase in the mass of a reproductive structure with a low nitrogen concentration than a structure with a high nitrogen concentration. This may be one of reasons for a large variation in CO_2 response of reproductive yield.

9.5 Canopy

Leaf canopy is a unit of photosynthesis at the ecosystem level. It is a collection of leaves that are exposed to a large gradient of light availability and have different photosynthetic characteristics depending on their microclimate. An important question is whether enhancement of canopy photosynthesis at elevated CO_2 is solely ascribed to enhanced leaf photosynthetic rate or also involves alteration in canopy structure.

9.5.1 Effect of elevated CO_2 on canopy photosynthesis: Does leaf area index respond to growth CO_2?

Reviewing studies on canopy photosynthesis, Drake and Leadley (1991) showed that elevated CO_2 increased canopy photosynthesis in almost all cases. The extent to which canopy photosynthesis increases, however, depends on species and on the availability of other resources (Bazzaz, 1990; Arp, 1991; McConnaughay et al., 1993). The rate of canopy photosynthesis is affected not only by photosynthetic rates in leaves but also by leaf area index (LAI, leaf area per unit ground area) in the canopy. There are disagreements about the effect of elevated CO_2 on leaf area development: LAI increased with elevated CO_2 in the canopy of perennial ryegrass (Nijs et al., 1988), soybean (Campbell et al., 1990), and rice (Rowland-Bamford et al., 1991), while it remained the same in artificial tropical forest ecosystems (Körner and Arnone, 1992) and experimental stands of annuals (Hirose et al., 1996).

Leaf area development is strongly determined by nitrogen availability (Anten et al., 1995). Hirose et al. (1996) found a strong correlation between LAI and aboveground plant nitrogen regardless of growth CO_2 levels in annual stands, suggesting that an increase in LAI at elevated CO_2 will occur only if plants simultaneously take up more nitrogen, through increased root growth and/or through increased root activity. However, Harz-Rubin and DeLucia (2001) found that vegetation stands under elevated CO_2 had greater LAI even when compared at the same nitrogen uptake. Kim et al. (2001) also found LAI for a given nitrogen uptake to be greater for plants under elevated CO_2, but only when nitrogen uptake itself was high, and not when it was low.

Although an increase in LAI enhances canopy photosynthesis due to increased light interception, when nitrogen in the canopy is limited, an increase in LAI reduces leaf nitrogen per unit leaf area, leading to a decline in photosynthetic capacity of leaves. There exists an optimal LAI at which the canopy photosynthetic rate for a given canopy nitrogen is maximised (Anten et al., 1995; Hirose et al., 1997). It has been shown that predicted LAI values are strongly correlated with measured LAIs (Anten et al., 2000). Anten et al. (2004) applied the concept of optimal LAI to stands of rice grown under free air CO_2 enrichment (FACE). In this experiment, LAI increased with increasing nitrogen availability

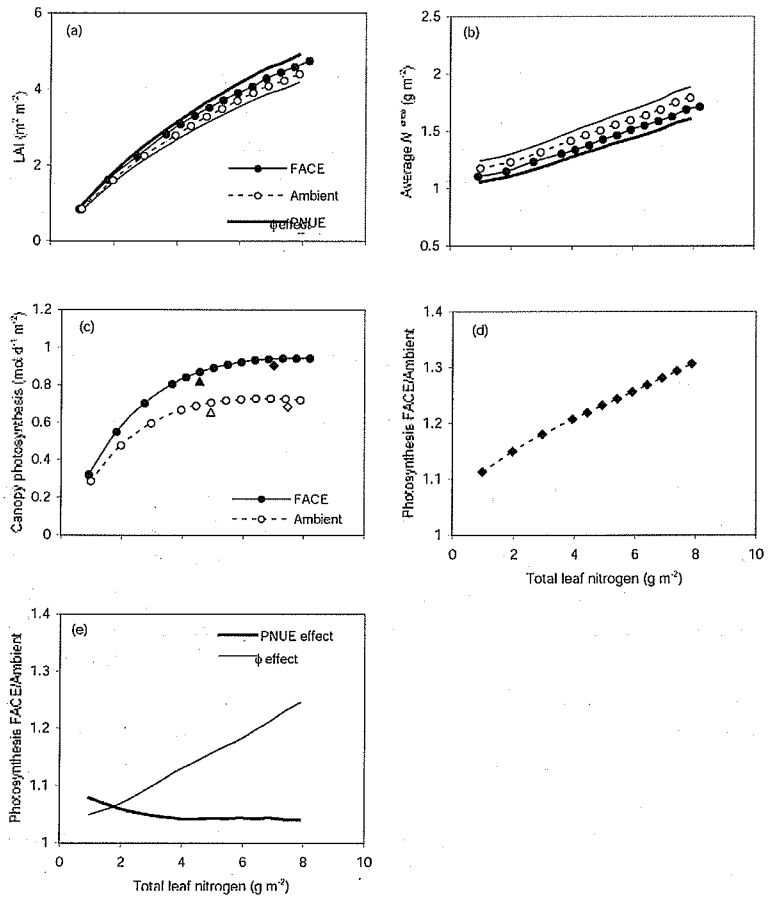

Figure 9.3 Effects of CO_2 elevation on the relationship between LAI (leaf area index), canopy photosynthesis and leaf nitrogen. (a) Optimal LAI for maximum carbon gain as a function of total amount of leaf nitrogen in the canopy (N_{canopy}) and (b) associated optimal average leaf nitrogen content (optimal N_{area} = N_{canopy}/optimal LAI) and (c) net daily canopy carbon gain. Canopy photosynthesis at actual N_{canopy} and LAI values are also given in (c) (open symbols, ambient CO_2; closed symbols, ambient plus 200 μmol mol^{-1} CO_2; triangles, standard nitrogen (9 g N m^{-2}); diamonds, high nitrogen (15 g N m^{-2})). (d) Ratio of canopy photosynthesis in elevated CO_2 (FACE, free air CO_2 enrichment) to that in ambient CO_2 (FACE : ambient). (a,b) Optimal LAI values also calculated; (e) FACE : ambient calculated assuming all characteristics form ambient plots, then separately changing either the photosynthetic capacity – N_{area} relationship (PNUE effect) or the quantum yield (□, □ effect) to the values found for FACE plants. Calculations were made with canopy characteristics averaged for the four replicate plots. Redrawn from Anten et al. (2003).

but was not affected by elevated CO_2 (Figure 9.3a). Elevated CO_2 did not affect total plant nitrogen in the stand but slightly reduced leaf nitrogen per unit ground area due to reduced allocation of nitrogen to leaves (Figure 9.3b). These results indicate that elevated CO_2 increases LAI when compared at the same leaf nitrogen, which is consistent with the model prediction. However, the increase in LAI by elevated CO_2 was only 6-8% both in the experiment and the prediction, suggesting that nitrogen availability is the most important factor for leaf development even under elevated CO_2.

Anten et al. (2004) further analysed the canopy photosynthetic rates in the rice stands. There are clear indications that the positive effect of elevated CO_2 on canopy carbon gain increases with nitrogen availability (Figure 9.3c, d). So far this interactive effect of CO_2 and nitrogen has been attributed to two mechanisms. First, inhibition of leaf photosynthesis by carbohydrate accumulation at elevated CO_2 tends to be stronger under low than under high nitrogen availability (Rogers et al., 1996). Second, nitrogen uptake increases under elevated CO_2 only when nitrogen availability is high, and not when it is low (Stitt and Krapp, 1999). Anten et al. (2004) proposed a mechanism of an interactive effect of nitrogen and CO_2 that is independent of the above two factors. When nitrogen availability is low, the canopy is relatively open and most leaves receive relatively high light. Under these conditions, the effect of elevated CO_2 on canopy photosynthesis will be predominantly through its effect on the light-saturated rate of photosynthesis of leaves (Figure 9.3e). But as nitrogen availability increases, the canopy becomes denser and lower leaves become increasingly shaded. Under these conditions the enhanced quantum yield under elevated CO_2 will have an increasingly positive effect on canopy photosynthesis (Figure 9.3e).

9.6 Population

Plant population consists of individuals varying in size. Competition for light has been suggested as an important factor for the development of size inequality (Weiner, 1990). Using even-aged monospecific stands of an annual herb, we studied the effect of elevated CO_2 on competition between individuals and the mechanism of development of size inequality.

9.6.1 Effects of elevated CO_2 on size distribution of individuals in a monospecific stand

Competition among individuals in plant populations are categorised with respect to symmetry in competition: symmetric and asymmetric competition (Weiner, 1990). Symmetric competition indicates that individuals in a stand acquire resources in proportion to their size while in asymmetric competition large individuals acquire more than proportional amounts of resources. It has been

suggested that competition for light is asymmetric (Ford and Diggle, 1981; Weiner, 1986; Jurik, 1991; Nagashima, 1999; Hikosaka et al., 1999), while that for nutrients is more symmetric (Weiner et al., 1997; Hikosaka and Hirose 2001). The mode of competition is critical in development of size inequality in the stand. Size inequality is assessed with the coefficient of variation (CV) (Weiner, 1990). Symmetric competition, where plant growth is proportional to the size, does not alter size inequality, while asymmetric competition increases size inequality in the stand.

Since diffusion of CO_2 within plant stands is very fast, competition for CO_2 is unlikely to occur among individuals (Jones, 1992). Even though elevated CO_2 benefits all individuals in the stand, the enhancement of growth by elevated CO_2 may indirectly alter the mode of competition (Wayne and Bazzaz, 1997). There are two alternative hypotheses in this respect. One is that elevated CO_2 makes the competition more asymmetric and increases size inequality in the stand. It occurs when enhanced growth of larger individuals suppresses light acquisition of smaller individuals. The other is that elevated CO_2 decreases the degree of asymmetry in competition and consequently size inequality. This is because the end-product inhibition of photosynthesis due to elevated CO_2 (Stitt and Krapp, 1999) may be stronger in larger plants exposed to high light, and because the reduction of the light compensation point of photosynthesis at elevated CO_2 will benefit the smaller shaded individuals more than the larger ones (Osborne et al., 1997).

To test these hypotheses, we established even-aged monospecific stands of an annual, *Chenopodium album*, at ambient and doubled CO_2 with high and low nutrient availabilities in open top chambers (Nagashima et al., 2003). The growth of individual plants was monitored non-destructively every week until flowering. Elevated CO_2 significantly enhanced plant growth at high nutrients, but did not at low nutrients. The size inequality represented by CV tended to increase at elevated CO_2. Size structure of the stands was analyzed by the cumulative frequency distribution of plant size (Figure 9.4). At early stages of plant growth, CO_2 elevation benefited all individuals and shifted the whole size distribution of the stand to large size classes. At later stages, dominant individuals were still larger at elevated than at ambient CO_2, but the difference in small subordinate individuals between two CO_2 levels became smaller. Although these tendencies were found at both nutrient availabilities, difference in size distribution between CO_2 levels was larger at high nutrients. The CO_2 elevation did not significantly enhance the growth rate as a function of plant size except for the high nutrient stand at the earliest stage, indicating that the higher biomass at elevated CO_2 at later stages in the high nutrient stand was caused by the larger size of individuals at the earliest stage. Thus, elevated CO_2 seems to increase size inequality in vegetation stands and this effect becomes stronger at high nitrogen availability.

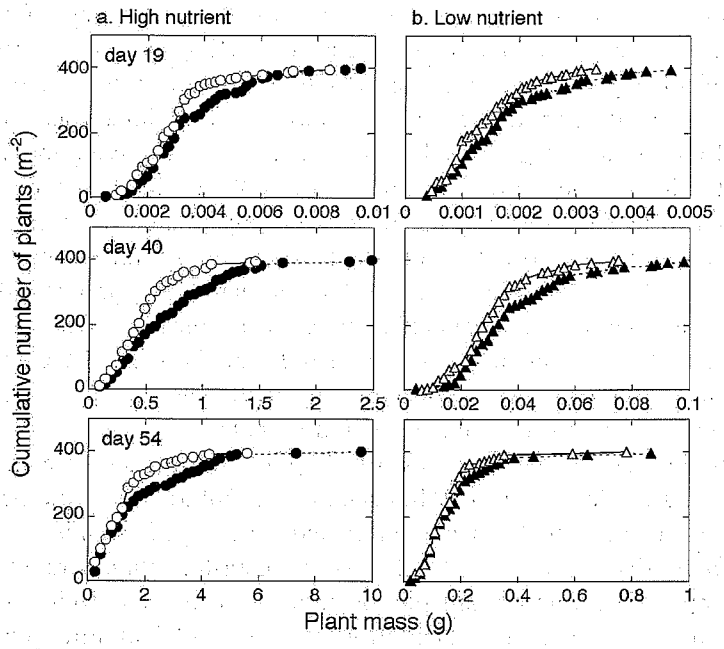

Figure 9.4 Comparisons of cumulative frequency distributions of biomass in the even-aged stand of *Chenopodium album* between ambient (360 μmol mol^{-1}, open symbols) and elevated CO_2 concentrations (700 μmol mol^{-1}, closed symbols) at high (a) and low (b) nutrients (3.6 and 0.36 g N m^{-2} $week^{-1}$, respectively). These results are shown for 19 40 and 54 days after emergence. Redrawn from Nagashima et al. (2003).

9.6.2 Effects of elevated CO_2 on light competition: an individual-based analysis of light acquisition and utilisation

We then investigated the physiological factors that underlie the effects of elevated CO_2 on the competitive interactions between plants. As mentioned above, difference in size structure results from different size-dependent growth rates of individuals in the stand. In a dense stand, large dominant individuals have an advantage in capturing light because they place their leaves in the highest most illuminated parts of the canopy. Small subordinate individuals, on the other hand, may have an advantage because they need less investment of biomass in support tissues because they maintain leaves at lower positions (Givnish, 1982). As a result they can allocate relatively more biomass to leaf area growth, and this can mitigate the negative effects of shading (Anten and Hirose, 1998). To indicate the efficiency of biomass use to capture light, Hirose and Werger (1995) introduced the parameter Φ_{mass}, defined as photon flux captured per unit aboveground mass.

They suggested that Φ_{mass} might not differ between dominant and subordinate species in multispecies systems. However, plant growth is determined not only by the amount of acquired resources, but also by the efficiency of resource use (growth per unit amount of resource acquired). Hikosaka et al. (1999) defined light-use efficiency of photosynthesis (LUE) as photosynthesis per unit photon interception, and described the photosynthesis of individuals as the product of Φ_{mass} and LUE: RPR = Φ_{mass} x LUE, where RPR is the relative photosynthetic rate (photosynthetic rate per unit aboveground mass). Provided that plant growth is proportional to leaf photosynthesis, RPR is closely related to the relative growth rate (RGR). With a modification of the canopy photosynthesis model of Hirose and Werger (1987), Hikosaka et al. (1999) estimated the photosynthetic rate of individuals in a natural monospecific stand of an annual, *Xanthium canadense*. They found that Φ_{mass} was higher in larger individuals, while LUE was highest in intermediate individuals. As a consequence, RPR was high in intermediate and larger individuals, and lowest in smaller individuals.

The model described above was then applied to monospecific stands growing at ambient and at elevated CO_2 (Hikosaka et al., 2003). As in the previous study (Nagashima et al., 2003), we established even-aged stands of an annual, *Chenopodium album*, at two CO_2 levels in open-top chambers with sufficient nutrient supply. The whole-plant photosynthesis of every individual in the stand was calculated from (1) the distribution of light and leaf nitrogen and (2) the relationships between photosynthetic parameters and leaf nitrogen content per area. Elevated CO_2 increased light-saturated rates of photosynthesis by 10-15% and the initial slope of the light-response curve by 11%, but had no effect on dark respiration. The relative rate of photosynthesis (RPR, the rate of photosynthesis per unit above-ground mass) was analysed as the product of light capture (Φ_{mass}, the photon flux captured per unit above-ground mass) and light-use efficiency (LUE, plant photosynthesis per unit photon capture) (Figure 9.5). At an early stage of stand development (33 days after germination), RPR was nearly constant and no difference was found between ambient and elevated CO_2. However, CO_2 elevation influenced the components of RPR differently. Elevated CO_2 reduced Φ_{mass}, which offsets the increase in LUE. Later (47 days), RPR was positively correlated with plant mass at both CO_2 concentrations. When compared at an equal plant mass, RPR was lower at elevated CO_2, which was caused by a reduction in Φ_{mass} despite some compensation by higher LUE. We conclude that elevated CO_2 increases size inequality of a stand through enhanced photosynthesis and growth of dominants, which reduce the light availability for subordinates and consequently increase size inequality in the stand.

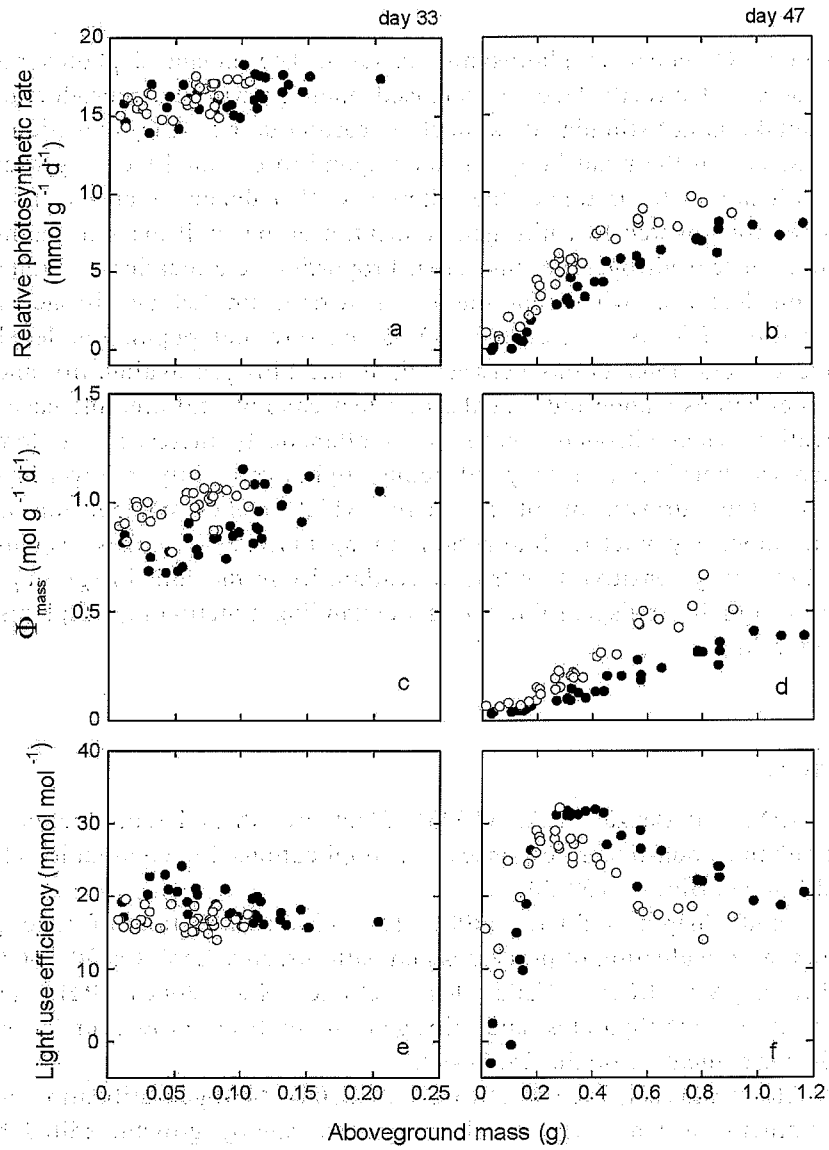

Figure 9.5 Relative photosynthetic rates (RPR, whole-plant photosynthetic rate per unit above-ground mass; a, b), Φ_{mass} (photon flux captured per unit above-ground mass; c, d), and light use efficiency (LUE, photosynthesis per unit captured photon; e, f), as a function of above-ground dry mass at 33 (a, c, e) and 47 (b, d, f) days after emergence. RPR = Φ_{mass} x LUE. Open circles, ambient; closed circles, elevated CO_2 (360 and 700 μmol mol^{-1}, respectively). Redrawn from Hikosaka et al. (2003).

9.7 Conclusion

Elevated CO_2 enhances photosynthetic rates. The enhanced photosynthesis, however, does not directly lead to increased plant growth and reproduction. As nitrogen uptake is not stimulated as much as carbon uptake, CO_2 elevation alters the C/N balance in the plant body. Plants respond to elevated CO_2, by changing biomass allocation to mitigate the altered C/N balance. Increase in LMA compensates for lowered leaf nitrogen concentration per unit mass to maintain a certain level of leaf nitrogen per unit area. Proportionate allocation of biomass to reproduction decreases when reproductive growth is limited by nitrogen rather than by carbon. Effects of elevated CO_2 at canopy and population levels are manifested through interactions between light and nitrogen availability and also through interactions among individuals. In a leaf canopy, leaf area increases with CO_2 elevation when nitrogen uptake is simultaneously increased. If dominant plants increase their leaf area, they will reduce light availability in lower layers of canopy and thus growth of plants there, which makes competition among individuals more asymmetric. Interaction among individuals makes responses to elevated CO_2 fairly sensitive to nitrogen availability in the soil. Integrating these responses would be indispensable for understanding functioning of plants in a high CO_2 world.

References

Ackerly, D.D., and Bazzaz, F.A., (1995), Plant growth and reproduction along CO_2 gradients: non-linear responses and implications for community change, Global Change Biol, 1, 199-207.

Aerts, R., and Chapin, F.S.III, (2000), The mineral nutrition of wild plants revisited: a re-evaluation of processes and patterns, Adv Ecol Res 30, 1-67.

Allen, L.H.J., Vu, J.C.V., Valle, R.R., Boote, K.J., Jones, P.H., (1988), Nonstructural carbohydrates and nitrogen of soybean grown under carbon dioxide enrichment, Crop Sci 28, 84-94.

Anten, N.P.R., Hikosaka, K., and Hirose, T., (2000), Nitrogen utilization and the photosynthetic system, Leaf development and canopy growth, edited by In: Marshal B, Roberts J., Sheffield Academic Press, Sheffield, pp, 171-203.

Anten, N.P.R., and Hirose, T., (1998), Biomass allocation and light partitioning among dominant and subordinate individuals in Xanthium canadense stands, Ann Bot 82, 665-673.

Anten, N.P.R., Hirose, T., Onoda, Y., Kinugasa, T., Kim, H.Y., Okada, M., and Kobayashi, K., (2003), Elevated CO_2 and nitrogen availability have interactive effects on canopy carbon gain in rice, New Phytol 161, 459-472.

Anten, N.P.R., Schieving, F., Medina, E., Werger, M.J.A., and Schuffelen, P., (1995), Optimal leaf area indices in C3 and C4 mono- and dicotyledonous

species at low and high nitrogen availability, Physiol Plant, 95, 541-550.
Arp, W.J., (1991), Effects of source-sink relations on photosynthetic acclimation to elevated CO_2, Plant Cell Environ, 14, 869-875.
Bazzaz, F.A., (1990), The response of natural ecosystems to the rising global CO_2 levels, Annu Rev Ecol Syst, 21, 167-196.
Brouwer, R., (1962), Nutritive influences on the distribution of dry matter in the plant, Netherland J Agri Sci, 10, 399-408.
Campbell, W.J., Allen, Jr. L.H., and Bowes, G., (1990), Response of soybean canopy photosynthesis to CO_2 concentration, light, and temperature J Exp Bot, 41, 427-433.
Cure, J.D., and Acock, B., (1986), Crop responses to carbon dioxide doubling: a literature survey, Agric Forest Meteor, 38, 127-145.
Curtis, P.S., (1996), A meta-analysis of leaf gas exchange and nitrogen in trees grown under elevated carbon dioxide, Plant Cell Environ, 19, 127-137.
Drake, B.G., and Leadly, P.W., (1991), Canopy photosynthesis of crops and native plant communities exposed to long-term elevated CO_2, Plant Cell Environ, 14, 853-860.
Evans, J.R., (1989), Photosynthesis and nitrogen relationships in leaves of C3 plants, Oecologia, 78, 9-19.
Evans, J.R., and Seemann, J.R., (1989), The allocation of protein nitrogen in the photosynthetic apparatus: costs, consequences and control, In: Briggs WR (ed) Photosynthesis, edited by Alan, R., pp, 183-205, Liss, New York.
Farnsworth, E.J., and Bazzaz, F.A., (1995), Inter- and intra-generic differences in growth, reproduction, and fitness of nine herbaceous annual species grown in elevated CO_2 environments, Oecologia, 104, 454-466.
Farquhar, G.D., von Caemmerer, S., and Berry, J.A., (1980), A biochemical model of photosynthetic CO_2 assimilation in leaves of C3 species, Planta, 149, 78-90.
Fajer, E.D., Bowers, M.D., and Bazzaz, F.A., (1991), Performance and allocation patterns of the perennial herb Plantago lanceolata in response to simulated herb ivory and elevated carbon dioxide environments, Oecologia 87, 37-42.
Ford, E.D., and Diggle, P.J., (1981), Competition for light in a plant monoculture modelled as a spatial stochastic process, Ann Bot 48, 481-500.
Givnish, T.J., (1982), On the adaptive significance of leaf height in forest herbs, Amer Nat 120, 353-381.
Harz-Rubin, J.S., and DeLucia, E.H., (2001), Canopy development of a model herbaceous community exposed to elevated CO_2 and soil nutrients, Physiol Plant 113, 258-266.
Hikosaka, K., (1997), Modelling optimal temperature acclimation of the photosynthetic apparatus in C3 plants with respect to nitrogen use, Ann Bot 80, 721-730.
Hikosaka, K., (2004), Interspecific difference in the photosynthesis-nitrogen relationship: patterns, physiological causes, and ecological importance, J Plant Res, in press.
Hikosaka, K., and Hirose, T. (1998), Leaf and canopy photosynthesis of C3 plants

at elevated CO_2 in relation to optimal partitioning of nitrogen among photosynthetic components: Theoretical prediction, Ecol Model 106, 247-259.
Hikosaka, K., and Hirose, T., (2001), Nitrogen uptake and use of competing individuals in a Xanthium canadense stand, Oecologia 126, 174-181.
Hikosaka, K., Murakami, A., and Hirose, T., (1999), Balancing carboxylation and regeneration of ribulose-1,5-bisphosphate in leaf photosynthesis: Temperature acclimation of an evergreen tree, Quercus myrsinaefolia, Plant Cell Environ 22, 841-849.
Hikosaka, K., Onoda, Y., Kinugasa, K., Anten, N.P.R., Nagashima, H., and Hirose, T., (2005), Plant responses to elevated CO_2 concentration at different scales: leaf, whole plant, canopy, and population, Ecol Res, 20, 243-253.
Hikosaka, K., Sudoh, S., Hirose, T. (1999), Light acquisition and use by individuals competing in a dense stand of an annual herb, Xanthium canadense, Oecologia, 118, 388-396.
Hikosaka, K., and Terashima, I., (1995), A model of the acclimation of photosynthesis in the leaves of C3 plants to sun and shade with respect to nitrogen use, Plant Cell Environ 18, 605-618.
Hikosaka, K., Yamano, T., Nagashima, H., Hirose, T., (2003), Light-acquisition and use of individuals as influenced by elevated CO_2 in even-aged monospecific stands of Chenopodium album, Funct Ecol, 17, 786-795.
Hilbert, D.W., (1990), Optimization of plant root:shoot ratios and internal nitrogen concentration, Ann Bot, 66, 91-99.
Hirose, T., (1987), A vegetative plant growth model: adaptive significance of phenotypic plasticity in matter partitioning, Funct Ecol, 1, 195-202.
Hirose, T., (1988), Nitrogen availability, optimal shoot/root ratios and plant growth, In: Werger MJA, can der Aart PJM, During HJ, Verhoven JTA (eds) Plant form and vegetation structure, pp, 135-145, SPB Academic Publishing, The Hague.
Hirose, T., Ackerly, D.D., Traw, M.B., and Bazzaz, F.A., (1996), Effects of CO_2 elevation on canopy development in the stands of two co-occurring annuals, Oecologia, 108, 215-223.
Hirose, T., Ackerly, D.D., Traw, M.B., Ramseier, D., and Bazzaz, F.A., (1997), CO_2 elevation, canopy photosynthesis and optimal leaf area index, Ecology, 78. 2339-2350.
Hirose, T., and Werger, M.J.A., (1987), Maximizing daily canopy photosynthesis with respect to the leaf nitrogen allocation pattern in the canopy, Oecologia, 72, 520-526.
Hirose, T., and Werger, M.J.A., (1995), Canopy structure and photon flux partitioning among species in a herbaceous plant community, Ecology, 76, 466-474.
IPCC, (2001), Climate change 2001: the Scientific Basis, Contribution of Working Group I to the Third Assessment Report of the Intergovernmental Panel on Climate Change, (Houghton JT, Ding Y, Griggs DJ et al, eds), Cambridge University Press, Cambridge.

Jablonski, L.M., Wang, X.Z., and Curtis, P.S., (2002), Plant reproduction under elevated CO_2 conditions: a meta-analysis of reports on 79 crop and wild species, New Phytol, 156, 9-26.

Jones, H.G., (1992), *Plants and microclimate*, 2nd edn, Cambridge University Press, Cambridge.

Jurik, T.W., (1991), Population distribution of plant size and light environment of giant ragweed (Ambrosia trifida L.), Oecologia 87, 539-550.

Kim, H.Y., Lieffering, M., Miura, S., Kobayashi, K., and Okada, M., (2001), Growth and nitrogen uptake of CO_2-enriched rice under field conditions, New Phytol, 150, 223-229.

Kimball, B.A., (1983), Carbon dioxide and agricultural yield: an assemblage and analysis of 430 prior observations, Agron J, 75, 779-789.

Kimball, B., Kobayashi, K., and Bindi, M., (2002), Responses of agricultural crops to free-air CO_2 enrichment, Adv Agro, 77, 293-368.

Kinugasa, T., Hikosaka, K., and Hirose, T., (2003), Reproductive allocation of an annual, Xanthium canadense, at an elevated carbon dioxide concentration, Oecologia, 137, 1-9.

Larigauderie, A., Hilbert, D.W., and Oechel, W.C., (1988), Effect of carbon dioxide enrichment and nitrogen availability on resource acquisition and resource allocation in a grass Bromus-mollis, Oecologia, 77, 544-549.

Lutze, J.L., and Gifford, R.M., (1998), Acquisition and allocation of carbon and nitrogen by Danthonia richardsonii in response to restricted nitrogen supply and CO_2 enrichment, Plant Cell Environ, 21, 1133-1141.

Makino, A., Harada, M., Kaneko, K., Mae, T., Shimada, T., and Yamamoto, N., (2000), Whole-plant growth and N allocation in transgenic rice plants with decreased content of ribulose-1,5-bisphosphate carboxylase under different CO_2 partial pressures, Aust J Plant Physiol, 27, 1-12.

Makino, A., and Mae, T., (1999), Photosynthesis and plant growth at elevated levels of CO_2, Plant Cell Physiol, 40, 999-1006.

Makino, A., Shimada, T., Takumi, S., Kaneko, K., Matsuoka, M., Shimamoto, K., Nakano, H., Miyao-Tokutomi, M., Mae, T., and Yamamoto, N., (1997), Does decrease in ribulose-1,5-bisphosphate carboxylase by antisense rbcS lead to a higher nitrogen-use efficiency of photosynthesis under conditions of saturating CO_2 and light in rice plants? Plant Physiol, 114, 483-491.

McConnaughay, K.D.M., Berntson, G.M., and Bazzaz, F.A., (1993), Limitations to CO_2-induced growth enhancement in pot studies, Oecologia, 94, 550-557.

Medlyn, B.E., (1996), The optimal allocation of nitrogen within the C3 photosynthetic system at elevated CO_2, Aust J Plant Physiol, 23, 593-603.

Medlyn, B.E., Badeck, F.W., De, Pury, D.G.G., Barton, C.V.M., Broadmeadow, M., Ceulemans, R., De, Angelis, P., Forstreuter, M., Jach, M.E., Kellomaki, S., Laitat, E., Marek, M., Philippot, S., Rey, A., Strassemeyer, J., Laitinen, K., Liozon, R., Portier, B., Roberntz, P., Wang, K., and Jarvis, P.G., (1999), Effects of elevated [CO_2] on photosynthesis in European forest species: A meta-analysis of model parameters, Plant Cell Environ, 22, 1475-1495.

Nagashima, H., (1999), The processes of height-rank determination among individuals and neighborhood effects in Chenopodium album L, stands, Ann Bot, 83, 501-507.
Nagashima, H., Yamano, T., Hikosaka, K., and Hirose, T., (2003), Effects of elevated CO_2 on the size structure of even-aged monospecific stands of annual, Chenopodium album, Global Change, Biol 9, 619-629.
Nijs, I., Impens, I., and Behaeghe, T., (1988), Effects of rising atmospheric carbon dioxide concentration on gas exchange and growth of perennial ryegrass, Photosynthetica, 22, 44-50.
Onoda, Y., Hikosaka, K., and Hirose, T., (2005a), Seasonal change in the balance between capacities of RuBP carboxylation and RuBP regeneration affects CO_2 response of photosynthesis in Polygonum cuspidatum, J Exp Bot, 56, 755-763.
Osborne, C.P., Drake, B.G., LaRoche, J., et al, (1997), Does long-term elevation of CO_2 concentration increase photosynthesis in forest floor vegetation? Indian strawberry in a Maryland forest, Plant Physiol, 114, 337-344.
Peterson, A.G., Ball, J.T., Luo, Y., Field, C.B., Curtis, P.S., Griffin, K.L., Gunderson, C.A., Norby, R.J., Tissue, D.T., Forstreuter, M., et al, (1999), Quantifying the response of photosynthesis to changes in leaf nitrogen content and leaf mass per area in plants grown under atmospheric CO_2 enrichment, Plant Cell Environ, 22, 1109-1119.
Poorter, H., (1993), Interspecific variation in the growth response of plants to an elevated ambient CO_2 concentration, Vegetatio, 104/105, 77-97.
Rogers, G.S., Milham, P.J., Gillings, M., and Conroy, J.P., (1996), Sink strength may be the key to growth and nitrogen responses in N-deficient wheat at elevated CO_2, Aust J Plant Physiol, 23, 253-264.
Rowland-Bamford, A.J., Baker, J.T., Allen, Jr. L.H., and Bowes, G., (1991), Acclimation of rice to changing atmospheric carbon dioxide concentration, Plant Cell Environ, 14, 577-583.
Sage, R.F., (1994), Acclimation of photosynthesis to increasing atmospheric CO_2: the gas exchange perspective, Photosynth Res, 39, 351-368.
Shitaka. Y., and Hirose, T., (1998), Effects of shift in flowering time on the reproductive output of Xanthium canadense in a seasonal environment, Oecologia, 114, 361-367.
Stitt, M., and Krapp, A., (1999), The interaction between elevated carbon dioxide and nitrogen nutrition: the physiological and molecular background, Plant Cell Environ, 22, 583-621.
Sugiyama, H., and Hirose, T., (1991), Growth schedule of Xanthium canadense: Does it optimize the timing of reproduction? Oecologia, 88, 55-60.
Ward, J.K., and Strain, B.R., (1999), Elevated CO_2 studies: Past, present and future, Tree Physiol, 19, 211-220.
Wayne, P.M., and Bazzaz, F.A., (1997), Light acquisition and growth by competing individuals in CO_2-enriched atmospheres: consequences for size structure in regenerating birch stands, J Ecol, 85, 29-42.
Webber, A.N., Nie, G.Y., and Long, S.P., (1994), Acclimation of photosynthetic

proteins to rising atmospheric CO_2, Photosynth Res, 39, 413-425.
Weiner, J., (1986), How competition for light and nutrients affects size variability in Ipomoea tricolor populations, Ecology, 67, 1425-1427.
Weiner, J., (1990), Asymmetric competition in plant populations, Tre Ecol Evo, 5, 360-364.
Weiner. J., Wright, D.B., and Castro, S., (1997), Symmetry of below ground competition between Kochia scoparia individuals, Oikos, 79, 85-91.
Wilson, K.B., Baldocchi, D.D., and Hanson, P.J., (2000), Quantifying stomatal and non-stomatal limitations to carbon assimilation resulting from leaf aging and drought in mature deciduous tree species, Tree Physiology, 20, 787-797.
Wullschleger, S.D., (1993), Biochemical limitations to carbon assimilation in C3 plants: A retrospective analysis of the A/Ci curves from 109 species, J Exp Bot, 44, 907-920.
Ziska, L.H., Weerakoon, W., Namuco, O.S., and Pamplona, R., (1996), The influence of nitrogen on the elevated CO_2 response in field-grown rice, Aust J Plant Physiol, 23, 45-52.

Chapter 10

Dynamic Global Vegetation Model

-Linkage between Water and Carbon Cycles-

Akihiko Ito
Frontier Research Center for Global Change,
Japan Agency for Marine-Earth Science and Technology (JAMSTEC)
3173-25 Showa-machi, Kanazawa-ku, Yokohama 236-0001, Japan
Tel: +81-45-778-5599
Fax: +81-45-778-5706
e-mail: itoh@jamstec.go.jp

10.1 Introduction

Terrestrial ecosystems play important roles in the water and carbon cycles at different temporal and spatial scales. We are becoming gradually aware of the nature of the land-atmosphere interaction processes through recent research in the fields of ecology, biogeochemistry, meteorology and hydrology. A drastic change in terrestrial ecosystems can affect atmospheric composition and dynamics, i.e. the climate system of the Earth. Accordingly, it is likely that coherent continental scale alterations of ecological and physiological processes in response to climatic change will exert feedback effects (either in a positive or negative direction to the initial impact). Similarly, a great variety of human impacts on terrestrial ecosystems (e.g. deforestation and land-use) may affect the climate system via various processes.

Terrestrial ecosystems have several peculiarities in comparison with atmospheric and oceanic systems, making it difficult to predict the impacts of and feedbacks to global change. First, a terrestrial ecosystem is a complex system composed of many different components such as plants (producers), animals (consumers), microbes (decomposers), and the physical and chemical environments. Second, land surface is extremely heterogeneous, due to topography, geology, meteorology, and other disturbances, making it difficult to extrapolate from local-scale empirical data to that on a broad-scale. Third, terrestrial ecosystems change at various time scales ranging from minutes (e.g. wildfire and landslide) to centuries or longer (e.g. succession and evolution). Forth, terrestrial ecosystems are fragile and sensitive to environmental changes. For example, many experimental studies suggest that plant photosynthesis and

transpiration respond to elevated atmospheric CO_2 concentration, but with different sensitivity among different plant species.

Therefore, we are in urgent need of understanding and predicting the impacts of global environmental change on terrestrial ecosystems. In addition to empirical and experimental approaches, model simulation has become an essential method to assess the terrestrial ecosystem processes under global change. Model simulation allows the integration of various components into a single system providing the ability to make quantitative consideration at global and long-term scales. In fact, many terrestrial models have been developed for different purposes (Arora, 2002). They are categorized into four types. (A) Land surface parameterization models, which simulate exchanges of energy, water, and materials with the atmosphere. (B) Carbon cycle models, which simulate major biogeochemical carbon flows such as photosynthesis, respiration, and decomposition and carbon pools of biomass and soil organic matter. (C) Ecosystem dynamics models, which simulate interactions such as competition and succession between organisms. (D) Integrated models, which include all the ecosystem processes (A~C) and their interactions (Figure 10.1). In hydrological and meteorological studies, the type-A models have typically been used (e.g., Sellers et al., 1997), whereas ecological and biogeochemical studies adopt the type-B or type-C models. Recently, as the importance of interdisciplinary approach is recognized, the type-D or integrated models have been developed by several institutes.

In general, terrestrial ecosystem models including vegetation dynamics processed at continental-scales are called Dynamic Global Vegetation Models

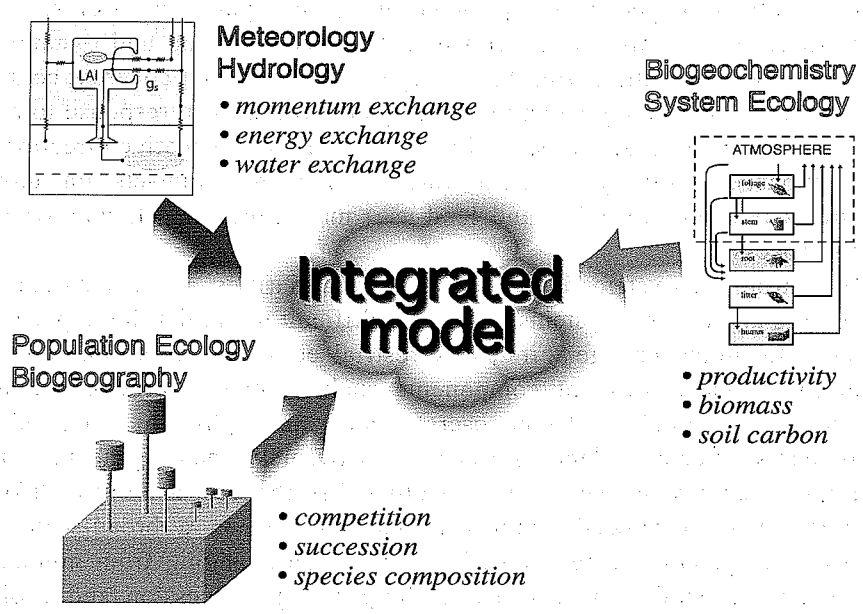

Figure 10.1 Categories of terrestrial ecosystem models.

(DGVM). These models can estimate the dynamic transition and consequences of plant competition for specific locations, that is, the distribution of vegetation types (biogeography) such as tropical rain forest, temperate deciduous forest, boreal forest, woodland, shrub land, grassland, or desert. Since most DGVMs include hydrological and carbon biogeochemical processes, these types of models are roughly equivalent to the type-D integrated model. Development of DGVMs was begun in the middle of the 1990s. Woodward et al. (1995) and Foley et al. (1996) presented biogeographic models, DOLY and IBIS respectively, which included terrestrial water and carbon cycle processes. Since then, a number of DGVMs have been developed: LPJ by Sitch et al. (2003), TRIFFID by Cox (2001), Hybrid by Friend and White (2000), SDGVM by Woodward and Lomas (2004), and CLM by Bonan et al. (2003).

Apparently, development of DGVMs is a new (or immature) growth area in the study of global change, and they are to be included into Earth-System models to predict climatic change including biotic feedback processes (Foley, 2000). For example, as exemplified by Cox et al. (2000), terrestrial carbon cycles can act as strong feedback mechanisms to global warming caused by anthropogenic greenhouse gas emissions. Furthermore, these models are useful as a tool to analyze the linkage between water cycles and carbon cycles in terrestrial ecosystems. However, these models provide relatively inconsistent results of the current and future states of terrestrial ecosystems (e.g., Cramer et al., 2001), because they adopt different parameterizations of carbon and water cycles and vegetation dynamics.

This text is intended to explain the basic structure of terrestrial ecosystem models and to summarize the current achievements, problems, and opportunities in the research field. Hopefully, the knowledge will facilitate the understanding of land hydrologic systems.

10.2 Global distribution of vegetation types

Terrestrial vegetation is composed of over 250,000 higher plant species (trees and grasses) and enormous numbers of animal, insect, and microbe species. Our knowledge on the biodiversity of the biosphere is far from sufficient, and it is impossible to consider the whole of terrestrial vegetation at a species level. Historically, biogeographical and bioclimatological studies have categorized terrestrial vegetation on the basis of physiognomy (appearance), such as tropical rain forest, temperate grassland, or tundra. Global patterns have been correlated with environmental gradients of temperature and water availability, allowing the understanding of how climate determines vegetation distribution (e.g., schemes by Köppen, Kira, Holdridge, Budyko, etc.) under a given environmental condition. In these correlations, the potential vegetation distribution was exclusively discussed

and transitional states and human modifications were not included. Although these studies did not account for the underlying mechanisms of vegetation distribution, the evolutional convergence of plant structure and function carried important implications.

Later, in the early 1990s, several semi-mechanistic schemes were developed to correlate global vegetation patterns with plant physiological properties: BIOME by Prentice et al. (1992) and MAPSS by Neilson et al. (1992). They proposed a new vegetation category, termed plant functional type (PFT). This concept aggregates plant species into a small number of groups on the basis of differences in the functions of atmosphere-ecosystem exchange and biogeochemistry. For example, grass species are divided into two PFTs, C_3-grass and C_4-grass, which have different photosynthetic pathways and differ in environmental dependencies. Tree species are divided into broad-leaf/needle-leaf and evergreen/deciduous PFTs, which differ in atmosphere-canopy exchange characteristics. Broad-leaf species have, in general, a larger number of stomata than needle-leaf species, and deciduous forests show more evident seasonal changes in photosynthesis and transpiration than evergreen forests. Although the PFT-based schemes enabled the interpretation of vegetation distribution in ecophysiological manners, they still estimate potential vegetation distributions under static conditions.

Transitional shift of continental-scale vegetation distribution has mainly been investigated in terms of paleobotany and palynology (e.g. vegetation shift since the Last Glacial era), because it was believed to occur at nearly geological time-scales. On the other hand, ecological studies have investigated transitional changes in local-scale vegetation (termed succession), including the development of ecosystem dynamics model (called gap model). Recent studies suggest that the actual vegetation distribution is often substantially different from the potential distribution owing to the effects of disturbances (such as degradation of succession stage or following recoveryfrom wildfire or landslide), human land-use, and climatic change. In fact, almost all terrestrial ecosystems are affected by human activities, and more than 10% of land area has been converted into urban and cropland sectors. Therefore, to capture the actual vegetation distribution, it is a challenge for biogeographical models to take account of disturbances, transitional recovery, and human land-use changes.

10.3 Carbon and water cycles in terrestrial ecosystems

10.3.1 Overview of modeling

To deal with a complex terrestrial ecosystem in practice, it is essential to extract, conceptualize, and simplify the system. Frequently, focus is placed on the flows and pools of specific physical and chemical attributes such as energy, water, carbon, nutrient, etc. For example, hydrological models focus on water flows such

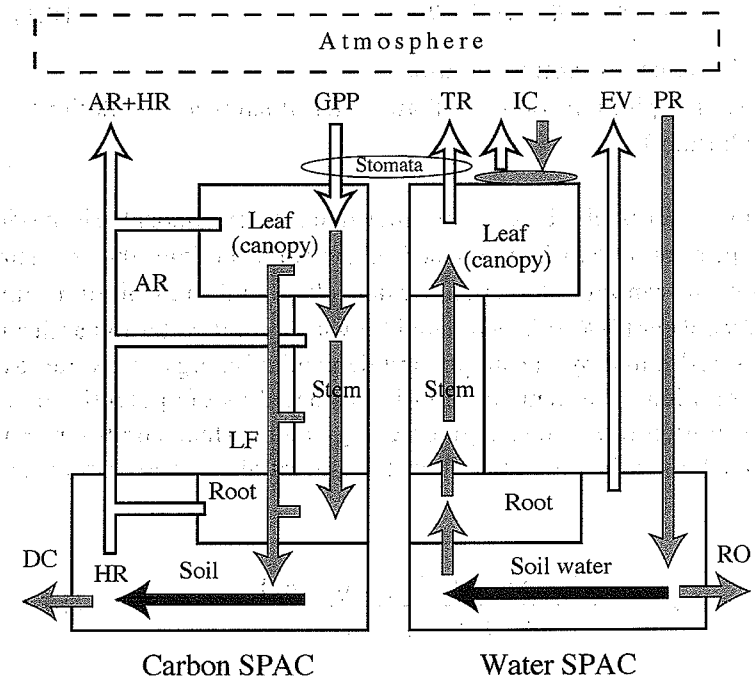

Figure 10.2 Schematic diagrams of the soil-plant-atmosphere continua (SPAC) of carbon (left) and water cycles (right) in terrestrial ecosystems.

as precipitation, evapotranspiration, and runoff, and the water budget of soil and vegetation moisture contents. The flows of water and energy are frequently simulated with an electronic-circuit approach (i.e. potential difference and resistance); these models are generally called soil-plant-atmosphere continuums (SPAC; Figure 10.2). Thus, an ecosystem is reduced to a simple box-flow system, which is readily applicable to ecological analyses. Such simplification is effective to clarify key factors and processes, but neglect potentially important interactions with other mechanisms. Different vegetation types are characterized by parameter values related to soil properties and plant physiology. Most models assume *a priori* vegetation types such as tropical rain forest and savanna, derived from field surveys and satellite image analyses.

10.3.2 Water cycle

In most terrestrial ecosystems, water availability is one of the important limiting factors of plant productivity and is closely coupled with carbon and nutrient cycles (e.g., Jackson et al., 2001). Appropriate simulation of the water budget is necessary, not only for hydrological models, but also for carbon cycle and ecosystem dynamics models. The ecosystem water budget is represented by a SPAC scheme (Figure 10.2); here, the water budget of soil moisture (M_S) is given by the following equation:

$$\frac{dM_S}{dt} = PR - AET - RO \tag{10.1}$$

AET: actual evapotranspiration
PR: precipitation (rain and thaw water of snow accumulation)
RO: runoff

Precipitation (PR) is obtained from input datasets or atmospheric models. Actual evapotranspiration (AET) is composed of evaporation from the soil surface (EV), evaporation of canopy-intercepted water (IC), and transpiration through leaf stomata (TR). Runoff (RO) is estimated by various soil water dynamics models.

AET is co-limited by the supply and demand of energy and water available for evapotranspiration. The demand term is evaluated as the potential or equilibrium evapotranspiration rate, under a given energy and surface condition. For example, the Penman-Monteith equation gives the potential evapotranspiration (PET) as follows:

$$PET = \frac{\Delta \cdot (R_n - G) + \rho \cdot C_p \cdot g_a \cdot (e_s - e_a)}{\Delta + \gamma \cdot (1 + g_a / g_c)} \tag{10.2}$$

e_a: air vapor pressure
e_s: saturated vapor pressure at leaf surface temperature
g_a: aerodynamic conductance
g_c: canopy conductance
C_p: specific heat capacity
G: ground heat flux
R_n: net radiation
r: air density
γ: psychrometer constant
Δ: slope of temperature – saturated vapor pressure

Note that there are a couple of methods to obtain the potential evapotranspiration (see Jones, 1992). The supply term (β), or evapotranspitration efficiency,

represents a limitation by the deficit of soil water (M_s) and precipitation (PR):

$$AET = \beta\left(M_s, PR\right) \cdot PET \tag{10.3}$$

Empirical parameterizations (e.g., quadratic equations in Ito and Oikawa, 2002) are often used to obtain the term β.

In practice, most environmental variables in equation (10.2) are obtained using physical equations, while the canopy conductance (g_c) is determined in an ecophysiological manner. For example, leaf-level stomatal gas conductivity (g_s) is given by the Ball-Berry model revised by Leuning (1995):

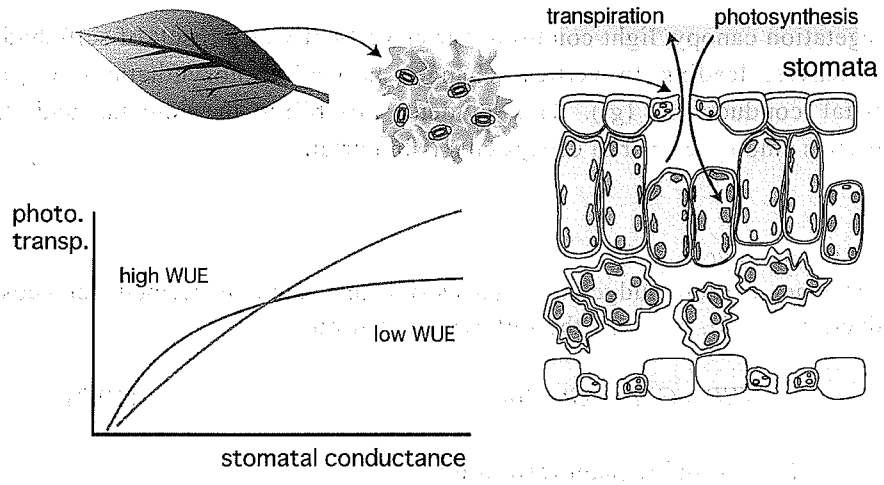

Figure 10.3 Exchange of vapor and CO_2 through leaf stomata.

$$g_s = a + b \cdot \frac{A}{\left(C_i - \Gamma\right) \cdot \left(1 + VPD/c\right)} \tag{10.4}$$

a, b, c: specific parameters
A: leaf net photosynthetic rate
C_i: intercellular CO_2 partial pressure
VPD: vapor pressure deficit at leaf surface
Γ: photosynthetic CO_2 compensation point

Accordingly, leaf-level transpiration (TR) is given as follows:

$$TR = g_s \cdot (e_s - e_a) = \frac{(e_s - e_a)}{r_s} \tag{10.5}$$

where r_s ($=1/g_s$) is the stomatal resistance. Then, canopy conductance (g_c) is obtained by integrating g_s for the whole canopy:

$$g_c = \int_0^{LAI} g_s \, dF \tag{10.6}$$

LAI: leaf area index, that is, leaf area per unit ground area

In vegetation canopy, light condition varies vertically as a result of self-shading of plant leaves, leading to vertical changes in leaf photosynthetic rate (A) and stomatal conductance (g_s). This evident variability in stomatal and canopy properties among terrestrial ecosystems is important.

10.3.3 Carbon cycle

The net carbon budget of a terrestrial ecosystem is termed net ecosystem production (NEP), given by the following equation:

$$NEP = GPP - AR - HR \tag{10.7}$$

AR: autotrophic plant respiration
GPP: gross primary production
HR: heterotrophic soil microbial respiration

A positive value of NEP indicates a net uptake from the atmosphere to ecosystem (sink), while a negative value indicates a net release to the atmosphere (source). Net primary production (NPP) is the most important index of plant productivity, related to plant adaptation and crop and woody yields available for consumers:

$$NPP = GPP - AR \tag{10.8}$$

Table 10.1 shows the global total values of area, biomass, and NPP for major biomes. A positive value of NPP indicates plant growth, while a negative value indicates degradation.The carbon cycle of a terrestrial ecosystem is frequently represented by a box-flow model, that is, carbon SPAC (Figures 10.2 and 10.4).

The temporal change in plant (W_p), soil (W_s), and ecosystem ($W_e = W_p + W_s$) carbon pools is formulated as follows:

$$\frac{dW_p}{dt} = GPP - AR - LF = NPP - LF \tag{10.9}$$

$$\frac{dW_s}{dt} = LF - HR \tag{10.10}$$

$$\frac{dW_e}{dt} = \frac{dW_p}{dt} + \frac{dW_s}{dt} = NEP \tag{10.11}$$

LF: litter fall (deposition of dead biomass)

Actually, other carbon flows such as biomass burning, soil erosion and leaching, and human harvest can have a considerable effect on the ecosystem carbon budget (sometimes, known as net biome production, *NBP*).

Ecosystem carbon assimilation rate, *GPP*, is obtained by integrating the leaf-level CO_2 assimilation rate (P) for the whole canopy:

$$GPP = \int_0^{LAI} P \, dF \tag{10.12}$$

Table 10.1 Area, biomass, and net primary productivity per biome (Saugier et al., 2001).

Biome	Area (10^6 km^2)	Biomass (Pg C)	NPP (Pg C yr^{-1})
Tropical forests	17.5	340	21.9
Temperate forests	10.4	139	8.1
Boreal forests	13.7	57	2.6
Arctic tundra	5.6	2	0.5
Mediterranean shrublands	2.8	17	1.4
Crops	13.5	4	4.1
Tropical savanna and grasslands	27.6	79	14.9
Temperate grasslands	15	6	5.6
Deserts	27.7	10	3.5
Ice	15.5		
	149.3	652	62.6

The single-leaf photosynthesis rate (P) is primarily a function of the irradiance of photosynthetically active radiation (PAR, wavelengths of 400 to 700 nm). The single-leaf photosynthetic rate increases with PAR irradiance under dark conditions and gradually becomes saturated under bright conditions, as approximated by the following equations:

$$P \approx \frac{P_{\max} \cdot \phi \cdot I}{P_{\max} + \phi \cdot I} \tag{10.13}$$

$$\approx \frac{(\phi \cdot I + P_{\max}) - \sqrt{(\phi \cdot I + P_{\max})^2 - 4 \cdot \theta \cdot \phi \cdot I \cdot P_{\max}}}{2 \cdot \theta} \tag{10.14}$$

I: irradiance of PAR
P_{max}: maximum photosynthetic rate
ϕ: apparent light-use efficiency
θ: convexity of light-photosynthesis curve

Here, the physiological parameters (P_{max} and ϕ) vary with plant species and in

response to environmental and biological conditions such as temperature, ambient CO_2 concentration, soil water, leaf age, and nitrogen level (Figure 10.4). Therefore, more mechanistic photosynthesis models (Farquhar et al., 1980; Collatz et al., 1992) are used in many recent terrestrial ecosystem models. The net photosynthetic rate (A) used in equation (10.4) is defined by the following:

$$A = P - R_d = \frac{g_s}{1.56} \cdot (C_b - C_i) \tag{10.15}$$

C_b: partial pressure of CO_2 at leaf boundary layer

where the denominator 1.56 is a conversion coefficient for CO_2 diffusion. Monsi and Saeki (1953, 2005) found that PAR irradiance varies vertically in plant canopies and presented the following equation:

$$I(F) = I_0 \cdot \exp(-K \cdot F) \tag{10.16}$$

F: cumulative leaf area from the top of the canopy
I_0: PAR irradiance at the top of the canopy
K: light attenuation coefficient

Autotrophic plant respiration (AR) is evaluated with a two-component model:

$$AR = ARM(W_p, T_p) + ARG(\Delta W_p) \tag{10.17}$$

ARG: growth respiration
ARM: maintenance respiration
T_p: plant body temperature
ΔW_p: plant growth rate

ARM increases with temperature exponentially (approximately doubling with every 10°C of warming), whereas ARG increases with biomass growth rate. Specific rates of ARM and ARG differ among plant species and organs. Heterotrophic soil microbial respiration (HR) is a function of soil temperature (T_s) and soil moisture content (M_s):

$$HR = HR(W_s, T_s, M_s) \tag{10.18}$$

The environmental dependencies are parameterized in various manners: an

exponential curve for temperature, and a saturation curve for moisture.

Intra-ecosystem carbon transportation occurs by photosynthate allocation, litter fall, and soil formation, each of which are strongly regulated by physical and biological factors and difficult to simulate in a mechanistic manner. Thus, they are represented by some semi-empirical parameterization schemes on the basis of observations. For example, leaf phenology of temperate deciduous forest is usually determined by the cumulative temperature value (degree days) above a critical temperature.

10.3.4 Parameter calibration and model validation

Model parameter values should be appropriately determined on the basis of observational data to capture the water and carbon cycle and ecosystem dynamics. Leaf photosynthetic properties are available for many PFTs, while little data is available for plant respiration and root turnover rates. Therefore, many parameter values are determined through trial-and-error processes (calibration or tuning), so that model outputs come close to those of the observational data of for example, biomass or net primary productivity.

In many cases, validation of model results is a difficult issue, because there is not enough large-scale data, especially at the global scale. The International Biological Programme (IBP) provides an invaluable dataset of vegetation structure and functions such as biomass and net primary productivity. Also, the U.S. Oak Ridge National Laboratory provides a public database of NPP and other ecosystem properties through the web site (http://www-eosdis.ornl.gov/). Recently, several new technologies are expected to provide independent validation data for ecological models: remote sensing, tower-based flux measurement, and forward and inverse atmospheric transport models.

10.4 Ecohydrology

Both water (H_2O) and carbon (C) are essential resources for organisms, as most organic matter is composed of carbohydrates ($[CH_2O]_n$, e.g., starch and cellulose).

$$n \cdot CO_2 + n \cdot H_2O \leftrightarrow [CH_2O]_n + n \cdot O_2 \qquad (10.19)$$

Terrestrial plants acquire water mostly by root uptake. and carbon by photosynthesis, to build up their structure. However, they lose carbon by metabolic respiration, herbivory, and tissue and individual mortality, and water by transpiration. Water and carbon cycles are intimately linked through various

mechanisms, but to different degrees among terrestrial ecosystems. As mentioned above, the soil-plant-atmosphere continua (SPAC) concept provides us a useful framework in terms of water and carbon cycles in terrestrial ecosystems. For both water and carbon SPACs (Figure10.2), solar radiation is the primary driver while active exchange of water (vapor) and carbon (carbon dioxide) occurs at leaf surface stomata. In plant stems, water is transported upward by xylem, whereas carbon is transported downward by phloem.

Leaf area index (*LAI*) and canopy conductance (g_c) are key parameters when considering terrestrial water and carbon cycles. As shown in Eq. (10.4), carbon (*A*) and water (*VPD*) conditions affect stomatal gas conductivity, which regulates the rates of photosynthesis and transpiration. Water-use efficiency (*WUE*) is an index of the carbon-water relationship, defined at different scales:

$$WUE_{stomata} = \frac{GPP}{TR} \tag{10.20}$$

$$WUE_{canopy} = \frac{GPP - AR_{leaf}}{TR + IC} \tag{10.21}$$

$$WUE_{ecosystem} = \frac{GPP - AR}{TR + IC + EV} = \frac{NPP}{AET} \tag{10.22}$$

Globally, annual terrestrial *NPP* and *AET* are estimated as approximately 60 x 10^{15} g C yr^{-1} and 70 x 10^{15} kg H_2O yr^{-1}, respectively. Thus, average $WUE_{ecosystem}$ of the terrestrial biosphere is estimated to be 0.86 g C (kg H_2O)$^{-1}$; however, note that this varies widely among specific terrestrial ecosystems from deserts to humid forests.

Another important interface of the water and carbon cycles in terrestrial ecosystems likely takes place at the root surface, where soil water uptake and rhizodeposition (fine root turnover and exudation) occur simultaneously. Vertical distribution of plant roots was parameterized on the basis of many observations (Zeng, 2001):

$$F(d) = 1 - \frac{1}{2}\left(e^{-a \cdot d} + e^{-b \cdot d}\right) \tag{10.23}$$

a, *b*: parameters
d: depth
F(*d*): cumulative root fraction from soil surface to the depth *d*

The parameters (*a*, *b*) differ among PFTs: *a*, from 4.372 for (semi-) desert to 10.7 for short grass; *b*, from 0.978 for (semi-) desert to 2.614 for cropland. Additionally, the difference of rooting depth characterizes the hydrological

conditions of PFTs, ranging from 0.5 m in tundra with impermeable permafrost to 4.0 m in desert with deep weathering.

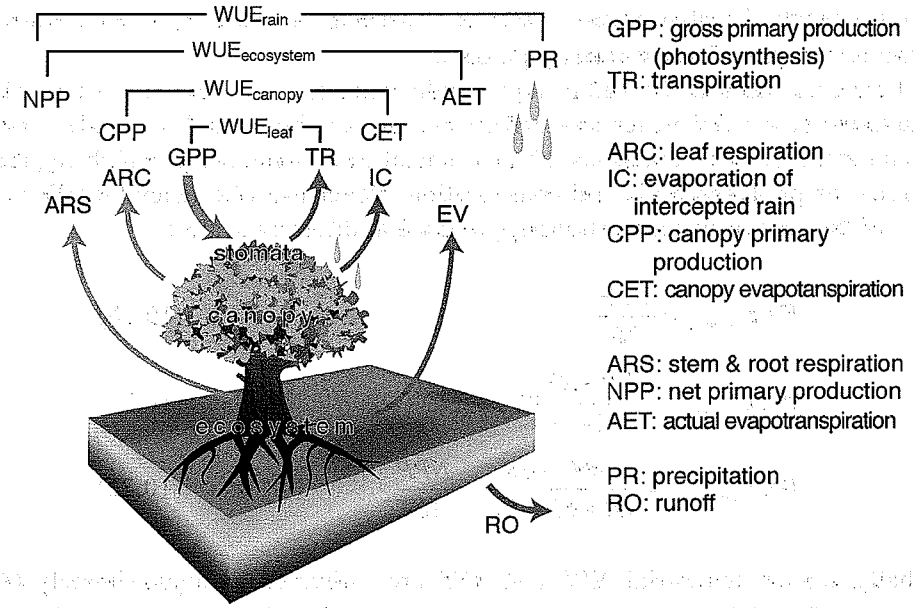

Figure 10.5. Water use efficiencies of a terrestrial ecosystem.

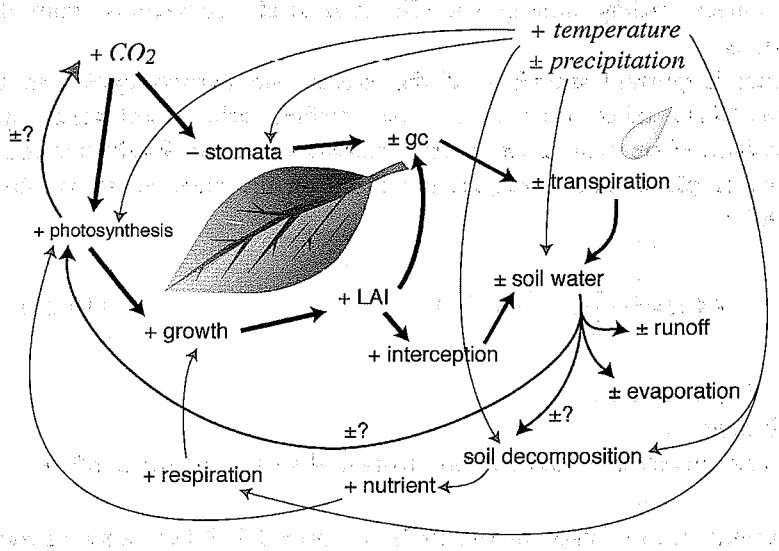

Figure 10.6. Physiological interactions of terrestrial ecosystem water and carbon cycles under global environmental change.

10.5 Ecosystem dynamics: climatic change and biome shift

Dynamic models are used to simulate transitional change in ecosystem structure (i.e. density, height, and species composition; Figure 10.7) that results as

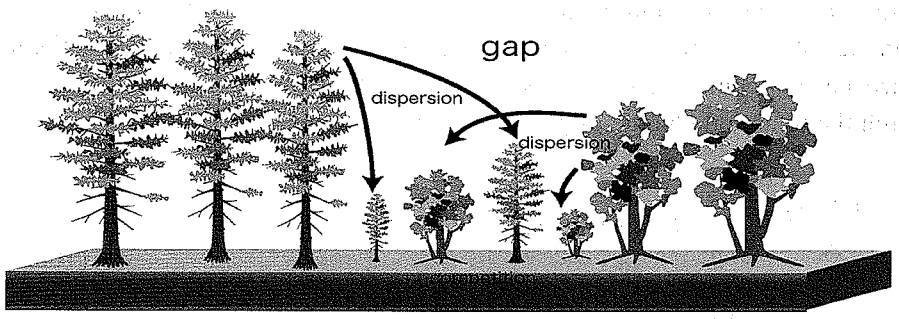

Figure 10.7. Concept of vegetation dynamics and biome shift.

a consequence of environmental survivorship and plant competition between individuals. However, competition a very complicated processes with respect to the acquisition of multiple resources such as light, water, and nutrients. Sometimes, obvious conflict takes place using allelopathy.

It is expected that global warming will result in re-distribution of vegetation types, generally toward higher latitudes and higher altitudes. Because elevated CO_2 concentration may lead to stomatal closure (saving water) and photosynthetic enhancement, some biomeshift would occur toward dryer regions, in addition to the effect of change in precipitation. Former models estimated the consequence of competition on the basis of primary productivity, because higher productivity of a plant type may imply better adaptation to a given environmental condition than other plant types. Since there is no general model to represent the competition process, the present DGVMs mimic competition in various conventional ways. For example, TRIFFID adopts a theoretical approach using the Lotka-Volterra model, in which biotic interactions are formulated by elementary differential equations.

$$\frac{dN_i}{dt} = r_i N_i \left(\frac{K_i - N_i - \sum_j c_{ij} N_j}{K_i} \right) \qquad (10.24)$$

c_{ij}: competitive effect from PFT j to PFT i

r_i: growth coefficient of PFT i
K_i: environmental capacity of PFT i
N_i: population size of plant functional type (PFT) i

Here, the strength of the competition effect is assumed to be proportional to population size; this model may be too simple to take into consideration the coexistence mechanism by niche-separation. Several models adopt a theoretical approach of population dynamics (e.g., MINoSGI by Watanabe et al., 2004), in which the temporal change of plant size-distribution is expressed by:

$$\frac{\partial f^i(t,h)}{\partial t} = \frac{1}{2}\frac{\partial^2}{\partial h^2}\left[D^i(t,h)f^i(t,h)\right] - \frac{\partial}{\partial h}\left[G^i(t,h)f^i(t,h)\right] - M^i(t,h)f^i(t,h) \tag{10.25}$$

i: species identifier
h: height class
t: time
f: population density
G: mean height growth rate
D: variance of height growth rate
M: mortality

Recently, a few DGVMs (e.g., Hybrid model by Friend and White, 2000; SEIB model by Sato et al., submitted) simulate the competition process in an explicit manner, using individual-based gap models. In these models individual trees are explicitly simulated in a small three-dimensional space; they appear, grow up, and die under a given environmental condition. If the net carbon budget of an individual becomes negative as a result of interference from other individuals or harsh environmental conditions (e.g. shading and chilling), it cannot survive any longer. Consequently, such individual-based DGVMs can take the time lags of ecosystem transition into account, but they require great computational power.

10.6 Applications

10.6.1 Local simulation

Terrestrial ecosystem models including DGVM are applicable to interpret local-scale atmosphere-land surface exchanges, biogeochemical and hydrological

cycles, and ecosystem dynamics. One of the recent applications is a model analysis of tower-based flux measurement data by means of the eddy-covariance method (cf. Fluxnet; Baldocchi et al., 2001). The data show diurnal, seasonal, and interannual variability in net ecosystem CO_2 exchange (*NEE*, = *–NEP*), but do not provide physiological or ecological mechanisms. Figure 10.8 represents an example of a plot-scale model simulation (Ito et al., in press) for a cool-temperate deciduous broad-leaved forest in Takayama, central Japan. This study revealed that leaf aging is an important factor for the seasonal change in *NEE*, in addition to environmental conditions and leaf phenology.

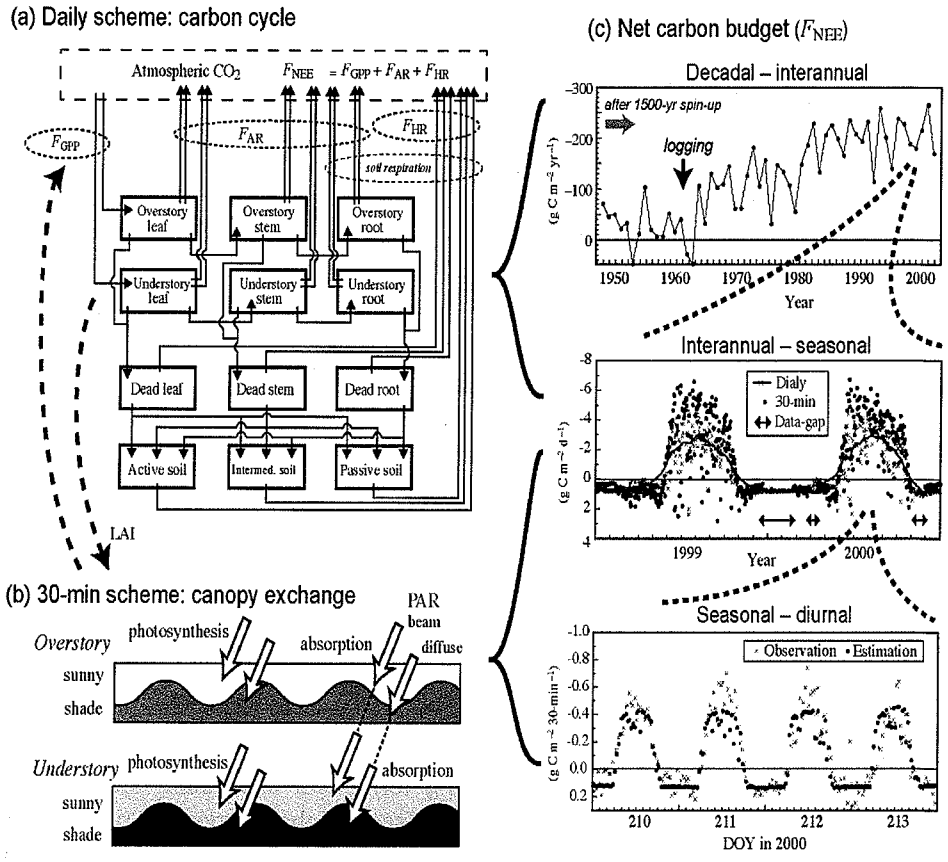

Figure 10.8 Simulation results of carbon cycle at Takayama site, Japan, for different time scales from hours to decades, using a model developed by Ito et al. (in press). (a) Schematic diagram of carbon cycle, (b) sunny/shade parameterization of canopy photosynthesis, and (c) estimated net ecosystem carbon budgets.

10.6.2 Regional simulation

Terrestrial ecosystem models have been used to simulate broad-scale carbon and water cycles, in, for example, the Asian region. Appropriate datasets of vegetation, land-use, soil, topography, and climate are required to perform such broad-scale simulations. Ito (2003) developed a model simulating the East Asian carbon cycle, using a satellite-based land-cover map (Figure 10.9). Such regional models will be useful for analyzing country- and watershed-level budgets of carbon and water and for planning management strategies of terrestrial ecosystems (e.g., carbon management for the Kyoto Protocol).

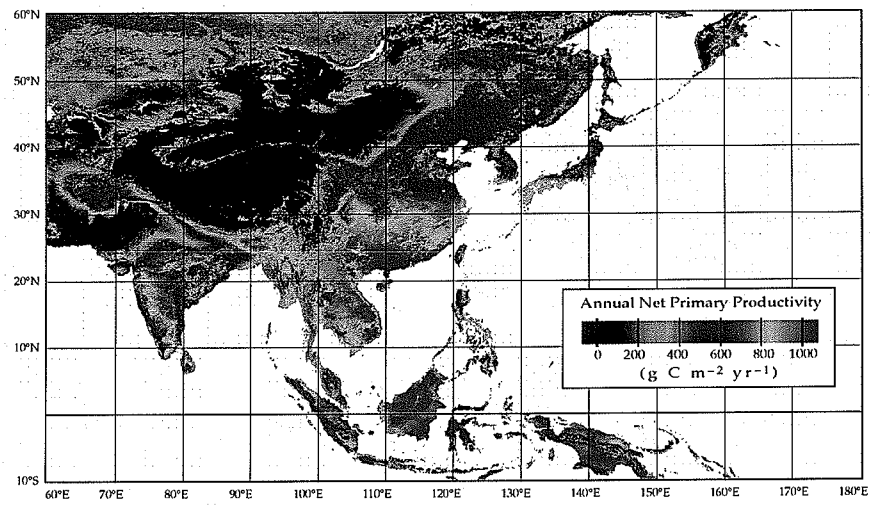

Figure 10.9 Net primary productivity of terrestrial ecosystems estimated by a process-based model Sim-CYCLE developed by Ito and Oikawa (2002).

10.6.3 Global simulation

Since the first attempt by Esser (1987), terrestrial ecosystem models have been widely applied to numerical global analyses. Global terrestrial net primary productivity under the current and global-warming conditions was estimated by Melillo et al. (1993). Cramer et al. (2001) compared the simulation results by six DGVMs with respect to PFT distribution and water and carbon cycles, under the contemporary and changing conditions. Figure 10.10 shows the seasonal and latitudinal patterns of global terrestrial water and carbon cycles using a process-based model Sim-CYCLE (Ito and Oikawa, 2002, 2004). Taken together, terrestrial ecosystem models have become an effective tool to analyze the impacts of climatic change on terrestrial ecosystems and the feedback from the ecosystems

through atmosphere-land surface exchange processes.

Recently, the Sim-CYCLE and a newly developed dynamic vegetation scheme have been included as components of the integrated Earth System model developed at the Frontier Research Center for Global Change (Kawamiya et al., in press). This model is operating on the Earth Simulator (the 7th fastest super-computer in the world) and is expected to provide novel predictions about future global change.

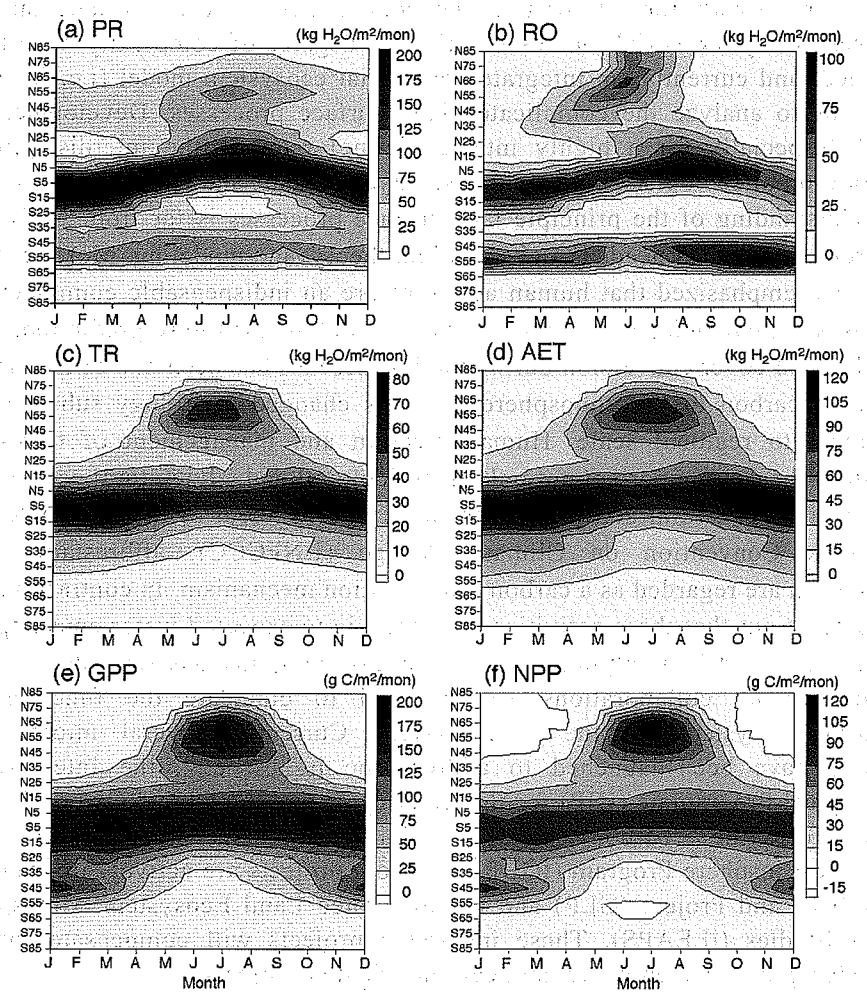

Figure 10.10 An example of global simulation results with Sim-CYCLE. Seasonal-latitudinal patterns of (a) PR, precipitation, (b) RO, runoff, (c) TR, transpiration, (d) AET, actual evapotranspiration, (e) GPP, gross primary production, and (f) NPP, net primary production.

10.7 Concluding remarks

As our understanding of land surface processes advances, an integrated point of view becomes increasingly important for predicting the response of terrestrial ecosystems to environmental impacts. In particular, when considering long-term changes in land surface processes, we cannot neglect the growth and dynamics of terrestrial ecosystems. The concept of coupled water and carbon cycles provide us a useful framework for interpreting the complicated features of land surface processes. Many terrestrial models of different degrees of complexity have been developed, and currently, an integrated terrestrial ecosystem model (i.e. DGVM) enables us to analyze the complicated land surface processes. Development of DGVM (especially for a highly integrated one) requires the interdisciplinary collaboration of ecologists, biogeochemists, hydrologists, and meteorologists.
Our understanding of the principle land surface processes is far from sufficient, and further research is needed in observation, theory, and modeling. More recently, it has been emphasized that human activities are an indispensable component of the ecosystem dynamics and climate system modeling for future predictions. For example, land cover conversion during the last decades has been one of the largest sources of carbon to the atmosphere, and has changed hydrology substantially from local to regional scale. Human creation and management of terrestrial ecosystems became important not only in agricultural and silvicultural ecosystems but also in most natural ecosystems. In the Kyoto Protocol of the United Nation Framework Convention on Climate Change (UNFCCC), afforestation and reforestation are regarded as a carbon sequestration mechanism. In contrast, recent studies point out that these activities can result in unexpected water consumption (Jackson et al., 2005), implying the importance of integrated assessments.

International collaborations are essential to elucidate the functions of terrestrial ecosystems in the earth system. Currently, several international programs have been launched to address the issues: e.g., the International Hydrological Programme (IHP) for the water cycle and the Global Carbon Project (GCP) for the carbon cycle. Additionally, in the International Geosphere-Biosphere Program (IGBP), two core projects are actively in progress: the Global Land Project (GLP) and the Integrated Land Ecosystem Atmosphere Process Studies (iLEAPS). These integrated projects will compensate for the knowledge gaps between water- and carbon-oriented projects.

Acronyms

AET: Actual Evapotranspiration
CLM: Community Land Model
DGVM: Dynamic Global Vegetation Model
IBIS: Integrated Biosphere Simulator
LPJ: Lund-Potsdam-Jena (model)
MAPSS: Mapped Atmosphere-Plant-Soil System
MINoSGI: Multilayered Integrated Numerical Model of Surface Physics Growing Plants Interaction
PET: Potential Evapotranspiration
PFT: Plant Functional Type
TRIFFID: Top-down Representation of Interactive Foliage and Flora Including Dynamics
SDGVM: Sheffield Dynamic Global Vegetation Model
SEIB: Spatially Explicit Individual-Based (model)
Sim-CYCLE: Simulation model of Carbon cYCle in Land Ecosystems
SPAC: Soil-Atmosphere-Plant Continuum

References

Arora, V., K., (2002), Modeling vegetation as a dynamic component in soil-vegetation-atmosphere transfer schemes and hydrological models, Reviews of Geophysics, 40, doi: 10.1029/2001RG000103.

Baldocchi, D., et al, (2001), FLUXNET: a new tool to study the temporal and spatial variability of ecosystem-scale carbon dioxide, water vapor, and energy flux densities, Bulletin of the American Meteorological Society, 82, 2415-2434.

Bonan, G.B., et al, (2003), A dynamic global vegetation model for use with climate models: concepts and description of simulated vegetation dynamics, Global Change Biology, 9, 1543-1566.

Collatz, G.J., et al, (1992), Coupled photosynthesis-stomatal conductance model for leaves of C4 plants, Australian Journal of Plant Physiology, 19, 519-538.

Cox, P.M., (2001), *Description of the "TRIFFID" dynamic global vegetation model*, Hadley Centre technical note, Hadley Centre, UKMO, 16 pp.

Cox, P.M., et al, (2000), Acceleration of global warming due to carbon-cycle feedbacks in a coupled climate model, Nature, 408, 184-187.

Cramer, W., et al, (2001), Global response of terrestrial ecosystem structure and function to CO_2 and climate change: results from six dynamic global vegetation models, Global Change Biology, 7, 357-373.

Esser, G., (1987), Sensitivity of global carbon pools and fluxes to human and potential climatic impacts, Tellus, 39B, 245-260.
Farquhar, G.D., et al, (1980), A biochemical model of photosynthetic CO_2 assimilation in leaves of C3 species, Planta, 149, 78-90.
Foley, J.A., et al, (1996), An integrated biosphere model of land surface processes, terrestrial carbon balance, and vegetation dynamics, Global Biogeochemical Cycles, 10, 603-628.
Foley, J.A., et al, (2000), Incorporating dynamic vegetation cover within global climate models, Ecological Applications, 10, 1620-1632.
Friend, A.D., and White, A., (2000), Evaluation and analysis of a dynamic terrestrial ecosystem model under preindustrial conditions at the global scale, Global Biogeochemical Cycles, 14, 1173-1190.
Ito, A., (2003), High-resolution mapping of the net primary productivity of terrestrial ecosystems in East Asia using a process-based model, Journal of Agricultural Meteorology, 59, 23-34.
Ito, A., and Oikawa, T., (2002), A simulation model of the carbon cycle in land ecosystems (Sim-CYCLE): A description based on dry-matter production theory and plot-scale validation, Ecological Modelling, 151, 147-179.
Ito, A., and Oikawa, T., (2004), Global mapping of terrestrial primary productivity and light-use efficiency with a process-based model, in Global Environmental Change in the Ocean and on Land, edited by M, Shiyomi, pp, 343-358, TERRAPUB, Tokyo.
Ito, A., et al, (2005), Modeling of gross and net carbon dioxide exchange over a cool-temperate deciduous broad-leaved forest in Japan: Analysis of seasonal and interannual change, Agricultural and Forest Meteorology, 134, 122-134.
Ito, A., et al, (2006), Seasonal variation in leaf properties and ecosystem carbon budget in a cool-temperate deciduous broad-leaved forest: simulation analysis at Takayama site, Japan, Ecological Research, 21, 137-149.
Jackson, R.B., et al, (2001), Water in a changing world, Ecological Applications, 11, 1027-1045.
Jackson, R.B., et al, (2005), Trading water for carbon with biological carbon sequestration, Science, 310, 1944-1947.
Kawamiya, M., et al, (in press), Development of an Integrated Earth System Model on the Earth Simulator, Journal of the Earth Simulator.
Leuning, R., (1995), A critical appraisal of a combined stomatal-photosynthesis model for C3 plants, Plant, Cell and Environment, 18, 339-355.
Melillo, J.M., et al, (1993), Global climate change and terrestrial net primary production, Nature, 363, 234-240.
Neilson, R.P., et al, (1992), Toward a rule-based biome model, Landscape Ecology, 7, 27-43.
Prentice, I.C., et al, (1992), A global biome model based on plant physiology and dominance, soil properties and climate, Journal of Biogeography, 19, 117-134.
Sato, H., et al, (in press), SEIB–DGVM: A new Dynamic Global Vegetation Model using a spatially explicit individual-based approach, Ecological

Modelling.
Saugier, B., et al, (2001), Estimations of global terrestrial productivity: Converging toward a single number?, in Terrestrial Global Productivity, edited by J, Roy, et al., pp, 543-557, Academic Press, San Diego.
Sellers, P.J., et al, (1997), Modeling the exchanges of energy, water, and carbon between continents and the atmosphere, Science, 275, 502-509.
Sitch, S., et al, (2003), Evaluation of ecosystem dynamics, plant geography and terrestrial carbon cycling in the LPJ dynamic global vegetation model, Global Change Biology, 9, 161-185.
Watanabe, T., et al, (2004), Developing a Multilayered Integrated Numerical model of Surface physics-Growing plants interaction (MINoSGI), Global Change Biology, 10, 963-982.
Woodward, F.I., et al, (1995), A global land primary productivity and phytogeography model, Global Biogeochemical Cycles, 9, 471-490.
Woodward, F.I., and Lomas, M.R., (2004), Vegetation dynamics-simulating responses to climatic change, Botanical Review, 79, 643-670.
Zeng, X., (2001), Global vegetation root distribution for land modeling, Journal of Hydrometeorology, 2, 525-530.

Further readings

Beerling, D.J., and Woodward, F.I., (2001), *Vegetation and the Terrestrial Carbon Cycle*, Cambridge University Press, Cambridge, 405pp.
Bonan, G., (2002), *Ecological Climatology: Concepts and Applica*tions, Cambridge University Press, Cambridge, 678pp.
Jones, H.G., (1992), *Plants and Microclimate, 2nd ed.*, Cambridge University Press, Cambridge, 428pp.
Larcher, W., (2001), *Physiological Plant Ecology: Ecophysiology and Stress Physiology of Functional Groups, 4th Edition, 4th ed.*, Springer-Verlag, 513pp.
Woodward, F.I., (1987), Climate and Plant Distribution, Cambridge University Press, Cambridge.

Part II

Outline of the Training Course in 2005

Outline

As part of the Japanese contribution to the International Hydrological Programme (IHP), a short course for participants from the Asia-Pacific region will be conducted on Water and Carbon Cycles in Terrestrial Ecosystems, from 26 February to 11 March 2006, at the Hydrospheric Atmospheric Research Center (HyARC) and Graduate School of Environmental Studies, Nagoya University, Nagoya, Japan. The course will include a series of lectures in English, practice sessions and technical tours to the Center for Environmental Remote Sensing (CEReS), Chiba University, the Earth Simulator Center, Japan Agency for Marine-Earth Science and Technology (JAMSTEC).

Part of this IHP training course is co-organized by the 21st Century COE Program at Nagoya University: Dynamics of the Sun-Earth-Life Interactive System (SELIS). Thus some candidates will be financially supported, in part, by funds from the 21st Century COE Program.

Objectives

The general aim of the 15th IHP short course is to help participants develop their basic knowledge of the Water and Carbon Cycles in Terrestrial Ecosystems in the solution of current global environmental problems. To detect and predict responses of terrestrial ecosystems to global change is one of the important scientific issues in global environmental studies. To cope with such issues, a basic understanding of physical and biogeochemical nature of water and carbon cycles in various terrestrial ecosystems is required. Micrometeorological and biogeochemical knowledge and techniques, including use of stable isotopes of H_2O and CO_2 and numerical modeling, are the basis for this understanding.

The course will focus on two major subjects. The first is the examination of leaf- and canopy-scale exchange processes of heat, H_2O, and CO_2 with the surrounding atmosphere. The second is the study of the relationships of the vegetation dynamics with future climate feedbacks. The lectures and practice sessions will be conducted at Nagoya University and Chiba University.

Course Contents (convener: T. Hiyama)

Lecturers

A. Higuchi (Center for Environmental Remote Sensing (CEReS), Chiba University)
K. Hikosaka (Graduate School of Life Sciences, Tohoku University)
T. Hiyama (Hydrospheric Atmospheric Research Center (HyARC), Nagoya University)
A. Itou (Japan Agency for Marine-Earth Science and Technology (JAMSTEC))
E. Konohira (Graduate School of Environmental Studies, Nagoya University)
T. Ohta (Graduate School of Bioagricultural Sciences, Nagoya University)
H. Shibata (Field Science Center for Northern Biosphere, Hokkaido University)
Y. Yamaguchi (Graduate School of Environmental Studies, Nagoya University)
T. Yamanaka (Terrestrial Environment Research Center (TERC), University of Tsukuba)
T. Yasunari (Hydrospheric Atmospheric Research Center (HyARC), Nagoya University)

List of Participants

1) UNESCO-IHP Participants

Mr. Bounhieng, Souvannahane (Lao P.D.R.)
Affiliation: Ministry of Agriculture and Forestry, Department of Meteorology and Hydrology (DMH)
Address: Luangprabang Road No 13, Ban Akad, Sikottabong Dist., P.O.Box 811 Vientiane Lao P.D.R.

Ms. Maria Antonia, N., Tanchuling (Philippines)
Affiliation: Department of Civil Engineering, College of Engineering, University of the Philippines
Address: Diliman, Quezon City 11 Metro Manila, Philippines

Ms. Yustiawati Syawal (Indonesia)
Affiliation: Research Centre for Limnology, Indonesian Institute of Sciences
Address: Kompleks LIPI Cibinong, Jl. Raya Jakarta - Bogor, KM 46, Cibinong Bogor Jawa Barat 16911, Indonesia

Ms. Tin Tin Htwe (Myanmar)
Affiliation: Department of Meteorology and Hydrology
Address: Kaba-Aye, Pagoda Road, Mayangon 11061, Yangon, Myanmar

Mr. Rupak Man Rajbhandari (Nepal)
Affiliation: Department of Meteorology, Trichandra Campus, Tribhuvan University
Address: Post Box # 328, Kathmandu, Nepal

Mr. Maino Virobo (PNG)
Affiliation: Department of Environment and Conservation
Address: P.O. Box 6601, Boroko, National Capital District, Papua New Guinea Street, 5th Floor Somare Foundation Building Conor Sir John Guise Drive, WAIGANI National Capital District, Papua New Guinea

Mr. Le Xuan Tuan (Vietnam)
Affiliation: Mangrove Ecosystem Research Division (MERD), Centre for Natural Resources and Environmental Studies (CRES)
Address: Centre for Natural Resources and Environmental Studies (CRES), VNU No. 22, Luong Su B, Quoc Tu Giam St., Vietnam

2) Participants funded from 21st Century COE Program (SELIS)

Ms. Megan Elizabeth Berkle (USA)
Affiliation: Cooper City High School, Science Department
Address: 9401 Stirling Road, Cooper City, Florida 33328, USA

Ms. Armi May Mineza Torrechilla (Philippines)
Affiliation: Remote Sensing and Geographic Information Systems (FoS), School of Advanced Technologies, Asian Institute of Technology
Address: P.O. Box 4, Klong Luang, Pathumthani, 12120 Thailand

Mr. Andreas Albertino Hutahaean (Indonesia)
Affiliation: Research Center for Maritime Territories & Non-Living Resources (WILNON), Agency for Marine and Fisheries Research (BRKP)
Address: Jalan. MT. Haryono, Kav 52-53, 1st Floor, Jakarta 12770, Indonesia

Mr. Li Dan (China)
Affiliation: START-TEA, Institute of Atmospheric Physics, Chinese Academy of Sciences
Address: START-TEA, Institute of Atmospheric Physics, Chinese Academy of Sciences, Beijing, 100029, P. R. China

Mr. Toan Minh Hoang (Vietnam)
Affiliation: Aero-Meteorological Observatory
Address: Aero-Meteorological Observatory, Research. Add: 5/62 Nguyen Chi Thanh, Dong Da. Hanoi, Vietnam

Mr. Jirakorn Musikapunt (Thailand)
Affiliation: Research and Training Center on Resource Management and Geoinformatic System, Faculty of Engineering, Kasetsart University
Address: RM-GIS Center (Hansa Lab.), Room #4206, Engineering Computor Center, Faculty of Engineering, Kasetsart University, 50 Paholyothin Rd., Jatujak, BKK 10900, Thailand

3) Participants from Graduate School of Environmental Studies, Nagoya University

Mr. Jingmin Li (China)
Affiliation: Graduate School of Environmental Studies, Nagoya University, Japan
Address: Furo-cho, Chikusa-ku, Nagoya, Aichi 464-8601, Japan

Lectures

L0 Introduction..... T. Hiyama
- Guidance and outline of this IHP short course

L1 Canopy-Scale Fluxes of Heat, Water Vapor, and Carbon Dioxide in Various Terrestrial Ecosystems..... T. Hiyama
- Basic equations for the turbulent transport
- Eddy covariance technique for the surface flux estimation
- Carbon dioxide fluxes and net ecosystem exchange (NEE) in a terrestrial ecosystem
- Modeling of soil - vegetation - atmosphere transfers

L2 Water Cycle in Forested Area..... T. Ohta
- Water budget and vegetation
- Forest effects of water cycle -physiological effects and structural effects-
- Climate conditions and water cycle in forests
- Winter hydrological processes in forests

L3 Biogeochemical Processes of Carbon in Forested Ecosystem..... H. Shibata
- General principle of carbon cycling in a forested ecosystem
- Monitoring and analytical method of carbon dynamics
- Case studies of carbon dynamics in a forested basin

L4 Biogeochemical Processes of Nitrogen in Forested Ecosystem..... E. Konohira
- General principle of nitrogen cycling in a forested ecosystem
- Nitrogen in stream and forest environments
- Implications of carbon and nitrogen dynamics in forested ecosystem

L5 Assessment of Plant-Water Relations using Stable Isotope Tracers ..... T. Yamanaka
- Fundamentals of stable isotopes
- Methods for water sampling, extraction and analysis
- Water sources of plants and inter-specific interactions
- Canopy fluxes partitioning and water use efficiency
- Catchment water balance and ecosystem dynamics

L6 Integrated Use of Vegetation Indices and Surface Temperature Space obtained from Earth Observation Satellites Dataset..... A. Higuchi
- Introduction: Basics of optical and thermal-IR channels
- Examples of combined usage of vegetation indices and surface temperature
- Possibility for the detection of water and energy related information by the integrated uses of satellite remote sensing

L7 Observation of Global Vegetation Variations by Satellite Remote Sensing ..... Y. Yamaguchi
- Fundamentals of multi-spectral data analysis

- Vegetation indices
- Relationships between global vegetation variations and climate
- Estimation of terrestrial net primary production (NPP)

L8 Role of Vegetation for the Earth Climate System..... T. Yasunari
- Role of Tibetan Plateau and vegetation on Asian monsoon climate
- Climate and vegetation - an interactive and symbiotic system -
- Possible impact of vegetation change on the earth climate system

L9 Plant Responses to Elevated CO_2 Concentration at Different Scales: Leaf, Whole Plant, Canopy, and Population
..... K. Hikosaka
- Effect of seasonal acclimation on photosynthesis at elevated CO_2
- Nitrogen limits seed production of annuals at elevated CO_2
- Canopy structure and photosynthesis at elevated CO_2
- Competition for light in mono-specific stands of annual plants at elevated CO_2

L10 Dynamic Global Vegetation Model (DGVM)..... A. Itou
- Effectiveness of model simulation for global change
- How will terrestrial ecosystems respond to global warming ?
- Dynamic models of water and carbon cycles in terrestrial ecosystems
- Earth-system modeling for advanced prediction of climatic change

Practice Sessions

P1 Measurement and Estimation of Canopy-Scale Fluxes..... T. Hiyama
- Eddy covariance techniques for canopy-scale fluxes
- Bulk transfer equations for canopy-scale fluxes

P2 Satellite Measurements of Vegetation Condition and NPP..... Y. Yamaguchi
- Visualization of satellite remote sensing data
- Calculation of NDVI and estimation of NPP

P3 Satellite Measurements of Vegetation and Hydrologic Condition.. A. Higuchi
- Comparison of canopy-scale fluxes with remotely sensed variables
- Ts/VI technique to detect soil moisture condition

Technical Tours

T1 Flux Research Site of a Secondary Forest at Seto..... T. Ohta

T2 Terrestrial Environment Research Center (TERC), University of Tsukuba
..... T. Yamanaka

T3 Center for Environmental Remote Sensing (CEReS), Chiba University
..... A. Higuchi

T4 The Earth Simulator Center, JAMSTEC..... A. Itou & T. Yasunari
- Visit to Center for The Earth Simulator Center for atmospheric, terrestrial and oceanic simulations with satellite earth observation

Schedule (26 February - 11 March, 2006)

26 (Sunday) Feb., 2006	Arrival at Nagoya	Stay in Nagoya
27 (Monday)	Guidance (Lecture 0), Lectures 1 & 2 Reception at Nagoya University	Stay in Nagoya
28 (Tuesday)	Lecture 4, Technical Tour 1	Stay in Nagoya
01 (Wednesday) Mar., 2006	Lecture 5 Practice 1	Stay in Nagoya
02 (Thursday)	Lectures 6 & 7	Stay in Nagoya
03 (Friday)	Practice 2, Lecture 8	Stay in Nagoya
04 (Saturday)	Discussion	Stay in Nagoya
05 (Sunday)	Japanese Culture Introduction and Free Time	Stay in Nagoya
06 (Monday)	Lectures 9 & 10	Stay in Nagoya
07 (Tuesday)	Lecture 3, Technical Tour 2 (move to Tsukuba & Chiba)	Stay in Chiba
08 (Wednesday)	Technical Tour 3, Practice 3	Stay in Chiba
09 (Thursday)	Technical Tour 4	Stay in Chiba
10 (Friday)	Closing Ceremony	Stay in Chiba
11 (Saturday)	Departure from Narita Airport	